UNIVERSITY OF SOUTHAMPTON

FACULTY OF HUMAN AND SOCIAL SCIENCES

Mathematical Sciences

Advanced numerical methods for neutron star interfaces

by

John Christopher Muddle

Thesis for the degree of Doctor of Philosophy

February 2015

UNIVERSITY OF SOUTHAMPTON

ABSTRACT

FACULTY OF HUMAN AND SOCIAL SCIENCES
Mathematical Sciences

Doctor of Philosophy

ADVANCED NUMERICAL METHODS FOR NEUTRON STAR INTERFACES

by John Christopher Muddle

This thesis investigates advanced numerical methods for neutron star interfaces. Neutron star binary mergers are considered a strong source of gravitational waves. However, accurate gravitational wave templates are required to detect them. In turn, these templates require accurate numerical neutron star models.

Neutron star interiors are thought to consist of several different regions, which are separated by thin transition layers. Millmore and Hawke developed a framework that approximates these transitions as infinitely thin interfaces and allows one to incorporate them into a numerical neutron star model. As modern neutron star models, used to calculate gravitational wave templates, include a magnetic field, we have extended the framework of Millmore and Hawke to incorporate a magnetic field. We show that this extension introduces a new physical effect that facilitates the redistribution of angular momentum within the star. This redistribution could lead to a change in the time taken for the merged neutron stars to collapse into a black hole.

We have also developed a new approximate solution to the multi-material Riemann problem called the multi-material Riemann Ghost Fluid Method (mRGFM). This method allows the combination of two different systems of hyperbolic conservation laws across an interface. We demonstrate that this approach is capable of correctly capturing the locations of strong shock waves. Strong shock waves will develop during the chaotic merger phase.

Finally, we have presented the first coupling between a fluid interior and a vacuum exterior for a toy star. This result can mimic the surface of a star. Current simulations approximate the surface of a neutron star with an unphysical atmosphere. We use the mRGFM to apply realistic boundary conditions at the surface.

Contents

List of Figures

List of Tables

Declaration of Authorship

I, John Christopher Muddle, declare that the thesis entitled *Advanced numerical methods for neutron star interfaces* and the work presented in the thesis are both my own, and have been generated by me as the result of my own original research. I confirm that:

- this work was done wholly or mainly while in candidature for a research degree at this University;
- where any part of this thesis has previously been submitted for a degree or any other qualification at this University or any other institution, this has been clearly stated;
- where I have consulted the published work of others, this is always clearly attributed;
- where I have quoted from the work of others, the source is always given. With the exception of such quotations, this thesis is entirely my own work;
- I have acknowledged all main sources of help;
- where the thesis is based on work done by myself jointly with others, I have made clear exactly what was done by others and what I have contributed myself;
- none of this work has been published before submission

Signed:.....

Date:.....

Acknowledgements

First, I would like to thank my supervisor Ian Hawke for all of his help and guidance throughout my degree. His friendly, open door and honest approach to tutoring was very much appreciated. This approach encapsulates the general ethos of the general relativity group at Southampton, and I feel incredibly lucky to have been given the opportunity to be a member of it. Therefore, I thank all those members who's time has overlapped with mine and made it so enjoyable.

I would like to acknowledge the studentship funding from the STFC and the use of the IRIDIS High Performance Computing Facility, and associated support services at the University of Southampton, in the completion of this work. I would also like to recognise the helpful discussions I have had with Nils Andersson, Kiki Dionysopoulou, Stephanie Erickson, Carsten Gundlach, Tim Lemon and Steve Millmore while undertaking this research. Finally, I would like to thank my examiners Ian Jones and Mark Hannam for their fair and insightful questioning.

As I reach the end of my time in Southampton, I would like to thank all of the friends that I've made over the past eight years. This is especially true for a small cohort who also went on to study a PhD. I am also grateful to all of the many housemates I have lived with who made Southampton feel like home.

I would like to take this opportunity to acknowledge the support of all my friends from home. In particular, I would like to single out Carl Brooker and Graeme Thompson for their encouragement, their phone calls and providing me with opportunities to escape Southampton and relax over the last four years.

One person in particular deserves a special mention. I would like to thank Vanessa Graber for feeding me, providing me with a home, proofreading this thesis and the endless supply of hugs and encouragement. Thank you.

Finally, all of this could not have been possible without the love and support of my family. I wish to thank all of them for the sacrifices that they have made to provide me with the opportunities that I have had.

I dedicate this thesis to my grandparents:

Frank and Barbara Muddle

&

Arthur and Gillian Roberts

Chapter 1

Introduction

This thesis introduces advanced numerical methods that can be used to build and evolve a relativistic multi-component neutron star model. These new methods make it possible to construct a neutron star model that includes a neutron star's internal structure and magnetic field. Including these physical features within a model will improve the accuracy of gravitational-wave templates calculated from numerical simulations. Accurate gravitational-wave templates are essential to detect gravitational waves directly, using laser interferometers.

Hulse and Taylor were the first to detect gravitational waves indirectly. They were awarded the 1993 Nobel Prize in Physics for this discovery [85, 171]. This indirect detection came from observing the binary pulsar PSR B1913+16. A pulsar is a rotating neutron star that emits beams of electromagnetic radiation from its magnetic poles. These beams rotate about the neutrons star's spin axis like a lighthouse. The detected signal is a pulse, hence the name pulsar. Binary systems, such as the one containing the Hulse-Taylor pulsar, are strong candidates for the first direct gravitational wave detection.

Directly detecting a gravitational wave is only possible if the gravitational-wave power produced by a system is sufficiently large. The gravitational-wave power emitted from a binary system is proportional to the total mass of the system divided by the separation to the fifth power [115]. A neutron star can have a mass between $1M_{\odot}$ and $3M_{\odot}$, with a typical mass of $1.4M_{\odot}$ [98]. A neutron star's radius cannot be measured directly, but it is possible to approximate it from the star's mass and an appropriate equation of state (EOS). A consequence of this is that radius estimates can vary from 6km to 15km, depending on the EOS; the canonical radius is 12km [98]. A binary system's separation can decrease to tens of kilometres due to a neutron star's compactness. Therefore, a binary system, containing a compact object, will produce a large amount of gravitational-wave power prior to coalescing due to the small separation and large total mass of the system.

A neutron star's exact components are unknown, but they are predicted to include nuclei, free nucleons, free electrons, quarks, kaons and other strange matter [98]. Its internal structure is complex and exotic due to its diverse constituents and compactness. It is predicted to have a stratified interior analogous to the Earth; each layer has a distinct physical character. Transitions between layers are complex and represent a phase transition in the physical matter. These transitions can have a physical size on the order of centimetres, such as the Ekman layer, which is the viscous boundary between the star's elastic crust and its fluid core [9].

A binary's merger phase is highly chaotic and relativistic; only a numerical simulation will accurately reproduce a system's dynamics. The first general-relativistic, numerical, double neutron star binary system simulation was performed by Shibata and Uryū in 1999 [161]. Since then, more sophisticated and complex simulations have been performed resulting in increasingly accurate gravitational-wave templates. However, modern numerical simulations are unable to resolve transitions between layers precisely due to a lack of computational power. Millmore and Hawke have developed a fully general-relativistic framework that approximates these transitions as infinitely thin interfaces [114]. The work presented in this thesis builds upon and extends their work. Including these interfaces, within binary neutron star simulations, will lead to new and exciting results.

This thesis also aims to extend Millmore and Hawkes work by including a magnetic field. Neutron star observations have suggested that a neutron star's magnetic field strength is enormous. One can approximate a pulsar's magnetic field strength from its observed pulse. If a pulsar's magnetic field is assumed to be dipolar, a reasonable approximation [144], one can show that the surface magnetic field strength squared, B^2, is proportional to the spin period, P, multiplied by its derivative with respect to time, $\dot{P}$ [105],

$$B^2 \propto P\dot{P}. \tag{1.1}$$

Since their discovery, hundreds of pulsars have been observed. Their magnetic fields have been approximated to be between 10^8G [144] and 10^{15}G [52], with a typical value of 10^{12}G [98]. As a comparison, a neutron star's magnetic field is up to six orders of magnitude stronger than the strongest pulsed source on Earth [32].

The following paragraphs outline the remainder of the introduction and motivation. Firstly, the majority of this chapter will explore a neutron star's complex and varied interior. It will detail the different layers and transitions that occur between a star's centre and exterior. Currently, these transitions are absent from modern numerical simulations. The work presented in this thesis will enable their inclusion along with a magnetic field.

Secondly, this introduction briefly examines the reasoning behind and the implications of including general relativity within a neutron star model. It will also explore the experiments that aim to detect gravitational waves directly from neutron stars.

Finally, the chapter discusses current simulations in numerical relativity. This section will outline some approaches to splitting space and time to allow numerical integration. Binary black hole simulations will be considered next, because they have acted as a forerunner. It will then examine the brief history of neutron star simulations and summarise the current status.

Neutron stars are the most extreme, exotic and exciting astronomical objects. General relativity is a well-tested physical theory that is on a par with quantum mechanics. Numerical relativity is a young and active research area that will pave the way for the direct detection of gravitational waves and a new era of multi-messenger astronomy. These three reasons have motivated us to develop the numerical methods presented in this thesis.

1.1 Neutron Stars

Neutron stars present a unique opportunity to explore the extremes of condensed matter and magnetic fields. They are among the most exotic and complex phenomena in the Universe. They contain roughly one and a half times the Sun's mass within a volume that is fourteen orders of magnitude smaller. They also possess the strongest known magnetic fields within the Universe. The work presented in this thesis will lead to better neutron star simulations and therefore a better understanding of their physical counterparts.

The existence of neutron stars was first predicted by Baade and Zwicky in 1934, based on their supernova population analysis [15]; this prediction was made just after Chadwick's discovery of the neutron in 1932 [35]. They predicted that as a star's nuclear fuel ran out it would produce a supernova, which would leave a remnant containing a neutron star. Hewish et al. first discovered a pulsar in 1967 [78]. The pulsar they observed emitted a pulse with a frequency of 0.747Hz. Gold then proposed in 1968 that the newly discovered pulsar was a rotating neutron star [67]. He based his proposal on the idea that no other theoretical or known astronomical object could possess such a short periodicity. To date, observations have led to the identification of over two thousand neutron stars [126].

1.1.1 Neutron star formation

Neutron star formation is key to understanding why neutron stars possess such extreme physical properties. Stellar evolution suggests that a neutron star is formed from a supernova, just as Baade and Zwicky had proposed. Two of the youngest observed neutron stars, the Crab pulsar and the Vela pulsar, are both contained within their supernova remnants; the Crab's supernovae was observed by ancient astronomers [97, 142, 166]. A supernova occurs, when the progenitor star can no longer maintain hydrostatic equilibrium after its nuclear fuel has run out. The star can no longer produce enough thermal pressure to counteract its self-gravity. What happens to the progenitor next is primarily determined by its mass.

If the progenitor's mass is between $1M_\odot < M \lesssim 8M_\odot$ [157], then the gravitational pressure within the core is large enough to facilitate the production of heavier elements up to oxygen. At this point, the gravitational pressure dominates and the core collapses to form a white dwarf; material expelled during the collapse, between $0.1M_\odot$ and $1M_\odot$, is believed to form planetary nebulae. The electron degeneracy pressure, due to the Pauli exclusion principle, prevents the white dwarf from further collapse. The Pauli exclusion principle states that two fermions cannot occupy the same quantum state at the same time. Therefore, the electrons form a Fermi gas that exerts a pressure that counteracts the gravitational pressure. In 1931, Chandrasekhar calculated the maximum mass that can be supported by degenerate, relativistic electrons to be approximately $1.44M_\odot$ [37]. If a white dwarf exceeds this mass through some mechanism such as accretion, it will collapse into a neutron star or a black hole.

If the progenitor's mass is greater than eight solar masses, $M > 8M_\odot$, then the gravitational pressure in the centre is large enough to facilitate the production of heavier elements up to nickel. An inert iron-nickel core will form within the progenitor. As before, the electron degeneracy pressure will prevent the core from collapsing. Once the Chandrasekhar limit has been breached, the core continues to collapse and the outer layers fall inwards, reaching relativistic velocities. Inside the core, electrons and protons fuse to form neutrons and neutrinos through inverse beta decay,

$$p + e^- \rightarrow n + \nu_\mathrm{e}. \tag{1.2}$$

Neutrons are also fermions and are subject to the Pauli exclusion principle like electrons. Therefore, a degeneracy pressure forms that halts the core collapse producing a neutron star. This sudden halting causes the core to bounce, which creates a shock wave that propagates away from the core. The shock wave becomes optically transparent to the neutrinos produced in the core and stalls [59]. The shock leaves an entropy profile behind that is convectively unstable. If this region can gain enough energy, a successful supernova explosion can occur; this is known as a Type II supernova. The mechanism that restarts the shock is currently unknown. Some possible mechanisms involve neutrinos, rotation, convection and magnetic fields [98].

The final scenario happens when the neutron degeneracy pressure can no longer prevent a neutron star's core collapsing to a black hole. The collapse occurs when the mass of the core exceeds the Tolman-Oppenheimer-Volkoff limit, which is analogous to the Chandrasekhar limit [122].

1.1.2 Neutron star structure

Having discussed neutron star formation, the next section will focus on a neutron star's internal structure. It will concentrate on a neutron star that has reached what can be considered an equilibrium state. A neutron star's density is of the order of the nuclear density due to its compactness. The nuclear density, $\rho_{\mathrm{N}} = 2 \times 10^{14}\mathrm{g\ cm}^{-3}$, is the density of the atomic nucleus [157]. A neutron star's density is believed to vary from $0.5\rho_{\mathrm{N}}$ at the surface to $10\rho_{\mathrm{N}}$ at its core [98].

Another important variable to consider is the temperature within the neutron star. Neutron stars have an internal temperature in the range of 10^6 – 10^8K [6]. This is below the star's Fermi temperature, $T_{\mathrm{Fermi}} \approx 10^{12}$K [6]; the Fermi temperature corresponds to the energy difference between the highest and the lowest occupied quantum state. As a consequence of star's temperature being below its Fermi temperature, the EOS can be approximated to be a function of the density alone and is barotropic [145]. In reality, this is a simplification that is not true during the merger phase of a neutron star binary, but one can gain a good understanding of the internal structure without considering temperature dependent EOSs .

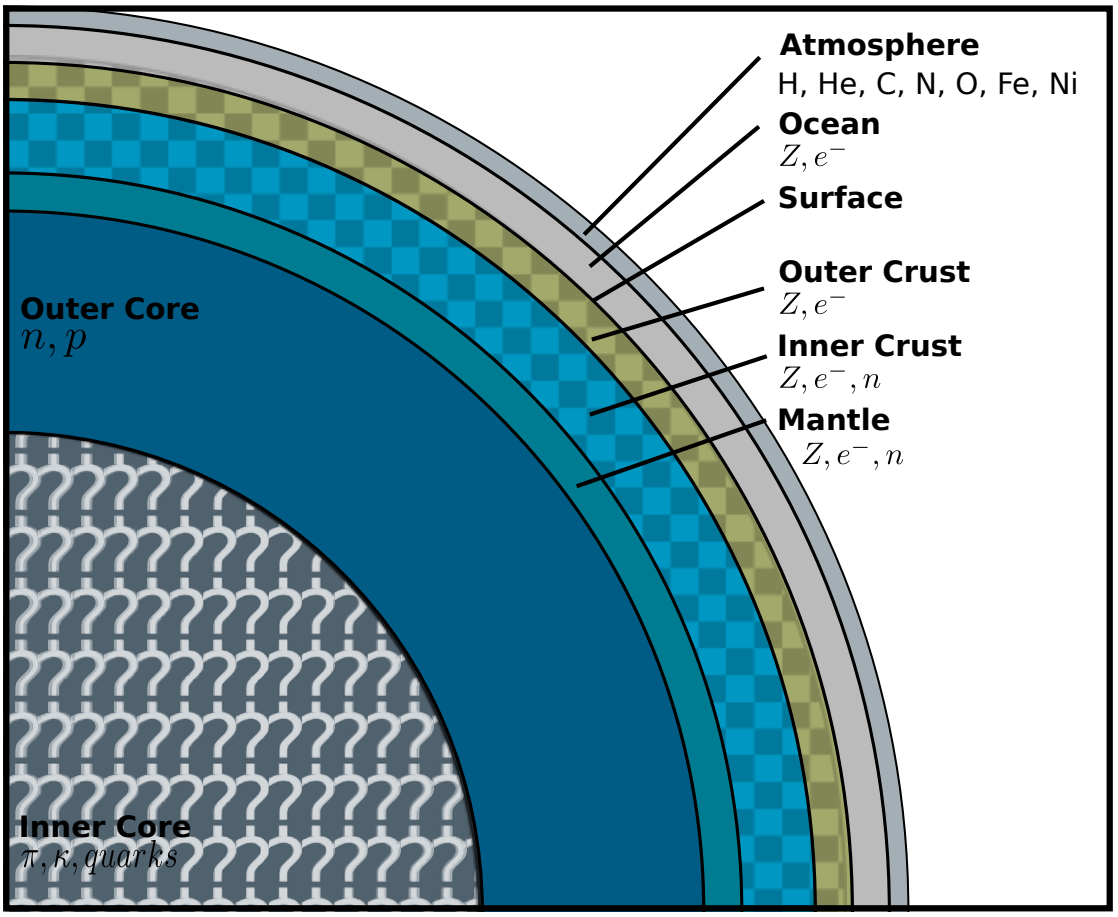

Figure 1.1 – A representative cross-section of a neutron star with the important layers labelled. The labels list the constituents of each layer with π for pions, κ for kaons, and Z for ions. The checker-board pattern indicates where there is a crystalline structure. The question marks indicate that the constituents of the core could contain exotic states of matter. A black line marks the transition region between two layers.

It is currently not possible to probe a neutron star's internal structure via its electromagnetic signals. In the future, gravitational waves will allow researchers to constrain the EOS and determine the star's interior structure. For now, researchers must use their best theoretical models to develop a picture of the interior. The majority of models assume that a neutron star has a stratified interior with distinct layers, separated by transition bands [98]. In order of decreasing density, these regions are the inner core, outer core, mantle, inner crust, outer crust, ocean and atmosphere. This structure is visible in Figure 1.1. The regions in the figure differ in constituents and structure, e.g. the crust contains a crystalline lattice, while the core is fluid. In Figure 1.1, the transition between one region to the next is represented by a black line. The star's physical properties change significantly over a short distance at these transitions. The Ekman layer which is the transition between the crust and the outer core has a thickness of $\approx 1 - 10$cm [9].

1.1.2.1 Atmosphere

The neutron star's atmosphere is the outermost layer and has a thickness of approximately 1cm. It is a layer of plasma that produces the star's thermal electromagnetic spectrum [138]. The plasma consists of charged atoms, molecules and ions. The atmosphere's effective temperature is $T_{\text{eff}} \sim 10^6$K. The effective temperature is the temperature of a black body with the same luminosity per surface area. The atmospheric density is approximately 10^6g cm^{-3}. This is several orders of magnitude lower than the interior density.

1.1.2.2 Ocean

Along with the atmosphere, the ocean is sometimes referred to as an envelope. The major constituents of the ocean are nuclei and degenerate electrons. As the name suggests, the ocean is in a liquid phase and it has a thickness of approximately 10cm [138]. The ocean plays an important role in the transport and release of thermal energy from the star's surface [98].

1.1.2.3 Crust

Like the Earth, a neutron star is believed to have a solid crust. The crust's depth is approximately 1km and is subdivided into several regions: outer crust, inner crust and mantle. Due to the effect of gravity, it becomes energetically favourable for inverse beta decay, given by equation (1.2), to occur. As a result, 90% of the nucleons are neutrons [36]. These neutron-rich nuclei populate the outer crust and form a crystalline lattice that behaves physically like elastic matter.

The transition from the outer to the inner crust occurs at a depth of about 300m at the "neutron drip" density of 4×10^{11}gcm^{-3}. At this density, neutrons dissociate from the nuclei [29]. These free neutrons form a neutron fluid, which permeates the nuclear lattice and could be in a superfluid state [25].

As the density within the crust approaches the nuclear density, the nuclei separate into neutrons and protons. This separation is called the "pasta" phase or the mantle, which is the transition from the inhomogeneous crust to the homogeneous core [126]. It is called the "pasta" phase due to the shape of the nuclear lattice as it transitions; the 3D lattice becomes 2D lines and finally 1D slabs. Its thickness is of the order of metres [137]. After the mantle, the transition from crust to core is complete.

1.1.2.4 Core

The core contains the majority of a neutron star's volume and mass; as much as 99%. It is usually split into two distinct regions: inner and outer core. The latter is believed to consist of two main components: superfluid neutrons and superconducting protons [11]. The density within the outer core can reach twice the nuclear density.

As the density increases beyond $2\rho_{\mathrm{N}}$, the outer core transitions into the inner core. The inner core is the region theorists are most uncertain about and is represented by question marks in Figure 1.1. The density within the inner core is predicted to reach up to approximately $10\rho_{\mathrm{N}}$ at the centre, well beyond any laboratory experiment. At densities this high, species of matter could be exotic and quite literally strange. One such exotic species of matter are hyperons: hyperons are baryons with at least one strange quark. There could also be kaons and pions; these are mesons that could form Bose condensates [25]. Within the core there could also be deconfined quarks [138].

Whether the inner core exists and contains these exotic forms of matter is dependent on the EOS. Its existence requires the neutron star's central density to exceed $2\rho_{\mathrm{N}}$, which is determined by the neutron star's compactness (M/R). Accurate measurements of mass and radius through electromagnetic and gravitational radiation will constrain the EOS.

1.1.3 Neutron star exterior and magnetic field

This section will examine a neutron star's exterior and its magnetic field. It will follow the description of a pulsar's magnetic field given by Goldreich and Julian [68].

As mentioned earlier, neutron stars can have magnetic fields up to 10^{15}G [144], with a typical magnetic field strength of 10^{12}G. These are the strongest known magnetic fields in the Universe. A neutron star's magnetic field is believed to be approximately dipolar like the Earth's magnetic field as shown in Figure 1.2. The light cylinder, represented by the dashed lines in Figure 1.2, is the maximum distance at which a particle can co-rotate with the star without exceeding the speed of light. Field lines passing through the light cylinder become more radial and enter a region known as the wind zone.

A neutron star's exterior is not a vacuum, but contains charged particles. The particles form a force-free plasma; this means that the Lorentz force is zero. There are two processes that lead to this plasma formation. Firstly, charged particles can only travel along field lines. In young, hot neutron stars, protons and electrons flow outwards. In colder, older stars, only the electrons can leave, creating a potential gap. Secondly, when the potential reaches a critical voltage, electron-positron pair creation is energetically possible. The electrons flow back to the star and the positrons flow away, completing the circuit. We will primarily focus on the region close to the neutron star within the light cylinder.

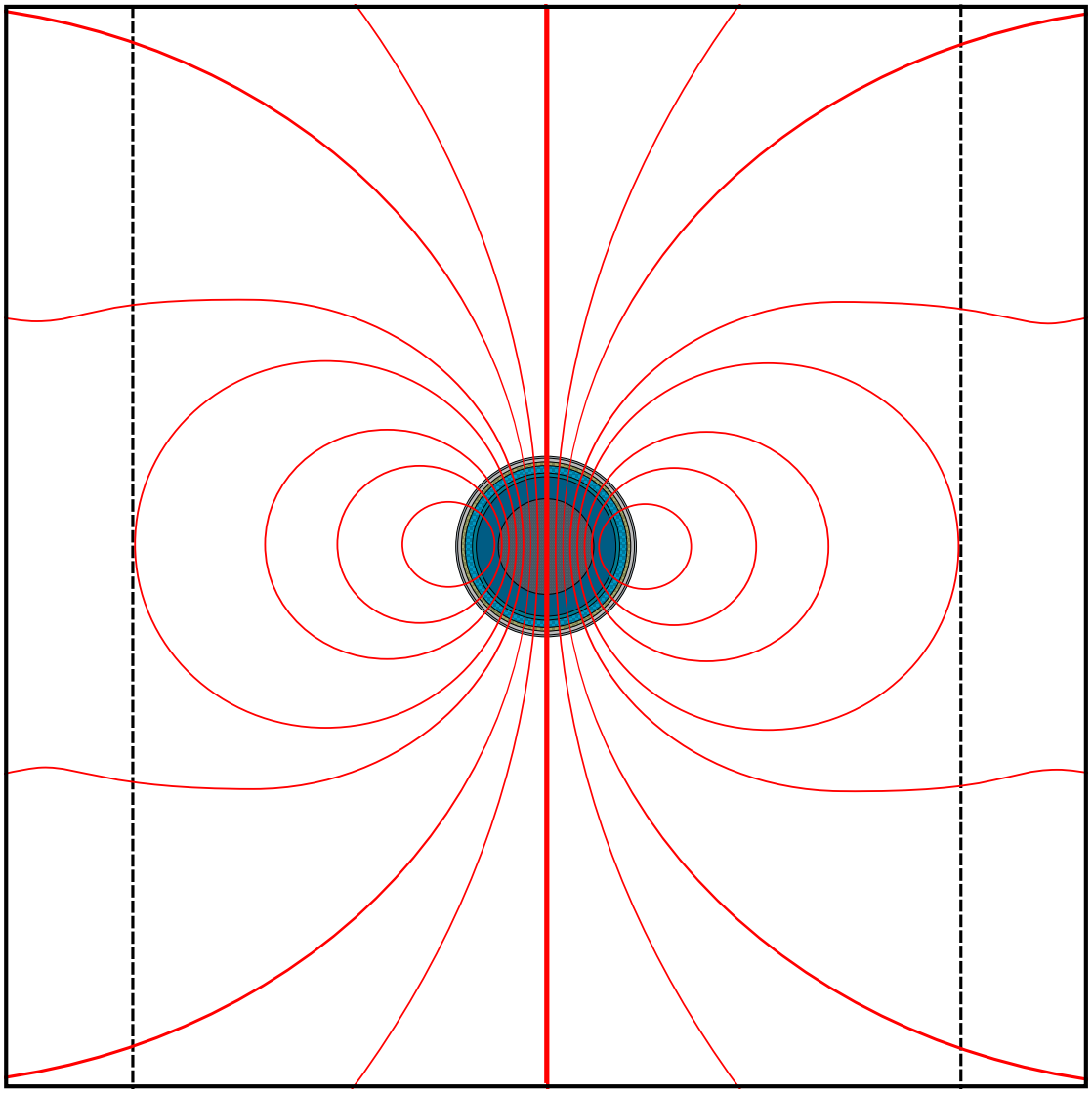

Figure 1.2 – A diagram of the magnetic field configuration of a neutron star where the field lines are red. The magnetic field is dipolar near the star and radial beyond the light cylinder. The dashed lines indicate the light cylinder. In this diagram, the field was aligned with the axis of rotation, but in general this will not be the case and is not true for any observed pulsar.

1.1.4 Classes of neutron stars

This final subsection will examine the different types of neutron star that exist. It will focus on these three: pulsars, magnetars and millisecond pulsars. Figure 1.3 shows that each of these three types occupies a different region in the period derivative against period plot. The figure illustrates the location of every known pulsar that has a measured period derivative and period in the ANTF pulsar catalogue, to date [108]. The figure also indicates the characteristic magnetic field from equation (1.1) and the characteristic age which is given by

$$\tau = \frac{P}{2\dot{P}}, \tag{1.3}$$

where τ is the characteristic age [53]. Figure 1.3 shows that the majority of pulsars have a period of one second, while magnetars are much younger and have a longer period. Millisecond pulsars have the shortest and most stable periods and are usually found in a binary.

1.1.4.1 Pulsars

Hewish et al. detected the first pulsar in 1967 [78]. A pulsar emits beams of electromagnetic radiation from its magnetic poles. Due to its rotation, detectors see this as a pulse. The emitted radiation can be in several different frequency bands at the same time: radio, optical, X-ray and gamma. The majority of pulsars are slowing down due to magnetic breaking and this is characterised by a braking index,

$$n = \frac{\nu\ddot{\nu}}{\dot{\nu}^2}, \tag{1.4}$$

where n is the braking index, ν is the frequency of the pulsar and dots indicate derivatives with respect to time [52]. The braking index describes the motion of the pulsar in the $\dot{P}$ vs P diagram. Espinoza et al. investigated the braking indices of young pulsars and showed their periods to be increasing [52]. Recently, work has been done to improve the braking index calculation to include the effect of a superfluid interior [81]. Some pulsars have extremely regular periods; they could replace atomic clocks in the future [82].

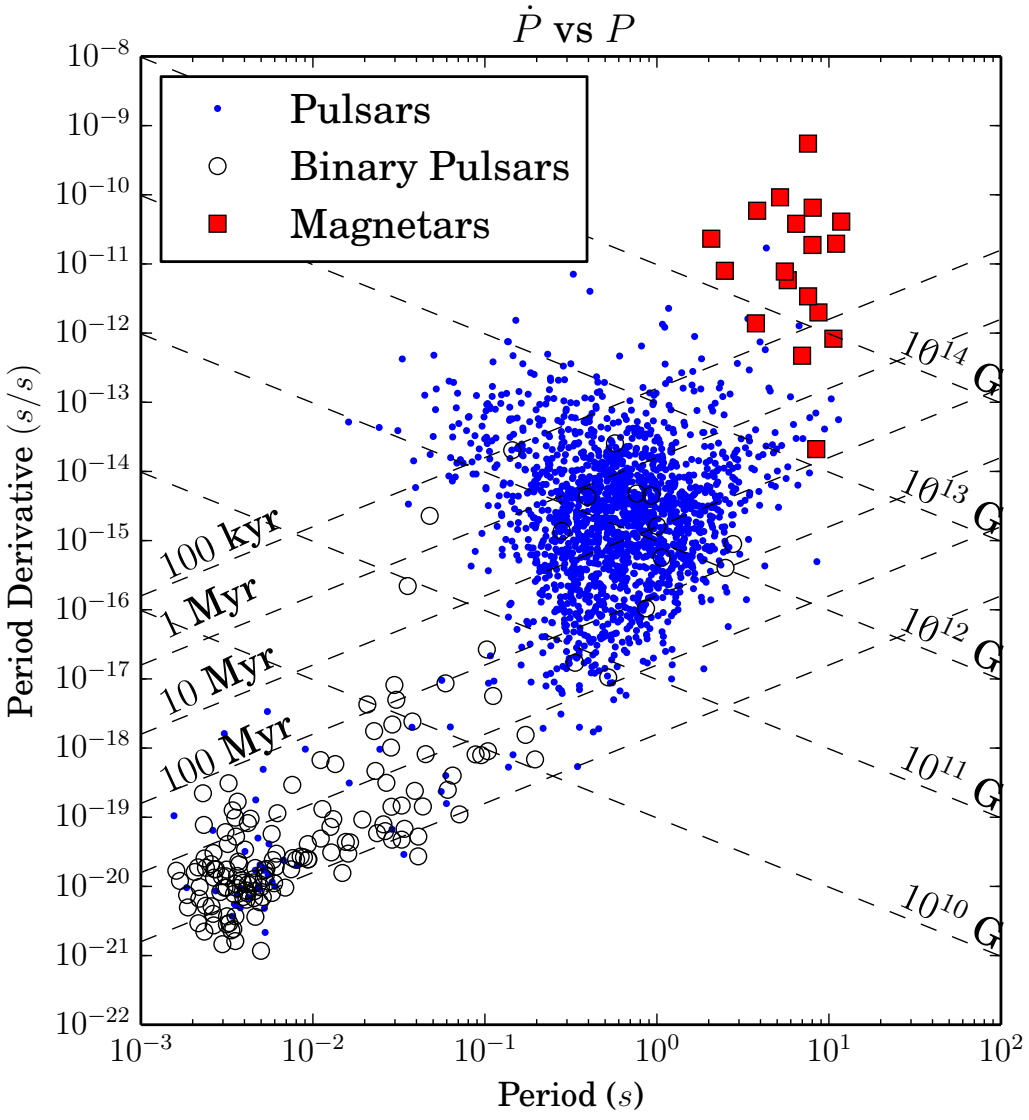

Figure 1.3 – A $\dot{P}$ vs P plot of pulsars from the ANTF catalogue [108]. The figure shows three different classes of neutron star: magnetars in the top right, ordinary pulsars in the middle and binary pulsars in the bottom left. Millisecond pulsars have the shortest and most stable periods, 1.4ms $\lesssim P \lesssim$ 30ms [105], and are usually found in a binary. The plot also indicates the characteristic age and magnetic field. As a pulsar spins down, its magnetic field strength decreases.

1.1.4.2 Magnetars

Magnetars, located in the top right of Figure 1.3, are predicted to have the strongest magnetic fields in the known Universe of around $10^{14} - 10^{15}$G. Their existence was first proposed by Duncan and Thompson in 1992 as the source of soft gamma-ray repeaters [49].

The first magnetar observation came by accident in 1979, when several satellites detected a gamma-ray signal. The source was determined to within two-arc-seconds precision and coincided with a supernova remnant in the Large Magellanic Cloud [49]. After the initial burst of gamma rays, there were twenty more bursts with a period of eight seconds. As well as soft gamma-ray repeaters, magnetars have been proposed as the source of anomalous X-ray pulsars [75]. Thus far, only twenty-eight magnetars have been observed [121].

1.1.4.3 Millisecond pulsars

The third class of neutron stars are the millisecond pulsars that occupy the bottom left of the figure. The majority of millisecond pulsars are in a binary system. Although believed to be much older than normal pulsars due to their weak magnetic fields, they spin much faster. They have periods in the range 1.4ms $\lesssim P \lesssim$ 30ms [105]. This spin-up is due to matter accreting onto the star from its stellar partner [105]. Accretion can also reduces the strength of the pulsar's magnetic field; one suggested reason is that the magnetic field is buried by the accreting matter [52, 180].

1.2 General Relativity

One of the primary goals of this research is that, with a more accurate neutron star model, researchers will be able to produce more accurate gravitational-wave templates. Gravitational waves are a manifestation of a relativistic theory of space and time; realistic models should be built using relativity. Not only is relativity needed for gravitational waves, but for modelling the star itself; a neutron star is a highly relativistic object. Its compactness warps space-time to such an extent that light emitted from the star's far side is visible from its near side. The maximum mass limit of a neutron star is a relativistic effect; there exists no such limit in a Newtonian theory. This section will explore the results that led Albert Einstein to formulate his theory of relativity.

At the beginning of the twentieth century, the need for an alternative explanation of gravity was evident; Newton's theory of gravitation could not explain several observed phenomena. One such example, at the time, was a deviation between the classical prediction and the observed rate of Mercury's perihelion precession [45]. In response to the need for an alternative description, Einstein developed his theory of general relativity over several years; this culminated in "Die Feldgleichungen der Gravitation" published in 1915 [50], in which he presented his field equations. One of Einstein's early successes was solving Mercury's precession problem described above: general relativity added a correction, which accounted for the deviation [45].

The theory of general relativity couples space and time into a single manifold that is often referred to as space-time. The curvature of space-time is deformed by the presence of mass-energy; in the limit of zero mass-energy, space-time tends towards a Minkowskian manifold, which is flat [45]. The curvature of space-time determines the motion of a mass within it. In flat space, special relativity determines the dynamics of a particle. This new description of gravity allows physics in the strong-field regime to be explored, i.e. black holes and neutron stars.

1.2.1 Relativistic notation

Throughout this work, equations are given in geometric units: Newton's gravitational constant G, the speed of light c and the solar mass $M_\odot$ are set to one unless specifically stated,

$$G = c = M_\odot = 1. \tag{1.5}$$

Tensors are a relativist's primary tool; throughout this text, different tensor indices are used. Greek indices such as μ and ν correspond to a four-vector ($\mu = 0, ..., 3$), such as the four-velocity u^μ. Roman indices such as i and j correspond to space-like quantities with ($i = 1, ..., 3$), such as the velocity v^i. Throughout this thesis, the Einstein summation convention is used as well as a flat metric with a signature of $(-1, 1, 1, 1)$.

1.2.2 Gravitational waves

One of the key predictions from Einstein's field equations is the emergence of gravitational waves: these are ripples in the space-time curvature [91]. They provide a mechanism for energy loss from a system and once detected will form a new branch of astronomy. The most promising sources of detectable gravitational waves are massive compact objects such as black holes and neutron stars, but even these only produce minute fluctuations in the space-time curvature at Earth. These waves carry energy known as gravitational radiation and travel at the speed of light [157]. They carry information about their source that is not accessible from electromagnetic radiation.

1.2.2.1 Linearised gravitational waves

Gravitational waves can be derived in the weak-field limit by linearising the Einstein field equations about a small perturbation $h_{\mu\nu}$ in the background space-time metric $g^{(B)}_{\mu\nu}$ [115]. A more detailed derivation can be found in *Gravitation* by Misner, Thorne and Wheeler [115].

The Einstein field equations are

$$G_{\alpha\beta} = R_{\alpha\beta} - \frac{1}{2} g_{\alpha\beta} R, \tag{1.6a}$$

$$G_{\alpha\beta} = 8\pi T_{\alpha\beta}, \tag{1.6b}$$

where $G_{\alpha\beta}$ is the Einstein tensor, $R_{\alpha\beta}$ is the Ricci tensor, $g_{\alpha\beta}$ is the metric, R is the Ricci scalar and $T_{\alpha\beta}$ is the stress-energy tensor. The Einstein field equations demonstrate the coupling between the space-time $G_{\alpha\beta}$ and the matter given by $T_{\alpha\beta}$.

The analysis of these equations can be simplified by making some physical assumptions about the system; the wave's wavelength λ is much less than the radius R of the background space-time curvature,

$$\lambda \ll R. \tag{1.7}$$

The metric's, $g_{\mu\nu}$, deviation from the background metric, $g^{(B)}_{\mu\nu}$, determines the perturbation, $h_{\mu\nu}$, due to the gravitational waves. The background metric, $g^{(B)}_{\mu\nu}$, gives a measure of the curvature. It can be calculated by averaging the metric, $g_{\mu\nu}$, over many wavelengths,

$$g^{(B)}_{\mu\nu} = \langle g_{\mu\nu} \rangle, \tag{1.8}$$

where $g^{(B)}_{\mu\nu}$ is a solution to the averaged Einstein field equations.

The full metric is the sum of the average background metric and the metric perturbation,

$$g_{\mu\nu} = g^{(B)}_{\mu\nu} + h_{\mu\nu}. \tag{1.9}$$

A coordinate system has been chosen such that $|h_{\mu\nu}| \ll 1$.

The Einstein field equations (1.6) can be expanded in powers of $h_{\mu\nu}$ and then linearised. The Riemann tensor is given by,

$$R^{\alpha}{}_{\beta\gamma\delta} = \frac{1}{2}(h^{\alpha}{}_{\delta,\beta\gamma} - h_{\beta\delta,}{}^{\alpha}{}_{\gamma} - h^{\alpha}{}_{\gamma,\beta\delta} + h_{\beta\gamma,}{}^{\alpha}{}_{\delta}), \tag{1.10}$$

where a comma indicates a partial derivative to the indices that follow.

The Ricci tensor and scalar can then be derived from the Riemann tensor by contracting on the first and third index and then finding the trace,

$$R_{\alpha\beta} = \frac{1}{2}(h^{\epsilon}{}_{\beta,\alpha\epsilon} - h_{\alpha\beta,}{}^{\epsilon}{}_{\epsilon} - h^{\epsilon}{}_{\epsilon,\alpha\beta} + h_{\alpha\epsilon,}{}^{\epsilon}{}_{\beta}), \tag{1.11}$$

$$R = -(\Box h - h^{\alpha\beta}{}_{,\alpha\beta}), \tag{1.12}$$

where $\Box = \partial^{\mu}\partial_{\mu}$ is the d'Alembertian operator and $\Box h = h^{\mu}{}_{\mu,\alpha}{}^{\alpha}$. The linearised equations are then substituted into the Einstein field equations (1.6) and simplified by replacing the metric perturbation with the trace-reversed metric perturbation,

$$\bar{h}_{\mu\nu} \equiv h_{\mu\nu} - \frac{1}{2}g^{(B)}_{\mu\nu}h. \tag{1.13}$$

With this substitution the Einstein tensor is given by

$$G_{\mu\nu} = -\frac{1}{2}[\bar{h}_{\mu\nu,\alpha}{}^{\alpha} + g^{(B)}_{\mu\nu}\bar{h}_{\alpha\beta,}{}^{\alpha\beta} - \bar{h}_{\mu\alpha,\nu}{}^{\alpha} - \bar{h}_{\nu\alpha,\mu}{}^{\alpha}]. \tag{1.14}$$

Imposing Lorenz gauge $h_{\mu\nu},{}^{\nu} = 0$, without loss of generality, on the equation above (1.14) gives a wave equation for the metric perturbation,

$$\Box\bar{h}_{\mu\nu} = -16\pi T_{\mu\nu}. \tag{1.15}$$

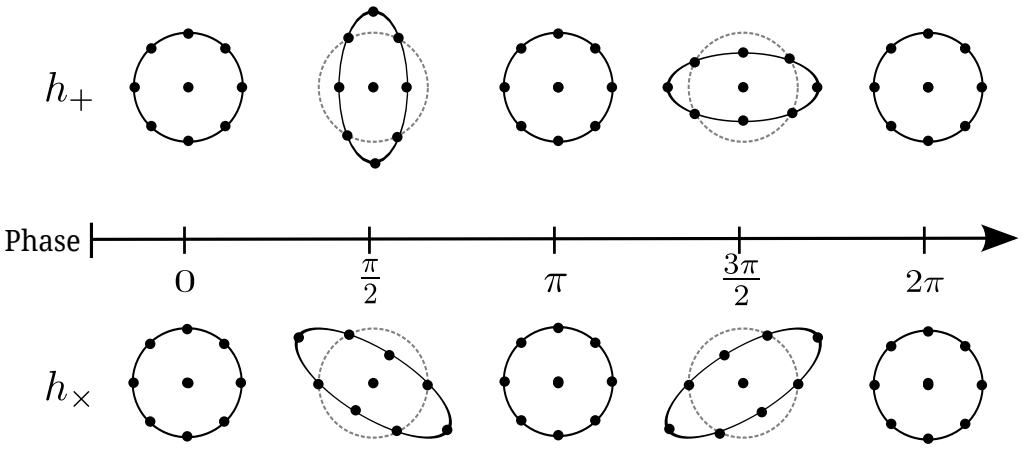

Figure 1.4 – The effect of a gravitational wave on a ring of free masses. The two polarisations are shown with plus shown above cross.

1.2.2.2 Quadrupole formula

The solution to the perturbation wave equation (1.15) can be solved by a retarded Green's function,

$$\bar{h}_{\mu\nu}(t,\mathbf{x}) = 4\int \frac{T_{\mu\nu}(t'=t-|\mathbf{x}-\mathbf{x}'|,\mathbf{x}')}{|\mathbf{x}-\mathbf{x}'|}\,\mathrm{d}^3\mathbf{x}'. \tag{1.16}$$

If we assume that the source is moving slowly, $v \ll c$, then the energy density is dominated by the mass distribution. The solution to the Green's function can be given in terms of the second time derivative of the quadrupole mass moment. This solution is called the quadrupole formula,

$$\bar{h}_{ij}(t,r) = \frac{2}{r}\ddot{\mathcal{I}}_{ij}(t-r), \tag{1.17}$$

where $r = |\mathbf{x}-\mathbf{x}'|$. The quadrupole mass moment is given by

$$\mathcal{I}_{ij} \equiv \int \rho x_i x_j\,\mathrm{d}^3\mathbf{x}, \tag{1.18}$$

where $\mathcal{I}_{ij}$ is the quadrupole mass and ρ is the mass density. This result is most commonly given in terms of the reduced quadrupole moment,

$$\mathcal{I}_{ij} \equiv \int \rho\left(x_i x_j - \frac{1}{3}r^2\delta_{ij}\right)\,\mathrm{d}^3\mathbf{x}, \tag{1.19}$$

and in transverse-traceless gauge is equal to

$$\bar{h}_{ij}^{\mathrm{TT}}(t,r) = \frac{2}{r}\ddot{\mathcal{I}}_{ij}^{\mathrm{TT}}(t-r). \tag{1.20}$$

One can calculate the gravitational wave polarisation from the quadrupole formula (1.20). A gravitational wave has two polarisations: cross and plus. The name of each polarisation is due to the effect they have on a ring of free masses. Figure 1.4 shows these effects.

1.2.3 Tests of general relativity

General relativity's validity has been tested numerous times since its formulation. As mentioned previously, the first proof of its validity was provided by its ability to predict the orbit of Mercury correctly, by including the precession of its perihelion [45]. Further validation came from the indirect detection of gravitational waves.

1.2.3.1 Indirect detection of gravitational waves

Researchers have not yet detected gravitational waves directly [91], but indirect evidence of their existence has been found. Hulse and Taylor [85, 171] received the 1993 Nobel Prize in Physics for showing that the rate of decrease in the orbital separation of the binary pulsar PSR1913+16 matched the rate predicted by the loss of energy through gravitational wave emission [171] to within 0.4%. Recent measurements [184] have continued to show agreement, as shown in Figure 1.5.

1.2.3.2 Ground-based detectors

Gravitational waves have, thus far, eluded all attempts made to detect them. A major reason is that gravitational waves couple weakly with matter [153]. However, they have a distinct advantage over electromagnetic waves as an observational tool. Electromagnetic radiation scatters many times on its way to Earth, but gravitational waves arrive in their original state [153].

It is easy to understand the methods used to detect gravitational waves by understanding how the waves affect "free masses." As shown in Figure 1.4, gravitational waves produce a tidal force on a system of particles. Gravitational waves change all proper distances by the same ratio [157]. The proper length is the distance between two points that is the same for all observers; it is therefore an invariant quantity. As a consequence, two or more masses are required to observe this effect.

Since their prediction, there has been an effort to detect gravitational waves directly with ground-based detectors. The first ground-based detectors were developed by Weber in 1968 [183]. They consisted of two large aluminium cylinders, one with a diameter of 0.61m and the other one of 0.20m, and both had a length of 1.52m, separated by a distance of 2km. These detectors are only capable of detecting gravitational waves with a large amplitude such as those produced by a supernova within the Milky Way.

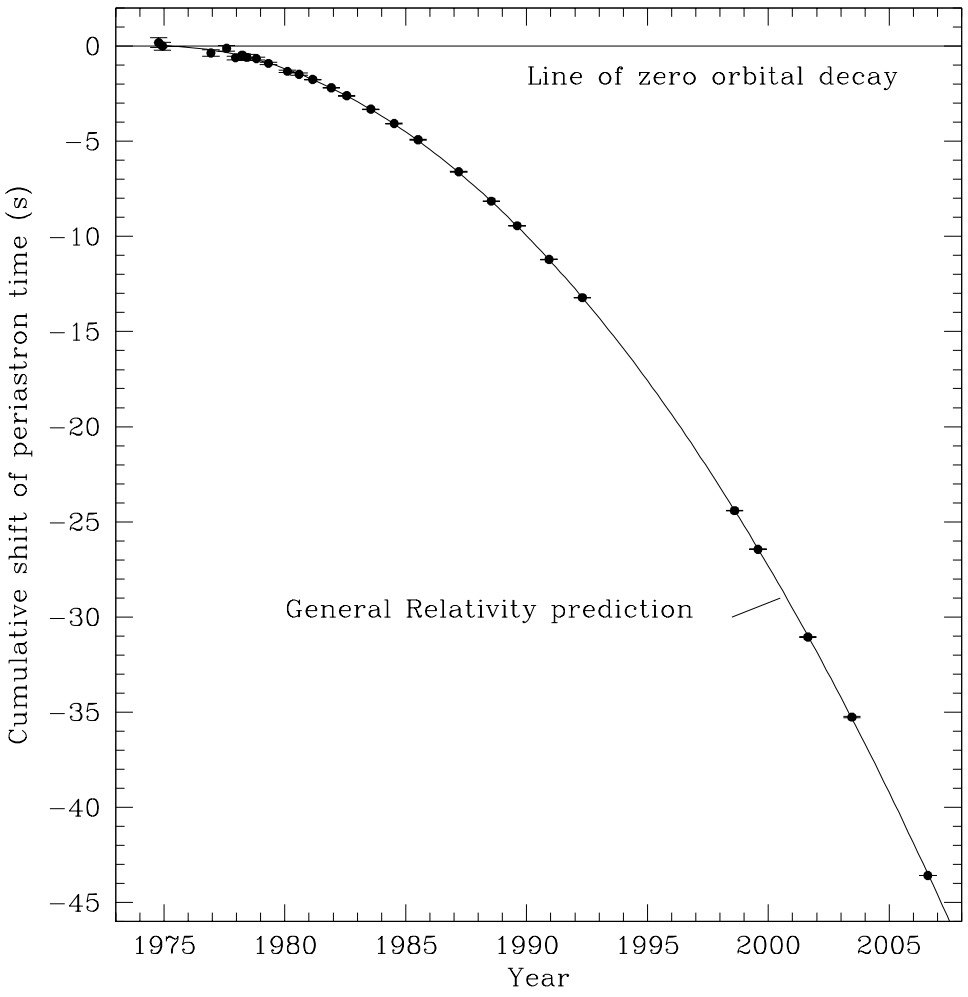

Figure 1.5 – The orbital decay of the binary system compared to the prediction from general relativity. This plot is from the 2010 paper by Weisberg et al. [184]. The prediction from general relativity is correct to 0.2%.

The most promising type of ground-based detector is a large Michelson interferometer. There are several detectors located around the Earth: three in The United States of America (Advanced LIGO), one in Germany (GEO-HF), one in Italy (Advanced VIRGO) and one in Japan (KAGRA). These interferometers have arm lengths of several kilometres, held at near vacuum. Current detectors use a laser-based system to measure the distance between two "free masses." They hope to measure a quantity known as the gravitational strain [157],

$$h = \frac{\Delta L}{L}, \tag{1.21}$$

where the gravitational strain is h and the proper length travelled by the laser in the interferometer is L.

As mentioned above, gravitational waves interact weakly with matter and therefore the gravitational strain, given in the strain equation (1.21), is tiny for all gravitational waves. Not only is it tiny in terms of magnitude, but it is also tiny compared to the noise generated by objects near the detector and thermal noise in the detector; overcoming this is a major problem for the detectors and analysis algorithms.

The gravitational strain can be estimated by using the flux formula (1.22), which relates luminosity to the time variation of the strain, and this is exact for the gravitational waves that bathe the Earth [6],

$$|\dot{h}|^2 = \frac{4}{r^2}\frac{\mathrm{d}E}{\mathrm{d}t}, \tag{1.22}$$

where E is the luminosity radiated from the source, which is a distance r away. This formula gives an estimate for the strain, which can be parametrised to give a value based on a typical source,

$$h \approx 5 \times 10^{-22} \left(\frac{E}{10^{-3} M_{\odot} c^2}\right)^{1/2} \left(\frac{t}{1\mathrm{ms}}\right)^{-1/2} \left(\frac{f}{1\mathrm{kHz}}\right)^{-1} \left(\frac{r}{15\mathrm{Mpc}}\right)^{-1}. \tag{1.23}$$

The strain estimate in equation (1.23) is calculated for a typical source at 15Mpc. This distance is chosen so that the estimate includes sources from the Virgo cluster. Including the Virgo cluster increases the number of astronomical events that astronomers expect to observe over a year [6].

The interferometers work in the frequency range of 10Hz − 10kHz. This means that they are sensitive to binary mergers of neutron stars that are a promising source of gravitational waves [10]. Several factors limit the sensitivity of the detector: quantum shock noise, thermal noise and seismic noise [134].

Figure 1.6 shows the detector sensitivities. Several distinct features are visible within the sensitivity curves: there is a steep drop-off in sensitivity around 1Hz for all detectors followed by a shallow descent towards the maximum sensitivity. To the right of the maximum sensitivity, there is a shallow decrease in sensitivity above 200Hz. The shallower reductions in sensitivity correspond to seismic activity at a low frequency and thermal noise above 100Hz. Gravity-gradient noise prohibits ground-based detection below 1Hz [134].

The review article by Pitkin et al. [134] gives more information about sources of noise and ground-based detectors.

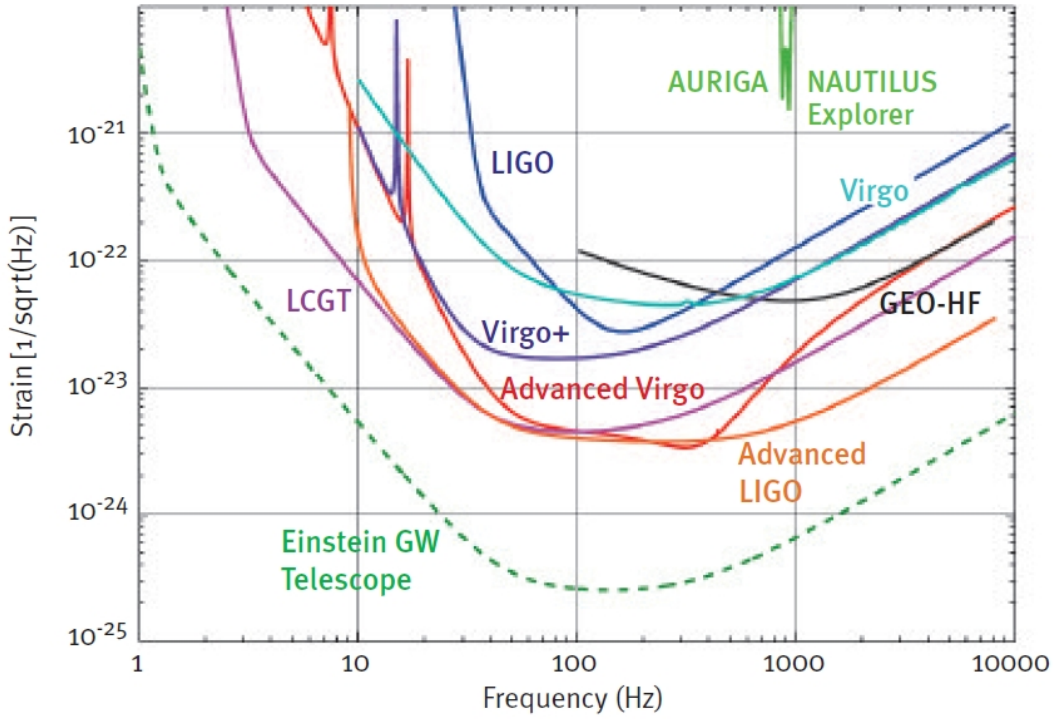

Figure 1.6 – A sensitivity curve of current and future ground-based detectors. The least sensitive detectors are those based on Weber's design. The most sensitive detectors are projected to be built within the next 50 years. This plot was produced for the Gravitational Wave International Committee Road-map [112].

1.3 Numerical Relativity

A neutron star's extreme compactness means that any model will have to consider the effect of general relativity. The equations of general relativity are non-linear and, in general, their solution requires the use of numerical techniques. Some exact solutions do exist, but these are for particular cases only. This section will briefly explain some of the techniques used in numerical relativity.

The equations of general relativity presented earlier (1.6) are fully covariant. Covariance means that the equations make no distinction between time and space. There exist, however, situations that require the separation of space and time; for example, the dynamical evolution of a neutron star binary system from a set of initial data.

There are several different formalisms to split space and time. These are usually named after how they split the four dimensions. One category is the "3+1" formalism, which splits space-time into a three-dimensional space-like surface and an orthogonal time-like surface. Arnowitt, Deser and Misner first developed this method and it is referred to as the ADM formalism [115]. The majority of modern simulations use the BSSN formalism of Baumgarte, Shapiro, Shibata and Nakamura [24, 158]. The development of BSSN from the ADM formalism has allowed long-term, stable evolutions. Another alternative is the "2+2" formalism of d'Inverno that splits space-time into two space-like two-surfaces and their orthogonal time-like two-surface elements [46]. We will focus on "3+1" formalisms, as the majority of the neutron star binary evolutions use this formalism.

The "3+1" formalism foliates space-time into a set of non-intersecting space-like hyper-surfaces [2]. This formalism gives two kinematic variables, the lapse and the shift, which describe the coordinate evolution between two surfaces. The lapse function α describes the advance of the proper time along a time-like unit vector normal to the surface. The shift function β^i represents the motion of coordinates with respect to the previous time slice. The general metric of this formalism, written as a line element, is

$$\mathrm{d}s^2 = -(\alpha^2 - \beta_i\beta^i)\mathrm{d}x^0\mathrm{d}x^0 + 2\beta_i\mathrm{d}x^i\mathrm{d}x^0 + \gamma_{ij}\mathrm{d}x^i\mathrm{d}x^j, \tag{1.24}$$

where γ_{ij} is the 3-metric associated with the current hyper-surface. The book by Alcubierre gives an excellent introduction to numerical relativity [2].

When there is matter present, such as in a binary system, the stress-energy tensor $T_{\mu\nu}$ is non-zero [115]. The divergence of the stress-energy tensor has to vanish and defines a set of equations that evolve the dynamic variables within the system. We will focus on these evolution equations, as the gravitational background of a single neutron star can be approximated to be fixed. This approximation is a reasonable one to make, because matter is weakly coupled to space-time. In a binary system, the space-time will need to be evolved and several community-maintained codes exist for this purpose, e.g. The Einstein Toolkit [104]. The next chapter will focus on the matter evolution equations.

1.3.1 Black-hole simulations

Researchers have successfully calculated complete gravitational-wave waveforms for double black-hole binary inspirals. These waveforms cover the whole evolution, including the inspiral, merger and ringdown to a single black hole [79]. The waveform calculation requires numerical simulations for the violent non-linear merger and ringdown phases. There are three main approaches that cover a large parameter space of masses. They are the effective-one-body formalism [17, 18], the self-force approach [22] and fully general-relativistic, dynamical simulations [79]. The last approach is the most similar to a neutron star binary simulation and was first demonstrated by Pretorius in 2005 [140]. This approach works best for systems with a comparable mass ratio [74].

1.3.2 Neutron star simulations

Neutron star numerical simulation is a relatively young and active research area. Researchers have produced many different and interesting simulations. Scenarios, which have been simulated, include: core-collapse supernova [125], oscillation modes [94, 95, 132], pulsar glitches [163] and double neutron star binaries [18, 19, 63, 146]. We are primarily interested in the inspiral and merger of a double neutron star binary system.

To calculate the gravitational wave signature from a double neutron star binary system, researchers use numerical simulations when the gravitational wave time-scale is comparable to the dynamical time-scale of a few milliseconds. Up to this point, the inspiral can be modelled by a post-Newtonian approximation. The post-Newtonian approximation adds general-relativistic correction terms to Newtonian gravity [30]. It is valid, when Newtonian gravity is dominant, but relativistic effects are important to the system's evolution.

The first general-relativistic binary system simulation, consisting of two neutron stars, was done by Shibata and Uryū in 1999 [161]. Their system contained equal mass neutron stars with a simple polytropic EOS. A polytropic EOS approximates an ideal gas and the next chapter will examine the approximation's validity.

Since 1999, researchers have developed more sophisticated and complex simulations, such as unequal mass binary systems [19, 160]. These simulations showed that the amount of gravitational wave power produced by the system was highly dependent on the system's total mass. Recent simulations have included the merger of neutron stars in a binary system, which lead to the formation of a magnetar-like star [61]. Others have considered the electromagnetic and gravitational-wave signals from a binary merger [128, 129].

1.4 Plan of Thesis

This thesis consists of eight chapters: introduction, developing a physical model, mathematical theory, numerical methods, multi-model interface methods, single-model results, multi-model results and discussion. The introduction has focused on the three key areas that underpin the background physics and the development of the field of research. Building on the introduction, the next chapter will take a more detailed approach and focus on the approximations taken in relation to a neutron star. It will also detail the approximations for which the model will be valid. The third chapter will look at the mathematical theory required for the multi-model approach. The fourth chapter considers the numerical methods associated with solving systems of non-linear, hyperbolic, partial differential equations. The fifth chapter validates the numerical algorithms used to solve the single-model problems and demonstrate the convergence of these methods. The sixth chapter contains the majority of the novel work and explains in detail the advanced numerical methods developed including the multi-material Riemann Ghost Fluid Method (mRGFM). The seventh chapter contains new and exciting results arising from the advanced interface methods presented in chapter six. Finally, chapter eight serves to discuss and conclude what has preceded it.

Chapter 2

Developing a Physical Model

2.1 Introduction

When designing a model, one wishes to be as accurate and true to the object as one can be. Starting from the basis that the laws of physics are universal, one would wish to include all mankind's understanding of the physical world. This, however, would be a complicated and prolonged task. Therefore, as sane human beings, one must make assumptions and approximations about the object that one is trying to model to reduce its complexity. This chapter aims to explain the assumptions and approximations made, when constructing a numerical model of a neutron star within a binary system undergoing merger.

Neutron stars are highly complex and exotic objects. The first assumption one could make, when modelling a neutron star, is about its composition. It is sensible to assume that the composition of a neutron star consists entirely of observed fundamental particles: quarks and leptons. The overwhelming majority of neutron star models have made this assumption and we will as well.

Our primary interest is modelling a neutron star that is in a coalescing binary system. There are three key stages during the coalescing: inspiral, merger and post-merger. The important physical length-scales and time-scales for each of these stages is different. It is, therefore, important to consider each stage individually.

2.2 Pre-merger Neutron Stars

Firstly, a neutron star within a binary system that is close to merging shall be considered. Based on current models of stellar evolution, it is believed that such a star would be older than 10^8years [159]. As a consequence of its age, it would be cold; its physical temperature would be significantly below its Fermi temperature [9]. It can, therefore, be approximated to have a temperature of absolute zero. This approximation has strong implications on the phases of matter and the interactions that occur within a neutron star.

Another intensive quantity that fundamentally determines the composition of a neutron star is its density. The density profile of a neutron star is not tightly constrained. As a result, a large number of EOSs exist. The majority of the methods demonstrated in this thesis are EOS independent. This variability arises, because the strong interaction at low temperatures and high densities is not well understood. As a result, different strange and exotic phases of matter have been predicted to exist within the core of a neutron star. Some of the phases predicted are free quarks, colour-flavour-locked quark matter and quark-gluon plasma. Recent observations of pulsar masses have begun to constrain these exotic phases of nuclear matter. They would be ruled out entirely, if the mass of the Black-Widow pulsar is shown to be $2.4\mathrm{M}_\odot$, as current observations are suggesting [179].

The characteristic pre-merger time-scale is the orbital period. As a first approximation, Kepler's third law can be used to approximate the orbital period of the binary. The law states that *the square of the orbital period is proportional to the cube of the semi-major axis*. The maximum separation before merger is on the order of kilometres. Such a small separation is due to the compactness of the neutron star. Then, the characteristic time-scale pre-merger is of the order of milliseconds.

The temperature profile of a neutron star is not expected to change over a characteristic time-scale, because the production of neutrinos will be at a minimum, close to merging [188]. Therefore, temperature changes can be ignored.

The pre-merger characteristic length-scale is the diameter of a neutron star, which is of the order of kilometres. Therefore, interactions at shorter length-scales can be neglected. As a result, interactions amongst individual particles can be ignored, because they have mean-free paths that are orders of magnitude smaller than the characteristic length-scale. Quantum interactions can also be neglected, because their de Broglie wavelengths are even smaller [8]. Both these points mean that the continuum approximation is valid and the star's interior is within the hydrodynamical regime. Therefore, the interior of a neutron star can be modelled as a fluid.

2.2.1 Fluid model

The advantage of the fluid model is that one can ignore the quantum dynamics of each particle, because they are averaged out by the substantial number of particles; this makes the fluid model consistent with general relativity [8]. Fluid models do not consider the individual trajectories and momenta of each particle; they consider a fluid element instead. A fluid element can be considered as a virtual box, where the number of particles contained inside is constant. The size of a fluid element compared to the entire neutron star is infinitesimal, but it still contains a large number of particles proportional to the Avogadro constant. The fluid model is only valid, if the total number of fluid elements is far greater than the number of particles they contain and their size is significantly smaller than the object they form.

In the fluid model, microscopic particle interactions are captured by macroscopic effects such as viscosity, heat transfer and shear stress. In the Navier-Stokes equations, these effects can lead to a change in the momentum of the fluid. The ratio between inertial and viscous forces is known as the Reynolds number. For a pre-merger neutron star in a binary system, the Reynolds number is much larger than unity, $\mathrm{Re} \gg 1$. Peralta et al. [133] gave a value of the Reynolds number for the outer core of

$$\mathrm{Re} = 1.67 \times 10^8 \left(\frac{\rho_\mathrm{n}}{10^{15} \mathrm{g\ cm^{-3}}} \right)^{-1} \left(\frac{T}{10^8 \mathrm{K}} \right)^2 \left(\frac{\Omega}{10^2 \mathrm{rad\ s^{-1}}} \right), \tag{2.1}$$

where Ω is the angular velocity. Therefore, in a neutron star close to merger, inertial forces dominate viscous forces. This means that the effects of shear viscosity and bulk viscosity on the momentum of the fluid are negligible.

Within a neutron star, heat is transported by neutrons and electrons [16], but the heat conductivity of protons is negligible [57]. As the neutron star being considered is old and cold, large temperature gradients will not be present and the heat flux will be small. Therefore, heat transport can also be neglected within the fluid model.

A fluid experiences a shear stress, when it flows along a boundary. The no-slip condition means that the fluid moves at the same velocity as the boundary. Away from the boundary the fluid travels at the bulk velocity. Shear stresses develop between the bulk and the boundary. The length-scale that this occurs on in a neutron star is tiny compared to the characteristic length-scale pre-merger. Therefore, the model can neglect the contribution from the shear stresses in the fluid. These assumptions lead to the conclusion that a pre-merger neutron star can be approximated by a perfect fluid.

One major advantage of these simplifications is that the perfect fluid approximation of the Navier-Stokes equations, the Euler equations, has a fully relativistic counterpart. The relativistic Euler equations are the conservation of baryon number, conservation of momentum and conservation of energy. The following equations can be used to evolve the fluid forward in time. The conservation of baryon number is

$$\nabla_\mu (nu^\mu) = 0, \tag{2.2}$$

where ∇_μ is the covariant derivative, n is the baryon number density and u^μ is the four-velocity of the fluid. The rest-mass density ρ_0 is defined as

$$\rho_0 = \sum_{(i)} n_{(i)} m_{(i)}, \tag{2.3}$$

where $m_{(i)}$ is the mass of the baryon labelled i. Hence, the conservation of rest-mass density is defined as

$$\nabla_\mu (\rho_0 u^\mu) = 0. \tag{2.4}$$

The conservation of energy and momentum is given by

$$\nabla_\mu T^{\mu\nu} = 0, \tag{2.5}$$

where $T^{\mu\nu}$ is the stress-energy tensor. The stress-energy tensor for an ideal fluid is given by

$$T^{\mu\nu} = \rho_0 h u^\mu u^\nu + p g^{\mu\nu}, \tag{2.6}$$

where h is the specific enthalpy, p the pressure and $g^{\mu\nu}$ is the space-time metric.

The enthalpy is a measure of the total energy of a fluid element; it is the sum of the internal energy and the work done by the fluid element on its environment. The specific enthalpy is the intensive equivalent and the general-relativistic version is

$$h = \frac{H}{\rho_0} = 1 + \epsilon + \frac{p}{\rho_0}, \tag{2.7}$$

where ϵ is the specific internal energy of the fluid. These are the equations of motion for a relativistic, perfect fluid in a curved space-time. They do not form a closed system; an equation of state is required to do so. Throughout this work, an ideal equation of state will be used.

2.2.2 Magnetic field

As mentioned earlier, a neutron star possesses a magnetic field that penetrates its interior. The magnetic field can be added to the fluid model by considering a charged fluid. The stress-energy tensor for a charged fluid includes an electromagnetic contribution. Maxwell's equations and Ohm's law are also required to close the system. The stress-energy tensor is

$$T^{\mu\nu} = \rho_0 h u^\mu u^\nu + p g^{\mu\nu} + \frac{1}{\mu_0}\left[F^{\mu\lambda}F^{\nu}{}_{\lambda} - \frac{1}{4}g^{\mu\nu}F^{\lambda\delta}F_{\lambda\delta}\right], \tag{2.8}$$

where $F^{\mu\nu}$ is the Faraday tensor and μ_0 is the magnetic permeability of free space. The Faraday tensor is an anti-symmetric rank-two tensor and therefore obeys the relation

$$\nabla_\sigma F_{\mu\nu} + \nabla_\mu F_{\nu\sigma} + \nabla_\nu F_{\sigma\mu} = 0. \tag{2.9}$$

The divergence of the Faraday tensor is required to calculate the divergence of the stress-energy tensor. The divergence of the Faraday tensor is

$$\nabla_\mu F^{\mu\nu} = 4\pi j^\nu, \tag{2.10}$$

where j^μ is the four-vector current. Splitting the four-vector current into time and space components gives

$$j^\mu = \left(c\sigma, J^i\right), \tag{2.11}$$

where σ is the charge density, c the speed of light, and J^i is the usual space-like current. The two equations (2.9), (2.10) given above, relating to the Faraday tensor, are Maxwell's equations in tensor form.

2.2.3 Maxwell's equations

Maxwell's equations are required to close the system of equations for a charged fluid. They also describe how the electric field E and the magnetic field B evolve in time. The usual form of Maxwell's equations can be recovered by relating the Faraday tensor to the four-vector potential A^μ,

$$F^{\mu\nu} = \nabla^\mu A^\nu - \nabla^\nu A^\mu. \tag{2.12}$$

The four-vector potential is

$$A^\mu = \left(\phi, A^i\right), \tag{2.13}$$

where ϕ is the electric potential and A^i is the vector potential. Although some implementations do use the vector potential formalism, we will use the vector fields.

Therefore, the vector fields E_i and B_i must be recovered from the Faraday tensor,

$$E_\alpha = -u^\beta F_{\beta\alpha}, \tag{2.14a}$$

$$B_\alpha = -u^\beta \left(\frac{1}{2}\epsilon_{\alpha\beta\gamma\delta}F^{\gamma\delta}\right), \tag{2.14b}$$

where $\epsilon_{\alpha\beta\gamma\delta}$ is the totally anti-symmetric four-tensor. The time-components of covariant electric and magnetic fields (2.14) are zero. Maxwell's equations can be written in their differential vector field form,

$$\nabla^i E_i = \frac{\sigma}{\epsilon_0}, \tag{2.15}$$

$$\nabla^i B_i = 0, \tag{2.16}$$

$$\epsilon^{ijk}\nabla_j E_k = -\frac{\partial B^i}{\partial t}, \tag{2.17}$$

$$\epsilon^{ijk}\nabla_j B_k = \mu_0 J^i + \frac{1}{c^2}\frac{\partial E^i}{\partial t}, \tag{2.18}$$

where ϵ_0 is the permittivity of free space and $c = \dfrac{1}{\sqrt{\mu_0\epsilon_0}}$.

As mentioned above, Maxwell's equations are useful, because they govern how the electromagnetic field evolves, but they do not explain how the electromagnetic field impacts on the dynamics of the charged fluid. It is the Lorentz force that describes how a charged fluid element moves in an electromagnetic field. The relativistic Lorentz force can be calculated

$$f_L^\nu = j_\mu F^{\mu\nu} = \sigma E^\nu - \epsilon^{\nu\mu\rho\gamma} j_\mu u_\rho B_\gamma + \frac{1}{c}u^\nu (j_\mu B^\mu). \tag{2.19}$$

The Lorentz force governs how a charged particle moves within an electromagnetic field. By taking the Newtonian limit and only considering spatial terms, the regular form of the Lorentz force is recovered,

$$f_L^i = \sigma E^i + \epsilon^{ijk} J_j B_k. \tag{2.20}$$

2.2.4 Ohm's law

The last equation that is required to close the system of equations (2.5) to evolve the charged fluid is Ohm's law. Ohm's law gives the relation amongst the current, the fluid and the electromagnetic field.

Andersson has derived a generalised Ohm's law for resistive, general-relativistic magnetohydrodynamics [7] from a multi-fluid approach [8]. He considered a two-fluid system, consisting of a proton fluid and an electron fluid. The multi-fluid approach describes the macroscopic properties of the combined fluid, using the individual fluxes and momenta. The Newtonian equivalent is given in the Appendix A.1. After a lengthy calculation, the Newtonian Ohm's law is

$$E_i + \epsilon_{ijk} v^j B^k = \eta \left(\frac{\rho}{n_\mathrm{e} e \rho_\mathrm{p}} \right)^2 J_i, \tag{2.21}$$

where ρ is the combined fluid density, ρ_p is the proton density, e is the electric charge of a single electron, n_e is the number density of electrons and η is the resistivity. As well as an Ohm's law, a momentum equation for the macroscopic fluid is obtained,

$$\rho(\partial_t + v^j \nabla_j) v_i + \nabla_i p = \epsilon_{ijk} J^j B^k. \tag{2.22}$$

The next section will use these results to obtain the equations of ideal magnetohydrodynamics (MHD). The MHD equations were first derived in a Newtonian framework, which we will follow.

2.2.5 Towards ideal magnetohydrodynamics

This section will introduce the approximations and assumptions made to arrive at the equations of ideal MHD. The ideal MHD equations, as the name suggests, are an idealisation of the actual physical scenario they approximate. The key assumption is that the resistivity of the fluid tends to zero. Hence, the conductivity tends towards infinity and the fluid behaves as a perfect conductor. As a consequence, magnetic reconnections cannot occur, which means that magnetic field lines cannot reconnect, even if it is energetically favourable to do so. Within the interior of a neutron star close to merger, it is expected that magnetic reconnections do not have a significant physical effect on the dynamics. Their significance is quantified by the magnetic Reynolds number, which is analogous to the fluid Reynolds number defined in equation (2.1). The magnetic Reynolds number is a measure of the coupling between the fluid flow and the magnetic field,

$$\mathrm{Rm} = \frac{\mu_0 l v}{\eta}, \tag{2.23}$$

where l is a characteristic length and v is a characteristic velocity of the fluid. The resistivity of an old pulsar is tiny [180]. Therefore, the magnetic Reynolds number is much larger than unity and one can ignore resistive effects within a neutron star before merger.

The first approximation, when taking the ideal MHD limit, is that the displacement current can be ignored in the Ampère-Maxwell equation (2.18). This is a reasonable approximation, because the change in the electric field with respect to time is expected to be small compared to the speed of light within the characteristic time-scale. The Ampère-Maxwell equation is now in the original form given by Ampère. This form gives the true current in terms of just the magnetic field,

$$\frac{1}{\mu_0}\epsilon_{ijk}\nabla^j B^k = J_i. \tag{2.24}$$

The Ohm's law (2.21) can be written in terms of the electric and magnetic fields only,

$$E_i = -\epsilon_{ijk}v^j B^k + \lambda\epsilon_{ijk}\nabla^j B^k, \tag{2.25}$$

where $\lambda \propto \eta$ contains the resistivity and other fundamental constants. Substituting the curl of the electromagnetic Ohm's law (2.25) into the Maxwell-Faraday equation (2.17), allows the Maxwell-Faraday equation to be rewritten without any reference to the electric field. This is known as the induction equation,

$$\frac{\partial B_i}{\partial t} = \epsilon_{ijk}\nabla^j\left(\epsilon^{klm}v_l B_m\right) + \lambda\nabla^j\nabla_j B_i. \tag{2.26}$$

The final step is to take the resistivity to zero, i.e. $\eta \to 0$, to recover the ideal MHD equations. This gives the evolution equation for the magnetic field in the ideal MHD limit,

$$\partial_t B_i = \epsilon_{ijk}\nabla^j(\epsilon^{klm}v_l B_m). \tag{2.27}$$

Substituting Ampère's law (2.24) for the current in the momentum equation (2.22) gives

$$\rho(\partial_t + v^j\nabla_j)v_i + \nabla_i p = \frac{1}{\mu_0}\left[B^j\nabla_j B_i - \frac{1}{2}\nabla_i\left(B_j B^j\right)\right]. \tag{2.28}$$

2.2.5.1 Flux freezing

One of the key results from taking the ideal MHD limit is that the magnetic field lines are tied to the fluid. As a consequence, the magnetic flux is zero and matter will only flow along field lines. This result can be shown by combining the evolution equation for the magnetic field (2.27) and the conservation of mass equation,

$$\frac{\partial\rho}{\partial t} + \nabla^i(\rho v_i) = 0. \tag{2.29}$$

This results in the material derivative of magnetic field divided by the density equalling zero,

$$\frac{D}{Dt}\left(\frac{B^i}{\rho}\right) \equiv \frac{\mathrm{d}}{\mathrm{d}t}\left(\frac{B^i}{\rho}\right) + v^j \nabla_j \left(\frac{B^i}{\rho}\right) = 0, \tag{2.30}$$

where v^i is the velocity field. This result means that the quantity B^i/ρ evolves in the same manner as the separation between two points in the fluid; the field lines are tied to the fluid.

2.2.6 General-relativistic, ideal magnetohydrodynamic equations

The ideal MHD limit can be applied to the stress-energy tensor for a charged fluid (2.8). If the interior fluid of a neutron star is assumed to be an ideal charged fluid that is a perfect conductor, then it has a stress-energy tensor given by [58, 62]

$$T^{\mu\nu} = \rho_0 h^* u^\mu u^\nu + p^* g^{\mu\nu} - b^\mu b^\nu, \tag{2.31}$$

where the pressure is the sum of the gas pressure and the magnetic pressure, given by

$$p^* \equiv p + b^2/2. \tag{2.32}$$

Lichnerowicz was the first to introduce the covariant magnetic field [101]. It was presented in the following form by Anile [12, 13],

$$b^\mu \equiv \left\{ W v^i B_i, \frac{B^j}{W} + W v^i B_i v^j \right\}, \tag{2.33}$$

where W is the Lorentz factor defined as

$$W \equiv \frac{1}{\sqrt{1 - v^i v_i}}. \tag{2.34}$$

The covariant magnetic field, b^μ, is orthogonal to the fluid four-velocity. This ensures that the electric field is zero in the plasma's rest-frame [20],

$$b^\mu u_\mu = 0. \tag{2.35}$$

The enthalpy also gains a term proportional to the magnetic pressure and is

$$h^* \equiv h + b^2/\rho_0. \tag{2.36}$$

With these definitions, the evolution equations for general-relativistic ideal MHD are given by [62]

$$\nabla_\mu \left(\rho_0 u^\mu\right) = 0, \tag{2.37}$$

$$\nabla_\mu T^{\mu\nu} = 0, \tag{2.38}$$

$$\nabla_\mu \left(b^\mu u^\nu - u^\mu b^\nu\right) = 0. \tag{2.39}$$

The final equation (2.39) is the tensor form of Maxwell's equations in the ideal MHD limit.

2.2.7 Neutron star exterior

The exterior of a pre-merger neutron star is not a true vacuum, but consists of a rarefied low-density plasma [68]. In this region, the magnetic pressure dominates the gas pressure. The plasma beta parameter parametrises the ratio between these two pressures,

$$\beta_\mathrm{m} \equiv \frac{p}{p_\mathrm{m}} = \frac{2p\mu_0}{B^2}. \tag{2.40}$$

Therefore, a small plasma beta parameter indicates a magnetically dominated regime.

Goedbloed and Poedts [66] characterise the plasma state by several properties. A plasma is an ionised gas, where the majority of electrons have separated from the molecules and atoms, leaving a gas of predominately positive ions and electrons. Chen describes a plasma as "a quasi-neutral gas of charged and neutral particles, which exhibits collective behaviour" [38]. It is this collective behaviour that this section will examine.

The Saha equation can be used to estimate the ratio of ions to neutral particles. The ratio of ions to neutral particles is approximately $n_i/n_n \approx 2\times10^{15}$, when considering the ionisation energy of hydrogen [66]. This ratio is similar for a neutron star exterior with a temperature of $T \approx 10^8\mathrm{K}$ and a total number density of $n \approx 10^{18}\mathrm{m}^{-3}$ [28]. Therefore, the plasma around a neutron star is highly ionised.

The characteristic time-scale of the pre-merger phase is of the order of milliseconds with a typical orbital frequency of $\Omega \approx 1.5\mathrm{rad/ms}$ [19]. Therefore, particle collisions can be ignored, as they occur on a time-scale that is much longer [66]. As a result, the Coulomb interaction dominates in the exterior of a neutron star. This results in charge particles behaving collectively i.e. a plasma.

There are several choices available to model this region: ideal MHD, force-free and electro-vacuum. Starting in reverse order, the electro-vacuum model describes the exterior as a complete vacuum, permeated by an electromagnetic field. In electro-vacuum the stress-energy tensor is given by

$$T^{\mu\nu} = \frac{1}{\mu_0}\left[F^{\mu\lambda}F^{\nu}{}_{\lambda} - \frac{1}{4}g^{\mu\nu}F^{\lambda\delta}F_{\lambda\delta}\right], \tag{2.41}$$

where the Faraday tensor still obeys the anti-symmetric property (2.9). The divergence of the Faraday tensor is no longer sourced by the current as in (2.10). Instead the divergence is now zero,

$$\nabla_{\mu}F^{\mu\nu} = 0. \tag{2.42}$$

Although the Faraday tensor is an exact solution to the Einstein field equations, it does not take into account the possibility of current sheets. Current sheets are believed to form at the equatorial plane of a rotating neutron star. Palenzuela has observed this phenomenon in the simulation of an aligned rotator [127].

The force-free formalism is the mass-less approximation of ideal MHD. This formalism is a good approximation, when the electromagnetic energy dominates the rest-mass energy. The stress-energy tensor is the same as in the electro-vacuum case (2.41). The key difference is that the covariant derivative of the Faraday tensor is once again the current (2.10). This is constrained, however, by the fact that the Lorentz force vanishes in the force-free approximation [68],

$$F_{\mu\nu}J^{\nu} = 0. \tag{2.43}$$

The system of evolution equations in the force-free limit is [93],

$$\frac{\partial B^i}{\partial t} + \epsilon^{ijk}\nabla_j E_k = 0, \tag{2.44}$$

$$\frac{\partial E^i}{\partial t} - \epsilon^{ijk}\nabla_j B_k = -J^i. \tag{2.45}$$

One significant difference between the exterior and the interior is that the positive charges in the exterior are positrons. The positron is the anti-particle of the electron and has the same mass. The previous Ohm's law, calculated for a proton-electron plasma, does not apply here. In the force-free limit, the current is now wholly dependent on the electromagnetic field. Presented here is the version given by Komissarov [93],

$$J^i = \nabla^r E_r\left[\frac{\epsilon^{ijk}E_j B_k}{B^l B_l}\right] + \frac{B_l\epsilon^{lmn}\nabla_m B_n - E_l\epsilon^{lmn}\nabla_m E_n}{B^r B_r}B^i. \tag{2.46}$$

The first part is the component normal to the magnetic field and comes from the vanishing of the Lorentz force. The second part is the component parallel to the magnetic field and comes from the fact that the electric field and the magnetic field are perpendicular. The advantage of using force-free over ideal MHD comes from its simplicity.

Finally, the majority of simulations, that include a magnetic field, use the equations of ideal MHD to simulate the exterior [5, 63, 146, 147]. The advantages of this approach are that only one system of equations has to be evolved and one does not need to impose boundary conditions at the surface. However, Paschalidis et al. [131] have developed an alternative approach that couples an ideal MHD interior to a force-free exterior at the surface, but have neglected the back reaction from the exterior field.

2.3 Merger and Post-merger Phase

The characteristic length-scale during merger and post-merger decreases significantly. It is expected that important physical effects will now occur on length-scales of centimetres compared to kilometres in the pre-merger phase. The majority of the assumptions and approximations made in the previous section do still hold. However, new effects on shorter length-scales must now also be considered.

2.3.1 Merger phase

The time-scale anticipated for the merger phase is of the order of tens of microseconds [159]. Therefore, the effects of viscosity and heating can still be assumed to be negligible. Interfaces are still necessary due to the lack of computational resolution.

During the turbulent merger phase, one phenomenon that is important are shock waves. Strong shock waves will be produced when the stars coalesce. The pressure ratio across a strong shock is of the order of a hundred. Such strong shocks are known to cause problems with the numerical methods that include interfaces [102, 152]. The mRGFM described in this thesis can handle strong shocks (see Chapter 7).

Another important effect is that regions of the neutron star's interior will behave differently to one another. It is also expected that interactions at the interfaces will affect the overall dynamics of the system. The interfaces, although important, are expected to be physically thin and tiny compared to the star. The expected length-scale of one such interface, the Ekman layer, was calculated by Andersson et al. to be between one and ten centimetres [9].

Including interfaces within a neutron star binary simulation is important, if one wishes to calculate an accurate gravitational-wave template. The physical behaviour of these interfaces can be approximated by infinitely thin interfaces with boundary conditions. The framework was developed by Millmore and Hawke [114]. The addition of interfaces does not change the underlying evolution equations. Therefore, interfaces can be added to the initial data without changing the dynamics in the pre-merger phase.

During this period the topology of the regions within a neutron star will distort and merge. It is important that any numerical method developed is capable of capturing this topology change. The advanced numerical methods developed in this thesis are capable of dealing with large topology change.

2.3.2 Post-merger phase

The period after merger is highly complex and dynamic. Current simulations show that there are three possible outcomes of a binary neutron star merger:

1. The remnant collapses and becomes a black hole on a dynamical time-scale.
2. The remnant forms a hyper-massive neutron star that then proceeds to collapse after several dynamical time-scales into a black hole.
3. The remnant forms a stable neutron star.

The outcome of the merger is determined by the masses of the objects within the binary system. The effect of the magnetic field on the outcome is uncertain. To determine the significance of the magnetic field, better numerical simulations are required that accurately model the transition from interior to exterior and possibly include resistive effects. First results have indicated that including the magnetic field leads to the development of new instabilities [5].

Baiotti et al. [19] showed that for a high-mass system with $M = 2.982\mathrm{M}_{\odot}$, the system collapsed to a black hole within 3ms for a polytropic EOS. A polytropic EOS is one, where the pressure, p, and the volume, V, follow this relation

$$pV^n = C, \tag{2.47}$$

where n is the polytropic index and C is a constant. Physically, this means that the entropy of the system does not change. For a low-mass system with $M = 2.681\mathrm{M}_{\odot}$, the system collapses to a black hole after 16ms for the same EOS.

The duration and dynamics of this period are not well understood and form a key area of research. Simulations of this period can be improved by better initial data, which will come from more accurate pre-merger and merger simulations. These in turn can be obtained by better observations, physical and numerical models.

2.4 Beyond Developing a Physical Model

This chapter has outlined the relevant physical approximations and assumptions that are made when modelling a neutron star. It has been shown that the interior of a neutron star pre-merger can be approximated to be a single, ideal, charged, relativistic fluid. This means that the equations of relativistic, ideal magnetohydrodynamics are suitable to model this part of the star. Externally, the force-free system of equations is suitable to evolve the exterior plasma region of the star. Both of these systems can be written in conservation law form, which is essential to correctly capture the location of shock waves that will be produced during merger. The equations of relativistic, ideal magnetohydrodynamics, however, are non-linear and will need to be solved numerically. To do this, an understanding of the mathematics that underpin these systems of equations is required. The next chapter will develop the idea of characteristic fields that propagate information in the systems. It will also consider the solution to the Riemann problem, which forms an essential part of the mRGFM and the numerical methods used to evolve these systems of equations.

The later chapters will build upon the idea of using interfaces to separate distinct physical models and develop methods to implement this. Key to these techniques is the solution to the Riemann problem and the next chapter examines that in detail.

Chapter 3

Mathematical Theory

This chapter discusses the mathematical background of the evolution equations. It first considers the differential and weak forms of a conservation law. Next, it examines the Riemann problem and its solution for the advection equation and Burgers' equation. Then, the solution of a general linear system is considered. This solution is an important component of the mRGFM. Finally, the chapter discusses each system of evolution equations separately. The order is as follows: Euler equations, special relativistic hydrodynamics, ideal magnetohydrodynamics and special relativistic, ideal magnetohydrodynamics.

The evolution equations are systems of non-linear, hyperbolic, partial differential equations written in conservation law form and are used to simulate the dynamics of a neutron star binary merger. During the merger phase, strong shocks and discontinuities will develop. We will use the conservation law form, because its weak form is valid for non-smooth data such as shock waves and discontinuities.

The solution to the Riemann problem is an essential part of this work. A Riemann problem is a conservation law with a single discontinuity in its initial data. These discontinuities can occur physically as shock waves and phase transitions. They can also be created by applying the finite volume method to discretise the numerical data. The exact solution of a Riemann problem can be used to test the accuracy of the numerical methods. Its approximate solution, on the other hand, can be used to develop numerical methods. The Riemann problem and its solution form an essential part of the mRGFM. Therefore, it is important to understand its solution for each system of conservation laws.

This chapter then reviews the different systems of equations, in order of increasing complexity, that have been used to test the mRGFM. It starts with the Euler equations, which are the Newtonian evolution equations for a perfect fluid. Next, it considers the equations of special relativistic hydrodynamics that demonstrate how the Lorentz factor changes the solution of the Riemann problem. Including a magnetic field makes the solution to the Riemann problem more complicated. Therefore, the Newtonian, ideal, magnetohydrodynamical equations are also discussed. Lastly, these two physical effects are combined and the equations of special relativistic, ideal magnetohydrodynamics are considered.

3.1 Conservation Laws

Conservation laws form the basis of several physical models. They are exact for various physical quantities such as momentum, mass-energy, and charge. This chapter will demonstrate that the conservation law form is essential for correctly evolving systems with discontinuities. They are the basis of our physical models.

Strong shock waves will be produced, when a neutron star binary system coalesces. These shock waves are discontinuities that propagate within the medium, e.g. the fluid core. Discontinuities are also expected to occur at the boundaries of layers and models must take this into account. Thus far, only the differential form of a conservation law has been presented (2.5). The differential form is no longer valid in the presence of a discontinuity. Therefore, a weaker integral form is needed. This section will give the weaker integral form for a general conservation law.

As stated previously, a conservation law naturally arises, when a physical quantity is conserved over the whole domain for any given period. Therefore, the amount of a conserved quantity leaving a volume must equal the amount entering that volume; hence, it must be balanced by the associated flux. This statement can be represented mathematically by the following surface integral

$$\oint_{\Sigma} f^{\mu} \hat{n}_{\mu} \, \mathrm{d}\Sigma = 0, \tag{3.1}$$

where Σ is the surface of the volume, f^{μ} is the flux and $\hat{n}_{\mu}$ is the unit-normal to the surface. By applying the divergence theorem to the equation above, assuming that the flux is sufficiently differentiable, it can be shown that

$$\int_{V} \nabla_{\mu} f^{\mu} \, \mathrm{d}V = 0, \tag{3.2}$$

where V is the volume of integration and ∇_{μ} is the covariant derivative. This equation states that the derivative of the flux with respect to time is balanced by the divergence of the flux.

For the particular case of baryon number conservation, the surface integral would be

$$\oint_{\Sigma} nu^{\mu}\hat{n}_{\mu}\ \mathrm{d}\Sigma = 0. \tag{3.3}$$

By applying the divergence theorem to the equation (3.3), one obtains

$$\int_{V} \nabla_{\mu}(nu^{\mu})\ \mathrm{d}V = 0. \tag{3.4}$$

This conservation law states that no baryons are created or destroyed within a closed volume.

The integral form of a conservation law is valid for non-smooth data. Therefore, the conservation law formalism is appropriate for situations with shocks and discontinuities. The weaker integral formulation will form the basis of our physical models.

Splitting space and time is required to evolve a conservation law forward in time. Performing a $1+1$ split on the covariant equation (3.2) gives

$$\partial_t q(x,t) + \partial_x f(q(x,t)) = 0, \tag{3.5}$$

where $q(x,t)$ is the conserved variable and $f(q(x,t))$ is the flux term. For a vector of conserved variables, the weaker integral form is

$$\frac{\mathrm{d}}{\mathrm{d}t}\int_{x_1}^{x_2} \mathbf{q}(x,t)\ \mathrm{d}x = \mathbf{f}(\mathbf{q}(x_1,t)) - \mathbf{f}(\mathbf{q}(x_2,t)). \tag{3.6}$$

From this point onwards, only the weak integral form will be considered and differential forms imply integral forms.

There are many weak solutions of the integral form (3.6). These multiple solutions arise from the fact that significant physical effects such as viscosity and heating have been ignored in the regions of shocks. To select the correct weak solution, a physical law is required. For the specific case when one is considering a fluid, this physical law is the second law of thermodynamics.

In some situations, a source term is needed to balance the conservation law. These equations are called balance-law equations. In Newtonian hydrodynamics, gravity is included by adding a source term. Source terms can also be required when the geometry of space-time is not flat or non-cartesian coordinates are used. Finally, sources can also be added to equations to prevent constraint violations. The balance-law form is

$$\frac{\mathrm{d}}{\mathrm{d}t}\int_{x_1}^{x_2} \mathbf{q}(x,t)\ \mathrm{d}x = \mathbf{f}(\mathbf{q}(x_1,t)) - \mathbf{f}(\mathbf{q}(x_2,t)) + \int_{x_1}^{x_2} \mathbf{s}(\mathbf{q}(x,t))\ \mathrm{d}x, \tag{3.7}$$

where $\mathbf{s}(\mathbf{q}(x,t))$ is the vector of source terms.

3.1.1 Riemann problem

A conservation law with discontinuous initial data is known as a Riemann problem. More formally, the Riemann problem is a conservation law with initial data given by two states $\mathbf{q}_{\mathrm{L}}$ and $\mathbf{q}_{\mathrm{R}}$ that are separated by a discontinuity. Here, the bold font refers to a vector with the subscript indicating the location of the state with respect to the discontinuity; L = left and R = right. The initial data is composed of the two states separated by a single discontinuity,

$$\mathbf{q}(x,0) = \begin{cases} \mathbf{q}_{\mathrm{L}}(x,0) & \text{if } x < 0, \\ \mathbf{q}_{\mathrm{R}}(x,0) & \text{if } x > 0. \end{cases} \tag{3.8}$$

The solution to the Riemann problem consists of N waves separating $N+1$ constant states for a system of size N. These waves can be discontinuous or rarefied depending on the physical situation. A discontinuous wave can be a shock, contact or rotational wave depending on the physical states. If the wave is rarefied, then it is a rarefaction wave. The solution to the Riemann problem is *self-similar* and can be written in terms of a single independent variable,

$$\xi = \frac{x}{t}. \tag{3.9}$$

This means that the waves admitted from the Riemann problem follow lines of $\xi =$ constant.

For some systems, an exact analytic solution to the general Riemann problem is not known. However, for particular systems, such as the ones considered in this thesis, the Riemann problem can be solved to arbitrary accuracy. The Riemann problem for the linear advection equation, for example, does have an exact solution and will be examined next.

3.1.2 Advection equation

The advection equation is a size one conservation law,

$$\partial_t q(x,t) + \partial_x (v q(x,t)) = 0, \tag{3.10}$$

where ∂_a indicates the partial derivative with respect to a and v is the constant velocity of the system. It can also be written in primitive form,

$$\partial_t q(x,t) + v \partial_x q(x,t) = 0. \tag{3.11}$$

The advection equation (3.10) given above is a quasi-linear, partial differential equation (PDE); it can be solved by using the self-similarity property of the Riemann problem.

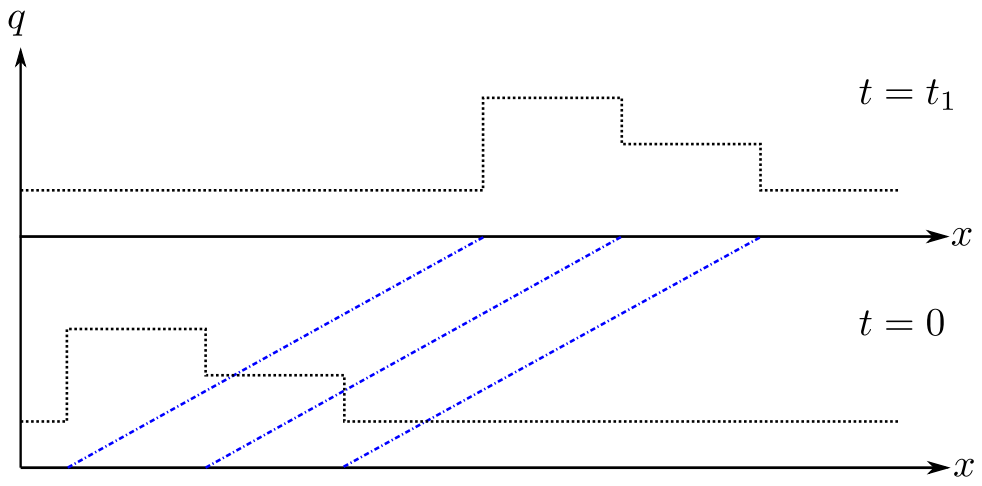

Figure 3.1 – The profile of the advected quantity $q(x,t)$ is unchanged as it is translated along with a velocity v. The blue dash-dot lines show the characteristics with gradient v.

Consider the advection equation (3.10) with Cauchy initial data [100]

$$q(x,0) = q_0(x), \tag{3.12}$$

defined on the domain

$$-\infty < x < \infty, \quad t \geq 0. \tag{3.13}$$

The solution to the advection equation with this initial data is

$$q(x,t) = q_0(x - vt), \tag{3.14}$$

for $t \geq 0$.

This solution is demonstrated in Figure 3.1. In the figure, the profile of q has not changed as it is advected along. Also shown are the characteristics that have gradient v. As this system is linear, all the characteristics have the same slope. The solution follows the characteristic lines and, because they are all parallel, the solution does not change.

The advection equation (3.10) can also be solved using the method of characteristics [100, 120]. Characteristics determine the information propagation in a differential equation. The characteristics can be obtained by first transforming the partial differential equation into an ordinary differential equation and expanding it using the chain rule,

$$\frac{\mathrm{d}}{\mathrm{d}s} q(x(s),t(s)) = \frac{\partial q}{\partial t}\frac{\mathrm{d}t}{\mathrm{d}s} + \frac{\partial q}{\partial x}\frac{\mathrm{d}x}{\mathrm{d}s} = 0. \tag{3.15}$$

Comparing the ordinary differential equation (3.15) with the primitive advection equation (3.11), one can equate the total derivates,

$$\frac{\mathrm{d}t}{\mathrm{d}s} = 1, \tag{3.16a}$$
$$\frac{\mathrm{d}x}{\mathrm{d}s} = v, \tag{3.16b}$$
$$\frac{\mathrm{d}q}{\mathrm{d}s} = 0. \tag{3.16c}$$

The solutions to these ordinary differential equations are called the characteristic curves and as s varies, they form a solution surface. The solutions to (3.16) are as follows

$$t = s + t_0, \tag{3.17a}$$
$$x = vs + x_0, \tag{3.17b}$$
$$q = q_0. \tag{3.17c}$$

As $t_0 = 0$, the second differential equation can be rewritten as

$$x = vt + x_0. \tag{3.18}$$

Therefore, the characteristic equations are straight lines in the $x - t$ plane with gradient v as shown in Figure 3.1.

3.1.3 Inviscid Burgers' equation

A more complicated conservation law is the inviscid Burgers' equation. It is a basic approximation to the equations of Newtonian hydrodynamics because it demonstrates the development of shocks and rarefactions associated with generic, smooth initial data for non-linear conservation laws. The inviscid Burgers' equation is a size one, non-linear PDE and has the form

$$\partial_t q(x,t) + \partial_x \left(\frac{1}{2} q(x,t)^2 \right) = 0. \tag{3.19}$$

This can be written in primitive form as

$$\partial_t q(x,t) + q(x,t) \partial_x q(x,t) = 0. \tag{3.20}$$

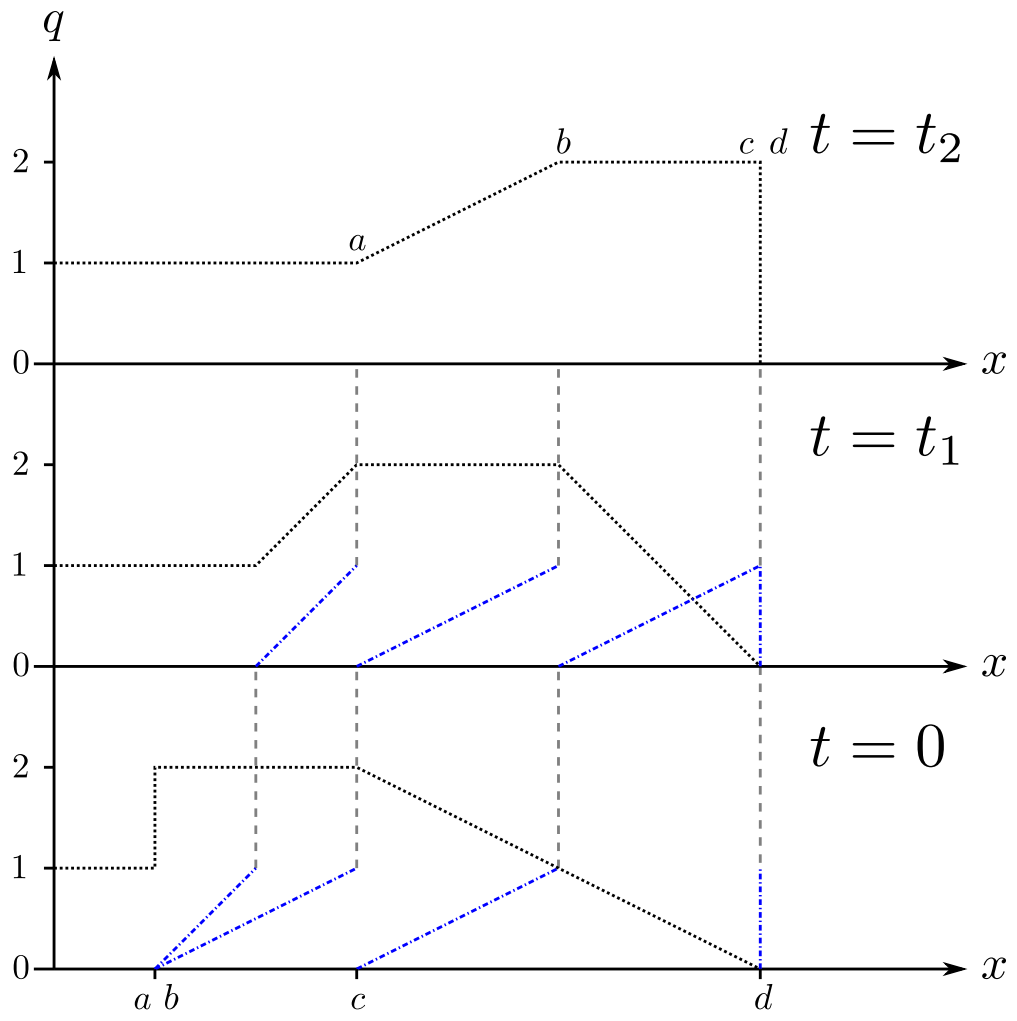

Figure 3.2 – The solution to the inviscid Burgers' equation at three different times for the dotted profile $q(x,t)$. The points a and b separate as their characteristics have different slopes. This results in a rarefaction wave. The points c and d converge to form a shock wave; at this point the diagram is an approximation as non-linear effects become important. The blue dash-dot lines represent the characteristics. The light dashed lines show where the points have moved to.

Comparing the primitive form of Burgers' equation (3.20) to the primitive form of the advection equation (3.11), one can see that the conserved quantity $q(x,t)$ will be advected along with velocity $q(x,t)$. Figure 3.2 shows the effect of Burgers' equation. This figure tracks four points (a,b,c,d) as the profile $q(x,t)$ is evolved forward in time. It shows that the points a and b separate to form a rarefaction wave. A rarefaction forms, because their characteristics, shown in blue, diverge. The points c and d converge to form a shock wave. At this point, the characteristics cross and more information is required to show the correct solution; the Rankine-Hugoniot conditions (see Equation (3.23)).

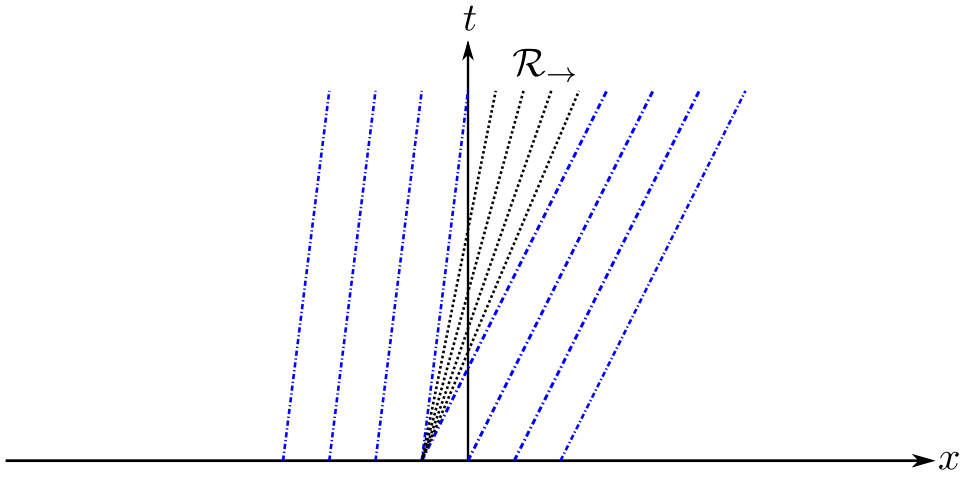

Figure 3.3 – A rarefaction wave. The characteristics diverge at a rarefaction wave. The rarefaction wave is bounded by the characteristic speeds either side.

3.1.3.1 Rarefaction wave

A rarefaction wave occurs, when the characteristics between two points or emanating from the same point diverge. Figure 3.3 shows a rarefaction fan and the diverging characteristics. This is true for a conservation law with a convex flux function [173]. Burgers' equation has a convex flux as do the equations of hydrodynamics. The entropy does not change across a rarefaction wave for the Euler equations.

The entire solution between two constant states q_{L} and q_{R} is

$$q(x,t) = q_{\mathrm{L}} \qquad \text{if} \qquad \frac{x - x_{\mathrm{L}}}{t} \leq \lambda_{\mathrm{L}}, \tag{3.21a}$$

$$\lambda(q) = \frac{x - x_{\mathrm{L}}}{t} \quad \text{if} \quad \lambda_L < \frac{x - x_{\mathrm{L}}}{t} < \lambda_{\mathrm{R}}, \tag{3.21b}$$

$$q(x,t) = q_{\mathrm{R}} \qquad \text{if} \qquad \frac{x - x_{\mathrm{R}}}{t} \geq \lambda_{\mathrm{R}}, \tag{3.21c}$$

where λ is the characteristic wave speed.

The solution is smooth between the two ends of the rarefaction fan. The solution described above is a physical solution, however, there exists a non-physical but mathematically possible solution called a rarefaction shock. The rarefaction shock is non-physical as it is unstable and violates the entropy condition [173].

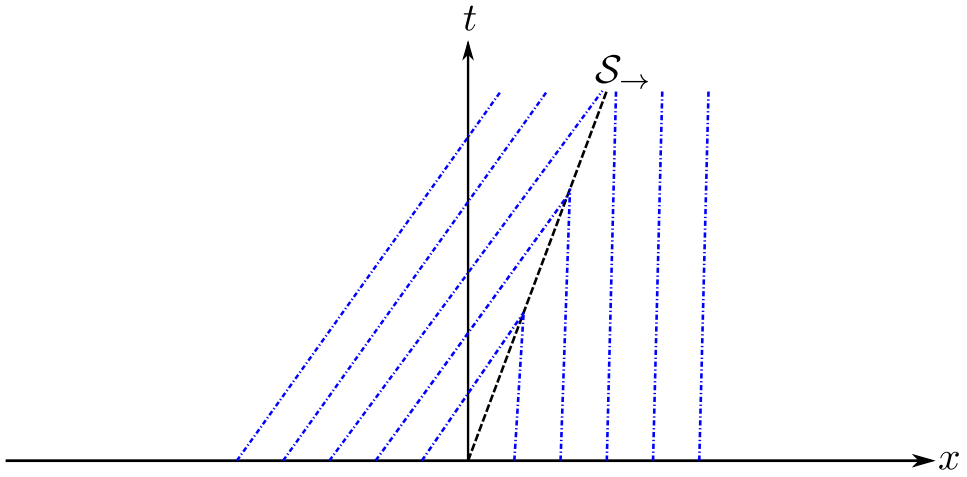

Figure 3.4 – The characteristics pin to the shock wave. The shock wave travels at a velocity determined by the Rankine-Hugoniot relations. All quantities change across a shock wave.

3.1.3.2 Shock wave

Burgers' equation given by (3.19), when solved using the method of characteristics, gives some interesting results. From the primitive version of Burgers' equation (3.20), it is easy to see that its characteristic curves are given by

$$x = q(x,t)t + x_0. \tag{3.22}$$

Therefore, the gradients of the curves are determined by the function $q(x,t)$ and this means that the curves can have different gradients. The possibility then arises that the characteristics intersect and a shock wave is formed [83]. The physical interpretation is that the function $q(x,t)$ describes the speed of particles in the fluid; a shock forms when the faster particles catch up with the slower ones [120]. Once the characteristics cross, the shock wave forms and the current approach breaks down. Another method must be used to determine the states either side of a shock wave.

When a conservation law has a discontinuity, the Rankine-Hugoniot conditions must be used. These conditions ensure conservation across a discontinuity. For a general system of conservation laws (3.5) with a solution, these conditions are

$$v_s[[\mathbf{q}]] = [[\mathbf{f}(\mathbf{q})]], \tag{3.23}$$

where $\mathbf{q}$ is the conserved quantity, $\mathbf{f}(\mathbf{q})$ is the flux and v_s is the shock speed.

The notation $[[\cdot]]$ indicates the difference in a quantity across the discontinuity,

$$[[\mathbf{q}]] = \mathbf{q}_{\{\mathrm{b}\}} - \mathbf{q}_{\{\mathrm{a}\}}, \tag{3.24}$$

where the subscript $\{\mathrm{a}\}$ is the state in front of the wave and $\{\mathrm{b}\}$ is the state behind the wave. For the specific case of the inviscid Burgers' equation (3.19), calculated using the Rankine-Hugoniot conditions (3.23), the shock speed is

$$v_s = \frac{1}{2}\left(q_{\{\mathrm{a}\}} + q_{\{\mathrm{b}\}}\right). \tag{3.25}$$

Another important reason for considering the conservation law form over any other, such as the primitive one, is that only the correct conservation form captures the physical shock wave speed. Consider a conservation law with the same primitive form as the inviscid Burgers' equation (3.20), but a different conservation form,

$$\partial_t \left(\frac{1}{2}q(x,t)^2\right) + \partial_x \left(\frac{1}{3}q(x,t)^3\right) = 0. \tag{3.26}$$

Using the Rankine-Hugoniot conditions (3.23), the shock speed for this equation is

$$v_s = \frac{2}{3}\frac{q_{\{\mathrm{b}\}}^3 - q_{\{\mathrm{a}\}}^3}{q_{\{\mathrm{b}\}}^2 - q_{\{\mathrm{a}\}}^2}. \tag{3.27}$$

This shock speed is different from the shock speed for the inviscid Burgers' equation (3.25). Therefore, the original conservation form (3.19) is the only version that accurately captures the shock wave speed. The primitive form, on the other hand, does not uniquely determine the correct conservation law form. A physical principle must be used to correctly determine the corresponding conservation law form.

3.1.3.3 Lax's entropy condition

Lax's entropy condition determines if a shock wave speed is physically admissible and sets a unique weak solution. The entropy condition states that for a genuinely non-linear field the shock speed v_s must lie between the characteristics. Consider a shock wave between a state $\mathbf{q}_{\{\mathrm{a}\}}$ and a state $\mathbf{q}_{\{\mathrm{b}\}}$, where the state $\{\mathrm{a}\}$ is in front of the wave and state $\{\mathrm{b}\}$ is behind. For the shock to be physically admissible, the following condition must hold for the shock speed

$$\lambda\left(q_{\{\mathrm{b}\}}\right) > v_s > \lambda\left(q_{\{\mathrm{a}\}}\right). \tag{3.28}$$

3.2 Linear Systems

So far, only PDE systems of size one have been considered. However, the equations of ideal magnetohydrodynamics form a size eight system of PDEs [34]. The next logical step is to consider linear systems. Linear systems are the simplest systems of equations. They also form an essential component of the mRGFM. Next, we will calculate the general solution for a linear system based on the work of Roe [149].

Consider a linear system of conservation laws of size N with a vector of conserved variables $\mathbf{q}$,

$$\partial_t \mathbf{q} + A(\mathbf{q})\partial_x \mathbf{q} = 0, \tag{3.29}$$

where $A(\mathbf{q})$ is the $N \times N$ Jacobian matrix, $\partial \mathbf{f}/\partial \mathbf{q}$.

Through a reformulation, the Riemann problem can be solved by transforming into a new set of variables, *the characteristic variables*. These variables are constant along characteristics.

To transform the system of equations into characteristic variables, one must first calculate the left and right eigenvectors, $\mathbf{l}^{(i)}$ and $\mathbf{r}^{(i)}$ respectively, of the matrix A. The eigenvectors are orthogonal, $\mathbf{l}^{(i)} \cdot \mathbf{r}^{(j)} = \delta_{ij}$, and have eigenvalues $\lambda^{(i)}$. It shall be assumed that they span the whole space. Here δ_{ij} is the Kronecker delta function,

$$\delta_{ij} = \begin{cases} 1 & \text{if } i = j, \\ 0 & \text{if } i \neq j. \end{cases} \tag{3.30}$$

One can then calculate the characteristic variables $\mathbf{w}^{(i)}$,

$$\mathbf{w} = L\mathbf{q}, \tag{3.31}$$

where L is the matrix of $\mathbf{l}^{(i)}$. The linear system of equations (3.29) can be rewritten in terms of the characteristic variables (3.31) giving

$$\partial_t \mathbf{w} + \Lambda \partial_x \mathbf{w} = 0, \tag{3.32}$$

where Λ is the diagonal matrix containing the eigenvalues $\lambda^{(i)}$. As a result of this transformation, the system of N equations is decoupled. Each equation forms an advection equation with velocity $v = \lambda^{(i)}$ for the $\mathbf{w}^{(i)}$ column vectors.

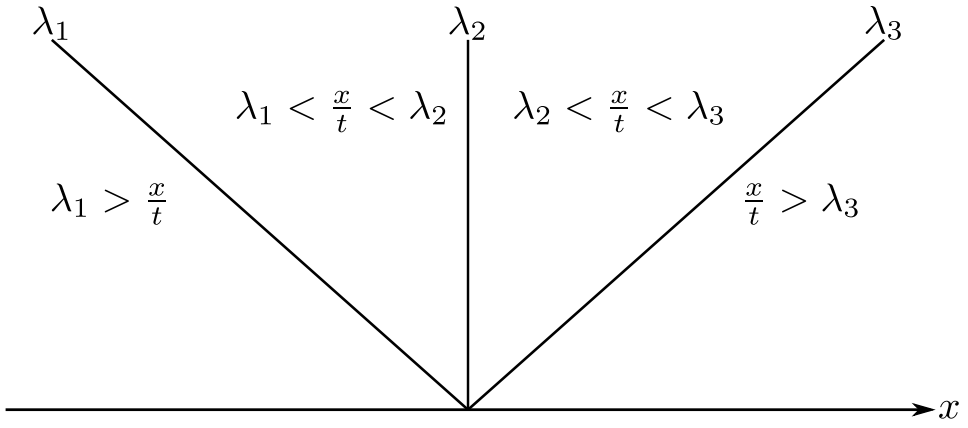

Figure 3.5 – The solution to the Riemann problem is defined by regions separated by the characteristics.

The solution to the Riemann problem can then be given in terms of the characteristic variables using the results for the advection equation in Section 3.1.2. The solution in two different but equivalent forms is

$$\mathbf{w}(t,x) = \mathbf{w}_\mathrm{L} + \sum_{i=1}^{j} \left(\mathbf{l}^{(i)} \otimes \Delta\mathbf{w}\right) \mathbf{r}^{(i)}, \tag{3.33a}$$

$$\mathbf{w}(t,x) = \mathbf{w}_\mathrm{R} - \sum_{i=j+1}^{N} \left(\mathbf{l}^{(i)} \otimes \Delta\mathbf{w}\right) \mathbf{r}^{(i)}, \tag{3.33b}$$

where $\Delta\mathbf{w} = \mathbf{w}_\mathrm{R} - \mathbf{w}_\mathrm{L}$ and j is defined by $\lambda^{(j)} \leq \dfrac{x}{t} \leq \lambda^{(j+1)}$ as shown in Figure 3.5.

The solution for the conserved variables $\mathbf{q}$ can be determined from the characteristic solution,

$$\mathbf{q} = R\mathbf{w}^{(i)}, \tag{3.34}$$

where R is the matrix of $\mathbf{r}^{(i)}$. A system of non-linear equations will be considered next, specifically, the Euler equations.

3.3 Newtonian Hydrodynamics - The Euler Equations

The Euler equations are the low-velocity, Newtonian limit of the hydrodynamical equations presented earlier in (2.2) and (2.5). In conservation law form, they are

$$\partial_t \rho + \partial_i \left(\rho v^i\right) = 0, \tag{3.35}$$

$$\partial_t S_j + \partial_i \left(\rho v^i v_j + \delta^i{}_j p\right) = 0, \tag{3.36}$$

$$\partial_t \mathcal{E} + \partial_i \left(\left[\mathcal{E} + p\right] v^i\right) = 0, \tag{3.37}$$

where ρ is the density, v^i is the velocity, p is the pressure, $S_i = \rho v_i$ is the momentum and $\mathcal{E}$ is the total energy. The total energy for an ideal gas is the sum of the internal energy and the kinetic energy. It is defined as

$$\mathcal{E} = \rho\epsilon + \frac{1}{2}\rho v^i v_i, \tag{3.38}$$

where ϵ is the specific internal energy. The enthalpy in the low-velocity limit is defined as

$$\tilde{h} = \epsilon + \frac{p}{\rho}. \tag{3.39}$$

This allows one to determine a set of primitive variables $\mathbf{u}$, which can be used to calculate all other quantities. The set of primitive variables used are

$$\mathbf{u} = [\rho, v^i, \epsilon]. \tag{3.40}$$

On the other hand, the conserved variables are

$$\mathbf{q} = [\rho, S^i, \mathcal{E}]. \tag{3.41}$$

An EOS must be specified to close this system of equations.

In Chapter 2, it was shown that the fluid within the interior of a neutron star can be approximated as an ideal fluid. Therefore, an appropriate EOS to use in Newtonian hydrodynamics is the gamma-law EOS. The gamma-law EOS relates the pressure to the density and the specific internal energy. It is given by

$$p = (\gamma - 1)\rho\epsilon, \tag{3.42}$$

where γ is the ratio of the specific heat capacities and is constant for each model.

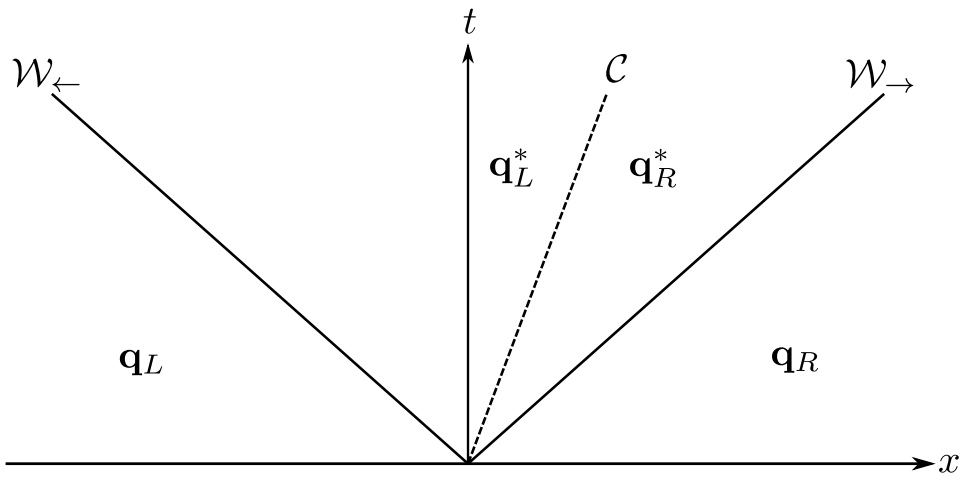

Figure 3.6 – The wave structure for the one-dimensional Riemann problem in Newtonian hydrodynamics. There are four constant states separated by three waves. The middle dashed-wave is a contact wave. The remaining waves can either be a shock wave or a rarefaction wave depending on the initial conditions.

Earlier it was stated that a physical principle is required to determine the correct physical solution to the Riemann problem. In the case of the Euler equations [173], this is the second law of thermodynamics,

$$\frac{\mathrm{d}\mathfrak{s}}{\mathrm{d}t} \geq 0, \tag{3.43}$$

where $\mathfrak{s}$ is the entropy. For a macroscopic system, the second law of thermodynamics states that the entropy within a closed system must either stay the same or increase with time.

As explained previously, the solution to the one-dimensional Riemann problem will consist of N waves for N conserved variables. There are three conserved variables in Newtonian hydrodynamics in one dimension. Therefore, the solution to the Riemann problem consists of four distinct states separated by three waves. Figure 3.6 shows this solution structure.

Figure 3.6 shows four constant states, $\{\mathbf{q}_{\mathrm{R}}, \mathbf{q}_{\mathrm{R}}^*, \mathbf{q}_{\mathrm{L}}^*, \mathbf{q}_{\mathrm{L}}\}$, separated by three waves $\{\mathcal{W}_{\leftarrow}, \mathcal{C}, \mathcal{W}_{\rightarrow}\}$. The middle dashed-wave, labelled $\mathcal{C}$, is known as the contact wave. The characteristics at a contact wave are parallel, because a contact wave is a linear wave. The remaining waves, $\{\mathcal{W}_{\leftarrow}, \mathcal{W}_{\rightarrow}\}$, can either be shock wave or rarefaction waves. In Newtonian hydrodynamics, the type of the wave $\mathcal{W}$ is determined by the change in the pressure across the wave. Therefore, we have

$$\mathcal{W} = \begin{cases} \mathcal{R}, & p^*_{\{\mathrm{b}\}} < p_{\{\mathrm{a}\}}, \\ \mathcal{S}, & p^*_{\{\mathrm{b}\}} > p_{\{\mathrm{a}\}}, \end{cases} \tag{3.44}$$

where $\mathcal{R}$ is a rarefaction wave and $\mathcal{S}$ is a shock wave.

3.3.1 Euler characteristics

The characteristic structure of the Euler equations is essential for the mRGFM and the solution to the Riemann problem. The first step is to calculate the Jacobian matrix

$$A(\mathbf{q}) = \begin{pmatrix} \frac{\partial f_1}{\partial q_1} & \cdots & \frac{\partial f_1}{\partial q_{\mathrm{N}}} \\ \vdots & \ddots & \vdots \\ \frac{\partial f_{\mathrm{N}}}{\partial q_1} & \cdots & \frac{\partial f_{\mathrm{N}}}{\partial q_{\mathrm{N}}} \end{pmatrix}. \tag{3.45}$$

This Jacobian matrix for the Euler equations is [173]

$$A(\mathbf{q}) = \begin{pmatrix} 0 & 1 & 0 & 0 & 0 \\ \hat{\gamma}\left(\frac{1}{2}v^2 + \tilde{h}\right) - v_x^2 - a^2 & (3-\gamma)v_x & \hat{\gamma}v_y & \hat{\gamma}v_z & \hat{\gamma} \\ -v_x v_y & v_y & v_x & 0 & 0 \\ -v_x v_z & v_z & 0 & v_x & 0 \\ \frac{1}{2}v_x\left[(\gamma-3)\left(\frac{1}{2}v^2 + \tilde{h}\right) - a^2\right] & \frac{1}{2}v^2 + \tilde{h} + \hat{\gamma}v_x^2 & \hat{\gamma}v_x v_y & \hat{\gamma}v_x v_z & \gamma v_x \end{pmatrix}, \tag{3.46}$$

where $\hat{\gamma} = (1-\gamma)$ and a is the speed of sound in a fluid that is defined as

$$a^2 = \left(\frac{\partial p}{\partial \rho}\right)_{\mathfrak{s}}. \tag{3.47}$$

For the gamma-law EOS the speed of sound is

$$a^2 = \frac{\gamma p}{\rho}. \tag{3.48}$$

Then, using the characteristic equation $|A - \lambda| = 0$, the eigenvalues are

$$\lambda_{(-)} = v - a, \quad \lambda_{2,3,4} = v_x, \quad \lambda_{(+)} = v + a. \tag{3.49}$$

The right eigenvectors are

$$\mathbf{r}^{(-)} = \begin{pmatrix} 1 \\ v_x - a \\ v_y \\ v_z \\ \frac{1}{2}v^2 + \tilde{h} - va \end{pmatrix} \quad \mathbf{r}^{(+)} = \begin{pmatrix} 1 \\ v_x + a \\ v_y \\ v_z \\ \frac{1}{2}v^2 + \tilde{h} + va \end{pmatrix}, \tag{3.50a}$$

$$\mathbf{r}^{(2)} = \begin{pmatrix} 1 \\ v_x \\ v_y \\ v_z \\ \frac{1}{2}v^2 \end{pmatrix}, \quad \mathbf{r}^{(3)} = \begin{pmatrix} 0 \\ 0 \\ 1 \\ 0 \\ v_y \end{pmatrix}, \quad \mathbf{r}^{(4)} = \begin{pmatrix} 0 \\ 0 \\ 0 \\ 1 \\ v_z \end{pmatrix}. \tag{3.50b}$$

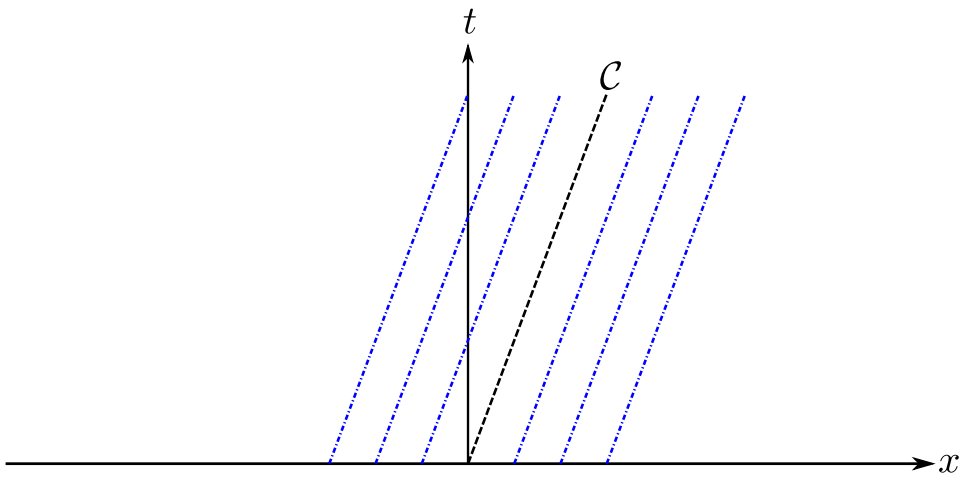

Figure 3.7 – A contact wave with characteristics parallel to the contact wave. The contact wave travels at the fluid velocity. Only the density can jump across the contact wave.

3.3.2 Euler contact wave

A contact wave separates two distinct states and the characteristics either side are parallel to the wave. As a result, no material flows across a contact wave. Figure 3.7 shows a contact wave with parallel characteristics. A contact wave travels with the fluid velocity.

In Newtonian hydrodynamics, the normal velocity and the pressure cannot jump across the wave. Only the density and the tangential velocity components can change across the wave. The jump conditions across the wave are

$$[[v_x^*]] = 0, \tag{3.51a}$$
$$[[p^*]] = 0, \tag{3.51b}$$
$$[[\rho^*]] \neq 0, \tag{3.51c}$$
$$[[v_y^*]] \neq 0, \tag{3.51d}$$
$$[[v_z^*]] \neq 0. \tag{3.51e}$$

The contact wave will be exploited in the development of the mRGFM as it is the *only* wave consistent with an interface. This is because no matter crosses a contact wave, which is also true at an interface.

3.3.3 The exact solution of the Euler Riemann problem

An exact solution to the Riemann problem for the Euler equations can be found if the initial states $\mathbf{q}_{\mathrm{L}}, \mathbf{q}_{\mathrm{R}}$ are known. The states $\mathbf{q}^*_{\mathrm{L}}, \mathbf{q}^*_{\mathrm{R}}$ can be determined by using the shock, rarefaction and contact relations. An implicit equation that is dependent on the star state pressure can be used to solve the Riemann problem [173].

The key is that the pressure and normal velocity are constant across the contact wave, (3.51a) and (3.51b). From the jump conditions, an implicit equation for the pressure p^* can be calculated. The implicit equation is

$$\mathcal{F}(p^*, \mathbf{q}_{\mathrm{L}}, \mathbf{q}_{\mathrm{R}}) \equiv \mathcal{F}_{\leftarrow}(p^*, \mathbf{q}_{\mathrm{L}}) + \mathcal{F}_{\rightarrow}(p^*, \mathbf{q}_{\mathrm{R}}) + \Delta v = 0, \tag{3.52}$$

where $\Delta v = v_{\mathrm{R}} - v_{\mathrm{L}}$ and

$$\mathcal{F}_{\mathrm{x}}(p^*, \mathbf{q}_{\mathrm{x}}) = \begin{cases} (p^* - p_{\mathrm{x}}) \left(\dfrac{A_{\mathrm{x}}}{p^* + B_{\mathrm{x}}} \right)^{1/2} & p^* > p_{\mathrm{x}}, \\ \dfrac{2a_{\mathrm{x}}}{\gamma_{\mathrm{x}} - 1} \left[\left(\dfrac{p^*}{p_{\mathrm{x}}} \right)^{(\gamma_{\mathrm{x}}-1)/(2\gamma_{\mathrm{x}})} - 1 \right] & p^* < p_{\mathrm{x}}, \end{cases} \tag{3.53}$$

where x indicates the left state L or the right state R. This solution has been extended so that the EOS can vary between the left and right states. Therefore, the contact can also represent an interface between two different fluids and the ratio of the specific heat capacities is fluid dependent and is labelled γ_x. The constants A_{x} and B_{x} are defined in the Appendix (B.10) and (B.11), respectively. The case distinction given above is equivalent to one given previously by (3.44) to determine the type of the wave.

Once the pressure p^* has been obtained, the velocity in the states $\mathbf{q}^*_{\mathrm{L}}, \mathbf{q}^*_{\mathrm{R}}$ can be determined from (B.12) or (B.19). Across a shock, the density is given by (B.8). For a rarefaction, the density is given by (B.16), due to the adiabatic nature of a rarefaction wave.

If one of the waves in the solution is a shock wave, then the Rankine-Hugoniot conditions can be applied to calculate its speed,

$$v_s = \frac{\rho_{\{\mathrm{b}\}} v_{\{\mathrm{b}\}} - \rho_{\{\mathrm{a}\}} v_{\{\mathrm{a}\}}}{\rho_{\{\mathrm{b}\}} - \rho_{\{\mathrm{a}\}}}. \tag{3.54}$$

However, if the wave is a rarefaction wave, then the Riemann invariant (B.14) can be used to determine the velocity and the speed of sound in the wave. Due to the adiabatic nature of the rarefaction wave, the pressure and density can be obtained from (B.18) and (B.17), respectively.

The exact solution of the Euler Riemann problem in one dimension can be solved numerically. This framework can be extended to all the following systems. The next section will investigate the effect of relativity on the solution structure.

3.4 Special-Relativistic Hydrodynamics

A relativistic numerical model is required to evolve a neutron star binary inspiral. Only special relativity will be considered in this work. However, Millmore and Hawke [114] demonstrated that the original ghost fluid method could easily be extended to general relativity. Therefore, this section will examine the equations of special relativistic hydrodynamics. These are the dynamic equations of motion for a relativistic fluid in a Minkowskian space-time. The Minkowskian line element in Cartesian coordinates is

$$\mathrm{d}s^2 = -\mathrm{d}t^2 + \mathrm{d}x^2 + \mathrm{d}y^2 + \mathrm{d}z^2, \tag{3.55}$$

with the metric $g_{\mu\nu}$ given by

$$g_{\mu\nu} = \begin{pmatrix} -1 & 0 & 0 & 0 \\ 0 & 1 & 0 & 0 \\ 0 & 0 & 1 & 0 \\ 0 & 0 & 0 & 1 \end{pmatrix}. \tag{3.56}$$

In the Minkowskian space-time, the covariant derivative reduces to the partial derivative as the Christoffel symbols vanish,

$$\nabla_\mu \to \partial_\mu. \tag{3.57}$$

The four-velocity u^μ in special relativity is written as

$$u^\mu = W(1, v^i)^T, \quad u_\mu = W(-1, v_i), \tag{3.58}$$

where W is the Lorentz factor (2.34) and v^i is the three-velocity of the fluid. Using the four-velocity definition (3.58) and the covariant derivative in special relativity (3.57), the conservation of the rest-mass density can be rewritten as

$$\partial_t \left(\rho W\right) + \partial_i \left(\rho W v^i\right) = 0. \tag{3.59}$$

Defining the rest-mass density in an Eulerian frame as

$$D = \rho W, \tag{3.60}$$

the rest-mass density conservation law reads as

$$\partial_t D + \partial_i \left(D v^i\right) = 0. \tag{3.61}$$

The total energy density, $\mathcal{E}$, measured in the Eulerian frame can be defined as

$$\mathcal{E} = \rho h W^2 - p, \tag{3.62}$$

where the specific enthalpy was defined earlier (2.7). The momentum, S^i, in the Eulerian frame is defined as

$$S^i = \rho_0 h W^2 v^i. \tag{3.63}$$

The momentum and the total energy density can be related by

$$S^i = (\mathcal{E} + p)\, v^i. \tag{3.64}$$

The time component of the conservation of the stress-energy tensor, calculated from (2.6), gives

$$\partial_\mu T^\mu{}_t = \partial_t T^t{}_t + \partial_i T^i{}_t = \partial_t \mathcal{E} + \partial_i \left[(\mathcal{E} + p)\, v^i\right] = 0. \tag{3.65}$$

Given the form above, one has a conservation law for the total energy density. However, in the low-velocity limit, the density contribution to the energy dominates and the energy density tends to the rest-mass density in the Eulerian frame. Numerically, this can lead to errors occurring in calculating the total energy density. Therefore, to avoid these errors, the total energy density is rescaled by removing the contribution from the rest-mass density leaving a kinetic dominated term τ,

$$\tau \equiv \mathcal{E} - D. \tag{3.66}$$

A new conservation law can be found for this new variable by subtracting the rest-mass density conservation law (3.61) from the total energy density conservation law (3.65) to give

$$\partial_t \tau + \partial_i \left[(\tau + p)\, v^i\right] = 0. \tag{3.67}$$

Additionally, the spatial components of the conservation of the stress-energy tensor give

$$\partial_\mu T^\mu{}_j = \partial_t T^t{}_j + \partial_i T^i{}_j = \partial_t S_j + \partial_i \left(S_j v^i + \delta^i{}_j p\right) = 0. \tag{3.68}$$

The conserved variables in special relativistic hydrodynamics are

$$\mathbf{q} = \left[D, S_j, \tau\right], \tag{3.69}$$

whereas the primitive variables are

$$\mathbf{u} = \left[\rho, v_j, \epsilon\right]. \tag{3.70}$$

The fluxes are

$$\mathbf{f}^{(i)} = \left[D v^i, S_j v^i + \delta^i{}_j p, (\tau + p)\, v^i\right]. \tag{3.71}$$

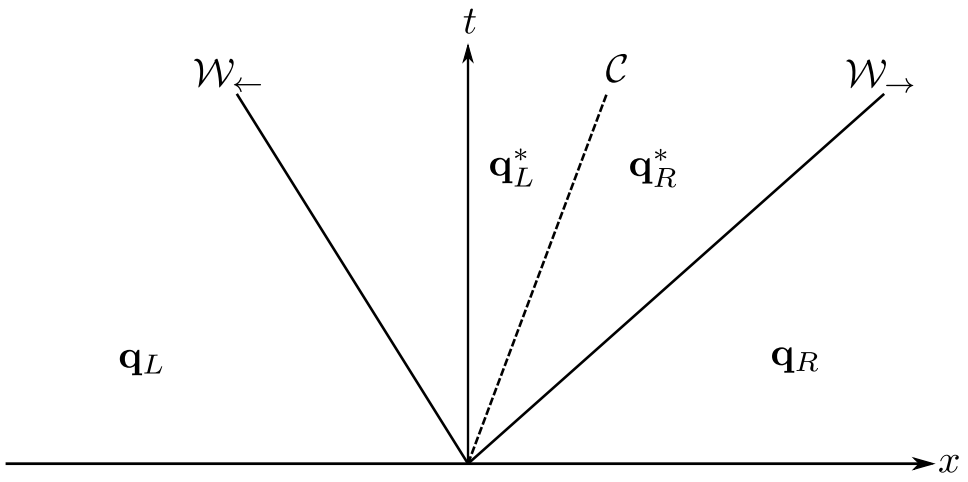

Figure 3.8 – The wave structure solution of the Riemann problem for special relativistic hydrodynamics has three distinct waves separating four states. The two non-linear waves are separated by the contact wave.

3.4.1 Special relativistic hydrodynamics characteristics

As in the Newtonian case, the characteristic information can be found by transforming the system of conservation laws into quasi-linear form by calculating the Jacobian. The addition of the Lorentz factor makes the calculation of the characteristic information more complicated. The three-dimensional eigenvalues and eigenvectors for special relativity were first calculated by Martí and Müller [111]. There are five waves in the special relativistic Riemann fan; two are non-linear and three are degenerate. Their eigenvalues are

$$\lambda_{2,3,4} = v_x, \tag{3.72}$$

$$\lambda_{\pm} = \frac{1}{1 - v^2 a^2}\left(v_x\left(1 - a^2\right) \pm a\sqrt{(1 - v^2)[(1 - v^2 a^2) - v_x^2(1 - a^2)]}\right), \tag{3.73}$$

where $v = \sqrt{v^i v_i}$.

The addition of relativity leads to a frame dependent effect on the characteristic velocities. In the laboratory frame, an asymmetry occurs in the characteristic velocities; the magnitudes of the left and right going characteristic velocities are different. Figure 3.8 shows the structure of the Riemann fan. As you can see, it is similar to the Newtonian case. However, in the frame of the contact the symmetry is restored. Another key effect introduced by the addition of relativity is that, through the Lorentz factor, the wave structure of the solution can be changed by varying the tangential velocities [4, 148].

The eigenvectors of special relativistic hydrodynamics are

$$\mathbf{r}^{(-)} = \begin{pmatrix} 1 \\ hW\mathcal{A}_-\lambda_- \\ hWv_y \\ hWv_z \\ hW\mathcal{A}_- - 1 \end{pmatrix}, \quad \mathbf{r}^{(+)} = \begin{pmatrix} 1 \\ hW\mathcal{A}_+\lambda_+ \\ hWv_y \\ hWv_z \\ hW\mathcal{A}_+ - 1 \end{pmatrix}, \tag{3.74a}$$

$$\mathbf{r}^{(2)} = \begin{pmatrix} \frac{1}{W} \\ v_x \\ v_y \\ v_z \\ 1 - \frac{1}{W} \end{pmatrix}, \quad \mathbf{r}^{(3)} = \begin{pmatrix} Wv_y \\ 2hW^2v_xv_y \\ h\left(1 + 2W^2v_yv_y\right) \\ 2hW^2v_yv_z \\ 2hW^2v_y - Wv_y \end{pmatrix}, \quad \mathbf{r}^{(4)} = \begin{pmatrix} Wv_z \\ 2hW^2v_xv_z \\ 2hW^2v_yv_z \\ h\left(1 + 2W^2v_zv_z\right) \\ 2hW^2v_z - Wv_z \end{pmatrix}, \tag{3.74b}$$

where

$$\mathcal{A}_\pm = \frac{1 - v_x^2}{1 - v_x\lambda_\pm}. \tag{3.75}$$

3.4.2 Special relativistic hydrodynamics contact wave

The contact wave in special relativistic hydrodynamics behaves exactly the same as its Newtonian counterpart. The characteristics at the contact are parallel, as shown in Figure 3.7, and are given by the normal velocity in the star state,

$$\lambda_{2,3,4} = v_x^*. \tag{3.76}$$

At the contact, only the density and the tangential components of the velocity can jump between the two star states $\mathbf{q}_\mathrm{L}^*, \mathbf{q}_\mathrm{R}^*$. The pressure and the normal velocity are constant across the two states. Therefore, the jump conditions at the contact are

$$[[v_x^*]] = 0, \tag{3.77a}$$

$$[[p^*]] = 0, \tag{3.77b}$$

$$[[\rho^*]] \neq 0, \tag{3.77c}$$

$$[[v_t^*]] \neq 0, \tag{3.77d}$$

where the subscript t indicates the tangential components y and z.

3.4.3 Transformation from conserved variables to primitive variables

The transformation from conserved variables $\mathbf{q}$ to primitive variables $\mathbf{u}$ is complicated by relativity. The Lorentz factor couples the variables in a non-trivial way. Unlike in Newtonian hydrodynamics, there is no analytical transformation from the conserved variables to the primitive variables. However, there are many possible ways of transforming the conserved variables to the primitive variables; see the review article by Martí and Müller [111]. The recovery of the primitive variables can be performed by a single variable root find on the pressure. The equation that the root find is performed on is [109]

$$(\gamma - 1)\left[\frac{\tau + D\,(1 - W) + p\left(1 - W^2\right)}{W^2}\right] - p = 0. \tag{3.78}$$

A standard root finder can be used with an initial guess provided by the arithmetic average of the maximum and minimum values of the pressure [109],

$$p_{\max} = (\gamma - 1)\tau, \tag{3.79}$$

$$p_{\min} = \sqrt{S^i S_i} - \tau - D. \tag{3.80}$$

Once the pressure has been recovered, the normal velocity can be obtained from the momentum energy equation (3.64). The Lorentz factor can then be determined, leaving a simple calculation of the density from the Eulerian rest-mass density (3.60). Finally, the specific energy can be calculated from the EOS.

3.5 Newtonian Ideal Magnetohydrodynamics

One of the major objectives of this thesis is to extend the framework developed by Millmore and Hawke [114] to include a magnetic field component. Before this can be achieved, the fluid model must be extended to a charged fluid. In Appendix A.1, the low-velocity equations of ideal magnetohydrodynamics (MHD) are derived from a multi-fluid perspective. Here, they are presented in conservation law form starting with the continuity equation

$$\partial_t \rho + \partial_i(\rho v^i) = 0. \tag{3.81}$$

The continuity equation is unchanged from the addition of the magnetic field, B^i. However, the momentum equation is modified. The fluid is subject to an additional magnetic pressure p_{m}, which can be added to the gas pressure p to form a new total pressure

$$p^* = p + p_m = p + \frac{1}{2}B^2, \tag{3.82}$$

where $B^2 = B^i B_i$.

The fluid is also subject to a tension, which acts to straighten magnetic field lines. This results in a stress tensor

$$\sigma^i{}_j = \rho v^i v_j + \delta^i{}_j p^* - B^i B_j. \tag{3.83}$$

Therefore, the momentum conservation law is given by

$$\partial_t S_j + \partial_i \sigma^i{}_j = 0. \tag{3.84}$$

The conservation of energy equation gains a Poynting flux like term has the form

$$\partial_t \mathcal{E} + \partial_i \left[\left(\mathcal{E} + p^* \right) v^i - B^i \left(B^k v_k \right) \right] = 0, \tag{3.85}$$

where the total energy density is defined as

$$\mathcal{E} = \rho\epsilon + \frac{1}{2} \left(\rho v^2 + B^2 \right). \tag{3.86}$$

Finally, as well as the evolution equations for the fluid, there are equations that govern the magnetic field components. These come from the induction equation and have the form

$$\partial_t B_j + \partial_i \left(v^i B_j - B^i v_j \right) = 0. \tag{3.87}$$

3.5.1 Ideal MHD characteristics

The number of waves in the ideal MHD Riemann problem is eight, as there are eight conserved variables. In the one-dimensional problem, this results in seven waves separating eight constant states. However, the evolution equation associated with the normal magnetic field in one-dimension reduces to

$$\partial_x B^x = 0. \tag{3.88}$$

The wave associated with the normal magnetic field is advected with the fluid and a degeneracy occurs at the contact. Figure 3.9 shows the wave structure.

There are four wave types in ideal MHD: fast, slow, Alfvén and contact. The fast and slow waves are both genuinely non-linear and can be either shock or rarefaction waves. They are similar to their hydrodynamical counterpart but have characteristic velocities fast and slower than a sound wave. They also differ from each other in how they treat the tangential components, see Torrilhon [175]. The contact wave behaves in a similar manner to the contact wave in hydrodynamics. The Alfvén waves are linear, rotational discontinuities. This means that the magnitude of the tangential components, B_t, can change across the wave and the orientation of the tangential field can rotate.

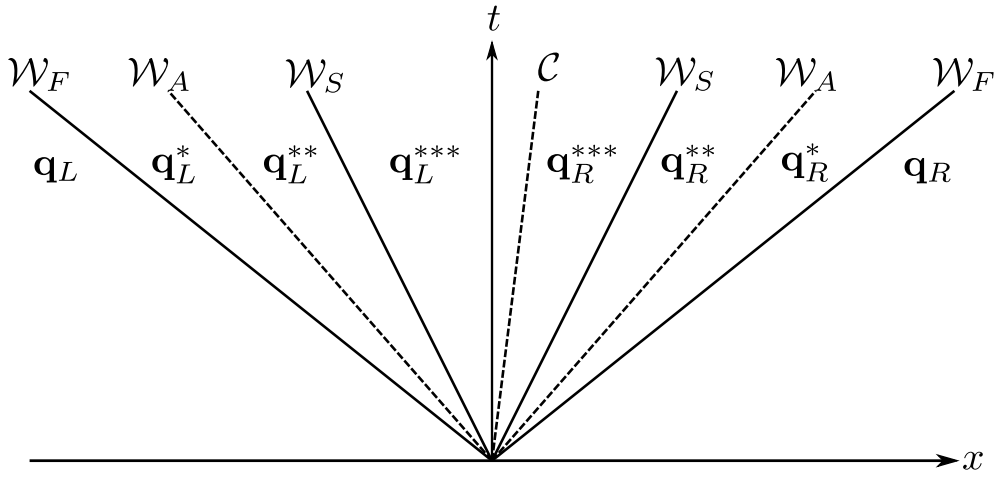

Figure 3.9 – The ideal MHD Riemann problem in one dimension, admits seven waves separated by eight constant states. There are four types of waves: fast, Alfvén, slow and contact. The Alfvén and the contact waves are linearly degenerate, whilst the fast and slow waves are genuinely non-linear. The Alfvén waves are rotational discontinuities.

The characteristics of ideal MHD are

$$\lambda_f^- = v - c_f, \quad \lambda_a^- = v - c_a, \quad \lambda_s^- = v - c_s, \tag{3.89}$$

$$\lambda_{4,5} = v, \tag{3.90}$$

$$\lambda_s^+ = v + c_s, \quad \lambda_a^+ = v + c_a, \quad \lambda_f^+ = v + c_f, \tag{3.91}$$

where $c_{f,s}$ are the fast and slow magneto-sonic velocities and c_a is the Alfvén velocity. From the most negative to most positive they are ordered

$$\lambda_f^- \leq \lambda_a^- \leq \lambda_s^- \leq \lambda_4 = \lambda_5 \leq \lambda_s^+ \leq \lambda_a^+ \leq \lambda_f^+. \tag{3.92}$$

The fast(+) and slow(-) magneto-sonic velocities are defined as

$$c_{f,s} = \sqrt{\frac{1}{2}\left[\frac{B^2}{\rho} + a^2\right] \pm \sqrt{\frac{1}{4}\left[\frac{B^2}{\rho} + a^2\right]^2 - a^2\frac{B_x^2}{\rho}}}\,. \tag{3.93}$$

The Alfvén velocity is defined as

$$c_a = \sqrt{\frac{B_x^2}{\rho}}\,. \tag{3.94}$$

It should be noted that the eigenvalues of ideal MHD are not distinct in certain situations. Therefore, the system of equations is only weakly hyperbolic. This means that degeneracies can occur and two or more eigenvalues are the same.

Powell et al. [139] gave a set of eigenvectors that remain independent when a degeneracy occurs. The degeneracy is dealt with by following the renormalisation of Roe and Balsara [150], which is based on the work of Brio and Wu [34]. The eight right eigenvectors are

$$\mathbf{r}^{(f\pm)} = \begin{pmatrix} \rho\alpha_f \\ \rho\alpha_f(v_x \pm c_f) \\ \rho\left(\alpha_f v_y \mp \alpha_s c_s \beta_x \beta_y\right) \\ \rho\left(\alpha_f v_z \mp \alpha_s c_s \beta_x \beta_z\right) \\ 0 \\ \sqrt{\rho}\,\alpha_s a \beta_y \\ \sqrt{\rho}\,\alpha_s a \beta_z \\ \rho\alpha_f\left(\dfrac{v^2}{2} \pm v_x c_f + \dfrac{a^2}{\gamma-1}\right) + \alpha_s\left(\beta_y v_y + \beta_z v_z\right)\left(\sqrt{\rho}\,a \pm \rho c_s \beta_x\right) \end{pmatrix}, \tag{3.95a}$$

$$\mathbf{r}^{(s\pm)} = \begin{pmatrix} \rho\alpha_s \\ \rho\alpha_s(v_x \pm c_s) \\ \rho\left(\alpha_s v_y \mp \alpha_f c_f \beta_x \beta_y\right) \\ \rho\left(\alpha_f v_z \mp \alpha_f c_f \beta_x \beta_z\right) \\ 0 \\ -\sqrt{\rho}\,\alpha_f a \beta_y \\ -\sqrt{\rho}\,\alpha_f a \beta_z \\ \rho\alpha_s\left(\dfrac{v^2}{2} \pm v_x c_s + \dfrac{a^2}{\gamma-1}\right) + \alpha_f\left(\beta_y v_y + \beta_z v_z\right)\left(\sqrt{\rho}\,a \pm \rho c_f \beta_x\right) \end{pmatrix}, \tag{3.95b}$$

$$\mathbf{r}^{(a\pm)} = \begin{pmatrix} 0 \\ 0 \\ -\beta_z\sqrt{\dfrac{\rho^2}{2}} \\ \beta_y\sqrt{\dfrac{\rho^2}{2}} \\ 0 \\ \pm\beta_z\sqrt{\dfrac{\rho}{2}} \\ \mp\beta_y\sqrt{\dfrac{\rho}{2}} \\ 0 \end{pmatrix}, \quad \mathbf{r}^4 = \begin{pmatrix} 1 \\ v_x \\ v_y \\ v_z \\ 0 \\ 0 \\ 0 \\ \dfrac{v^2}{2} \end{pmatrix}, \quad \mathbf{r}^5 = \begin{pmatrix} 0 \\ 0 \\ 0 \\ 0 \\ 1 \\ 0 \\ 0 \\ B_x \end{pmatrix}, \tag{3.95c}$$

where

$$\beta_x = \operatorname{sgn}\left(B_x\right), \quad \beta_y = \begin{cases} \dfrac{B_y}{B_t} & \text{if } B_t > 0, \\ \dfrac{1}{\sqrt{2}} & \text{if } B_t = 0, \end{cases} \quad \beta_z = \begin{cases} \dfrac{B_z}{B_t} & \text{if } B_t > 0, \\ \dfrac{1}{\sqrt{2}} & \text{if } B_t = 0, \end{cases} \tag{3.96}$$

where $B_t = \sqrt{B_y^2 + B_z^2}$ and

$$\alpha_f = \begin{cases} \sin\phi & \text{if } c_f^2 - c_s^2 = 0, \\ 0 & \text{if } a^2 - c_s^2 = 0, \\ \sqrt{\dfrac{a^2 - c_s^2}{c_f^2 - c_s^2}} & \text{if } c_f^2 - a^2 = 0, \\ \sqrt{\dfrac{a^2 - c_s^2}{c_f^2 - c_s^2}} & \text{otherwise,} \end{cases} \quad \alpha_s = \begin{cases} \cos\phi & \text{if } c_f^2 - c_s^2 = 0, \\ \sqrt{\dfrac{c_f^2 - a^2}{c_f^2 - c_s^2}} & \text{if } a^2 - c_s^2 = 0, \\ 0 & \text{if } c_f^2 - a^2 = 0, \\ \sqrt{\dfrac{c_f^2 - a^2}{c_f^2 - c_s^2}} & \text{otherwise.} \end{cases} \tag{3.97}$$

Finally

$$\phi = \arctan\left(\frac{\frac{B}{\sqrt{\rho}} - c_a}{|B_x| - a}\right). \tag{3.98}$$

3.5.2 Ideal MHD shock jump conditions

In the frame of a discontinuous wave, the mass flux can be defined from the first Rankine-Hugoniot condition [175] as

$$Q \equiv \rho v_x. \tag{3.99}$$

This allows the remaining Rankine-Hugoniot conditions to be written as

$$Q^2\left[[V]\right] + \left[\left[p + \frac{1}{2}B_t^2\right]\right] = 0, \tag{3.100a}$$

$$Q\left[[\mathbf{v}_t]\right] - B_x\left[[\mathbf{B}_t]\right] = 0, \tag{3.100b}$$

$$Q\left[[V\mathbf{B}_t]\right] - B_x[[\mathbf{v}_t]] = 0, \tag{3.100c}$$

$$\left[\left[\frac{\gamma}{\gamma - 1}pV + \frac{1}{2}Q^2V^2 + \left(V - \frac{B_x^2}{2Q^2}\right)B_t^2\right]\right] = 0, \tag{3.100d}$$

where $V = \dfrac{1}{\rho}$ is the specific volume.

3.5.3 Ideal MHD contact wave

As in the case of hydrodynamics, the contact wave does not allow any mass flow across it. The addition of the magnetic field does not change the situation at the contact wave significantly. All the variables, including the magnetic field, are continuous and identical across the contact wave except the density, if there exists a magnetic field normal to the interface,

$$[[v_i^{***}]] = 0, \tag{3.101a}$$
$$[[B_i^{***}]] = 0, \tag{3.101b}$$
$$[[p^{***}]] = 0, \tag{3.101c}$$
$$[[\rho^{***}]] \neq 0. \tag{3.101d}$$

However, if the normal magnetic field is zero then these are the jump conditions at the contact wave

$$[[v_x^{***}]] = 0, \tag{3.102a}$$
$$\left[\left[p^{***} + \frac{B^{2***}}{2}\right]\right] = 0, \tag{3.102b}$$
$$[[v_t^{***}]] \neq 0, \tag{3.102c}$$
$$[[B_t^{***}]] \neq 0, \tag{3.102d}$$
$$[[\rho^{***}]] \neq 0. \tag{3.102e}$$

3.5.4 Ideal MHD Alfvén wave

The addition of the magnetic field results in a second type of linear wave to the solution of the Riemann problem: the Alfvén wave. These waves were first proposed by Alfvén in 1942 [3] for an incompressible fluid; one of constant density. Their existence was confirmed by Lundquist in 1949 and their velocity matched that proposed by Alfvén [107]. The Alfvén waves are shear waves caused by the tension in the magnetic field lines.

If one applies the condition of constant density to the Rankine-Hugoniot conditions, the jump conditions for an Alfvén wave are obtained. Across an Alfvén wave several quantities do not jump. These are

$$[[\rho]] = 0, \quad [[p]] = 0, \quad [[B_t]] = 0, \quad [[v_x]] = 0, \quad [[B_x]] = 0. \tag{3.103}$$

Only the individual tangential components can change across an Alfvén wave

$$[[\mathbf{v}_t]] = \pm\frac{1}{\sqrt{\rho}}\,[[\mathbf{B}_t]]\,, \tag{3.104}$$

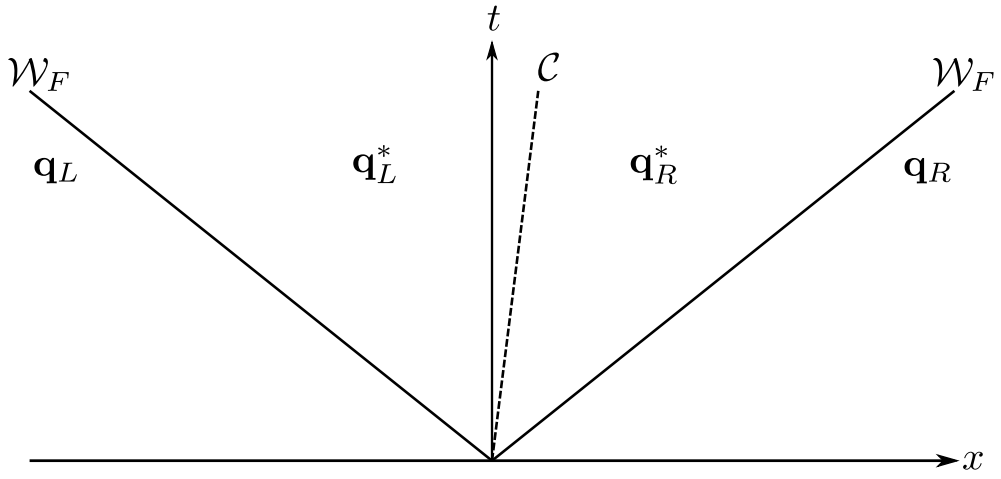

Figure 3.10 – When the normal component of the magnetic field is zero, the wave solution to the one-dimensional Riemann problem consists of a fast wave either side of a contact wave.

where $\pm$ indicates the direction of travel.

3.5.5 Ideal MHD degeneracies

Unlike the one-dimensional Euler equations, the one-dimensional equations of ideal MHD are not always strictly hyperbolic. This means that for certain values of the magnetic field degeneracies can occur. This is the case, when two or more waves have the same characteristic velocity.

The first such case occurs, when the normal magnetic field is zero and the tangential magnetic field is non-zero,

$$B_x = 0, \quad B_t \neq 0. \tag{3.105}$$

When this happens, the Alfvén characteristic velocity is zero. Both Alfvén waves and both slow waves coincide with the contact wave. This is because the Alfvén wave is a shear wave that travels transversely along the magnetic field line. This cannot happen if there is no normal magnetic field. The resulting wave structure is made up of the fast waves shown in Figure 3.10.

The second degeneracy occurs, when there is no tangential magnetic field and the speed of sounds is equal to the Alfvén velocity,

$$B_x \neq 0, \quad B_t = 0, \quad a = c_a. \tag{3.106}$$

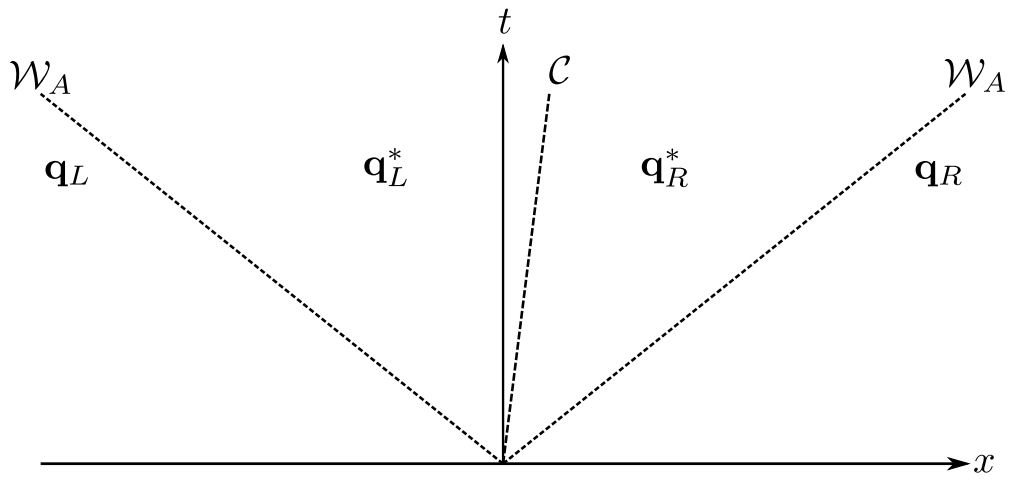

Figure 3.11 – A degeneracy occurs, when the tangential magnetic field is zero and the speed of sound is equal to the Alfvén velocity. The resulting wave solution to the one-dimensional Riemann problem consists of an Alfvén wave either side of a contact wave.

At this point, the characteristic speeds of the fast and slow waves coincide with the Alfvén wave. The resulting wave structure contains an Alfvén like wave either side of a contact wave and is shown in Figure 3.11.

The final degeneracy is observed, when the tangential components of the magnetic field are zero and the Alfvén velocity does not equal the speed of sound,

$$B_x \neq 0, \quad B_t = 0, \quad a \neq c_a. \tag{3.107}$$

There are two possible solutions to the conditions above. The Alfvén velocity is larger than the speed of sound or smaller. In the first case, the fast waves become degenerate with the Alfvén velocity. In the second case, the slow waves become degenerate with the Alfvén velocity,

$$c_a = \begin{cases} c_f & \text{if } c_a > a, \\ c_s & \text{if } c_a < a. \end{cases} \tag{3.108}$$

The resulting wave structure has two waves either side of the contact which is shown in Figure 3.12 and Figure 3.13.

3.6 Special Relativistic Magnetohydrodynamics

As with special relativistic hydrodynamics, the addition of relativistic effects complicates the solution to the Riemann problem. This thesis will only consider solutions on flat space-time with a Minkowskian metric (3.55). Therefore, the relations for the Lorentz factor (2.34) and the four-velocity (3.58) are still valid.

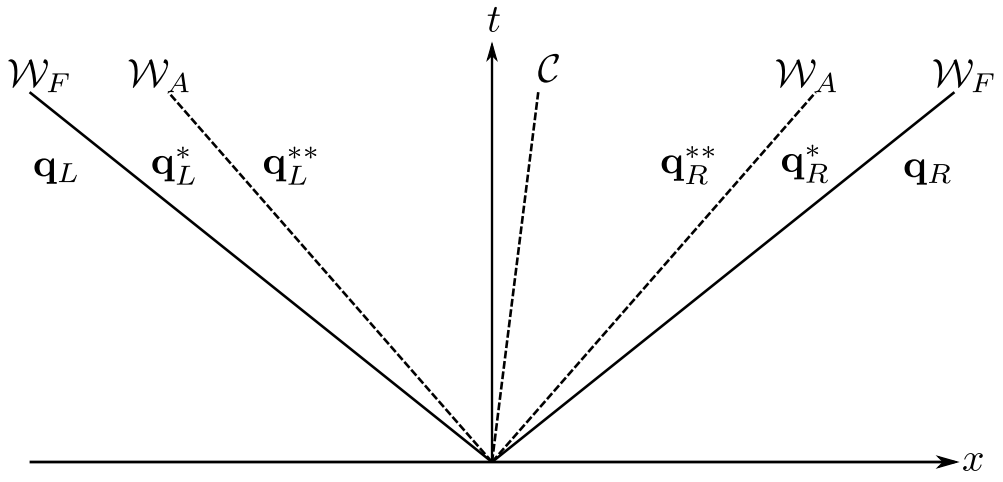

Figure 3.12 – A degeneracy occurs, when the tangential magnetic field is zero and the speed of sound is equal to the Alfvén velocity. The resulting wave solution to the one-dimensional Riemann problem consists of a fast wave and an Alfvén wave either side of a contact wave.

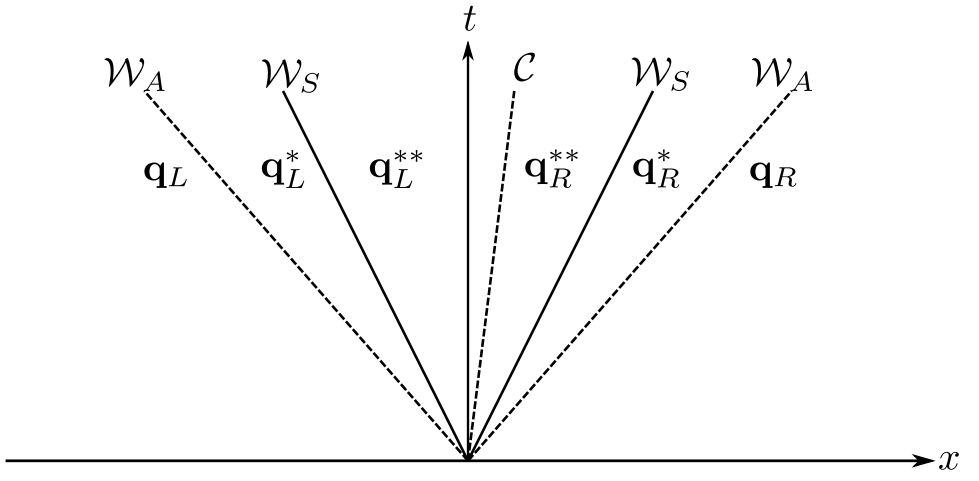

Figure 3.13 – A degeneracy occurs, when the tangential magnetic field is zero and the speed of sound is equal to the Alfvén velocity. The resulting wave solution to the one-dimensional Riemann problem consists of an Alfvén wave and a slow wave either side of a contact wave.

As in Newtonian, ideal MHD, the continuity equation is not affected by the addition of the magnetic field and has the same form as in special relativistic hydrodynamics (3.60). However, the stress-energy tensor gains a contribution from the magnetic field and in the ideal limit is given by

$$T^{\mu\nu} = \rho h^* u^\mu u^\nu + p^* g^{\mu\nu} - b^\mu b^\nu, \tag{3.109}$$

where $b^2 = b^\mu b_\mu$ and the pressure p^* is defined as

$$p^* = p + b^2/2. \tag{3.110}$$

The enthalpy h^* is given by

$$h^* = h + b^2/\rho. \tag{3.111}$$

The covariant magnetic field is

$$b^\mu \equiv \left\{ W(v^i B_i), \frac{B^j}{W} + W\left(v^i B_i\right) v^j \right\}, \tag{3.112}$$

where W is the Lorentz factor. The momentum conservation law, as in ideal MHD, gains a shear stress related to the magnetic field,

$$\partial_t S_j + \partial_i \left(S_j v^i + \delta^i{}_j p^* - b_j \frac{B^i}{W} \right) = 0. \tag{3.113}$$

The conservation of energy equation also gains a Poynting like term,

$$\partial_t \tau + \partial_i \left(\left[\tau + p^*\right] v^i - b^0 \frac{B^i}{W} \right) = 0. \tag{3.114}$$

The momentum and energy have been extended by contributions from the magnetic field and are

$$S^i = \rho h^* W^2 v^i - b^0 b^i, \tag{3.115}$$

$$\tau = \rho h^* W^2 - p^* - \left(b^0\right)^2 - D, \tag{3.116}$$

where D is the rest-mass in an Eulerian frame. Finally, the magnetic evolution equation is the same as in ideal MHD,

$$\partial_t B^j - \partial_i \left(v^i B^j - v^j B^i \right) = 0. \tag{3.117}$$

The vector of conserved variables is

$$\mathbf{q} = \left[D, S^i, \tau, B^i\right]^{\mathrm{T}}, \tag{3.118}$$

and the primitive variables are

$$\mathbf{u} = \left[\rho, v^i, \epsilon, B^i\right]^{\mathrm{T}}. \tag{3.119}$$

3.6.1 SRMHD characteristics

The derivation of the characteristic structure of the special relativistic, ideal MHD (SRMHD) equations was performed by Anile [13]. As with ideal MHD, Anile showed that there are seven waves separating eight constant states in the solution to the one-dimensional Riemann problem. The analysis was performed on the set variables $\tilde{u} = (u^\mu, b^\mu, p, \mathfrak{s})^{\mathrm{T}}$, where $\mathfrak{s}$ is the specific entropy. Following the presentation by Antón et al. [14], the characteristic velocities are given by

$$\mathcal{C} A^2 \mathcal{D}^2 \mathcal{N}_4 = 0, \tag{3.120}$$

where

$$\mathcal{D} = \mathcal{C} A^2 - \mathcal{B}^2, \tag{3.121}$$

$$\mathcal{N}_4 = \rho h \left(\frac{1}{a^2} - 1\right) A^2 - \left(\rho h + \frac{b^2}{a^2}\right) A^2 G + \mathcal{B}^2 G, \tag{3.122}$$

$$\mathcal{C} = \rho h + b^2, \tag{3.123}$$

$$A = u^\mu \phi_\mu, \tag{3.124}$$

$$\mathcal{B} = b^\mu \phi_\mu, \tag{3.125}$$

$$G = \phi^\mu \phi_\mu, \tag{3.126}$$

and $\phi_\mu = (-\lambda, 1, 0, 0)$. The contact wave is given by $A = 0$, while the Alfvén waves are given by $\mathcal{D} = 0$. Both cases have an analytical solution and the contact wave speed is

$$\lambda_{\mathrm{contact}} = v^x. \tag{3.127}$$

As with the special relativistic, hydrodynamical equations in the laboratory frame, the characteristic velocities are Lorentz contracted, but the symmetry is restored in the frame of the contact. The Alfvén wave speeds are given by

$$\lambda_a^{\pm} = \frac{b^x \pm \sqrt{\mathcal{C}} W v^x}{b^0 \pm \sqrt{\mathcal{C}} W}. \tag{3.128}$$

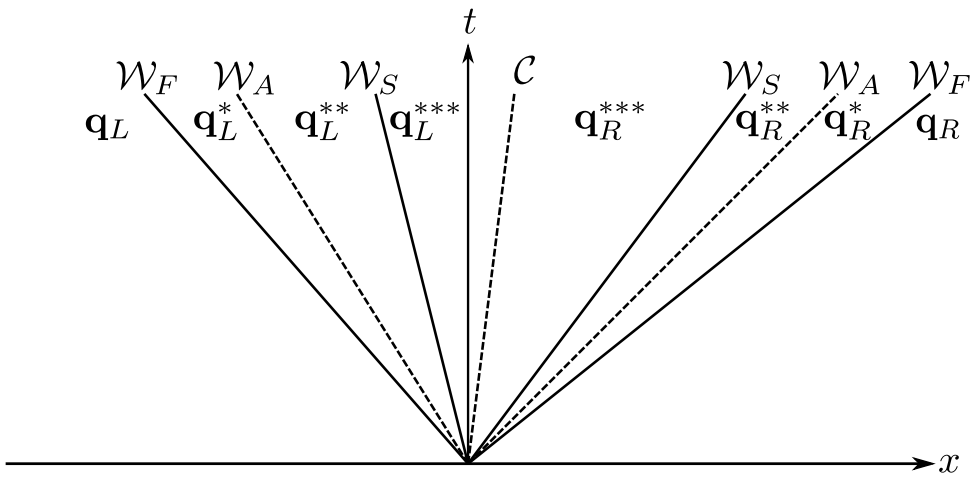

Figure 3.14 – The wave solution to the one-dimensional, special relativistic, ideal MHD Riemann problem. It shows that there are seven waves separating eight constant states as in the Newtonian case.

However, the magneto-sonic waves are obtained by solving

$$\mathcal{N}_4 = 0, \tag{3.129}$$

which is a quartic equation that must be solved numerically.

The wave structure for special relativistic, ideal MHD is given in Figure 3.14. It shows that in the typical case there are seven waves separating eight states. The eigenvalues for special relativistic, ideal MHD, like Newtonian, ideal MHD, are not distinct in certain situations. This means that the system of equations is weakly hyperbolic. It also implies that the system is susceptible to the same degeneracies. The degeneracy is frame independent and, therefore, will affect the right and left going waves equally.

The conserved eigenvectors are calculated by multiplying a set of covariant eigenvectors given by Antón et al. [14] by a Jacobian. These eigenvectors are based on the ones calculated by Anile [13] and are required by the mRGFM. They are given in the Appendix D.1. The matrix to calculate the conserved eigenvectors, for an ideal fluid, is

$$\frac{\partial q}{\partial \tilde{u}} = \begin{pmatrix} \rho & 0 & 0 & 0 & 0 & 0 \\ AWv^x & AW & 0 & 0 & -2b^0W^2v^x - b^x & 2b^xW^2v^x - b^0 \\ AWv^y & 0 & AW & 0 & -2b^0W^2v^y - b^y & 2b^xW^2v^y \\ AWv^z & 0 & 0 & AW & -2b^0W^2v^z - b^z & 2b^xW^2v^z \\ 2AW & 0 & 0 & 0 & -2b^0W^2 - b^0 & 2b^xW^2 - b^x \\ b^y & 0 & -b^0 & 0 & -u^y & 0 \\ b^z & 0 & 0 & -b^0 & -u^z & 0 \end{pmatrix}$$

$$\begin{pmatrix} 0 & 0 & \frac{W\rho}{\gamma p} & \frac{-W\rho}{\gamma} \\ 2b^yW^2v^x & 2b^zW^2v_x & TW^2v^x & \frac{-\rho}{\gamma}W^2v^x \\ 2b^yW^2v^y - b^0 & 2b^zW^2v^y & TW^2v^y & \frac{-\rho}{\gamma}W^2v^y \\ 2b^yW^2v^z & 2b^zW^2v^z - b^0 & TW^2v^z & \frac{-\rho}{\gamma}W^2v^z \\ 2b^yW^2 - b^y & 2b^zW^2 - b^z & TW^2 - 1 & \frac{-\rho}{\gamma}W^2 \\ W & 0 & 0 & 0 \\ 0 & W & 0 & 0 \end{pmatrix}, \tag{3.130}$$

where $\dfrac{\gamma^2 p + \gamma\rho - \rho}{\gamma p(\gamma - 1)} = T$.

3.6.1.1 SRMHD contact and exact solution

The jump conditions at the contact wave in SRMHD are the same as the Newtonian case given in Subsection 3.5.3.

$$[[v_i^{***}]] = 0, \tag{3.131a}$$
$$[[B_i^{***}]] = 0, \tag{3.131b}$$
$$[[p^{***}]] = 0, \tag{3.131c}$$
$$[[\rho^{***}]] \neq 0. \tag{3.131d}$$

The exact solution to the Riemann problem for SRMHD was calculated by Giacomazzo and Rezzolla [62]. Their exact solver requires accurate initial guesses for the majority of the variables in the states either side of the contact. They then use the jump conditions at the contact to constrain their solution. It has been used in this thesis to validate the numerical methods for the SRMHD equations.

3.6.2 SRMHD degeneracies

Similar to Newtonian, ideal MHD, the SRMHD system of equations is weakly hyperbolic. It is susceptible to several different degeneracies. Antón et al. [14] describe three different degeneracies. Type I occurs when $\mathcal{B} = 0$ and has the same effect as the ideal MHD case when $B_x = 0$. As a result of $\mathcal{B} = 0$, the Alfvén and slow waves propagate with the contact wave,

$$\lambda_a^- = \lambda_s^- = \lambda_{\text{contact}} = \lambda_s^+ = \lambda_a^+. \tag{3.132}$$

The wave structure is the same as in Figure 3.10. This is where the match with ideal MHD ends. Type II degeneracy is similar to Newtonian, ideal MHD, but can only affect one side of the Riemann fan. The Alfvén and slow waves or Alfvén and fast waves propagate at the same velocity,

$$\lambda_f^- = \lambda_a^- \text{ or } \lambda_a^- = \lambda_s^- \text{ or } \lambda_s^+ = \lambda_a^+ \text{ or } \lambda_a^+ = \lambda_f^+. \tag{3.133}$$

Type II' degeneracy occurs when

$$c_a = \sqrt{\frac{b^2}{\mathcal{C}}}. \tag{3.134}$$

This degeneracy results in both the slow and fast waves coinciding with the Alfvén wave on one side of the Riemann fan,

$$\lambda_f^- = \lambda_a^- = \lambda_s^- \text{ or } \lambda_s^+ = \lambda_a^+ = \lambda_f^+. \tag{3.135}$$

In the case where the tangential magnetic field vanishes, the usual Newtonian behaviour returns to the second and third degeneracies.

3.6.3 SRMHD conserved to primitive

As in the case of special relativistic hydrodynamics, the addition of relativistic effects means that there exists no analytical method of inverting the conserved variables of special relativistic MHD into the primitive variables. Several different approaches have been developed and six have been summarised by Noble et al. [119]. We have implemented the "2D" method of Noble et al. and the "1D" method of Del Zanna et al. [42]. It was found that the Del Zanna method was more robust and it is our preferred method. The method is a one-dimensional root find which calculates the variables v^2 and Ω, where Ω is defined as

$$\Omega = W^2(\rho + \rho\epsilon + \bar{p}). \tag{3.136}$$

Variables with an asterisk are the previous known values and those with a bar are guesses.

- Calculate a guess for the density from D and W,

$$\bar{\rho_0} = \frac{D}{W}. \tag{3.137}$$

- Calculate $\bar{p}$ from the equation of state and the primitive variables,

$$\bar{p} = |\epsilon^* \rho^*|(\gamma - 1). \tag{3.138}$$

- Calculate Ω from a combination of the previously values of the primitive variables and the conserved ones,

$$\Omega = W^2 \left(\bar{\rho}_0 + |\epsilon^* \rho^*| + \bar{p}\right). \tag{3.139}$$

- Calculate scalar quantities from the conserved variables, $B^2 = B^k B_k$, $\Pi = S^k B_k$ and $S^2 = S^k S_k$.

- Check that the value for Ω is large enough so that $v^2 < 1$; Ω must satisfy this inequality,

$$\Omega^2 \left(S^2 - B^4\right) > \left[\Omega^3 \left(\Omega + 2B^2\right) - \Pi^2 \left(2\Omega + B^2\right)\right]. \tag{3.140}$$

- Calculate v^2 from Ω,

$$v^2 = \frac{\Omega^2 S^2 \Pi^2 \left(B^2 + 2\Omega\right)}{\Omega^2 \left(B^2 + \Omega\right)^2}. \tag{3.141}$$

- Next, we perform a root find following the methods outlined by Dumbser et al. [48] and Del Zanna et al. [43], which returns values for v^2 and Ω.

- The primitive variables can be reconstructed from Ω and v^2 following the method outlined in Noble et al. [119].

3.7 Summary

This chapter has introduced the general form of a conservation law and considered the Riemann problem in one dimension. These concepts are fundamental for the numerical methods introduced in the numerical methods chapter, Chapter 4. They also form the bedrock of the mRGFM.

The equations of Newtonian hydrodynamics, special relativistic hydrodynamics, ideal MHD and special relativistic, ideal MHD have been given along with the solution structure for each case. Understanding the structure and the conversion between variables is essential in the development of the interface method and will be explored in more detail in the interface conditions chapter, Chapter 6.

Chapter 4

Numerical Methods

This chapter focuses on the numerical methods and techniques that have been used to solve the evolution equations presented in the previous chapter. These evolution equations are non-linear systems of hyperbolic conservation laws or balance laws. Many numerical methods exist to solve these sets of equations and this chapter will now present the techniques utilised in this thesis.

There are many advantages to solving systems of equations numerically, but this also introduces numerical errors to the solution. A balance must be made between reducing these numerical errors and the computational cost of the numerical method used. The numerical methods used in this thesis also require the discretisation of the domain. The discretisation of a continuum model will obviously introduce some error, but it is expected that through increased resolution these errors will reduce. Numerical methods with higher accuracy can also be used to reduce error. Therefore, selecting the right combination of numerical method and resolution for the amount of computational resources available is a key part of any numerical simulation.

This thesis requires a general approach to numerically solve systems of non-linear partial differential equations (PDEs). Many techniques have been developed to solve these equations numerically. Four of the most commonly used techniques are: finite volume [173], finite difference [96, 100], spectral methods [69, 86] and smoothed particle hydrodynamics [64, 117]. Choosing the appropriate method depends on the physical situation one is trying to simulate; each has its advantages and disadvantages.

Smoothed particle hydrodynamics is a Lagrangian method where the coordinate system moves with the fluid, and was originally developed for astronomical problems. One of the major advantages of this approach is that the conservation of mass is perfectly maintained within the system. However, spurious pressure forces on particles can occur in the region of a shock wave. Therefore, this approach is unsuitable for our problem [58]. Spectral methods are applicable for systems with smooth data that require high accuracy. However, non-linear systems of equations are expected to develop non-smooth regions, which means that spectral methods are not useful for our purposes. It is this non-smooth behaviour that ultimately determines are choice of numerical method. Finite volume methods have been especially developed to deal with this non-smooth behaviour. Although more computationally expensive, the benefit gained when dealing with shocks means that the finite volume approach will be used in the following.

4.1 Finite Volume Methods

Chapter 3 showed that the evolution equations of interest can be written in conservation or balance law form,

$$\frac{\partial}{\partial t}\mathbf{q}(x,t) + \frac{\partial}{\partial x}\mathbf{f}(\mathbf{q}(x,t)) = \mathbf{s}(\mathbf{q}(x,t)), \tag{4.1}$$

where $\mathbf{q}$ is an arbitrary state vector, $\mathbf{f}$ is the flux vector and $\mathbf{s}$ the source vector. This section will only consider "$1+1$" dimensional equations. However, these methods can be easily extended to higher dimensions. Many of the techniques and methods described in this chapter can be found in [173], [96] and [100].

Chapter 2 developed a set of evolution equations for a continuum model. These equations must be solved numerically; this requires a discretisation of the physical and numerical domain. This discretisation is done by splitting the spatial domain into small volumes. In the one-dimensional case, these volumes become cells of width Δx. Figure 4.1 shows such a cell. They are labelled I_i, where $i \in [1, N]$ and N is the number of cells. The location x at the centre of the cell is denoted x_i. The domain of a cell x_i is $\left[x_{i-1/2}, x_{i+1/2}\right]$, where $x_{i\pm1/2} = x_i \pm \frac{1}{2}\Delta x$.

The time domain is split into "levels" that are separated by a time-step Δt. Each "level" is denoted t^n, where $t^{n+1} = t^n + \Delta t$, and t^0 is the initial time. The resolution of a numerical simulation is determined by the values Δx and Δt.

Each cell is filled with the vector $\hat{\mathbf{q}}_i^n$, which is the integral average of the state vector $\mathbf{q}(t^n, x)$ within the cell. The integral average is defined as

$$\hat{\mathbf{q}}_i^n = \frac{1}{\Delta x}\int_{x_{i-1/2}}^{x_{i+1/2}} \mathbf{q}(t^n, x)\mathrm{d}x. \tag{4.2}$$

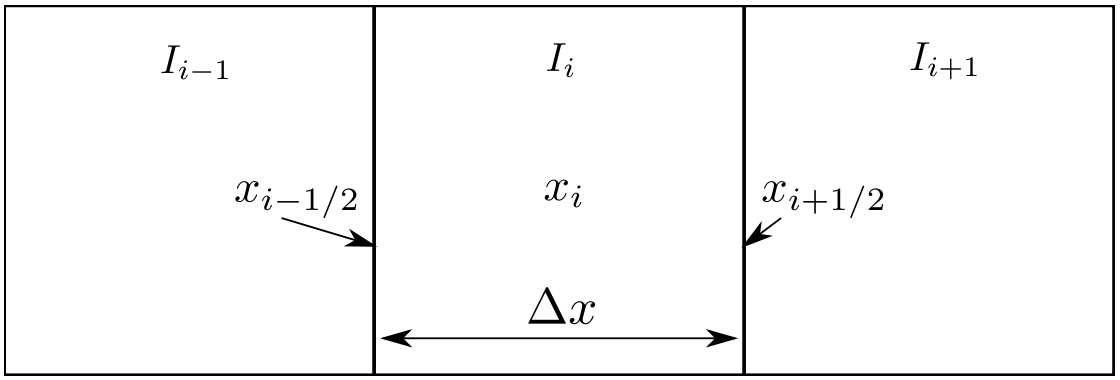

Figure 4.1 – The numerical domain is split into cells I_i, where $i \in [1, N]$ for N cells. The integral average is defined at the cell centre x_i. The Riemann problem needs to be calculated at the boundary $x_{i\pm1/2}$. The width of a cell is Δx.

4.2 Time Integration and Stability

4.2.1 Method of lines

The method of lines allows one to approximate a system of PDEs by a set of ordinary differential equations (ODEs). The method of lines is outlined in detail in the book by Schiesser [154]. Converting to a set of ODEs is useful, because stable numerical methods for solving ODEs are plentiful and easy to implement.

The method of lines replaces the spatial boundary problem with an approximation at each point. This leaves an initial value problem at each point that is only dependent on time. Applying the method of lines to the general weak form of the PDE (4.1) with $\mathbf{s} = 0$ and discretising in space only, one gets

$$\frac{\mathrm{d}}{\mathrm{d}t}\hat{\mathbf{q}}_i(t) = \frac{1}{\Delta x}\left[\mathbf{f}(\mathbf{q}(t, x_{i-1/2})) - \mathbf{f}(\mathbf{q}(t, x_{i+1/2}))\right]. \tag{4.3}$$

The equation (4.3) is an ODE for $\hat{\mathbf{q}}_i$ and to solve it the fluxes $\mathbf{f}$ must be known. These fluxes can be approximated by inter-cell fluxes $\hat{\mathbf{F}}_{i\pm1/2}$. Determining these inter-cell fluxes can be done in many different ways and will be considered in Section 4.4.

4.2.2 Stability

It is important that the numerical method used to integrate the ODE is stable. A stable numerical method does not introduce unphysical oscillations that are unbounded. One measure of stability that is commonly used is the *total variation*, (TV). The TV for a discretised vector is

$$TV\left(\hat{\mathbf{q}}^n\right) = \sum_{i=-\infty}^{\infty} |\hat{\mathbf{q}}_{i+1}^n - \hat{\mathbf{q}}_i^n|, \tag{4.4}$$

where the supremum means that all possible samples from the domain are included.

If the TV does not increase from one time step to the next, then the time integrator is *strong stability preserving* (SSP),

$$TV\left(\hat{\mathbf{q}}^{n+1}\right) \leq TV\left(\hat{\mathbf{q}}^n\right). \tag{4.5}$$

This is also a fundamental property of the exact solution of a scalar, non-linear conservation law. The total variation is a decreasing function in time [173]. Therefore, this thesis uses SSP time integrators such as the third order Runge-Kutta method introduced in Section 4.2.3 to mimic the behaviour of the exact solution.

A total variation diminishing (TVD) method is one that does not increase to TV through spatial reconstruction. This is important to consider in the presence of discontinuities. It is crucial to avoid the appearance of unphysical oscillations due to the Gibbs phenomenon. These oscillations can occur, when reconstructing across a discontinuity.

This thesis uses weighted, essentially, non-oscillatory (WENO) methods that obey a weaker condition, but allow higher-order reconstruction [162]. The condition is that the variation can increase by the grid spacing to some power r,

$$TV\left(\hat{\mathbf{q}}^{n+1}\right) \leq TV\left(\hat{\mathbf{q}}^n\right) + \mathcal{O}\left[(\Delta x)^r, (\Delta t)^r\right]. \tag{4.6}$$

In the limit as $\Delta t \to 0, \Delta x \to 0$ the WENO method approaches the SSP condition. For more details on stability see the book by Laney [96].

4.2.3 Runge-Kutta methods

Having converted the system of PDEs to a set of ODEs, using the method of lines, the Runge-Kutta methods [70] can be used to integrate the ODEs in time. The ODE has the form

$$\frac{\mathrm{d}}{\mathrm{d}t}\hat{\mathbf{u}} = -\hat{\mathbf{F}}(\hat{\mathbf{u}}). \tag{4.7}$$

The Runge-Kutta methods have been chosen, because they are of high order and simple to implement. The third order method, used in this thesis, is SSP; see Gottlieb et al. [71] for a review of high order SSP discretisation. The third order method is

$$\hat{\mathbf{u}}^{(1)} = \hat{\mathbf{u}}^n + \Delta t\hat{\mathbf{F}}(\hat{\mathbf{u}^n}), \tag{4.8}$$

$$\hat{\mathbf{u}}^{(2)} = \frac{1}{4}\left(3\hat{\mathbf{u}}^n + \hat{\mathbf{u}}^{(1)} + \Delta t\hat{\mathbf{F}}(\hat{\mathbf{u}}^{(1)})\right), \tag{4.9}$$

$$\hat{\mathbf{u}}^{n+1} = \frac{1}{3}\left(\hat{\mathbf{u}}^n + 2\hat{\mathbf{u}}^{(2)} + 2\Delta t\hat{\mathbf{F}}(\hat{\mathbf{u}}^{(2)})\right). \tag{4.10}$$

These methods are useful for systems of equations that are non-stiff. The ones in this thesis are non-stiff. However, source terms in the resistive MHD code of Dionysopoulou et al. [47] cause stiffness and they use the implicit-explicit Runge-Kutta method of Pareschi et al. [130].

4.2.4 The CFL condition

The Courant-Friedrichs-Lewy (CFL) condition states that the numerical domain of dependence must include the PDEs' domain of dependence. This is a necessary condition for stability, but not sufficient [39].

It ensures that all of the information required to update a point has time to propagate to that point. If this is not allowed to happen, oscillations within the solution can occur and lead to instabilities. This condition can be defined in terms of the Courant number CFL,

$$\mathrm{CFL} = \left|\frac{c\Delta t}{\Delta x}\right| \leq 1, \tag{4.11}$$

where c is the maximum characteristic speed of the system. Fewer integration steps are required, when the Courant number is closer to one. An important process is determining what value to set the Courant number. Reducing the total number of steps decreases the total numerical error because each step introduces numerical error. However, setting the Courant number too high could lead to an unstable numerical method. We use a typical value of CFL = 0.5.

4.2.5 The Lax-Wendroff theorem

Chapter 3 expressed the evolution equations in conservation or balance law form. By using a numerical method that is conservative, one can guarantee that the position of any discontinuity is correctly captured throughout the evolution. With a conservative method, the exact location of a discontinuity is not known but its location is contained within a region; this is known as *shock capturing*.

This property can be observed by considering the ODEs (4.3) on an arbitrary domain $[x_A, x_B]$. For a conservative method, the fluxes $\hat{\mathbf{f}}_{i+1/2} = \hat{\mathbf{f}}_{(i+1)-1/2}$ are equal. This means that the sum across the entire domain is

$$\frac{\mathrm{d}}{\mathrm{d}t}\sum_{i=A}^{B}\hat{\mathbf{q}}_i = \sum_{i=A}^{B}\frac{1}{\Delta x}\left(\hat{\mathbf{f}}_{i-1/2} - \hat{\mathbf{f}}_{i+1/2}\right) = \frac{1}{\Delta x}\left(\hat{\mathbf{f}}_{A-1/2} - \hat{\mathbf{f}}_{B+1/2}\right). \tag{4.12}$$

Therefore, if a discontinuity exist within the domain $[x_A, x_B]$, conservation still holds.

The Lax-Wendroff theorem states that a conservative method that converges to a consistent solution in the limit $\Delta x \to 0$ and $\Delta t \to 0$ will converge to a weak solution of the system of equations [99]. It is important that a solution of the evolution equations converges to a weak solution, because, along with the physical law, this ensures it converges to the correct solution.

4.3 Spatial Reconstruction to the Cell Boundary

Using the method of lines, the system of PDEs was converted to a set of ODEs (4.3). To solve these equations between the times t^n and $t^{n+1} = t^n + \Delta t$, one needs to calculate the inter-cell fluxes. The inter-cell flux can be approximated by the solution of the Riemann problem at the cell boundary. This procedure requires several steps to be performed. The average states at the centre of the cells need to be reconstructed at the boundary. This reconstruction gives the initial data for the Riemann problem that needs to be solved subsequently. The method chosen has a big impact on the overall accuracy of the finite volume method. However, as with the majority of numerical calculations, there is a trade-off between accuracy and computational time.

The exact solution of the Riemann problem usually requires a numerical root-finding algorithm. Therefore, the exact solution is computationally expensive and would not be suitable to use at every cell boundary. An alternative is to use approximate solutions that are usually analytic and require significantly less computational power.

Solving the approximate Riemann problem using reconstructed values was pioneered by Godunov [65]. Methods that follow this reconstruction approach are known as Godunov-type methods. Many different varieties have been developed to do this reconstruction. Several of them can be found in the book by LeVeque [100]. The simplest reconstruction is piecewise, linear reconstruction of the cell average to the boundary. This reconstruction was the original method of Godunov. The reconstructed variables at $x_{i+1/2}$ are

$$\bar{\mathbf{q}}^{-}_{i+1/2} = \hat{\mathbf{q}}_i, \quad \bar{\mathbf{q}}^{+}_{i+1/2} = \hat{\mathbf{q}}_{i+1}. \tag{4.13}$$

These reconstructed values give the left and right states to the Riemann problem,

$$\bar{\mathbf{q}}^{-}_{i+1/2} = \bar{\mathbf{q}}_L, \quad \bar{\mathbf{q}}^{+}_{i+1/2} = \bar{\mathbf{q}}_R. \tag{4.14}$$

The inter-cell flux $\bar{\mathbf{f}}_{i+1/2}$ can then be calculated from these reconstructed values by exactly or approximately solving the Riemann problem at the boundary.

The method proposed by Godunov is a first order, convergent, conservative method. However, higher-order methods exist. By performing higher-order conservative reconstruction, one can increase the global order of convergence. This approach is collectively known as *high-resolution shock-capturing* (HRSC) methods. Godunov showed that high-order reconstruction leads to oscillations for non-linear features [65]. Where smooth data exists, HRSC methods reconstruct data at orders as high as the numerical methods allow. At non-linear features, HRSC methods reduce to first order so that they do not introduce non-physical oscillations. Therefore, this thesis will use WENO methods, because they offer accuracy up to any order.

4.3.1 Essentially non-oscillatory reconstruction

The WENO method used in this thesis is constructed from the weighted sum of ENO reconstructed variables. The first implementation of an ENO reconstruction was performed by Harten et al. in 1987 [77]. This section follows the procedure outlined by Shu in 1998 [162].

The approach of the ENO methods is to choose a stencil of r cells that minimises the possibility of a discontinuity being included within the reconstruction. The ENO scheme can be made conservative by reconstructing the integral average, which is essential to accurately capture the location of non-linear features.

The following procedure describes the reconstruction of a scalar function V at the cell x_i with k order accuracy. Starting from the cell x_i, add more cells to the stencil until there are r cells. When adding a cell to the stencil, one chooses between the cells at the edge of the stencil. The cell with the smallest divided difference and hence the least oscillatory is added to the stencil. The divided differences are given in Shu [162] and Laney [96].

The values at the boundary are given by

$$\bar{q}_{i+1/2} = \sum_{j=0}^{k-1} c_{r,j} q_{i-r+j}, \quad \bar{q}_{i-1/2} = \sum_{j=0}^{k-1} c_{r-1,j} q_{i-r+j}. \tag{4.15}$$

Where $c_{r,j}$ and $c_{r-1,j}$ are constants for an structured grid and are given by Shu [162] for low orders. For extremely high orders see Gerolymos et al. [60].

4.3.2 Weighted essentially non-oscillatory reconstruction

The WENO method of reconstruction is the primary reconstruction method that is used in this thesis. The WENO method utilises a convex combination of all possible ENO reconstructions for a cell I_i that can be constructed using an ENO method [88, 103]. The major reason this thesis uses the WENO method is that it is smoother than the ENO approach. The WENO method also allows a higher-order of accuracy. It maximises the order of accuracy for the amount of information available.

The WENO procedure starts by calculating boundary values from all possible stencils,

$$q^{(r)}_{i+1/2} = \sum_{j=0}^{k-1} c_{r,j} q_{i-r+j}, \quad r = 0, \ldots, k-1. \tag{4.16}$$

The final boundary value is given by a convex combination of the calculated boundary values,

$$\bar{q}_{i+1/2} = \sum_{r=0}^{k-1} \omega_r q^{(r)}_{i+1/2}, \tag{4.17}$$

where ω_r are the weights. For stability and consistency, they are defined as

$$\omega_r \geq 0, \quad \sum_{r=0}^{k-1} \omega_r = 1. \tag{4.18}$$

The procedure for calculating the weights is given in the paper by Shu [162]. The weights allow the properties of the ENO methods to be maintained, while increasing the accuracy of the method for the same total information.

Torrilhon showed that standard second order reconstruction methods converge to the wrong solution for several ideal MHD tests [176]. These reconstruction methods did eventually converge to the correct solution, but only for extremely high resolutions. More recently, Torrilhon and Balsara have shown that WENO methods, although exhibiting the same non-uniform convergence, converge to the correct solution for coarser grids and at a quicker rate [177].

4.4 Approximate Riemann Solvers

Finite volume methods use the solution to the Riemann problem to determine the inter-cell fluxes. This means that a high resolution numerical simulation will require the solution to a large number of Riemann problems. The exact solution to the Riemann problem is computationally expensive and not always available as for example in the case of general relativistic elasticity [72]. It is, therefore, not appropriate to solve the Riemann problem exactly at each cell boundary.

Several approximate solvers have been developed that approximate the solution to the Riemann problem analytically. Obtaining an analytical approximate solution is computationally cheaper. A large number of approximate solvers are described in the book by Toro [173]. This section will discuss the approximate solvers used in this work.

4.4.1 Lax-Friedrichs flux

One of the methods used in this thesis is Lax-Friedrichs flux. While not developed as an approximate Riemann solver, it is a limit of the Harten-Lax-van Leer (HLL) solver [76]. The Lax-Friedrichs flux is used, because it is a very stable method [100]. The method is based on the assumption of two waves propagating with speed $\pm\alpha$. The inter-cell flux is defined as

$$\hat{\mathbf{f}}(\bar{\mathbf{q}}) = \frac{1}{2}\left[\mathbf{f}\left(\bar{\mathbf{q}}_{\mathrm{L}}\right) + \mathbf{f}\left(\bar{\mathbf{q}}_{\mathrm{R}}\right) + \alpha\left\{\bar{\mathbf{q}}_{\mathrm{L}} - \bar{\mathbf{q}}_{\mathrm{R}}\right\}\right], \tag{4.19}$$

where L, R indicate quantities that have been reconstructed to the boundary, where the flux is being calculated and α is the magnitude of the maximum wave speed across the whole domain. Typically this method uses zeroth-order reconstructed values and is derived from the following update equation

$$\mathbf{q}_i^{n+1} = \mathbf{q}_i^n + \frac{\Delta t}{\Delta x}\left[\mathbf{f}_{i-1}^n - \mathbf{f}_i^n\right]. \tag{4.20}$$

Using our high-order reconstruction and the diffuse Lax-Friedrichs scheme means that we can obtain high accuracy while maintaining stability.

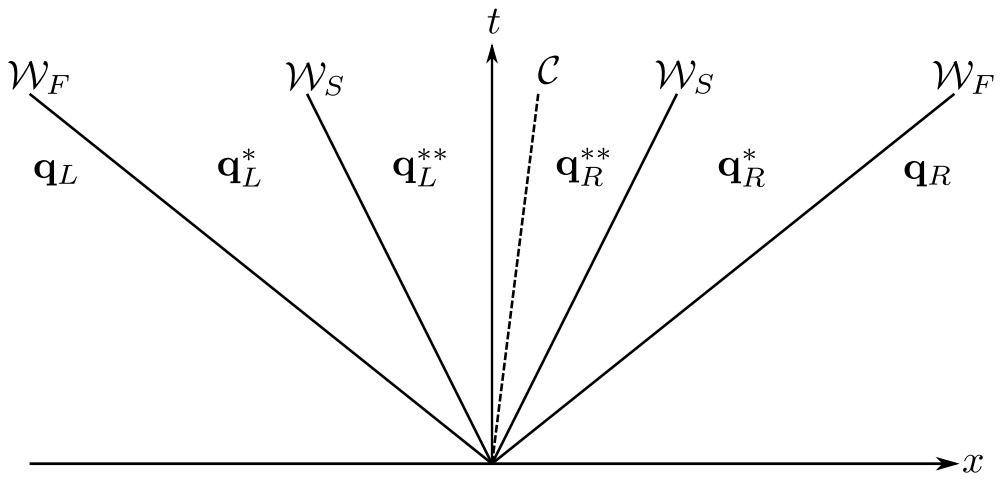

Figure 4.2 – The solution structure of the HLLD approximate Riemann solver for the equations of ideal magnetohydrodynamics.

4.4.2 HLLC and HLLD approximate Riemann solvers

The HLL [76] approximate Riemann solver is similar to the Lax-Friedrichs approach above in that it approximates the solution of Riemann problem to consist of two waves and three constant states. Toro et al. [174] introduced a new approximate Riemann solver, based on the HLL solver, that restored the contact wave, hence it was named the HLLC approximate Riemann solver. The approximate solution consisted of four states separated by three waves, the correct amount for the equations of Newtonian hydrodynamics.

The HLLD solver was introduced by Miyoshi and Kusano [116] and introduces two more waves to the HLLC solver to account for the Alfvén waves in the ideal magnetohydrodynamics equations. This is based upon the assumption that the normal velocity is constant across the solution. This means that slow shocks cannot form. The resulting solution structure is shown in Figure 4.2.

The procedure is outlined in full by Miyoshi and Kusano [116]. Their results show that the HLLD approximate Riemann solver is able to resolve sharp features that other approximate solvers smear out. Another advantage of the HLLD solver is that it is positively conservative. This means it will always produce physical states from physical inputs.

4.5 Dimensional Splitting

So far, this thesis has only considered the solution to "1 + 1" dimensional equations. The methods presented are extendable to higher dimensions. *Dimensional splitting* will be used to extend to higher dimensions [168]. To use this technique, one must write the system of equations with state vector $\mathbf{q}$ and spatial coordinates $\mathbf{x} = (x_1, x_2, x_3)^T$ in the form

$$\partial_t \mathbf{q} + \partial_{x_1} \mathbf{f}(\mathbf{q}, \mathbf{x}) + \partial_{x_2} \mathbf{g}(\mathbf{q}, \mathbf{x}) + \partial_{x_3} \mathbf{h}(\mathbf{q}, \mathbf{x}) = \mathbf{s}(\mathbf{q}, \mathbf{x}). \tag{4.21}$$

All of the systems of equations considered so far can be written in the form presented above (4.21). Therefore, one can reconstruct each spatial derivative using the techniques described in the reconstruction Section 4.3.

The update term is obtained in each direction by calculating the inter-cell fluxes at the appropriate cell edge,

$$\mathcal{F} = \hat{\mathbf{f}}_{i-1/2,j,k} - \hat{\mathbf{f}}_{i+1/2,j,k}, \tag{4.22}$$

$$\mathcal{G} = \hat{\mathbf{g}}_{i,j-1/2,k} - \hat{\mathbf{g}}_{i,j+1/2,k}, \tag{4.23}$$

$$\mathcal{H} = \hat{\mathbf{h}}_{i,j,k-1/2} - \hat{\mathbf{h}}_{i,j,k+1/2}, \tag{4.24}$$

where these quantities are evaluated for all (x_i, y_j, z_k). The right-hand side of the Runge-Kutta update is then determined from the sum of the fluxes

$$\hat{\mathbf{F}} = (\mathcal{F} + \mathcal{G} + \mathcal{H})\,. \tag{4.25}$$

When using dimensional splitting, one must be careful to ensure that the CFL condition (4.11) is still maintained. This can be ensured by considering the maximum wave-speed in all directions.

4.6 Divergence of the Magnetic Field

When dealing with a charged fluid, care must be taken to ensure that the magnetic field is non-divergent. The no-monopole Maxwell equation, first introduced in the physical model chapter (2.16), states that the divergence of the magnetic field B^i is zero,

$$\nabla^i B_i = 0. \tag{4.26}$$

However, numerically it is extremely difficult to maintain a quantity at zero. Even for initial data that is physically correct, small errors can develop due to numerical approximations. The problem is that the constraint is not controlled directly, but via evolution equations that control the field itself. Brackbill and Barnes showed that a small numerical error can lead to a non-physical force that can produce significant errors [33]. In an Eulerian frame, this error results in fluid transport across magnetic field lines, which is not possible in the ideal approximation [41].

The appearance of numerical monopoles is a major problem in charged fluid simulations. As a result, several different numerical schemes have been developed to prevent catastrophic failure by reducing or removing the errors or both. Tóth has reviewed seven different schemes that are compatible with finite volume methods [178].

This thesis has implemented three different methods to deal with the appearance of monopoles. This section will review the three methods: Powell's method, divergence cleaning and constrained transport.

4.6.1 Powell method

Powell et al. [139] developed an 8-wave method that augments the conservation laws into a balance form that reduces the effect of monopoles by adding source terms. This results in a new set of evolution equations. This was implemented for the Newtonian methods. Presented here is the Newtonian version

$$\partial_t \left(\rho v_i\right) + \partial_j \left(\rho v_i v^j + \delta_i^j p^* - B^j B_i\right) = -\left(\partial_k B^k\right) B_i, \tag{4.27}$$

$$\partial_t \mathcal{E} + \partial_j \left(\left(\mathcal{E} + p^*\right) v^j - B^j \left(v^k B_k\right)\right) = -\left(\partial_k B^k\right) B_l v^l, \tag{4.28}$$

$$\partial_t B_i + \partial_j \left(v^i B^j - v^j B^i\right) = -\left(\partial_k B^k\right) v_i. \tag{4.29}$$

A relativistic version has been developed [90, 92], but it has not been implemented in this thesis. As the Powell method only works well for situations, where there are no strong shocks [178], it is not suitable for modelling the neutron star merger scenario.

4.6.2 Divergence cleaning

The second method implemented was the divergence cleaning method of Dedner et al. [41]. This method has proven to be successful in special relativistic ideal MHD. It introduces a non-physical scalar field ψ that is used to damp the divergence of the magnetic field. The addition field is given by

$$\partial_t \psi + \partial_i B^i = -\frac{\psi}{c_p^2}, \tag{4.30}$$

where c_p is a free parameter. The addition of this field also changes the magnetic flux equation (3.87) to

$$\partial_t B^i + \partial_j \left[\left(v^j B^i - v^i B^j \right) + \delta^i_j \psi \right] = 0. \tag{4.31}$$

This is the method used in the multi-model approach as it propagates any divergences away from the interface boundaries.

4.6.3 Constrained transport

The final method implemented was used for both Newtonian and special relativity. It is a constrained transport method developed by Sriskantha and Ruffert [165], based on the method of Balsara and Spicer [21]. They modified the method of Balsara and Spicer to work with a dimensionally split code; see Section 4.5. The constrained transport method can maintain a divergence free code for single-model evolution to machine precision. However, it is not suitable for multi-model simulations that produce a divergent magnetic field when defining the interface boundary conditions.

The constrained transport approach was first developed by Evans and Hawley [54]. They used Faraday's law (2.17) to determine how the magnetic field changes in time. Their original method uses a staggered grid and was not implemented in this thesis as it would have required a major change in the numerical model.

Balsara and Spicer developed a constrained transport method that also used a staggered grid. They calculated the update to the face centred values of the magnetic field using the electric field at the edge of the cell. This electric field can be obtained from the magnetic fluxes. This allowed them to maintain a solenoidal magnetic field up to a discretisation error. Tóth took their algorithm and produced a cell centred version [178].

Sriskantha and Ruffert [165] modified Tóth's algorithm in such a way that the magnetic field at cell centres could be updated in a partially dimensionally split way. This allowed us to use a constrained transport method without modifying our code significantly.

They implemented a method that recalculates the update term in

$$\mathbf{B}_i^{n+1} = \mathbf{B}_i^n + \Delta\mathbf{B}_i. \tag{4.32}$$

The update term is calculated in a dimensionally-split approach. The x-direction update is as follows

$$\Delta B_x^{i,j+1} = \Delta B_x^{i,j+1} - \frac{1}{8}\frac{\Delta t}{\Delta y}\left(\hat{f}_7^{i+1/2,j} - \hat{f}_7^{i-1/2,j}\right), \tag{4.33a}$$

$$\Delta B_x^{i,j-1} = \Delta B_x^{i,j-1} + \frac{1}{8}\frac{\Delta t}{\Delta y}\left(\hat{f}_7^{i+1/2,j} - \hat{f}_7^{i-1/2,j}\right), \tag{4.33b}$$

$$\Delta B_y^{i,j} = \Delta B_y^{i,j} + \frac{1}{4}\frac{\Delta t}{\Delta x}\left(\hat{f}_7^{i+1/2,j} + \hat{f}_7^{i-1/2,j}\right), \tag{4.33c}$$

$$\Delta B_y^{i,j+1} = \Delta B_y^{i,j+1} + \frac{1}{8}\frac{\Delta t}{\Delta x}\left(\hat{f}_7^{i+1/2,j} + \hat{f}_7^{i-1/2,j}\right), \tag{4.33d}$$

$$\Delta B_y^{i,j-1} = \Delta B_y^{i,j-1} + \frac{1}{8}\frac{\Delta t}{\Delta x}\left(\hat{f}_7^{i+1/2,j} + \hat{f}_7^{i-1/2,j}\right). \tag{4.33e}$$

The y-direction update is as follows

$$\Delta B_y^{i,j+1} = \Delta B_y^{i,j+1} - \frac{1}{8}\frac{\Delta t}{\Delta x}\left(\hat{h}_6^{i,j+1/2} - \hat{h}_6^{i,j-1/2}\right), \tag{4.34a}$$

$$\Delta B_y^{i,j-1} = \Delta B_y^{i,j-1} + \frac{1}{8}\frac{\Delta t}{\Delta x}\left(\hat{h}_6^{i,j+1/2} - \hat{h}_6^{i,j-1/2}\right), \tag{4.34b}$$

$$\Delta B_x^{i,j} = \Delta B_x^{i,j} + \frac{1}{4}\frac{\Delta t}{\Delta y}\left(\hat{h}_6^{i,j+1/2} + \hat{h}_6^{i,j-1/2}\right), \tag{4.34c}$$

$$\Delta B_x^{i,j+1} = \Delta B_x^{i,j+1} + \frac{1}{8}\frac{\Delta t}{\Delta y}\left(\hat{h}_6^{i,j+1/2} + \hat{h}_6^{i,j-1/2}\right), \tag{4.34d}$$

$$\Delta B_x^{i,j-1} = \Delta B_x^{i,j-1} + \frac{1}{8}\frac{\Delta t}{\Delta y}\left(\hat{h}_6^{i,j+1/2} + \hat{h}_6^{i,j-1/2}\right). \tag{4.34e}$$

The equations can be extended to the 3-dimensional case by adding a z-directional update term and calculating the ΔB_z term in the previous updates.

Chapter 5

Single-model Results

Before developing and discussing the advanced numerical methods for neutron star interfaces, it is important that the numerical methods presented in the previous chapter are validated. Throughout this thesis, the solution of the Riemann problem has formed an integral part. The approximate solution makes Godunov-like methods viable. The linear solution will be used to construct the mRGFM. Finally, the exact solution can be used to demonstrate the validity of numerical methods.

A set of standard tests has been developed to test the validity of the numerical methods [20, 110, 111, 151, 164]. These standard tests, in one dimension, are collectively known as shock tube tests. They can be used to test the limits of the numerical methods implemented. This chapter will present standard shock tube tests for each of the systems of conservation laws considered previously: Newtonian hydrodynamics, ideal magnetohydrodynamics, special-relativistic hydrodynamics and special-relativistic, ideal magnetohydrodynamics. All the shock tube tests implement outflow boundary conditions.

These standard tests allow one to compare approximate results to exact solutions. The shock tube tests are one of the few examples where exact solutions are known for special-relativistic hydrodynamics and special-relativistic, ideal magnetohydrodynamics. An exact solver for special-relativistic hydrodynamics was developed by Pons et al. [136]. We have built our own solver based on their approach. An exact solver for special-relativistic, ideal magnetohydrodynamics was developed by Giacomazzo et al. [62]. We have used this solver to construct the exact solutions for special-relativistic, ideal magnetohydrodynamics.

It is also important to demonstrate the convergence of the chosen spatial reconstruction method. The WENO method introduced in Section 4.3.2 provides high-order convergence for smooth initial data [162]. Therefore, to test our WENO implementation, a sinusoidal profile will be advected through one time period with periodic boundary conditions and compared to its initial data.

After testing the numerical methods in one dimension, it is important to validate the methods in two dimensions. The addition of a second spatial dimension creates new numerical effects. Maintaining the non-divergence of the magnetic field becomes extremely important. The Orszag-Tang test [123] will be used to demonstrate that the numerical methods can prevent and reduce the appearance of a divergent magnetic field. This test uses periodic boundary conditions. Shock tube tests in two dimensions will also be used to validate the numerical methods.

5.1 One-dimensional Results

5.1.1 WENO convergence

The WENO method of spatial reconstruction should converge, for smooth data, at an order of $(2r-1)$, where r is the size of the stencil used [162]. Therefore, a WENO(r) reconstruction with $r = 2$ should converge at third order. Gerolymos et al. [60] have demonstrated that the WENO method is convergent up to seventeenth order. However, to achieve these results, they implemented a time-integrator of equal order. We have implemented the Runge-Kutta method up to fourth order. Therefore, only results for WENO2 and WENO3 are presented.

To calculate the convergence rate for the WENO method we used a sinusoidal profile, which was advected for one period with periodic boundary conditions. Therefore, after one period the exact solution is identical to the initial data. The point-wise error is calculated,

$$E_i = |a_i - e_i|, \quad i = 1, \ldots, N, \tag{5.1}$$

where E_i is the error, a_i is the approximate solution, e_i is the exact solution and N is the total number of points. The infinity norm is calculated by

$$||E||_\infty = \Delta x \cdot \max\left(E_1, E_2, \ldots, E_N\right), \tag{5.2}$$

where Δx is the cell width. The logarithms of the norms are plotted against the logarithm of the cell widths in Figure 5.1. The gradient of the line-of-best-fit determines the order of convergence.

We have compared the norms for resolutions between 0.1 and 0.01. Figure 5.1 shows that the WENO methods implemented in this thesis are convergent and converge at the expected rate. The WENO2 method has a convergence rate of 2.72. The WENO3 method's convergence rate is limited by the fourth order Runge-Kutta time-integrator to 4.00.

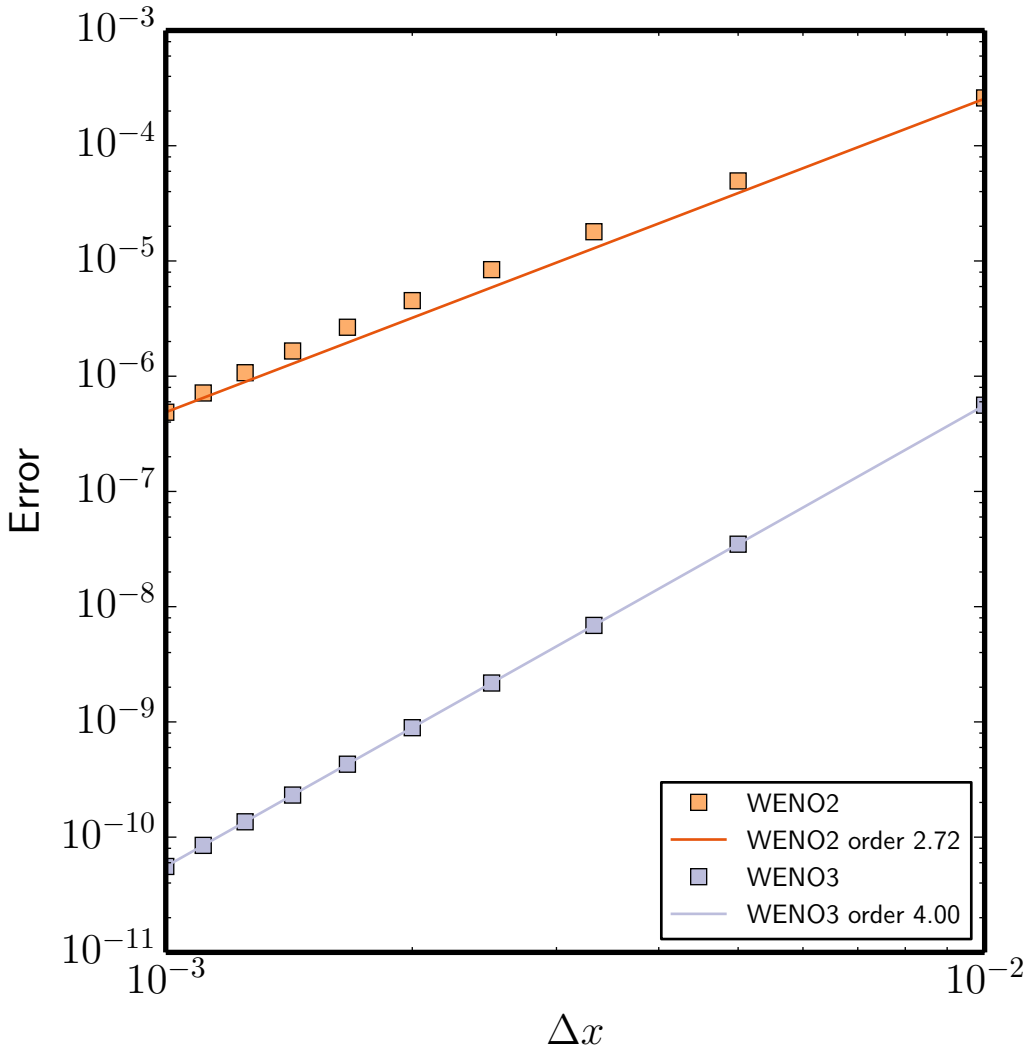

Figure 5.1 – This log-log plot shows that the WENO2 implementation has a convergence rate of 2.72, which is close to the expected third-order convergence. The WENO3 method should be fifth-order convergent. However, the results are limited by the fourth-order Runge-Kutta time integrator. Both tests compared a sinusoidal profile, which had been advected through one period with the initial data.

5.1.2 Newtonian hydrodynamics

Throughout this chapter, standard Riemann shock tube tests will be used to demonstrate the validity of our numerical methods. Therefore, we will start by presenting the standard shock tube test developed by Sod [164]. This test has been chosen, because its solution contains all three possible waves in Newtonian hydrodynamics: rarefaction, shock and contact discontinuity.

This initial data is given in Table 5.1. The Riemann problem, located at $x = 0$, is defined on the domain $-0.5 \leq x \leq 0.5$. The fluid is an ideal fluid with $\gamma = 1.4$. The total time is $T = 0.25$.

Test name: Sod shock tube						
	ρ	v^x	v^y	v^z	p	γ
left	1	0	0	0	1	1.4
right	0.125				0.1	
Total time: 0.25						

Table 5.1 – Initial conditions for the Sod test [164]. The Riemann problem, located at $x = 0$, is defined on the domain $-0.5 \leq x \leq 0.5$. The fluid is an ideal fluid with $\gamma = 1.4$. The total time is $T = 0.25$.

The results are given in Figure 5.2. Two resolutions are shown, 200 and 800 cells, with 50 cells plotted for clarity. All of the expected waves are present and their locations have been correctly captured. A subplot of the density, containing the contact wave, exhibits the smearing associated with single-model methods. The subplot of the pressure, containing the shock wave, demonstrates that the method converges with increased resolution. We can quantify the convergence rate by running the test over a range of resolutions, $N = 100$ to $N = 1000$. Figure C.1 shows that the density converges at a rate of 0.98. This is because the density contains discontinuities.

5.1.3 Special-relativistic hydrodynamics

5.1.3.1 Special-relativistic Sod shock tube

Standard Riemann shock tubes are one of the few types of problems in special-relativistic hydrodynamics that have an exact solution. Therefore, we can continue to use them to validate our numerical methods. Relativistic equivalents of the standard Newtonian shock tubes test exist [110, 111] and we will use the same Sod test as before. Its initial data is given in Table 5.2. The Riemann problem, located at $x = 0$, is defined on the domain $-0.5 \leq x \leq 0.5$. The fluid is an ideal fluid with $\gamma = 1.4$. The total time is $T = 0.4$. The results are given in Figure 5.3.

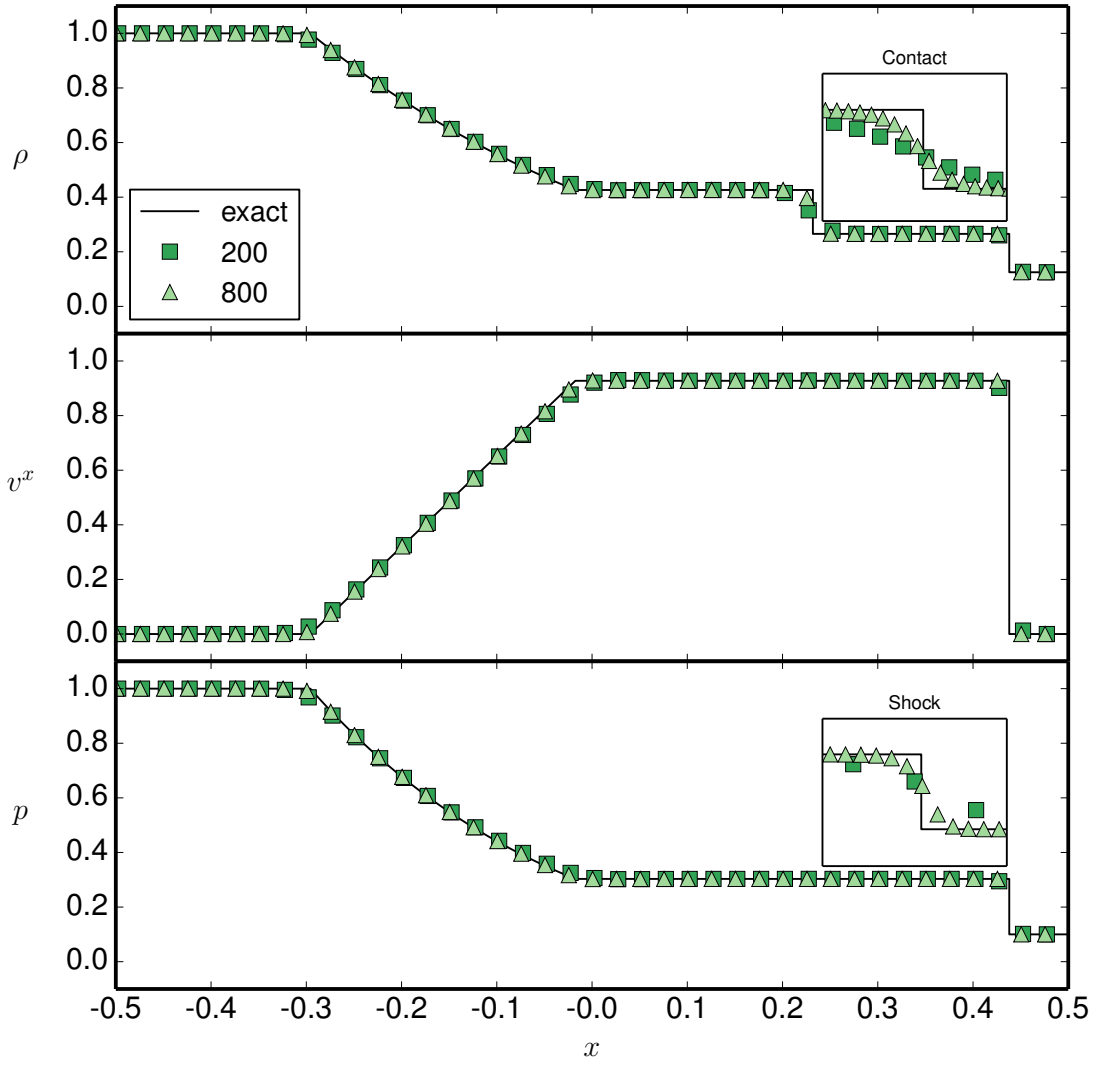

Figure 5.2 – Newtonian Sod test results. Two resolutions are shown: 200 and 800 cells. However, only 50 cells are shown for clarity. All three waves are present and correctly located. A subplot of the density, containing the contact wave, exhibits the smearing associated with single-model methods. Using multi-models methods removes this smearing completely. The subplot of the pressure, containing the shock wave, demonstrates that the method converges with increased resolution. The results are plotted at $T = 0.25$.

Test name: Special-relativistic Sod shock tube						
	ρ	v^x	v^y	v^z	p	γ
left	1	0	0	0	1	1.4
right	0.125				0.1	
Total time: 0.4						

Table 5.2 – Initial conditions for the relativistic Sod shock tube given by Martí and Müller [110]. The Riemann problem, located at $x = 0$, is defined on the domain $-0.5 \leq x \leq 0.5$. The fluid is an ideal fluid with $\gamma = 1.4$. The total time is $T = 0.4$.

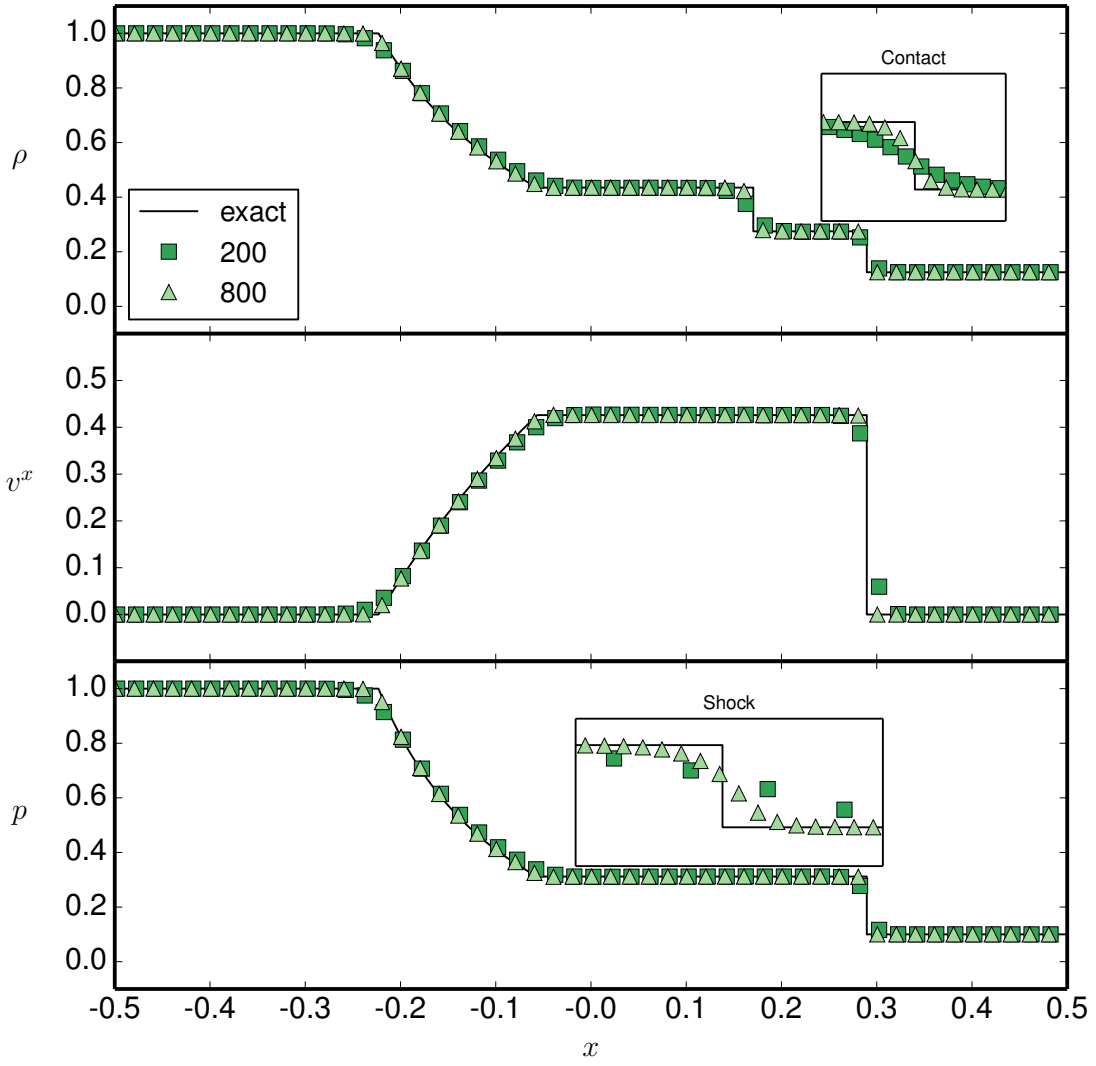

Figure 5.3 – Results for the Sod test for special-relativistic hydrodynamics given by Martí and Müller [110]. Two resolutions are shown: 200 and 800 cells. However, only 50 cells are shown for clarity. All three waves are present and correctly located. A subplot of the density, containing the contact wave, exhibits the smearing associated with single-model methods. The subplot of the pressure, containing the shock wave, demonstrates that the method converges with increased resolution. The results are plotted at $T = 0.4$.

In Figure 5.3 two resolutions are shown, 200 and 800 cells, with 50 cells plotted for clarity. All of the expected waves are present and their locations have been correctly captured. This subplot demonstrates the difference between the Newtonian and the relativistic versions. The shock wave has propagated a shorter distance compared to the Newtonian case due to Lorentz contraction. The subplot of the pressure, containing the shock wave, also demonstrates that the method converges with increased resolution. This is quantified in Figure C.2 where we see that the test converges at linear order. Again, like the Newtonian case, this is due to the discontinuities. The same resolutions were used as the previous test. The velocities in this test are too low to be considered in the relativistic regime. A more extreme test will be discussed next: the blast wave.

5.1.3.2 Blast wave

The blast wave is a relativistic test originally considered by Norman and Winkler [186]. Here, we present the version given by Martí and Müller [111]. The initial conditions contain a large pressure jump over several orders of magnitude that results in a strong shock and relativistic velocities. The initial conditions are given in Table 5.3. The Riemann problem, located at $x = 0$, is defined on the domain $-0.5 \leq x \leq 0.5$. The fluid is an ideal fluid with $\gamma = 5/3$. The total time is $T = 0.4$.

Test name: Special-relativistic Blast wave						
	ρ	v^x	v^y	v^z	p	γ
left	1	0	0	0	1000	5/3
right	0.125				0.01	
Total time: 0.4						

Table 5.3 – Initial conditions for the special-relativistic blast wave problem presented by Martí and Müller [111]. The Riemann problem, located at $x = 0$, is defined on the domain $-0.5 \leq x \leq 0.5$. It contains a pressure jump of five orders of magnitude. The fluid is an ideal fluid with $\gamma = 5/3$. The total time is $T = 0.4$.

The test was chosen, because strong shock waves will be created during a neutron star merger. Therefore, our numerical methods must be able to accurately capture the location of such discontinuities. The large pressure jump in the blast wave's initial conditions produces a strong shock wave and relativistic velocities. The density is shown in Figure 5.4 and the velocity and pressure are given in Figure 5.5.

Two resolutions are shown, 200 and 800 cells, with 50 cells plotted for clarity. All of the expected waves are present and their locations have been correctly captured. The density plot 5.4 demonstrates that high resolution is required to approximate the state between the contact and the shock. Although not considered in this thesis, the use of adaptive mesh refinement would resolve such situations [27]. The velocity and pressure plot 5.5 exhibits the extreme nature of this test. The maximum velocity is 0.9604 in geometric units, which equates to a Lorentz factor of 3.59. We can quantify the convergence rate by running the test over a range of resolutions, $N = 100$ to $N = 1000$. Figure C.3 shows that the density converges at a rate of 1.16. This is because the density contains discontinuities.

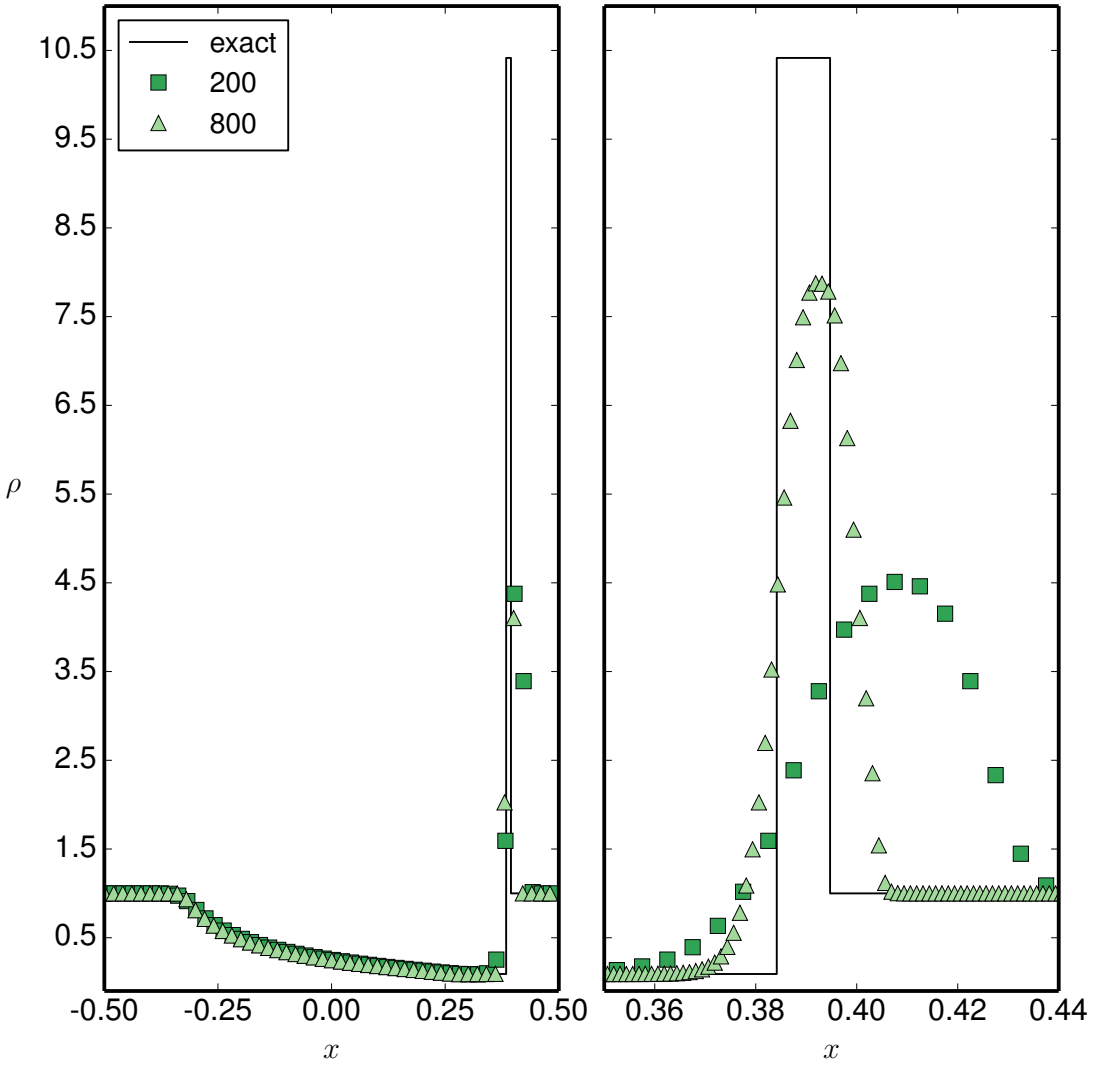

Figure 5.4 – Results for the blast wave test [111]. Two resolutions are shown: 200 and 800 cells. However, only 50 cells are shown for clarity. All three waves are present and correctly located. The second figure shows the contact and the shock wave. It demonstrates that high resolution is required to capture the state between. The results are plotted at $T = 0.4$.

5.1.4 Newtonian ideal magnetohydrodynamics

We will now test our methods for a charged fluid in the presence of a magnetic field. Again, a set of standard tests has been developed and they can be found in the paper by Ryu and Jones [151]. Here, we present their second test, because its solution contains all seven waves: fast, Alfvén, slow and contact discontinuity. The initial conditions are given in Table 5.4. The Riemann problem, located at $x = 0$, is defined on the domain $-0.5 \leq x \leq 0.5$. The fluid is an ideal fluid with $\gamma = 5/3$. The total time is $T = 0.2$. Results are shown in Figure 5.6.

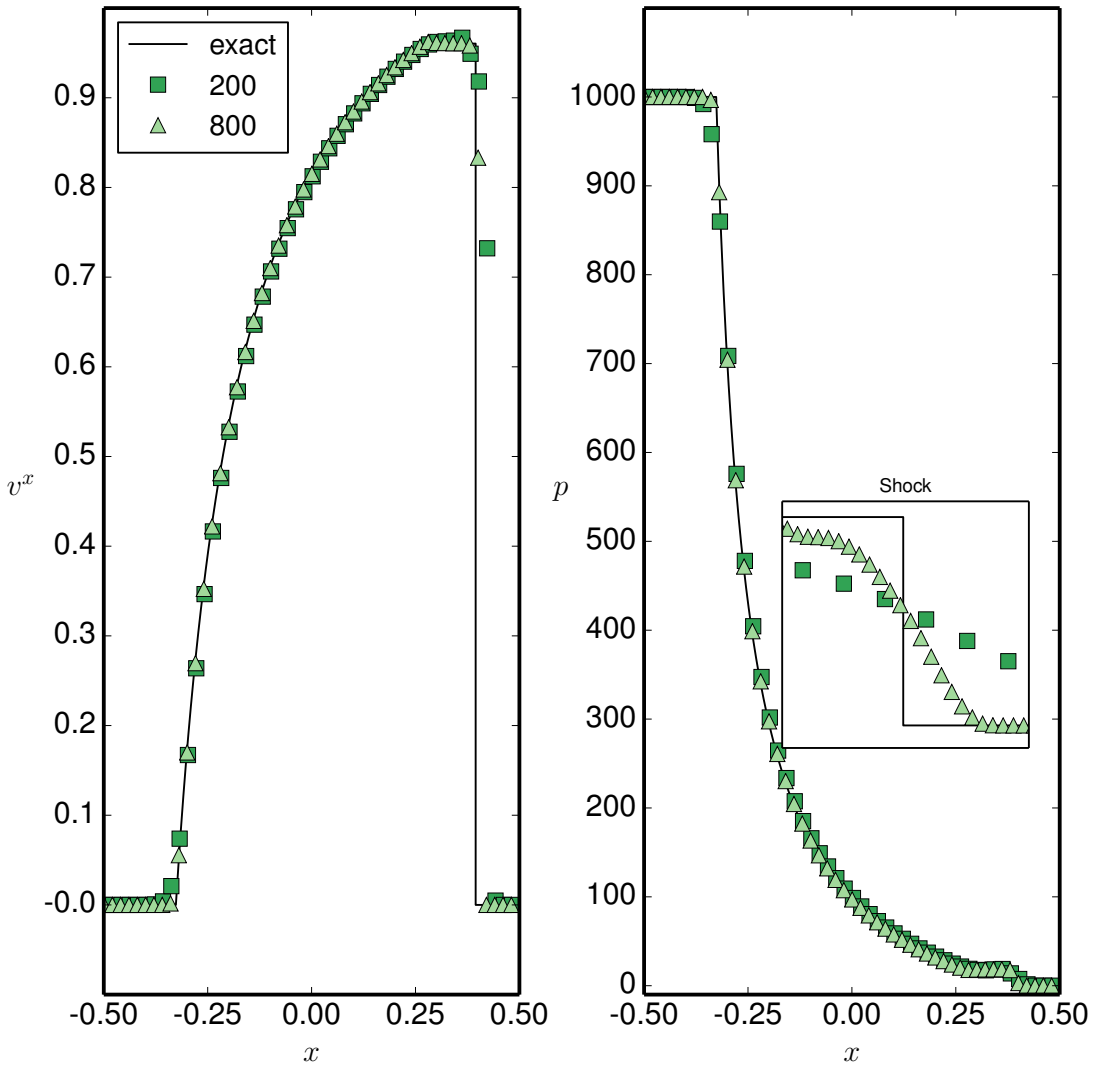

Figure 5.5 – Results for the blast wave test [111]. Two resolutions are shown: 200 and 800 cells. However, only 50 cells are shown for clarity. All the waves are present and correctly located. The subplot of the pressure shows that the method converges with resolution. The results are plotted at $T = 0.4$.

Test name: Ryu & Jones 2A									
	ρ	v^x	v^y	v^z	p	B^x	B^y	B^z	γ
left	1.08	1.2	0.01	0.5	0.95	$2\sqrt{4\pi}$	$3.6/\sqrt{4\pi}$	$2/\sqrt{4\pi}$	5/3
right	1	0	0	0	1		$4/\sqrt{4\pi}$		
Total time: 0.2									

Table 5.4 – The initial conditions for the Ryu and Jones test 2A [151]. The initial conditions are given in Table 5.4. The Riemann problem, located at $x = 0$, is defined on the domain $-0.5 \leq x \leq 0.5$. The fluid is an ideal fluid with $\gamma = 5/3$. The total time is $T = 0.2$.

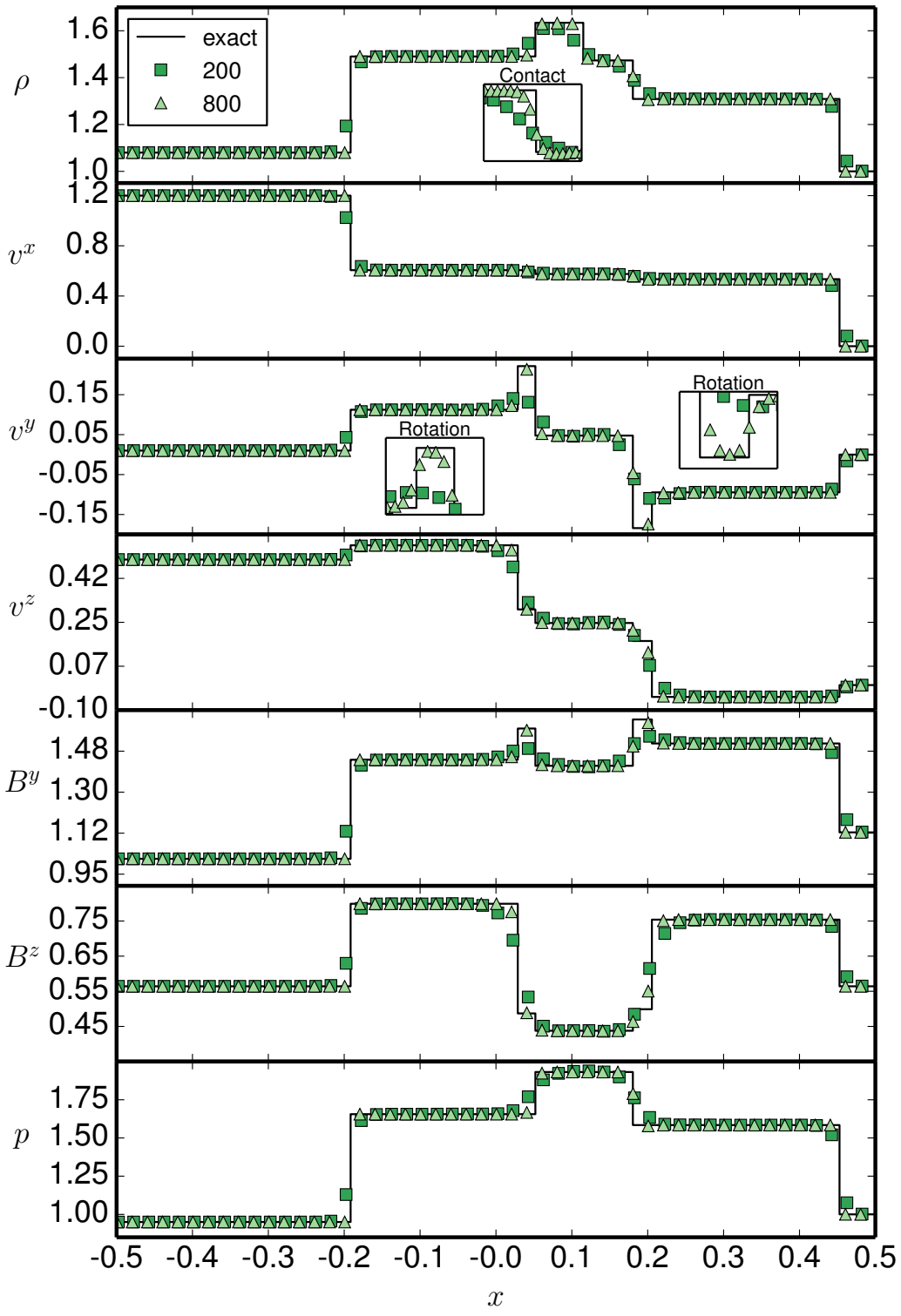

Figure 5.6 – Results for the Ryu and Jones 2A with initial data given in Table 5.4. Two resolutions are shown, 200 and 800 cells, with 50 cells plotted for clarity. All of the expected waves are present and their locations have been correctly captured. A subplot of the density, containing the contact wave, exhibits the smearing associated with single-model methods. In this particular test, the Alfvén and the slow velocity are very similar in magnitude. As a result, the 200 cell solution does not fully capture the state between the two waves. The 800 cell solution does capture it, as shown in the subplots. The results are plotted at $T = 0.2$.

Two resolutions are shown, 200 and 800 cells, with 50 cells plotted for clarity. All of the expected waves are present and their locations have been correctly captured. A subplot of the density, containing the contact wave, exhibits the smearing associated with single-model methods. In this particular test, the Alfvén and the slow velocity are very similar in magnitude. As a result, the 200 cell solution does not fully capture the state between the two waves. The 800 cell solution does capture it, as shown in the subplots. We can quantify the convergence rate by running the test over a range of resolutions, $N = 100$ to $N = 1000$. Figure C.4 shows that the density converges at a rate of 0.99. This is because the density contains discontinuities.

5.1.5 Special-relativistic, ideal magnetohydrodynamics

Next, we consider a shock tube test for special-relativistic, ideal magnetohydrodynamics. A set of standard tests have been devised by Balsara [20] with exact solutions given by Giacomazzo and Rezzolla [62].

We will consider a moderate blast wave test that has initial data given in Table 5.5. The Riemann problem, located at $x = 0$, is defined on the domain $-0.5 \leq x \leq 0.5$. The fluid is an ideal fluid with $\gamma = 5/3$. The total time is $T = 0.4$. Results are given in Figures 5.7 and 5.8.

Test name: Balsara blast wave									
	ρ	v^x	v^y	v^z	p	B^x	B^y	B^z	γ
left	1	0	0	0	30	5	6	6	5/3
right					1		0.7	0.7	
Total time: 0.4									

Table 5.5 – The initial conditions for the moderate blast wave problem of Balsara [20]. The Riemann problem is defined on the domain $-0.5 \leq x \leq 0.5$ with the jump at $x = 0.0$.; for a single relativistic ideal magnetohydrodynamics model with $\gamma = 5/3$ and for a total time of $T = 0.4$.

This test was chosen, because it combines a charged fluid and a blast wave. However, as only the tangential magnitude changes across the Riemann problem, there will be no rotation waves.

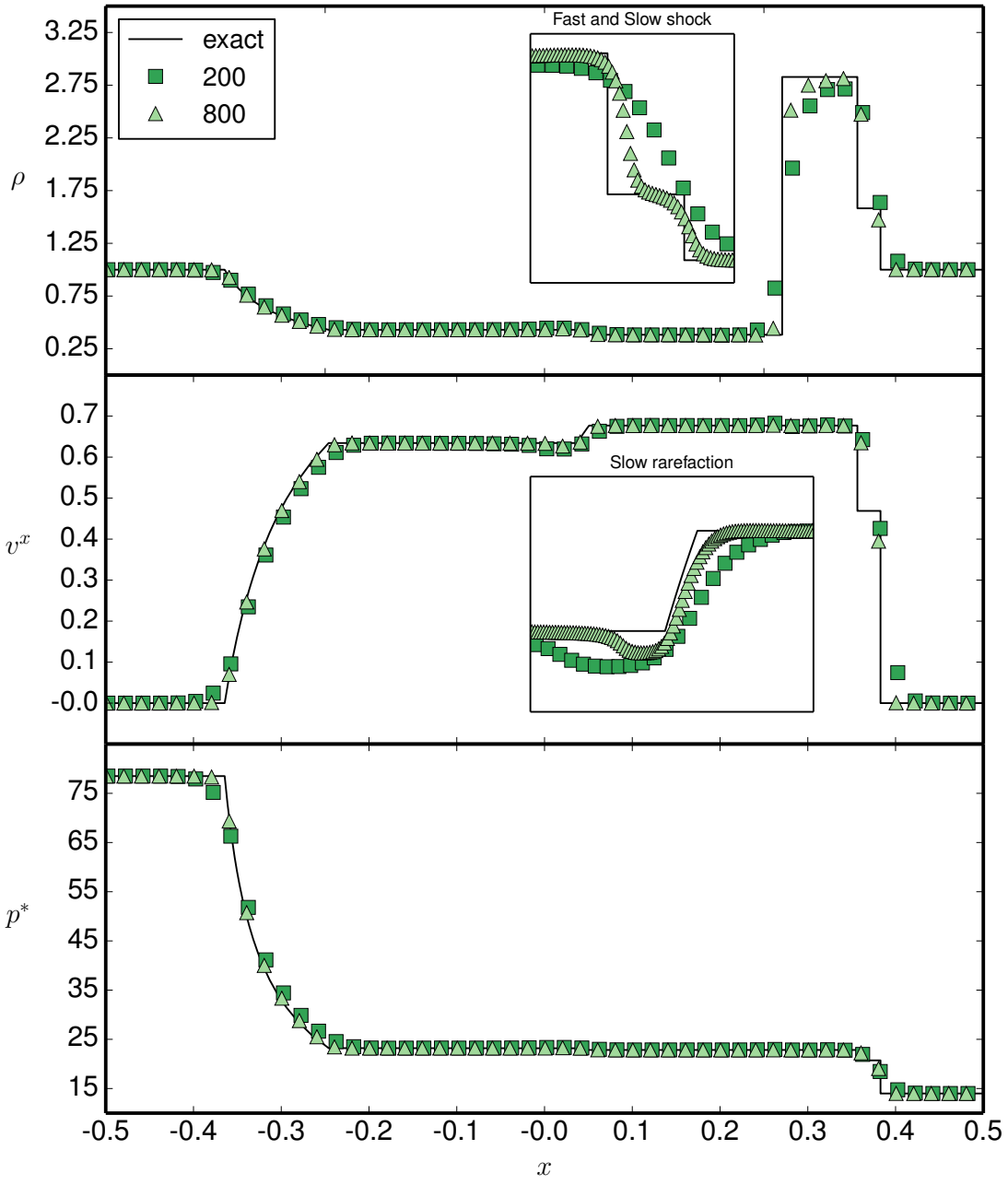

Figure 5.7 – The solution to the Riemann problem of the second blast test of Balsara [20]. Two resolutions are shown, 200 and 800 cells, with 50 cells plotted for clarity. All of the expected waves are present and their locations have been correctly captured. High resolution is required to accurately capture the states between the waves. This is demonstrated in the subplot of the density. The subplot of the velocity exhibits a common problem with this test. Balsara showed that with higher resolution the problem reduces, but due to the conservative nature of the methods used the other states will be accurate for lower resolutions [20]. Our results show agreement with the exact solution and Balsara's results. The results are plotted at $T = 0.4$.

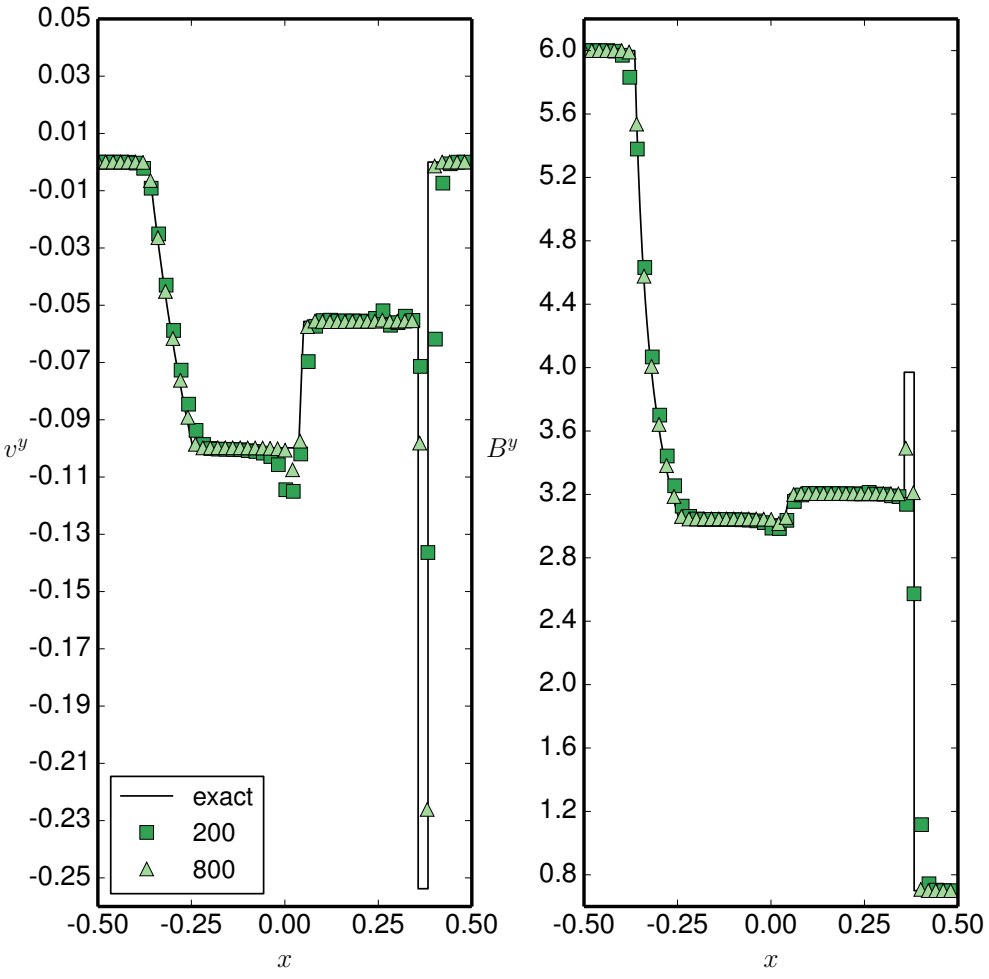

Figure 5.8 – The solution to the Riemann problem of the second blast test of Balsara [20] for the y components of the velocity and magnetic field. Due to the symmetric nature of the tangential components, the solution for the z components are identical. Two resolutions are shown, 200 and 800 cells, with 50 cells plotted for clarity. All of the expected waves are present and their locations have been correctly captured. High resolution is required to accurately capture the states between the waves. Again, the convergence problem of the slow wave is visible. The results are plotted at $T = 0.4$.

Two resolutions are shown, 200 and 800 cells, with 50 cells plotted for clarity. All of the expected waves are present and their locations have been correctly captured. Again, high resolution is required to accurately capture the states between the waves. This is demonstrated in the subplot of the density in Figure 5.7. The subplot of the velocity shows the tail of the rarefaction undershooting the exact solution. Balsara showed that with higher resolution the problem reduces, but due to conservative nature of the methods used, the other states will be accurate for lower resolutions [20]. Our results show agreement with the exact solution and Balsara's results. The second figure includes the y-component of the velocity and magnetic field. All of the expected waves are present and their locations have been correctly captured. High resolution is required to accurately capture the states between the waves. Again, the convergence problem of the slow wave is visible. We can quantify the convergence rate by running the test over a range of resolutions, $N = 100$ to $N = 1000$. Figure C.5 shows that the density converges at a rate of 1.06. This is because the density contains discontinuities.

In this section, we have shown that our numerical methods produce approximate solutions to Riemann problems that converge to the exact solution for the different systems of equations. We can, therefore, be confident that our numerical methods should produce accurate results for systems, where no exact solution exists.

5.2 Two-dimensional Problems

In the numerical methods chapter 4.5, we demonstrated that our numerical methods can be easily extended to higher dimensions. We will first consider Sod's shock tube in two dimensions with the Riemann problem located along the diagonal. We will also show that our numerical methods can prevent a divergent magnetic field from occurring. The Orszag-Tang vortex [123] is a well known test of divergence prevention. Without divergence cleaning, the test fails to complete or produces incorrect results.

5.2.1 Shock tubes

First, we consider the standard shock tube of Sod that was presented previously in Subsection 5.1.2. The Riemann problem is located along the diagonal, $y = -x$, on the domain $-0.5 \leq x, y \leq 0.5$. The fluid is an ideal fluid with $\gamma = 1.4$. The total time is $T = 0.25$. The initial data is given in Table 5.6.

Test name: Sod shock tube 2D						
	ρ	v^x	v^y	v^z	p	γ
left	1	0	0	0	1.0	1.4
right	0.125				0.1	
Total time: 0.25						

Table 5.6 – Sod shock tube in two dimensions [164]. The Riemann problem is located at $x + y = 0$ and defined on the domain $-0.5 \leq x, y \leq 0.5$. The fluid is an ideal fluid with $\gamma = 1.4$. The final time is $T = 0.25$.

Results are shown for the density on the whole domain in Figure 5.9 and for density, velocity and pressure along a diagonal slice perpendicular to the Riemann problem in Figure 5.10. The density figure shows the solution the Riemann problem in two dimensions for 800 x 800 cells. The solution matches the one-dimensional result along the line $y = x$. Away from this line, the outflow boundary conditions at the corners, have produced inflowing waves, changing the solution there. Therefore, we consider a slice along the $y = x$ line and plot the results for the density, velocity and pressure for comparison against the exact solution in Figure 5.10. The figures show that the two-dimensional results have good agreement with the original one-dimensional, exact solution. The velocity is the magnitude of the individual components.

We have demonstrated that our numerical methods can be extended to higher dimensions by considering the standard Sod shock tube on a two-dimensional grid. The results obtained match well with those obtained in one dimension.

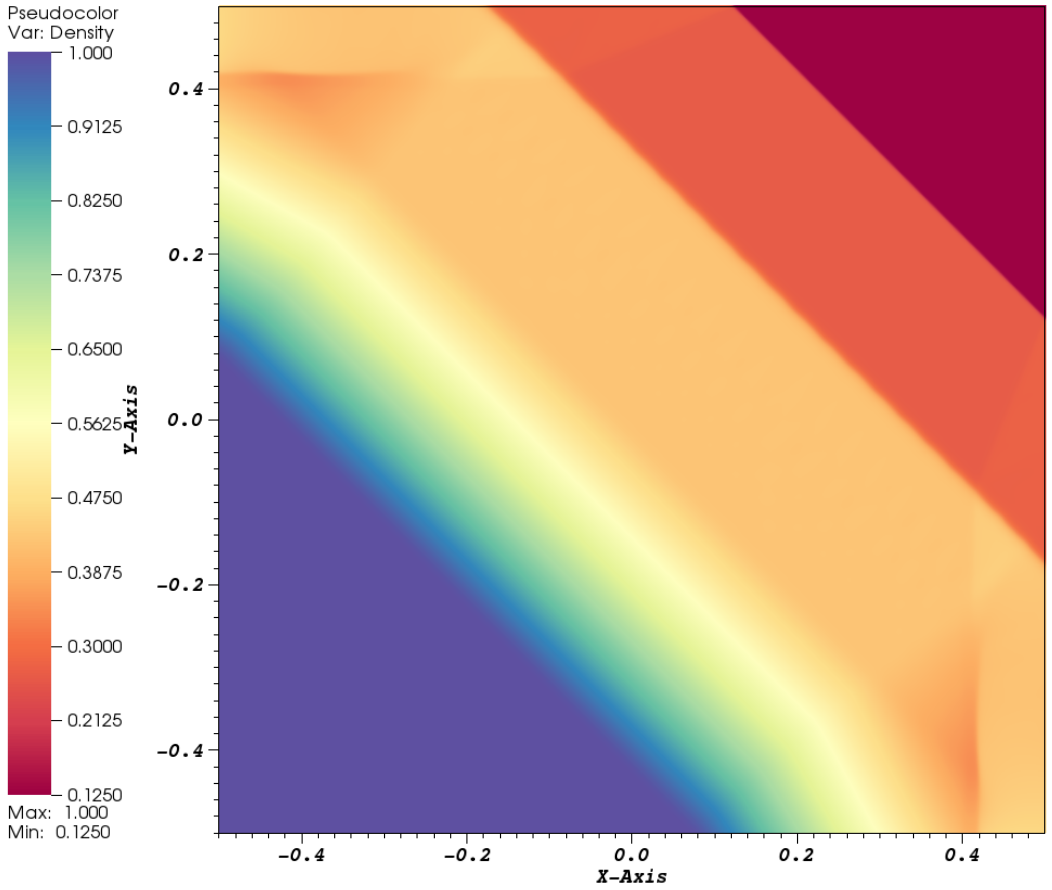

Figure 5.9 – The final density profile for the two-dimensional Sod test [164]. The solution shows 800 x 800 cells. The results along the line $y = x$ show good agreement with the one-dimensional results. The results are plotted at $T = 0.25$.

5.2.2 Orszag-Tang vortex test

In the numerical methods chapter we discussed the problem of maintaining zero divergence of the magnetic field, see Section 4.6. One of the standard tests used to examine one's numerical scheme is the vortex problem of Orszag-Tang [123]. Relativistic and Newtonian versions of the test exist and we will use both of them to demonstrate our code's ability to deal with the turbulent flow in magnetohydrodynamics.

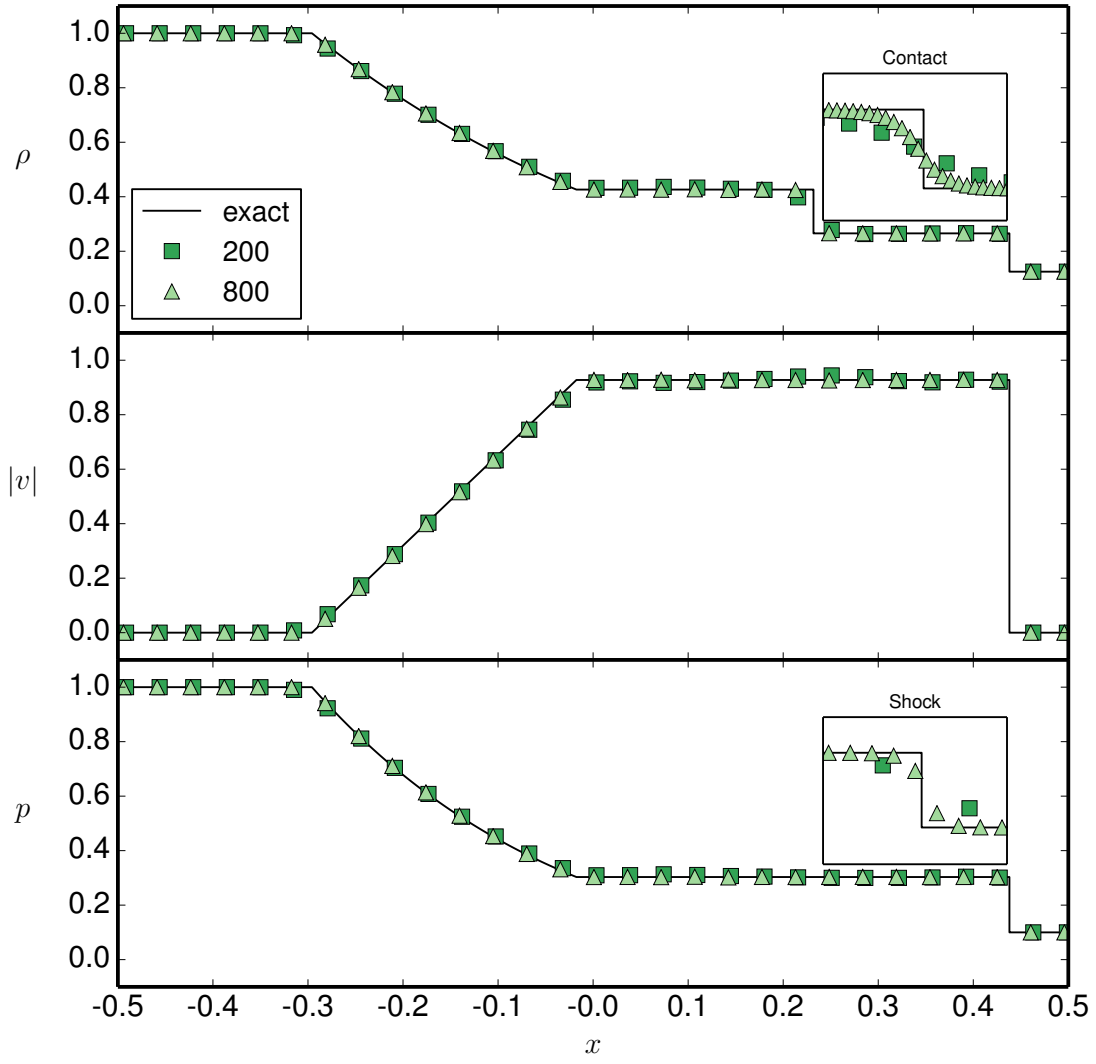

Figure 5.10 – The density, velocity magnitude and pressure for the two-dimensional Sod test [164] along the $y = x$ line. Two resolutions are shown, 200 and 800 cells, with 50 cells plotted for clarity. All of the expected waves are present and their locations have been correctly captured. The results agree well with the one-dimensional, exact solution. The results are plotted at $T = 0.25$.

5.2.2.1 Newtonian ideal magnetohydrodynamics

Sriskantha and Ruffert [165] provide the initial conditions for the Newtonian Orszag-Tang vortex test. The initial conditions are given in Table 5.7. The boundary conditions are periodic with a domain of $0.0 \leq x, y \leq 1.0$. The fluid is a perfect fluid with $\gamma = 5/3$. The final time is $T = 0.5$.

Test name: Newtonian Orszag-Tang								
ρ	v^x	v^y	v^z	p	B^x	B^y	B^z	γ
$\frac{25}{36\pi}$	$-\sin(2\pi y)$	$\sin(2\pi x)$	0.0	$\frac{5}{12\pi}$	$\frac{-\sin(2\pi y)}{\sqrt{4\pi}}$	$\frac{\sin(4\pi x)}{\sqrt{4\pi}}$	0	5/3
Total time: 0.5								

Table 5.7 – The initial conditions for the Orszag-Tang [123] as given by Sriskantha and Ruffert [165]. A constant density and pressure are defined across the domain $0.0 \leq x, y \leq 1.0$. Velocity vortices are positioned at the centre and the corners. The magnetic vortices are located $(0.5, 0)$, $(0.25, 0.5)$, $(0.75, 0.5)$, $(0.5, 1.0)$ and the corners.

The initial conditions are defined across the whole grid with velocity vortices at the centre and corners, which can be seen in Figure 5.11, and magnetic vortices at $(0.5, 0)$, $(0.25, 0.5)$, $(0.75, 0.5)$, $(0.5, 1.0)$ and the corners. This is shown in Figure 5.12.

Results for the density, gas and magnetic pressure are shown in Figures 5.13, 5.14, 5.15 and 5.16.

By inspection, these results agree with those presented by Sriskantha and Ruffert [165]. This is a standard test of the divergence constraint in magnetohydrodynamics. To achieve the correct results, the divergence of the magnetic field must remain as small as possible. Typically, for smooth data the divergence can be kept to machine precision. However, in extreme tests with large shocks, such as this one, the divergence of the magnetic field can only be contained to 10^{-4} away from shocks. Failure to control the divergence will result in this test failing and not maintaining 180° rotational symmetry. The divergence cleaning method we have implemented ensures this by reducing the impact of the divergence of the magnetic field by advecting it out of the numerical domain and damping it.

The density plot, in Figure 5.13, shows a colour map between 0.05 and 0.5 along with forty contour lines linearly spaced between those values. Steep density gradients indicate the location of the waves. The pressure plot, in Figure 5.14, is a colour map between 0.02 and 0.6 along with forty contour lines logarithmically spaced between those values. Steep pressure gradients indicate the location of shock waves. The magnetic pressure plot, in Figure 5.15, is a colour map defined logarithmically between 1.0×10^{-6} and 0.3 along with forty contour lines logarithmically spaced between those values. The regions with the largest magnetic pressure correspond to regions of low density and pressure. They are surrounded by large density and pressure gradients.

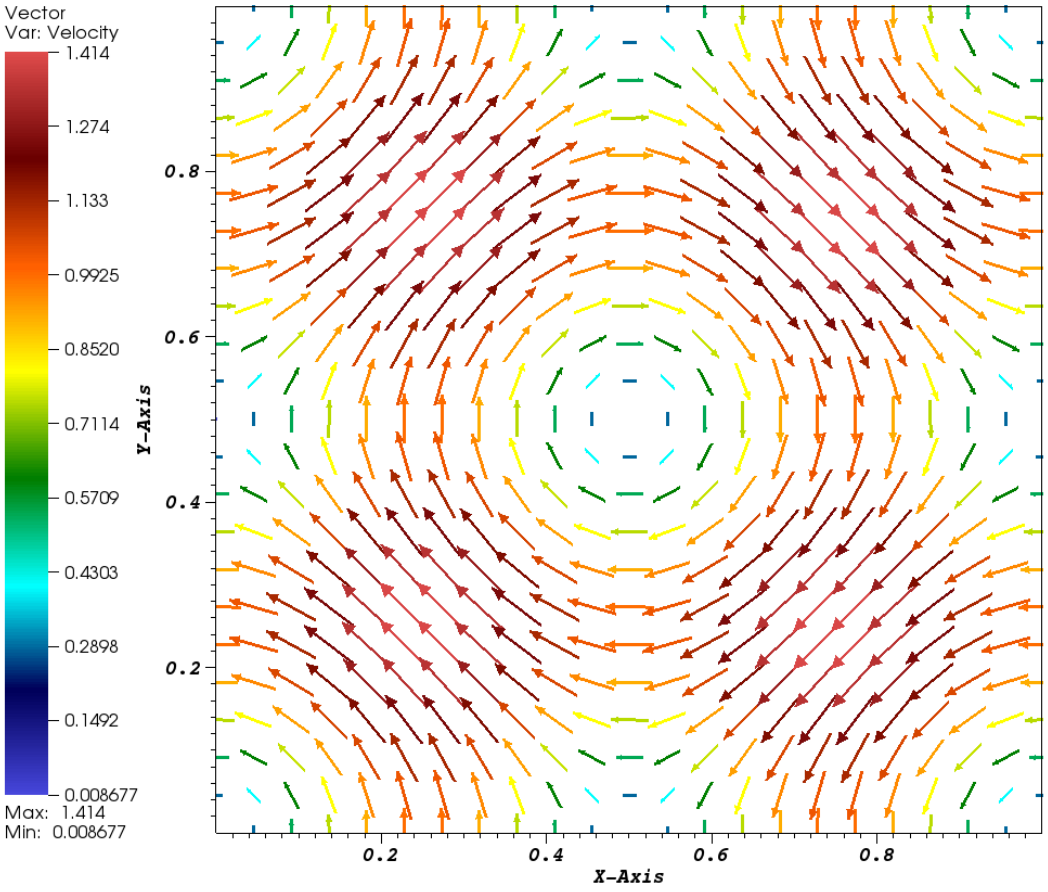

Figure 5.11 – The initial velocity vector field for the Orszag-Tang test. The colour corresponds to the velocity magnitude. The boundaries are periodic. Vortices can be seen at the corners and $(0.5, 0.5)$. The results are plotted at $T = 0.5$.

Figure 5.16 shows the divergence of the magnetic field for a resolution of 800 x 800. The divergence of the magnetic field is minimised by using the divergence cleaning method. The boundary conditions for the divergence cleaning method go to zero. Close to shock waves, the divergence can be high. However, once the shock has moved away from that region, the divergence cleaning method reduces it, which results in stable evolution.

5.2.2.2 Special-relativistic Orszag-Tang

The divergence of the magnetic field is as much of a problem is special relativity as it is in a Newtonian simulation. We will use a relativistic Orszag-Tang test to demonstrate the robustness of our numerical methods. The initial data for this test, from Beckwith and Stone [26], is given in Table 5.8. The boundary conditions are periodic with a domain of $0.0 \leq x, y \leq 1.0$. The fluid is a perfect fluid with $\gamma = 5/3$. The final time is $T = 1.0$.

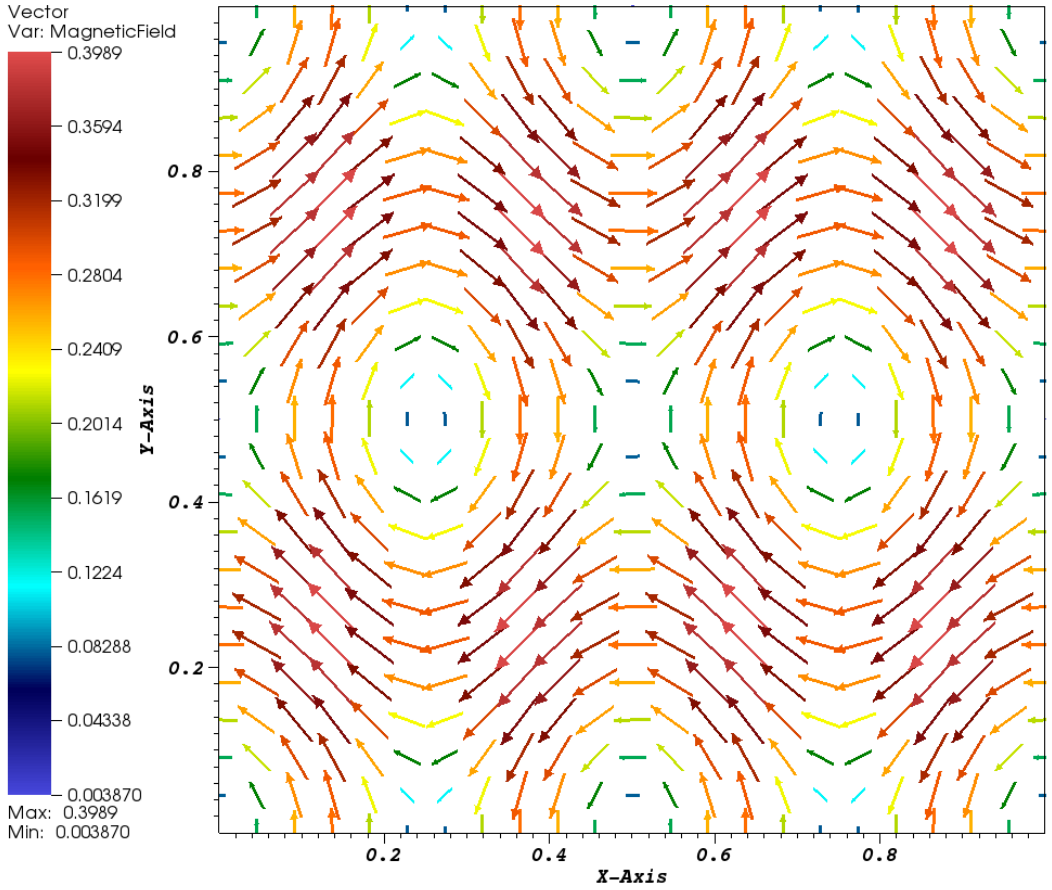

Figure 5.12 – The initial magnetic vector field for the Orszag-Tang test. The colour corresponds to the magnetic field magnitude. The boundaries are periodic. Vortices can be seen at $(0.5, 0)$, $(0.25, 0.5)$, $(0.75, 0.5)$, $(0.5, 1.0)$ and the corners. The results are plotted at $T = 0.5$.

Results for the density, gas and magnetic pressure and divergence of the magnetic field are shown in Figures 5.17, 5.18, 5.19 and 5.20.

Test name: Relativistic Orszag-Tang								
ρ	v^x	v^y	v^z	p	B^x	B^y	B^z	γ
$\frac{25}{36\pi}$	$-0.5\sin(2\pi y)$	$0.5\sin(2\pi x)$	0	$\frac{5}{12\pi}$	$\frac{-\sin(2\pi y)}{\sqrt{4\pi}}$	$\frac{\sin(4\pi x)}{\sqrt{4\pi}}$	0	5/3
Total time: 1.0								

Table 5.8 – The initial data for the relativistic Orszag-Tang test as given by Beckwith and Stone [26].

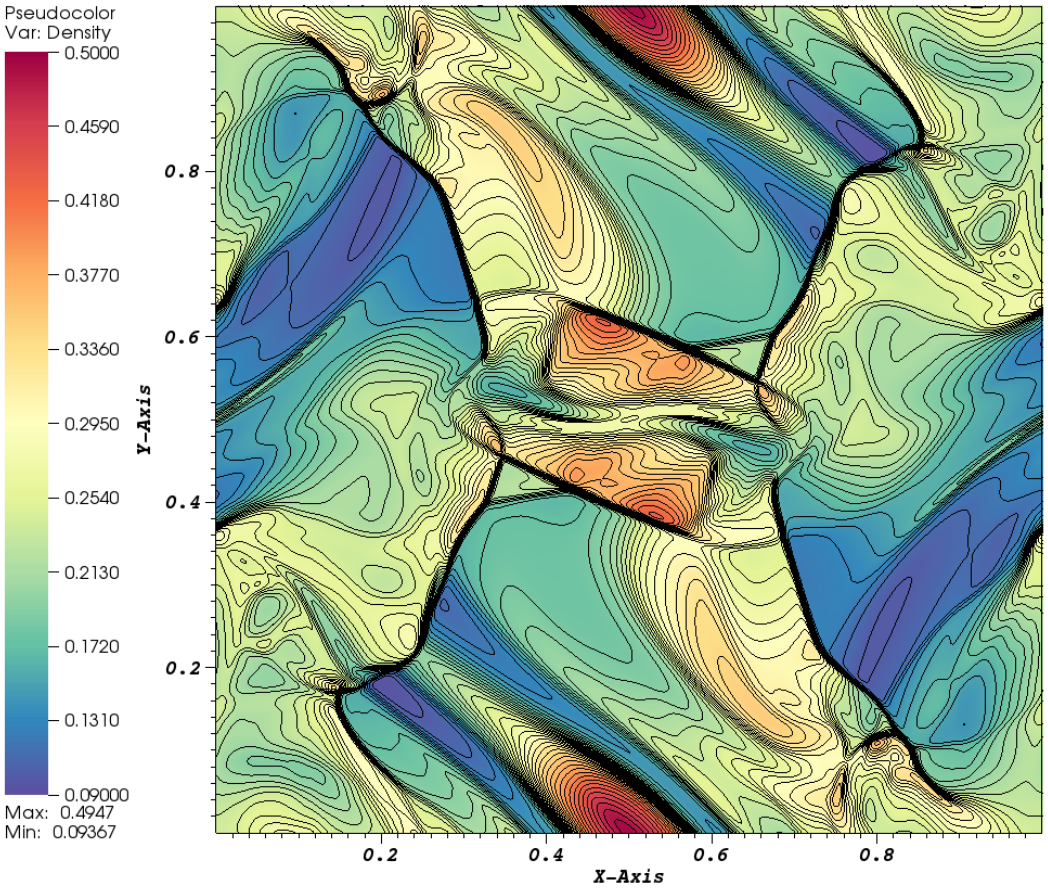

Figure 5.13 – This plot for the Orszag-Tang test shows the density at the final time. The results compare well with those given by Sriskantha and Ruffert [165]. The resolution is 512 x 512 with 40 contours spaced linearly between 0.09 and 0.5. Steep density gradients indicate the location of the waves. The results are plotted at $T = 0.5$.

These result are comparable, by inspection, to those published by Beckwith and Stone [26]. To achieve the correct results, the divergence of the magnetic field must remain as small as possible. Typically, for smooth data the divergence can be kept to machine precision. However, in extreme tests with large shocks, such as this one, the divergence of the magnetic field can only be contained to 10^{-4} away from shocks. Failure to control the divergence will result in this test failing and not maintaining 180° rotational symmetry. The divergence cleaning method we have implemented ensures this by reducing the impact of the divergence of the magnetic field by advecting it out of the numerical domain and damping it.

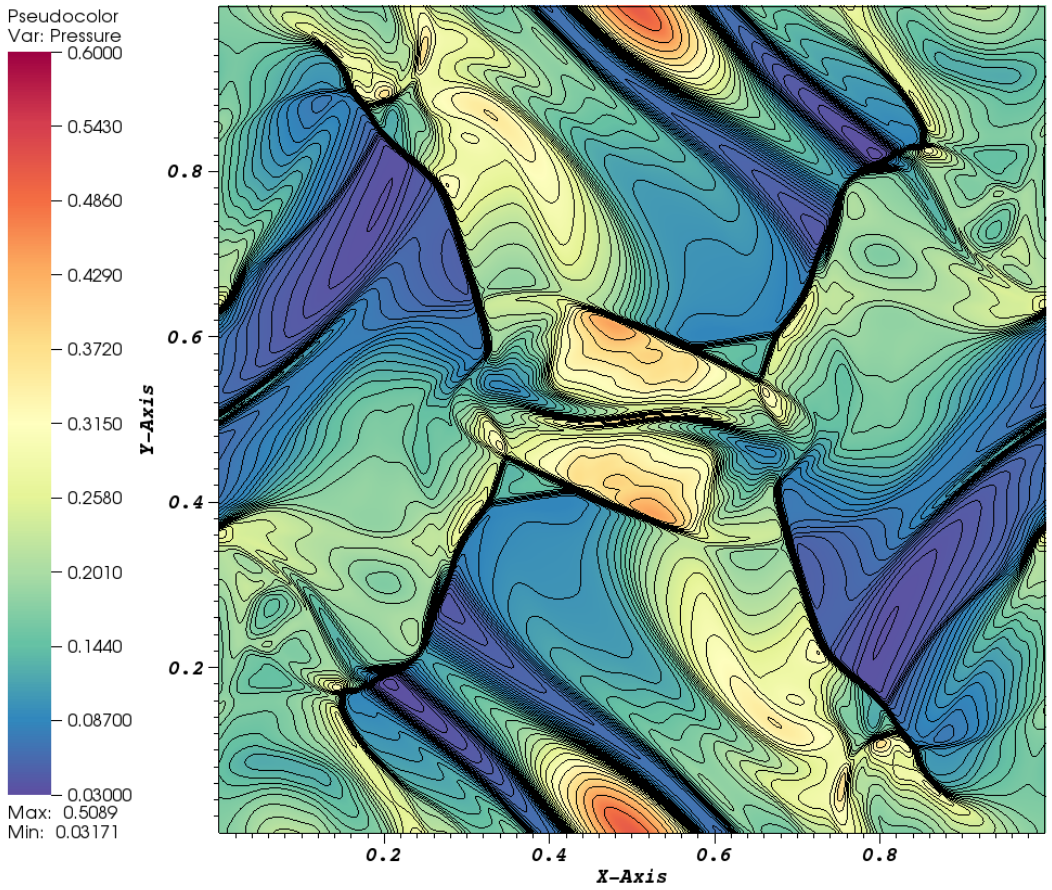

Figure 5.14 – This plot for the Orszag-Tang test shows the gas pressure at the final time. The results compare well with those given by Sriskantha and Ruffert [165]. The resolution is 512 x 512 with 40 contours spaced logarithmically between 0.03 and 0.6. Steep pressure gradients indicate the location of shock waves. The results are plotted at $T = 0.5$.

The density plot, in Figure 5.17, shows a colour map between 0.05 and 0.5 along with forty contour lines linearly spaced between those values. Steep density gradients indicate the location of the waves. The pressure plot, in Figure 5.18, is a colour map between 0.02 and 0.6 along with forty contour lines logarithmically spaced between those values. Steep pressure gradients indicate the location of the shock waves. The magnetic pressure plot, in Figure 5.19, is a colour map defined logarithmically between 1.0×10^{-6} and 0.3 along with forty contour lines logarithmically spaced between those values. The regions with the largest magnetic pressure corresponds to regions of low density and pressure. They are surrounded by large density and pressure gradients.

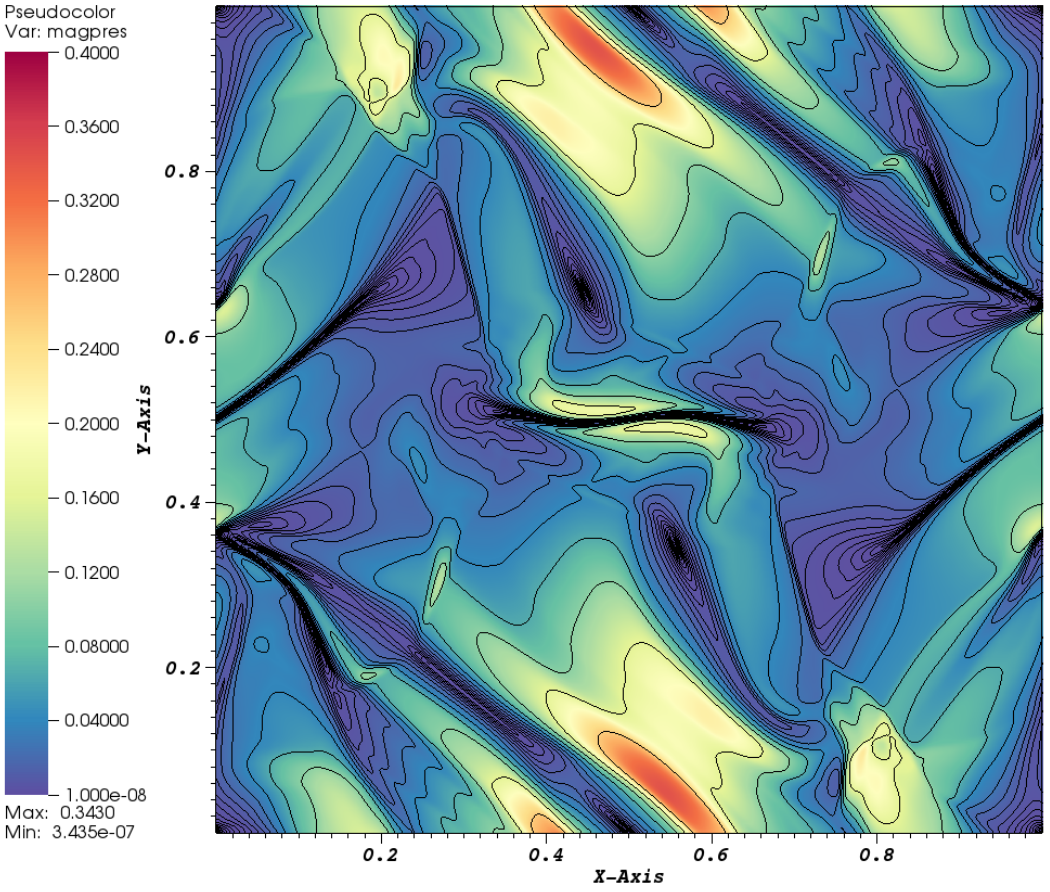

Figure 5.15 – This plot for the Orszag-Tang test shows the magnetic pressure at the final time. The results compare well with those given by Sriskantha and Ruffert [165].The resolution is 512 x 512 with 40 contours spaced logarithmically between 1.0×10^{-8} and 0.4. The regions with the largest magnetic pressure correspond to regions of low density and pressure. They are surrounded by large density and pressure gradients. The results are plotted at $T = 0.5$.

Figure 5.20 shows the divergence of the magnetic field for a resolution of 800 x 800. The divergence of the magnetic field is minimised by using the divergence cleaning method. The boundary conditions for the divergence cleaning method go to zero. Close to shock waves, the divergence can be high. However, once the shock has moved away from that region, the divergence cleaning method reduces it, which results in stable evolution.

In this section, we have demonstrated that our numerical methods can be extended to higher dimensions. We have also shown that our numerical methods are robust and minimise the divergence of the magnetic field in the presence of strong shock waves.

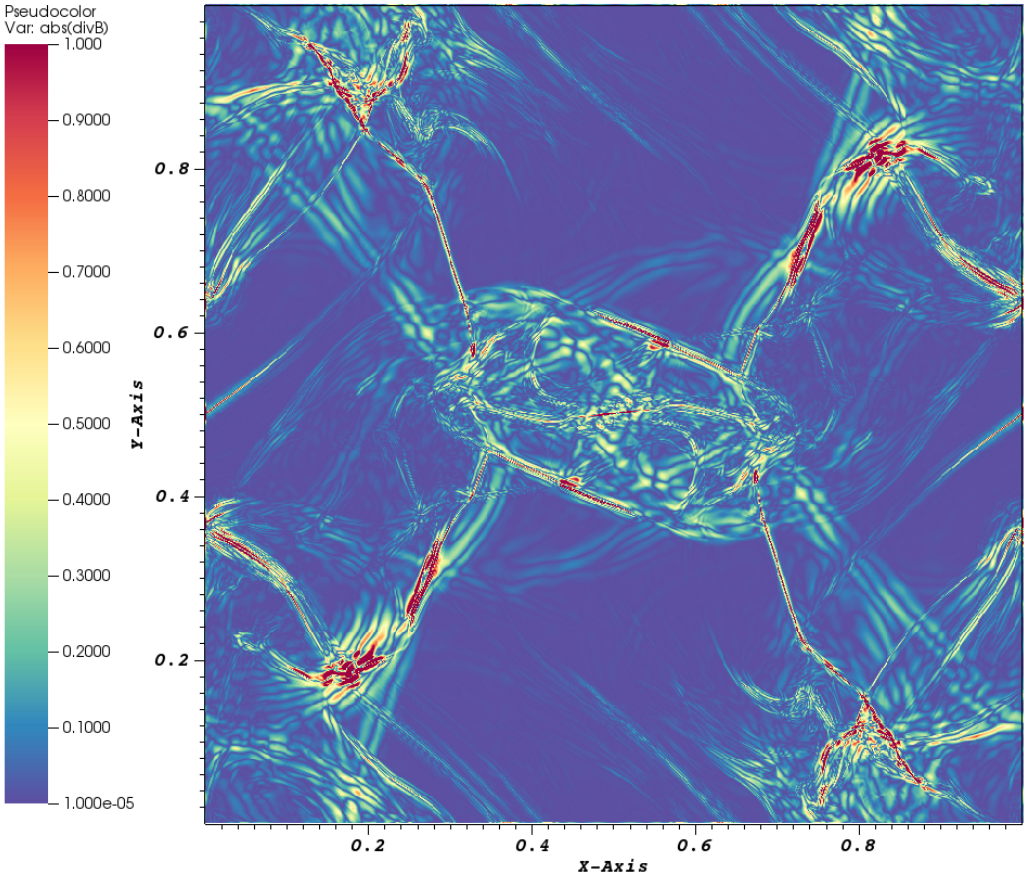

Figure 5.16 – This plot for the Orszag-Tang test shows the divergence of the magnetic field at the final time. The results compare well with those given by Sriskantha and Ruffert [165]. The resolution is 800 x 800. The divergence of the magnetic field is minimised by using the divergence cleaning method. The boundary conditions for the divergence cleaning method go to zero. Close to shock waves, the divergence can be high. However, once the shock has moved away from the region, the divergence cleaning method reduces, such that, stable evolution can occur. The results are plotted at $T = 0.5$.

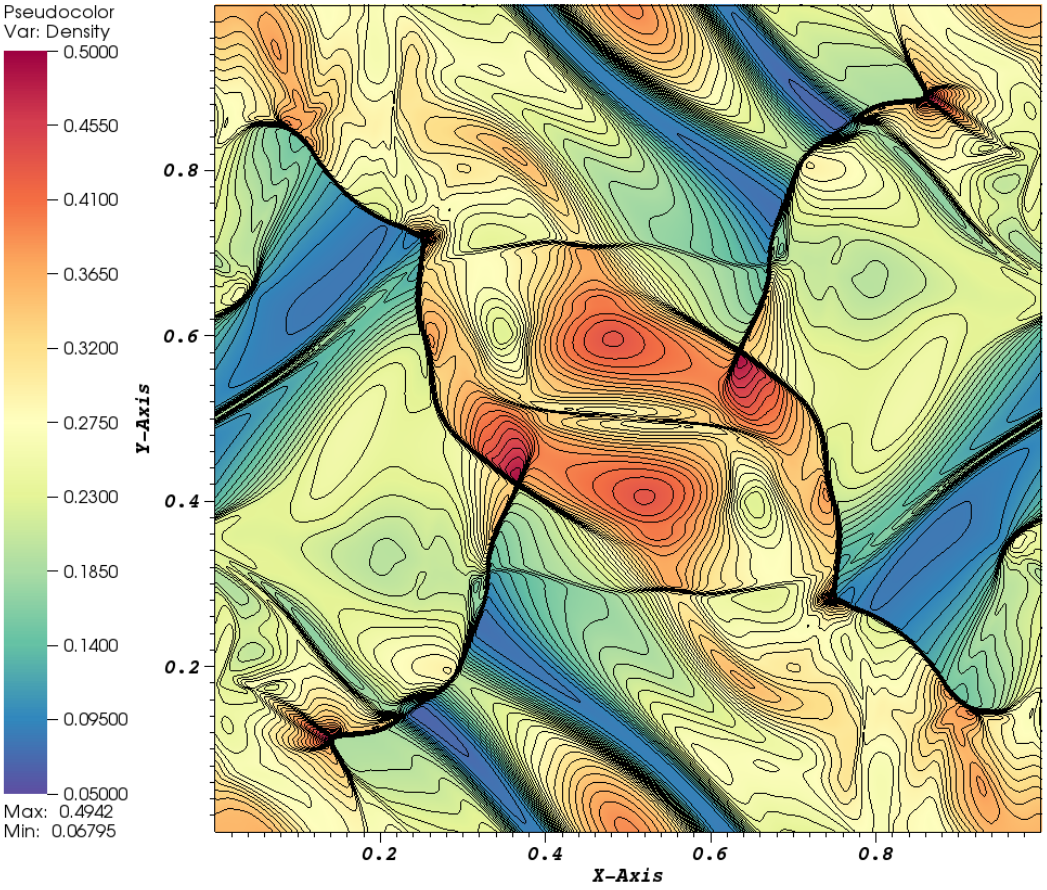

Figure 5.17 – This plot shows the final density for the special-relativistic Orszag-Tang test. This result is comparable to those published by Beckwith and Stone [26]. The resolution is 800 x 800 with 40 contours spaced linearly between 0.05 and 0.5. Steep density gradients indicate the location of the waves. The results are plotted at $T = 1.0$.

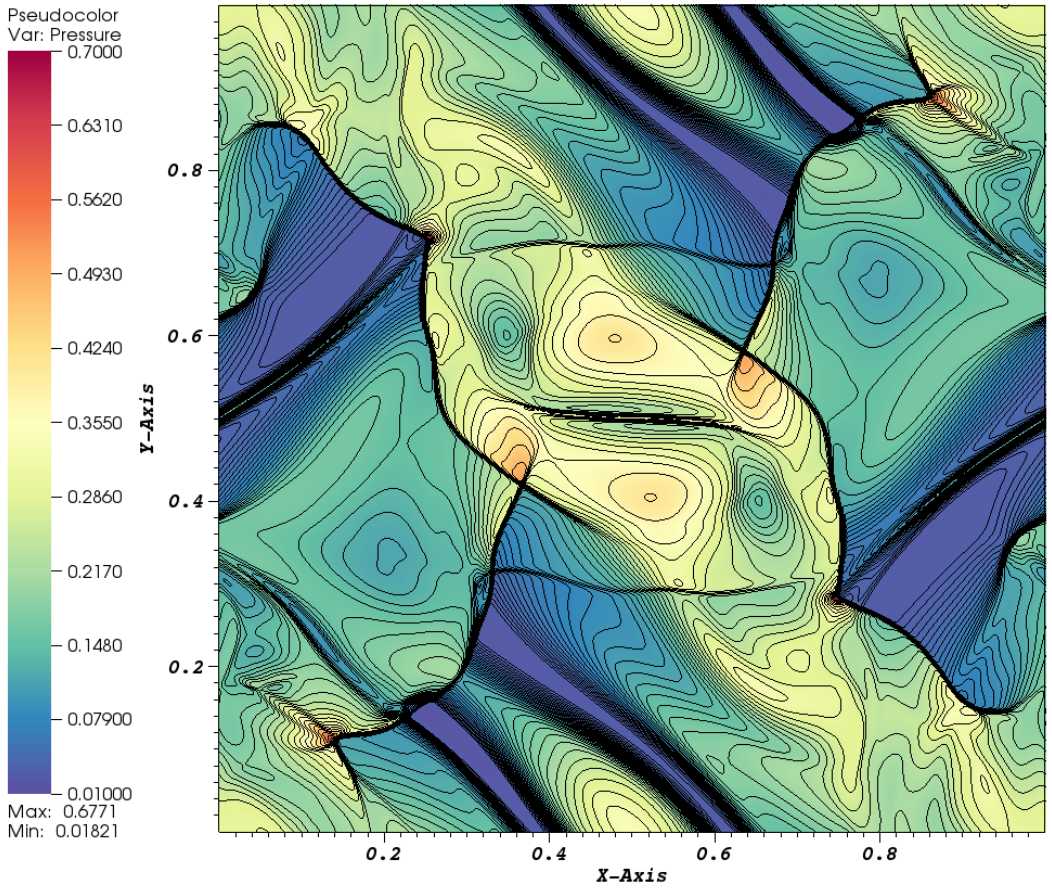

Figure 5.18 – This plot shows the final pressure for the special-relativistic Orszag-Tang test. This result is comparable to those published by Beckwith and Stone [26]. The resolution is 800 x 800 with 40 contours spaced logarithmically between 0.03 and 0.6. Steep pressure gradients indicate the location of shock waves. The results are plotted at $T = 1.0$.

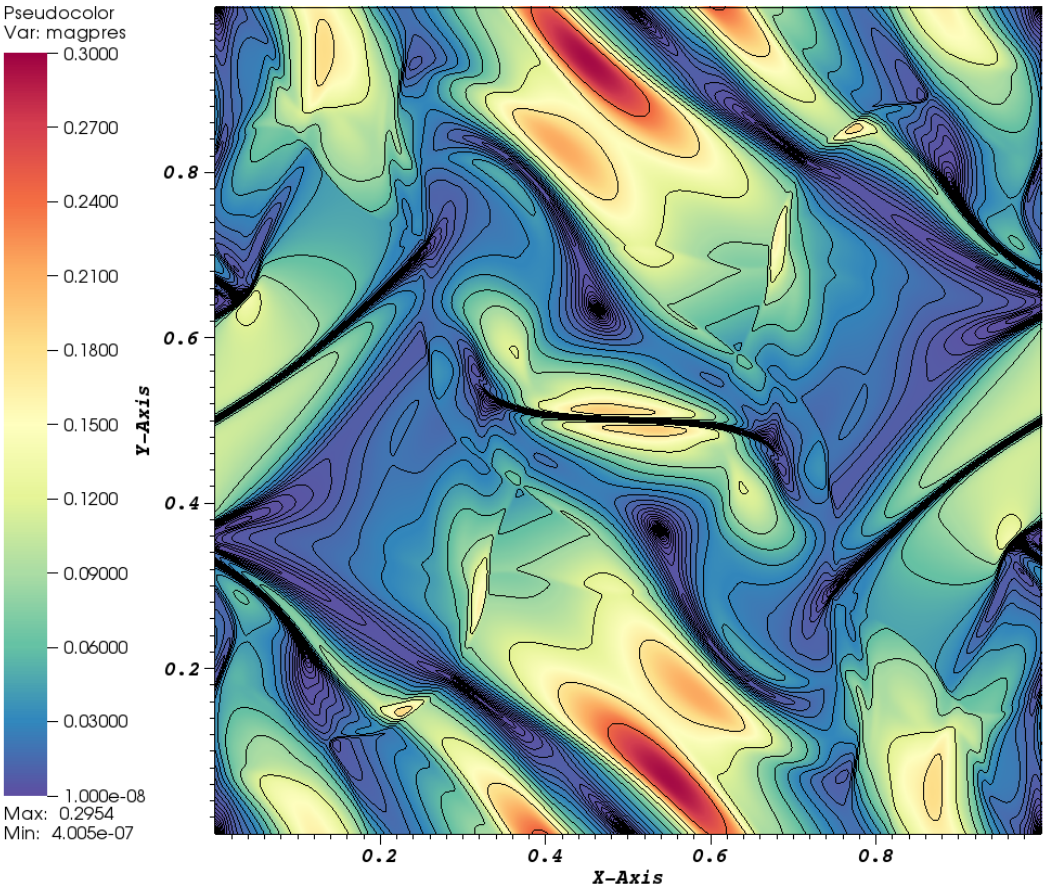

Figure 5.19 – This plot, for the relativistic Orszag-Tang, test shows the magnetic pressure at the final time. This result is comparable to those published by Beckwith and Stone [26]. The resolution is 800 x 800 with 40 contours between spaced logarithmically 1.0×10^{-6} and 1.0. The regions with the largest magnetic pressure correspond to regions of low density and pressure. They are surrounded by large density and pressure gradients. The results are plotted at $T = 1.0$.

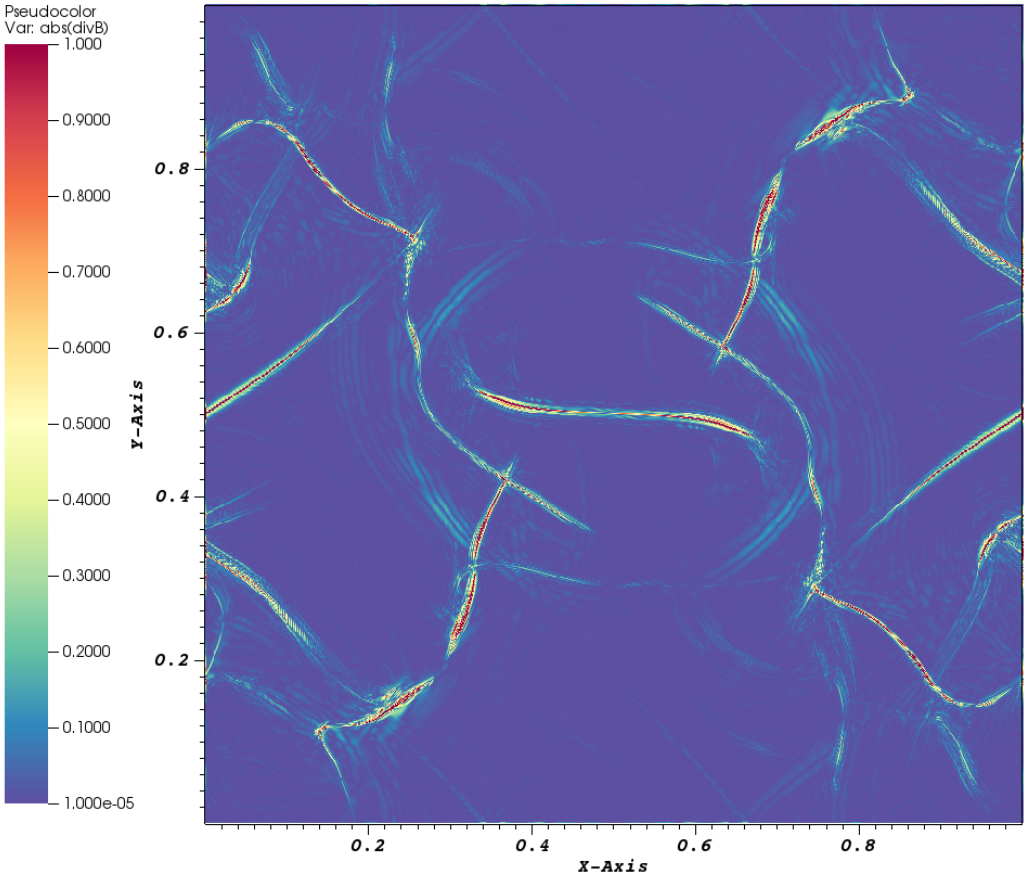

Figure 5.20 – This plot for the Orszag-Tang test shows the divergence of the magnetic field at the final time. The results compare well with those published by Beckwith and Stone [26].The resolution is 800 x 800. The divergence of the magnetic field is minimised by using the divergence cleaning method. The boundary conditions for the divergence cleaning method go to zero. Close to shock waves, the divergence can be high. However, once the shock has moved away from the region, the divergence cleaning method reduces, such that, stable evolution can occur. The results are plotted at $T = 1.0$.

Chapter 6

Advanced Neutron Star Interface Methods

This chapter introduces the majority of the novel work presented in this thesis. It will describe the advanced numerical methods for neutron star interfaces. This will include techniques to locate and construct a Riemann problem at an interface between two models. It will then give several different approaches to solving the interface Riemann problem, including our mRGFM. Next, numerical methods for tacking the interfaces and ensuring that matter models do not overlap will be given. Finally, the fast marching method of extrapolation will be described. All of these combined will allow one to construct multi-component models for neutron stars.

In the majority of neutron star binary simulations a neutron star is approximated to be a single (charged) fluid with an EOS that varies with radius. As shown in Chapter 2, the single-model is an excellent approximation, when the separation of the neutron stars is large. However, the approximation is no longer valid once the neutron star begins to merge with its companion. Physical effects, which are important on a much shorter length-scale than the radius of the star, will begin to affect the dynamics of the system. These effects will be important in the transition boundaries between distinct regions, such as the interface between the crust and the outer core. These effects will impact on the gravitational wave signal from a neutron star merger. It is therefore important that these transition boundaries are included in the numerical simulations.

It is also important to develop a proper treatment of the surface, where the density goes to zero. At this point, the ideal, magnetohydrodynamical approximation fails and is no longer valid for the exterior. In this region, the approximation must be replaced by a low density plasma. Recent simulations [47, 127, 128] have used a general-relativistic, resistive magnetohydrodynamics code developed by Palenzuela [127]. They adopt a general Ohm's law, which is a function of density, to approximate the transition from the interior to the exterior of a neutron star. This thesis will describe an approach to accurately capture the surface

Including a proper treatment of the surface and internal interfaces can be achieved by implementing and extending the framework developed by Millmore and Hawke [114]. Their approach extends the original Ghost Fluid Method (oGFM) of Fedkiw et al. [55] to include relativistic effects. They also utilised a captured boundary approach with the boundary location given by the zero contour of a level set function. Finally, they approximated the solution to the multi-material Riemann problem at the interface by replacing it with two single-material Riemann problems: one for each system of equations. *Ghost* cells were used so that the two individual Riemann problems gave the same results as if the full multi-material Riemann problem had been solved. Their framework was limited to fluid matter models only. We will extend this approach to any matter model that is in conservation or balance law form, such as special-relativistic, ideal magnetohydrodynamics.

Firstly, to achieve this, the Millmore and Hawke framework has been extended to include a magnetic field in the Newtonian formalism. In this case, all components of the velocity and magnetic field are continuous across the interface. Next, the relativistic case with a magnetic field is considered. Finally, a general framework is developed that allows one to combine any number of matter models in conservation or balance law form. An equivalent method was developed by Schoch et al. [155] following a rarefaction-shock approach. Our method uses Roe's linear approximation to the Riemann problem and is equivalent to their approach for certain situations. However, ours is a more general method that is extendable to relativity. This method is called the multi-material Riemann Ghost Fluid Method (mRGFM).

Before the mRGFM can be presented in full, the captured boundary approach must be described. This will be done by explaining the advantages that the captured boundary approach has over tracked boundary conditions. Secondly, the general Ghost Fluid Method will be discussed in two dimensions and the extension to higher dimensions demonstrated.

Following on from this, the oGFM of Fedkiw et al. [55] will be examined in detail. The oGFM has several problems associated with it and is not consistent in the presence of strong shocks. These problems can be overcome by using the modified Ghost Fluid Method (mGFM) of Liu et al. [102], which approximates the multi-material Riemann problem with an all-shock solution. Variants of the original mGFM have gone on to include rarefaction waves and solve the full problem. However, the modified approach is limited to interfaces, where the matter models are of the same type, e.g. fluid-fluid interfaces.

These limitations have led us to the development of the mRGFM that allows one to combine any two hyperbolic systems of conservation laws that represent a matter model at a single interface. The mRGFM will be given in full detail for a general system of hyperbolic conservation laws. It will then be specialised for each of the system of equations that have been presented in this thesis (see Sections 3.3, 3.4, 3.5 and 3.6).

Finally, a method for capturing the surface of a star will be given. This method can replace the use of the "atmosphere" in numerical simulations.

6.1 Multi-material Boundary Conditions

Let us consider the situation, where there are multiple matter models defined on a numerical domain, $\Omega \subset \mathcal{M}_4$, that is contained within the space-time $\mathcal{M}_4$. The space-time is split into subdomains, Ω_i, that intersect only at common boundaries, $\partial\Omega_i$, where $i \in \{1, 2, \ldots, N\}$ for N subdomains. Inside each subdomain is a single matter model with a single matter four-velocity u^μ. This follows the framework of Millmore and Hawke [114]. Figure 6.1 demonstrates this idea. It shows a two-dimensional, numerical domain Ω, bounded by the black line, split into three subdomains. These subdomains have common boundaries, which can be split into separate portions, $\Gamma_{i,j} = \partial\Omega_i \cap \partial\Omega_j$. Each subdomain Ω_i has a boundary $\partial\Omega_i$ represented by a dashed line. The boundary $\Gamma_{1,2}$ is terracotta. The boundary $\Gamma_{2,3}$ is dark blue. The boundary $\Gamma_{1,3}$ is dark green.

There are two questions that determine how one imposes the boundary conditions at the interface. Firstly, how does one determine the location of the boundary? Secondly, how does one impose the correct data at the boundary?

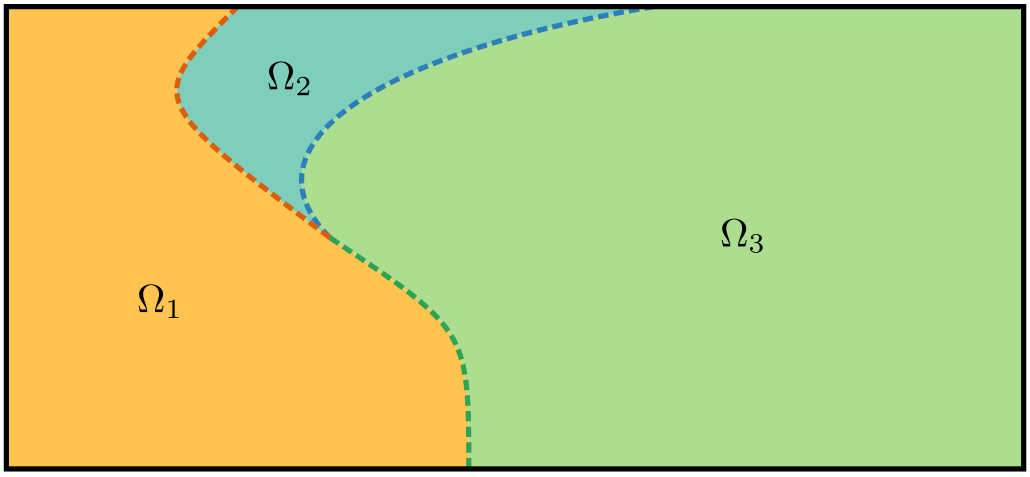

Figure 6.1 – The two-dimensional numerical domain Ω, bounded by the black line, is split into three subdomains. Each subdomain Ω_i has a boundary $\partial\Omega_i$ represented by a dashed line, where $i \in \{1, 2, 3\}$. The boundary $\Gamma_{1,2}$ is terracotta. The boundary $\Gamma_{2,3}$ is dark blue. The boundary $\Gamma_{1,3}$ is dark green.

First of all, we will answer how the location of the boundary is determined. Here, we list two approaches that have been developed for boundary tracking. The first is the tracked boundary approach. This is a Lagrangian method, where the coordinates move with the fluid. The second is the captured boundary approach that uses an implicit function to give the location of the boundary. During the merger phase there will be large topology changes and large shear stresses on the fluids. This can lead to situations, where the tracked boundary method fails: coordinates could cross one another. The captured boundary approach, on the other hand, does not fail in these circumstances. For this reason, we will use the captured boundary approach.

Now, we turn our attention to the question of how to impose the boundary conditions at the interface. Again, two different approaches have been developed. The Volume-of-Fluid (VOF) approach uses the exact location of the boundary to determine the data near the boundary. It splits cells next to the interface into the different materials. This VOF method is excellent at conserving mass across the interface. However, it is difficult to calculate the curvature of the interface [87]. The surface curvature is required to calculate the surface tension, which could be important when determining the boundary conditions at the surface [106]. The Ghost Fluid Method, on the other hand, extends a material beyond the boundary with *ghost* cells. This is demonstrated in Figure 6.2, which shows the *ghost* cells of the purple volume extending beyond the numerical boundary; this will be discussed in detail in Section 6.1.1. The number of *ghost* cells depends on the spatial reconstruction method. Enough *ghost* cells must be filled, such that the reconstruction can be completed for the *real* cells closest to the interface.

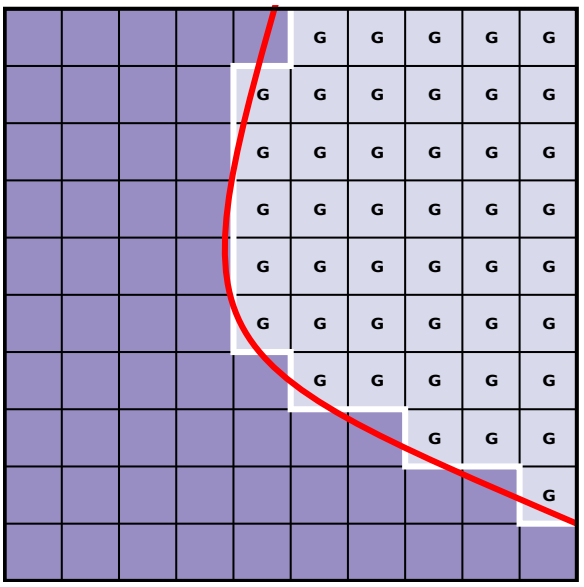

Figure 6.2 – The light purple cells are the *ghost* cells that are to be filled with data. The red line indicates the physical location of the interface. Its numerical location is given by the white line.

The key point to remember is that the *ghost* cells are filled in a way to ensure that the flux entering a *real* cell from a *ghost* cell simulates the effect of the material across the interface. These *ghost* cells are then filled with data to ensure the correct boundary conditions. The Ghost Fluid Method's advantage is its simplicity. It does not change the underlying integrating method and each cell is treated the same. Therefore, for ease of implementation we have used the Ghost Fluid Method. The Ghost Fluid Method, along with a captured boundary approach, allows surface tension and potentially other effects to be included [106, 143, 155].

6.1.1 Captured boundary approach

The captured boundary approach will be used to locate the physical boundaries. The location of the physical boundary, $\partial\Omega_i$, is given by the zero level set of a scalar function, ϕ_i, where $i \in \{1, 2, \ldots, N\}$. Losasso et al. [106] give several advantages of using N level sets for N volumes for physical simulations over the minimal number of N level sets for 2^N volumes. Therefore, we will use N level sets, ϕ_i, to locate the boundaries of N separate volumes, Ω_i. Level sets will be discussed in more detail in the next Subsection 6.1.2.

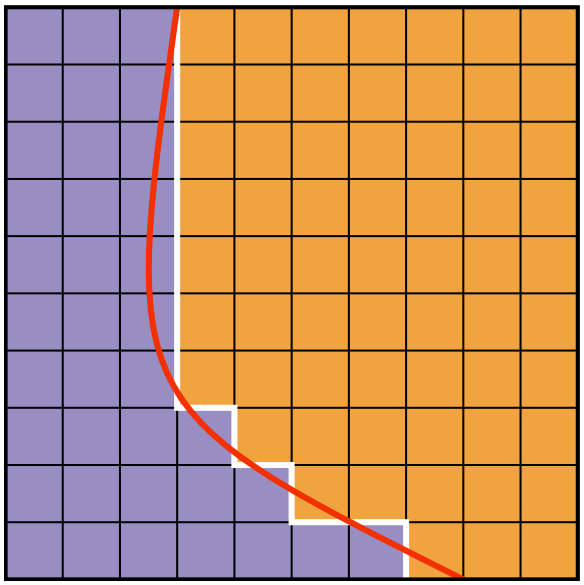

Figure 6.3 – This figure shows the captured boundary approach. The physical interface, shown in red, bisects several numerical cells. The numerical matter models on either side of the interface must be contained within grid cells. Therefore, the physical interface's location is captured by a numerical boundary given by the white line along the cell faces.

Each point within the numerical domain has an associated *real* physical model. The model m at the point is given by

$$\phi_m < \phi_i \quad \forall i \neq m. \tag{6.1}$$

For the model to be physical, the level set must be less than or equal to zero at the point,

$$\phi_m \leq 0. \tag{6.2}$$

This implies that there is only one physical model at each point.

Figure 6.3 shows how the captured boundary approach works. The physical interface, shown in red, bisects several numerical grid points. The matter models on either side of the interface must be contained within grid cells. Therefore, the physical interface's location is captured by a numerical boundary given by the white line along the cell faces. Because the physical boundary is captured, a small change in its location can lead to a large change in the numerical boundary. Figure 6.4 shows this effect. A small shift in the physical interface has led to a significant change in the white, numerical boundary when compared to Figure 6.3. The orange model has increased in size by six numerical cells; each new cell contains an asterisk.

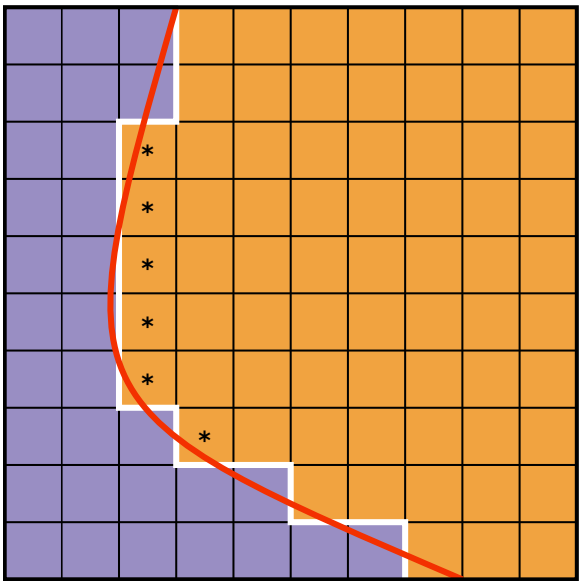

Figure 6.4 – A small shift in the physical interface has led to a significant change in the white, numerical boundary when compared to Figure 6.3. The orange model has increased in size by six numerical cells, indicated by an asterisk in each new cell.

The interface between two matter models can be viewed as a Riemann problem with the interface located at the physical boundary. The curvature of the interface and higher derivatives of the (generalised) Riemann problem could be important. This is especially true for regions where the spatial derivative of the density is large, for example at the surface of a neutron star. Although not considered explicitly in this thesis, the methods introduced are extendable to include such quantities.

It will be assumed that the boundary is planar at each point, where the boundary conditions must be specified. Therefore, the normal of the boundary can be calculated. This is a purely local operation and the normal is calculated by

$$\hat{\mathbf{n}}_m = \frac{\nabla \phi_m}{|\phi_m|}, \tag{6.3}$$

where ϕ_m is the level set associated with the model of the point at which the normal is being calculated. The normal can then be used to perform an appropriate coordinate transformation so that the one-dimensional Riemann problem along this normal can be solved. It is the solution to this Riemann problem that determines the data at the interface.

6.1.2 Level set methods

Level set methods allow one to track sharp features [124, 156]. A level set function is a scalar function that is defined across the whole numerical domain, $\mathbf{x}$. All level set functions in this thesis are denoted ϕ_i, where i is the model number. The zero contour of a level set function, $\phi_i(\mathbf{x}) = 0$, tracks the interface between the model i and all other models. The vector of level set functions at a point determines the *real* physical model at that point as given in equation (6.1). As stated previously, there are N level sets for N models.

Two of the main reasons the level set approach has been chosen are its proven record in relativity and multi-material simulations. Specifically, it has been used to capture the location of event and apparent horizons in black hole simulations [44, 172]. More over, level set methods have been widely employed alongside Ghost Fluid Methods [1, 23, 56, 169]. Alternative methods for tracking sharp features do exist. These alternative methods include particle level set techniques [51, 124], volume-of-fluid methods [80, 118, 185] or phase-field methods [167].

The level set approach is the ideal candidate to locate the interface in the captured boundary approach. In addition to the two reasons given above, the level set approach is also well suited for large topology changes. This is because only the precise location of the zero contour must be maintained to determine the interface position. The level set approach, when coupled with a signed distance function, allows one to accurately determine the distance to the interface and implement the method of Sambasivan and Udaykumar [152].

One of the most important aspects of the level set method is it initialisation. The level set zero contour must correspond to the physical location of the interface. It is then vital that the evolution of the level set zero contour matches the interface. The first of these is fairly simple for the test situations we have considered in this thesis. However, for a full neutron star merger simulation in "$3+1$" dimensions this may not be a simple task. For the majority of test cases, we can describe the shape of the contour and then subtract the interface location. So in the case of a one-dimensional problem, the level set functions with a single interface located at x_0 are given by

$$\phi_1(x) = x - x_0, \quad \phi_2(x) = -(x - x_0). \tag{6.4}$$

Determining the physical evolution of the level set requires one to consider the physical behaviour of the material at the interface. The physical condition imposed at the boundary is that there is no matter transfer across the interface; this means there is no diffusion across the interface. This approach has been chosen for conceptual and implementation simplicity. Therefore, it is a requirement of this approach that the normal velocity must be continuous across the interface. However, the evolution equations can be augmented to allow for transfer, melting and shattering. This relaxes the no-diffusion condition and will allow for a more realistic neutron star, binary simulation. As well as the no-diffusion condition, another requirement is that the interface is stable. This means that there must be a pressure balance across the interface. Any instability that develops, within the interface, will be visible up to a point, which is resolution dependant. Beyond this point the validity of the results are questionable.

The velocity constraint implies that the interface is advected with the material velocity. This means that the level set is Lie-dragged with the four-velocity of the fluid

$$\mathcal{L}_{\mathbf{u}}\phi = 0. \tag{6.5}$$

On a Cartesian grid with zero shift, this can be written as

$$\frac{\partial \phi}{\partial t} + v^i \frac{\partial \phi}{\partial x^i} = 0. \tag{6.6}$$

The advection equation is a non-conservative PDE. However, we have no need for a conservative form as we do not expect non-linear behaviour or discontinuous data. This is because we are only interested in the zero contour of the level set. Away from this the level set can be non-smooth. We only need to ensure that the level set in a region around the zero contour maintains smoothness.

As part of the captured boundary approach, we require a method of measuring the distance from the interface. If we use a signed distance function as a level set, we can determine the distance from the interface. This requires that the level set maintains this property away from the zero contour.

We therefore need some method of maintaining the signed distance function property and resetting the level set. We do this by reinitialising the level set away from the interface. Reinitialisation selects a band of points around the zero contour and then uses these to fill all of the points away from the band by extrapolation. This employs the fast marching method that is described in Section 6.6.

6.1.2.1 Projection method

Due to numerical errors, two level sets can disagree on the location of an interface. This can occur in two different scenarios. There is no level set less than zero at a point: a "vacuum" state exists. Alternatively, there are two level sets less than zero: an "overlap" exists. To project out these errors, the minimum level set ϕ_m and the "next smallest" level set with $\phi_m < \phi_n < \phi_i \; \forall i \neq m, n$, must be determined. A physical state can then be recovered by subtracting the arithmetic average of ϕ_m and ϕ_n from all level sets ϕ_i. This approach was developed by Losasso et al. [106]. In our simulations, this method has proven to be stable and consistent.

6.2 Multi-material Riemann Problem

For all the multi-material Riemann problems considered, the interface will correspond to a contact wave. As stated earlier in Subsection 3.3.2, a contact wave is a linearly degenerate wave that is advected along with the model velocity, $v_m^{\hat{n}}$, in the direction of the normal. Therefore, the solution to the Riemann problem also determines the velocity of the interface.

In this work, we follow the approach of Sambasivan and Udaykumar [152] and label the points closest to the interface as interface points. In our definition of interface points, we include all *real* and *ghost* points that neighbour the interface. These are the points that are updated by the solution of the Riemann problem. The Riemann problems associated with the interface points are solved one at a time. We recommend splitting the interface points into two heaps of *real* and *ghost* points. This allows one to treat them differently in the future. The points in each heap are solved in an order determined by their distance to the interface. This distance is equal to the value of its associated level set at that point. It should be noted that this is only true, if the level set is a signed distance function. This was discussed in Section 6.1.2. However, before solving this Riemann problem, the state either side of the interface must be acquired to determine the initial data. The next subsection will describe the approach of Sambasivan and Udaykumar and its advantages, when dealing with strong shocks.

It should be noted that the captured boundary approach, described above, is non-conservative. The solution from one side of the interface does not necessarily equal the solution on the other side of the interface. This is because a separate Riemann problem is calculated for each interface point. However, it is expected that this error will reduce with resolution.

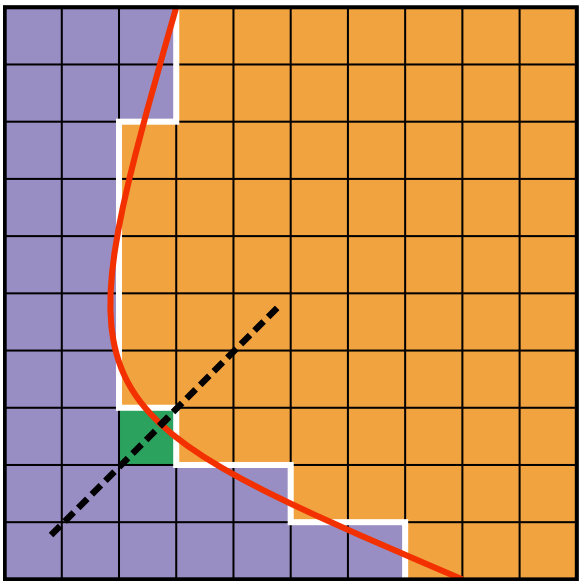

Figure 6.5 – The green cell is the interface point that will be updated using the solution of the multi-material Riemann problem. The Riemann problem is defined along the normal calculated at the green cell. The normal is calculated from the level set associated with the *real* model of the green cell. The normal is a normalised vector that points towards the interface.

6.2.1 Multi-material Riemann problem initial data

We wish to solve the multi-material Riemann problem at the interface to determine the data to fill the interface points. After selecting an interface point to update, the normal is calculated using equation (6.3) from the level set associated with the *real* model at that point. It is along this normal, at the boundary, that the multi-material Riemann problem must be solved. Therefore, a suitable coordinate transformation is performed to rotate into the coordinates normal to the boundary. Figure 6.5 demonstrates this idea. The figure shows the green interface cell, which will be updated with the solution of the multi-material Riemann problem. From the level set associated with the green interface cell, the normal is calculated and represented by the black, dashed line. The normal vector is perpendicular to the interface and always points away from the ghost cells.

Strong shocks will occur during the merger of a neutron star. Therefore, the numerical method used to approximate the multi-material Riemann problem must be consistent and robust in the presence of strong shocks. Sambasivan and Udaykumar [152] has suggested that the initial data for the multi-material Riemann problem should come from cells that are away from the interface. They showed that by following this approach, methods that approximated the Riemann problem consistently, would correctly capture the location of strong shock waves. Therefore, this thesis will follow this approach and the initial data for the left and right states will be determined from cells that are away from the interface.

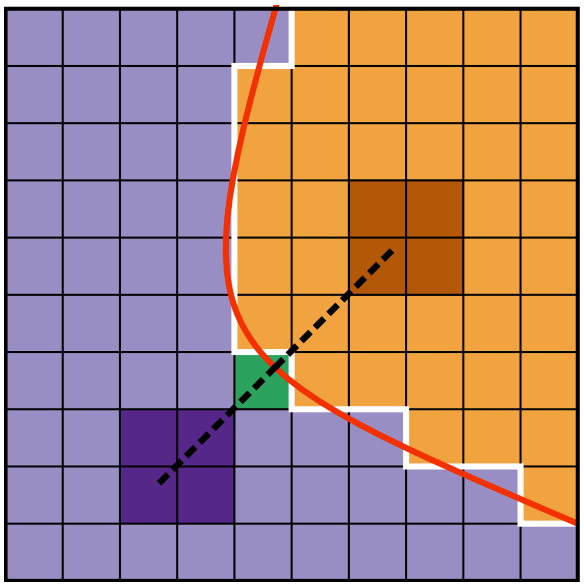

Figure 6.6 – The initial data is constructed from the 2^D cells either side of the interface along the normal. The cells are determined by the ends of the black dotted lines, which have equal length from the physical interface. A convex combination of the brown cells gives the state for the orange model. A convex combination of the purple cells gives the state for the light purple model.

They recommend that the states are a distance $1.5\Delta x$ away; this is to ensure that updated points from the previous time integration do not contaminate the initial data. However, we have found that in the presence of a magnetic field, a distance of $1.0\Delta x$ is preferred. In this case, the numerical error associated with the divergence of the magnetic field is reduced. It should be noted that, this is not a local operation and its impact in relativity has not been considered. Because the normal can be along any direction, the exact point $1.0\Delta x$ from the interface will generally be located away from the centre of a cell. Therefore, the state will be constructed from the 2^D cells nearest this point via convex interpolation, where D is the number of dimensions.

Figure 6.6 demonstrates the procedure of Sambasivan and Udaykumar using the green interface cell from Figure 6.5. The initial data is constructed from the 2^D cells either side of the interface along the normal. The cells are determined by the ends of the black dotted lines, which have equal length from the physical boundary. A convex combination of the brown cells gives the state for the orange model, whereas a convex combination of the purple cells gives the state for the light purple model.

Complex topologies such as "finger like" lobes can be present; this could result in the opposite state being constructed from cells that have the same *real* model as the interface cell. If this situation occurs, then a fallback, which is outline in the next subsection 6.2.2, is used. This could result in fewer cells being used to construct the state. These cells may also be located closer or further away from the interface. It should be noted that for every multi-material Riemann problem that is solved, only the *real* data is used to form the initial states.

6.2.2 Initial data fallback

There are several situations where the method for determining the initial data given previously can fail. One such example is when a thin, finger-like lobe forms. Such a lobe can have a thickness of a single numerical cell. Therefore, a point can neighbour an interface on two sides. In this case, the calculation of the normal would proceed as before. However, when the states are located $1\Delta x$ away from the centre of the cell, they will both be located in different model to point located in lobe. We need one of the states to be associated with the *real* model of the lobe cell. We know which model this is, so we can look at the four nearest cells, to the state location, to see if any of them match the *real* model of the lobe cell. If any do then the fallback uses them to construct the state. However, if none of these cells match then the surrounding twelve cells are searched. All cells that match the *real* model are used. At this point some accuracy is lost and it is recommended that the resolution should be increased. Considering a ring of cells was chosen because it does not prioritise any direction.

6.2.3 Algorithm to approximate the multi-material Riemann problem

Having constructed the initial data for the multi-material Riemann problem we go ahead and solve it using one of the following methods: the original GFM, the modified GFM or our mRGFM method. The solution to the multi-material Riemann problem is approximated by two single-material, individual Riemann problems that give the same solution in the *real* cells as if the multi-material Riemann problem has been solved. This concept is shown in Figure 6.7. This figure explains how the multi-material Riemann problem at the top is split into two single-material Riemann problems. In this particular situation, on the left-hand side the *real* material is an uncharged fluid and on the right-hand side the *real* material is a charged fluid. The total number of Riemann problems that must be solved across two points neighbouring the interface is four; two for each material, one for the *real* and *ghost* point. The *real* and *ghost* Riemann solutions differ, because their initial states could differ. This is due to possible differences in the normal and distance to the interface at each point.

When updating a point, care must be taken so that the Riemann problem across the interface is the same for all models at that point. The sign of the normal magnetic field in relativity breaks the symmetry in the solution to Riemann problem. Therefore, in this case the normal maxgnetic field direction determines which state is the left state and which is the right state. For all other systems considered in this thesis this is not required and the model of the point is chosen as the left state.

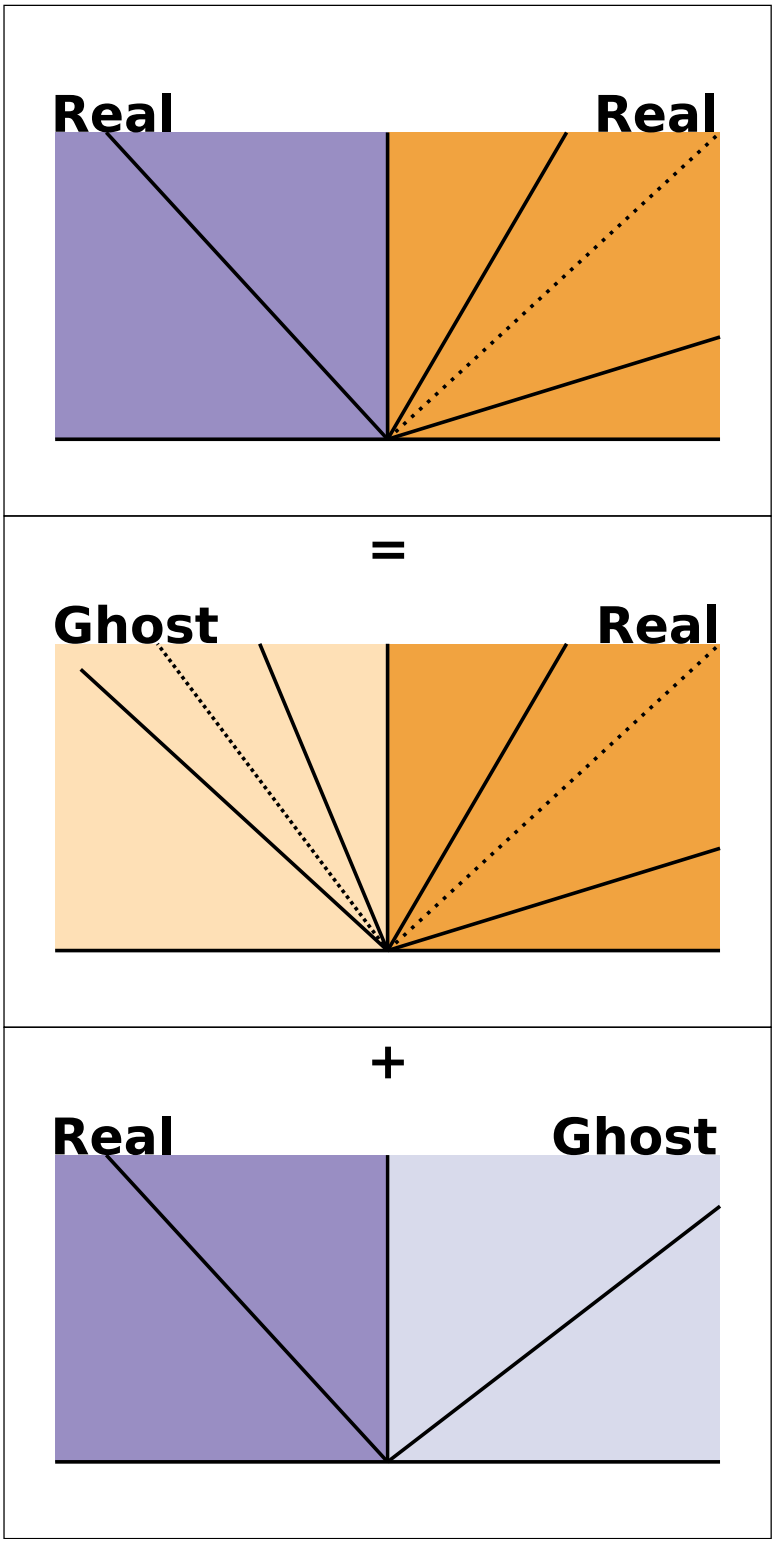

Figure 6.7 – The multi-material Riemann problem solution can be split into two separate single-material Riemann problems. The *ghost* data is chosen so that the wave structure in the *real* material is the same as if we had solved the multi-material Riemann problem. On the left-hand side the *real* material is an uncharged fluid and on the right-hand side the *real* material is a charged fluid.

There exist many different methods to approximate the solution of the Riemann problem at the interface. These Ghost Fluid Methods will be discussed in detail in Section 6.3. For now, we will assume that the solution is known.

Once we have solved the multi-material Riemann problem, the solution consists of two star states either side of the contact wave, one for the purple model and one for the orange model. The new state that corresponds to the material that is being updated, replaces the data at the green cell. However, the green cell is not immediately updated. The solution is stored, because the green cell could be used to construct the initial data for another Riemann problem.

To summarise, the algorithm and assumptions are as follow. For each level set ϕ_i associated with a model i:

1. Locate the boundary $\partial\phi_i$ and store the location of every point that neighbours it. The *real* interface points are cells where $\phi_i \leq 0$ and they neighbour a point where $\phi_i > 0$. *Ghost* interface points are cells where $\phi_i > 0$ and they neighbour a point where $\phi_i \leq 0$.

2. For each interface point:

   (a) Find the normal $\hat{\mathbf{n}}_i$ using equation (6.3).

   (b) Determine the *real* models either side of the interface located $1.0\Delta x$ away using equation (6.1). The model associated with the left Riemann state must be model i. The right state can be any other model apart from i.

   (c) Locate the 2^D cells that are $1.0\Delta x$ away from the interface location along the normal as demonstrated in Figure 6.6. The models in each of the cells must match the models from the previous step. If this is not the case, a fallback must be used.

   (d) Construct the two states by interpolating the data associated with the *real* model at those 2^D cells to the points $1.0\Delta x$ away from the interface. These states form the new initial data states. Remember that model i is always the left state.

   (e) Perform a coordinate transformation into the direction of the normal.

   (f) Solve the multi-material Riemann problem with the initial data.

   (g) Undo the coordinate transformation back to original direction.

   (h) Store the left star state next to the contact. This will be used to update the interface point.

3. Once every Riemann problem associated with an interface point has been calculated, the stored values can be used to update the interface points.

4. The *ghost* cells that are not interface points must now be filled. We use the fast marching method described in Section 6.6.

Figure 6.8 attempts to graphically demonstrate the algorithm described above at a single point. The green cell is a *real* interface point for the purple model. The normal indicated by the black, dashed line aligns the multi-material Riemann problem. The models at the end of the black line are calculated using equation (6.1). The dark purple square are the cells used to construct the data from the purple model. This forms the left state, when updating the green cell. The brown square are the cells used to construct the data from the orange model. This forms the right state. The states are rotated into the direction along the normal. Once the Riemann problem has been solved, the left star state is stored to update the *real* green cell for the purple model. The blue cell is a *ghost* interface point for the orange model located at the same point as the green cell. The normal, indicated by the black dashed line, aligns the multi-material Riemann problem. The models at the end of the black line are calculated using equation (6.1). The dark purple square are the cells used to construct the data from the purple model. This forms the right state, when updating the blue cell. The brown square are the cells used to construct the data from the orange model. This forms the left state. The states are rotated into the direction along the normal. Once the Riemann problem has been solved, the left star state is stored to update the blue *ghost* cell for the orange model.

We must now determine how to solve the multi-material Riemann problem. The first method considered is the oGFM of Fedkiw et al. [55]. This was one of the first methods to use captured boundaries and *ghost* cells. It led to a collection of methods being developed which are referred to as Ghost Fluid Methods.

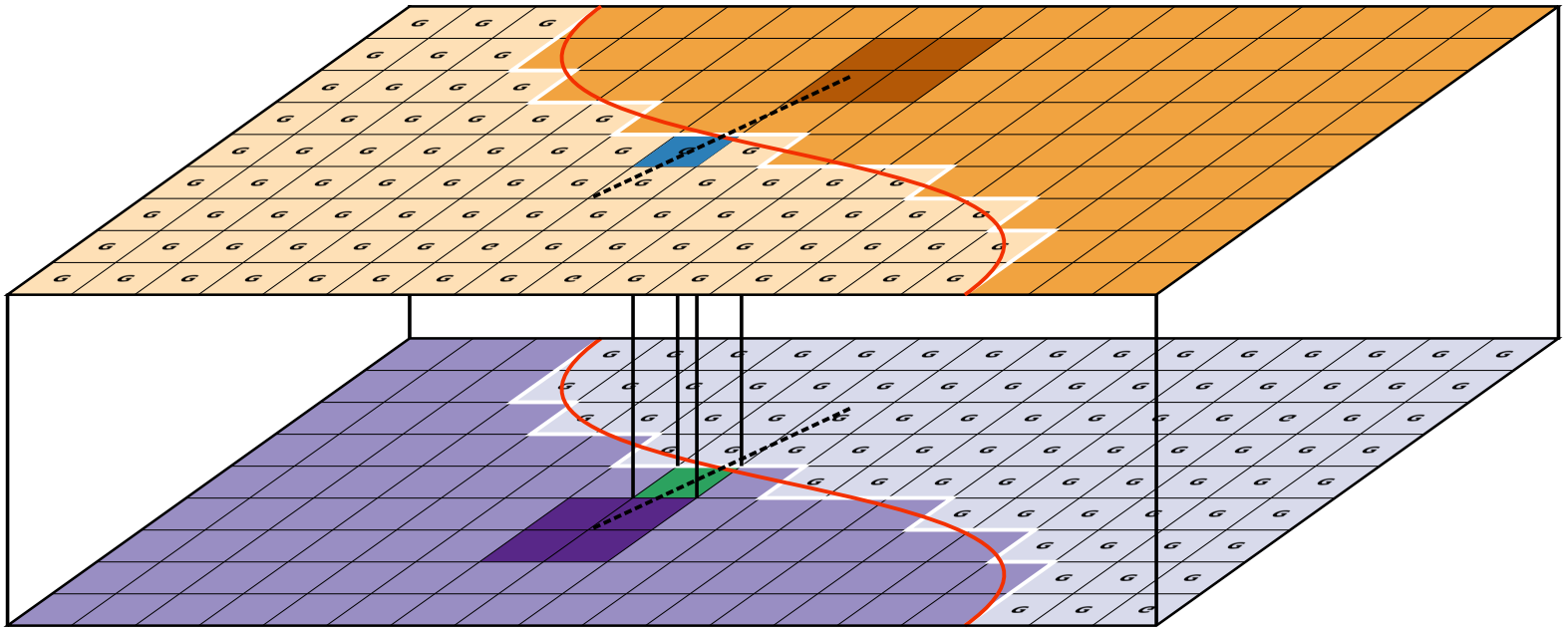

Figure 6.8 – This figure attempts to graphically demonstrate the algorithm at a single point. There are two Riemann problems: one for the model and one for the *ghost* model. The green cell is a *real* interface point for the purple model. The normal, indicated by the black dashed line, aligns the multi-material Riemann problem. The models at the end of the black line are calculated using equation (6.1). The dark purple square are the cells used to construct the data from the purple model. This forms the left state. The brown square are the cells used to construct the data from the orange model. This forms the right state. The states are rotated into the direction along the normal. Once the Riemann problem has been solved, the left star state is stored to update the *real* green cell for the purple model. The blue cell is a *ghost* interface point for the orange model located at the same point as the green cell. The normal, indicated by the black dashed line, aligns the multi-material Riemann problem. The models at the end of the black line are calculated using equation (6.1). The dark purple square are the cells used to construct the data from the purple model. This forms the right state. The brown square are the cells used to construct the data from the orange model. This forms the left state. Once the Riemann problem has been solved, the left star state is stored to update the blue *ghost* cell for the orange model.

6.3 Ghost Fluid Methods

The methods described in this section can be used to solve the multi-material Riemann problem described in the previous section.

6.3.1 Original GFM

The oGFM of Fedkiw et al. [55] was developed to reduce oscillations at a material interface in an Eulerian scheme. Using a level set function, they determined the exact subcell location of the material interface. Each material within the problem is defined over the entire numerical domain. They then defined a set of *ghost* cells for each material. The *ghost* cells for one material correspond to another material's *real* cells, such that there exists only one *real* material for each numerical cell, but there could be many *ghost* cells. It is through these *ghost* cells that information flows across the material interface.

The *ghost* cells extend the material into the volume of the neighbouring material. They are evolved forward in time along with the *real* cells using the standard methods. Their data determines the evolution of the *real* cells at the boundary.

At the interface, Fedkiw et al. approximated the solution to the multi-material Riemann problem in a similar manner to Davis [40]. This approximation reduced the solution of the Riemann problem to a single wave: a contact wave. The jump conditions across a contact wave are then applied across the interface to fill the corresponding ghost cells. This approach is much simpler than the algorithm depicted in Subsection 6.2.3. Only the ghost cells are updated and this is not limited to those neighbouring the interface. However, it has been shown to fail for strong shocks.

In the simple case of Newtonian hydrodynamics, using just a contact wave results in the pressure and the normal velocity being copied from the *real* material cells to the *ghost* cells of the other material and vice versa. This means that the blue cell in Figure 6.8 would get its new pressure and velocity from the green cell. This is because across the contact wave the pressure and normal velocity are continuous.

The oGFM makes the assumption that the entropy and the tangential velocities are constant across the interface. This assumption results in the entropy and tangential velocity being extrapolated, at zeroth order, from the closest *real* cell of a material across the interface into the same material's *ghost* cells that are being filled. This means that the blue cell in Figure 6.8 would get its new entropy and tangential velocity from the first orange cell along the normal. The density can then be recovered from the entropy, EOS and the other values in the *ghost* cell.

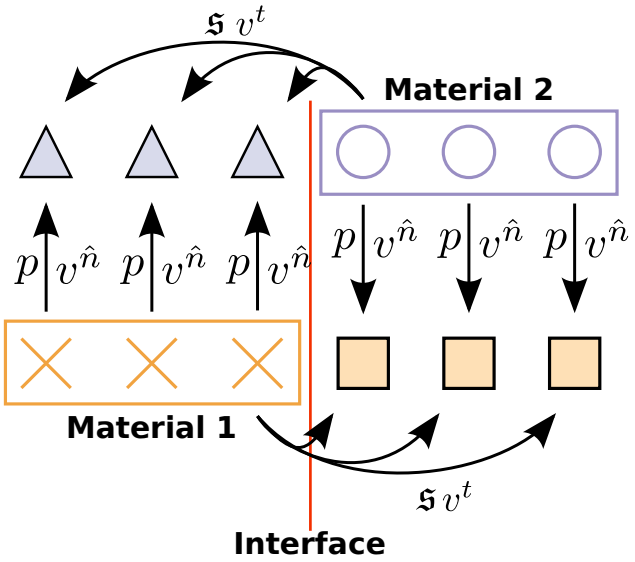

Figure 6.9 – The oGFM approximates the multi-material Riemann problem by considering only a contact wave solution. Each material has *real* cells (boxed) and *ghost* cells across the interface. The *ghost* cells are filled with the pressure and normal velocity from the *real* cell in the same physical location. This matches the jump conditions at the contact. The entropy of the *real* cell closest to the interface is copied into the ghost cells of the same material.

This process is summarised in Figure 6.9. The figure shows two numerical arrays defined on the same numerical grid that have been separated into *real* and *ghost* cells based upon the location of the material interface. The pressure and the velocity of material 1 is copied into the *ghost* cells of material 2 and vice versa. The entropy and the tangential velocity of the last *real* cell of material 1 is copied into the *ghost* cells of material 1. Again, the same is true for material 2.

Although it was a good starting point, the oGFM suffers from several issues. As mentioned previously, the isentropic fixing leads to the constant extrapolation of the entropy. This is inconsistent with the idea that a shock wave can impact on an interface as one would expect a jump in the entropy. In the original paper by Fedkiw et al., they dismissed this problem, because they stated that this jump would occur instantly. However, Liu et al. [102] showed algebraically that the oGFM was inconsistent and that this problem could not be ignored.

6.3.2 Modified GFM

The mGFM addresses some of the issues the oGFM has. Developed by Liu et al. [102], the mGFM approximates the solution of the Riemann problem by considering an all-shock solution. This means that in the case of Newtonian hydrodynamics both non-linear sound waves are shocks. To approximate the solution to the Riemann problem, an iterative method is used. The following two equations have to be solved, which are derived from the jump conditions at a shock wave,

$$\frac{p^* - p_{i-1}}{W_{\mathrm{L}}} + \left(v_n^* - v_{i-1}^n\right) = 0, \tag{6.7a}$$

$$\frac{p^* - p_{i+2}}{W_{\mathrm{R}}} - \left(v_n^* - v_{i+2}^n\right) = 0, \tag{6.7b}$$

where

$$W_{\mathrm{L}}^2 = \rho^{*L}\rho_{i-1}\frac{p^* - p_{i-1}}{\rho^{*L} - \rho_{i-1}}, \tag{6.8a}$$

$$W_{\mathrm{R}}^2 = \rho^{*R}\rho_{i+2}\frac{p^* - p_{i+2}}{\rho^{*R} - \rho_{i+1}}, \tag{6.8b}$$

where n indicated a quantity normal to the interface and i indicates the location of the cell and the interface is located between i and $i+1$. Quantities marked with a superscript $*$ are the updated values. Assuming a gamma-law EOS, the densities at the interface are given by

$$\rho^{*L} = \left[\frac{\frac{\gamma_{\mathrm{L}}}{\gamma_{\mathrm{L}}-1}p^* - \frac{1}{2}\left(p^* - p_{i-1}\right)}{\frac{\gamma_{\mathrm{L}}}{\gamma_{\mathrm{L}}-1}p_{i-1} + \frac{1}{2}\left(p^* - p_{i-1}\right)}\right]\rho_{i-1}, \tag{6.9a}$$

$$\rho^{*R} = \left[\frac{\frac{\gamma_{\mathrm{R}}}{\gamma_{\mathrm{R}}-1}p^* - \frac{1}{2}\left(p^* - p_{i+2}\right)}{\frac{\gamma_{\mathrm{R}}}{\gamma_{\mathrm{R}}-1}p_{i+2} + \frac{1}{2}\left(p^* - p_{i+2}\right)}\right]\rho_{i+2}. \tag{6.9b}$$

Once the states across the shock waves have been calculated, the modified GFM updates the *ghost* cells and the density in the closest *real* cell. The modified GFM procedure is shown in Figure 6.10. This figure shows the *ghost* cells for each material being updated by the corresponding star state.

The mGFM correctly captures the location of strong shock waves [187]. However, this solution to the multi-material Riemann problem is numerically expensive. It is also only suitable for materials described by systems of equations that have the same hyperbolic structure.

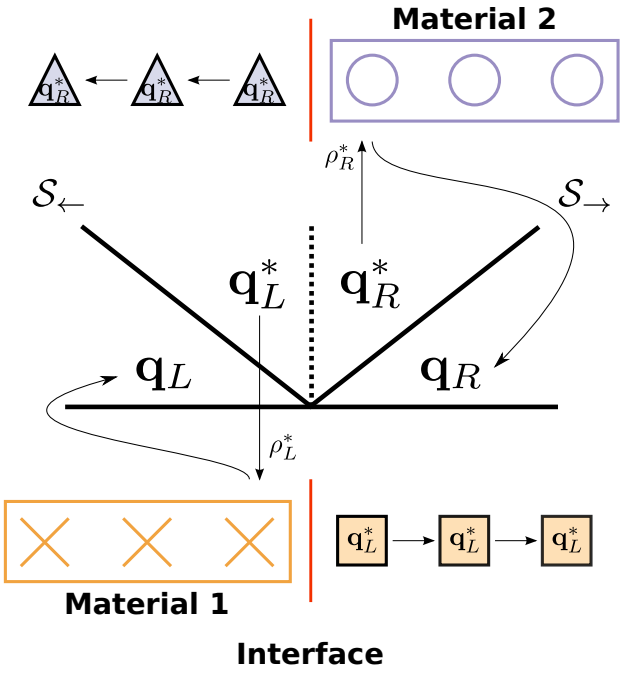

Figure 6.10 – The mGFM approximates the solution of the multi-material Riemann problem to only consist of shock waves. Once the star states have been found using an iterative method they are copied to the ghost cells. The mGFM also updates the cell closest to the interface by copying the density from the star state.

The interface Ghost Fluid Method (iGFM) of Hu and Khoo [84] uses the mGFM but solves two Riemann problems at the boundary. The real Ghost Fluid Method (rGFM) of Wang et al. [181] is similar to the iGFM but updates the interface boundary point as well, just as we do in our captured boundary approach.

6.3.3 Multi-material Riemann Ghost Fluid Method

The final method of approximating the multi-material Riemann problem we will consider is one based on Roe's linear approximation to the general Riemann problem. We have developed this method to extend the advantages of the modified method to situations, where the materials are not of the same conservation law type.

We remind ourselves of Roe's approximate solution to the Riemann problem for a single-material [173]. By linearising the system of conservation laws, one can decouple the system of equations. This was done in Chapter 3.2 and we use those results here (3.33a), (3.33b).

The solution at space-time point (t, x), where $\lambda^{(j)} \leq x/t \leq \lambda^{(j+1)}$, is given by either of

$$\mathbf{w}(t,x) = \mathbf{w}_{\mathrm{L}} + \sum_{i=1}^{j} \left(\mathbf{l}^{(i)} \otimes \Delta\mathbf{w}\right) \mathbf{r}^{(i)}, \tag{6.10a}$$

$$\mathbf{w}(t,x) = \mathbf{w}_{\mathrm{R}} - \sum_{i=j+1}^{N} \left(\mathbf{l}^{(i)} \otimes \Delta\mathbf{w}\right) \mathbf{r}^{(i)}, \tag{6.10b}$$

where $\Delta\mathbf{w} = \mathbf{w}_{\mathrm{R}} - \mathbf{w}_{\mathrm{L}}$. We will write this solution in the less explicit form

$$\mathbf{w}(t,x) = \mathbf{w}_{\mathrm{L}} + \sum_{i=1}^{j} C_i \mathbf{r}^{(i)}, \tag{6.11a}$$

$$\mathbf{w}(t,x) = \mathbf{w}_{\mathrm{R}} - \sum_{i=j+1}^{N} C_i \mathbf{r}^{(i)}, \tag{6.11b}$$

which will be used later.

We now consider the multi-material problem. To be explicit with the notation, we assume that we have two models M_{x}, where $\mathrm{x} \in \{\mathrm{L}, \mathrm{R}\}$ labels the left or right state. We assume that each model has N_{x} waves on either side of the contact that forms the interface between the two models. In addition, we assume that there exist precisely $N_{\mathrm{L}} + N_{\mathrm{R}}$ compatibility conditions linking the two models. These are relations that must apply at the interface; for simplicity, we will assume that these are algebraic relations.

As an explicit example, consider the cases of Newtonian hydrodynamics and ideal magnetohydrodynamics as shown in Figure 6.7. For Newtonian hydrodynamics, there are $N_{\mathrm{x}} = 1$ waves on either side, and two compatibility conditions (continuity of pressure and normal velocity) as shown in the bottom part of Figure 6.7 and given in the equations (3.51a) and (3.51b). For Newtonian ideal magnetohydrodynamics, there are $N_{\mathrm{x}} = 3$ waves on either side, and six compatibility conditions (continuity of pressure, all velocity components, and tangential magnetic field components) as shown in the middle of Figure 6.7 and given in the equations (3.101a), (3.101b) and (3.101c). The condition on the normal magnetic field is automatically achieved. For ideal magnetohydrodynamics coupled to Newtonian hydrodynamics, there are $N_{\mathrm{L}} + N_{\mathrm{R}} = 4$ waves and four compatibility conditions (continuity of pressure and normal velocity and vanishing of the tangential magnetic field components on the MHD side) as shown in the top third of Figure 6.7.

It is not possible to write down a Roe-type solution to the multi-material Riemann problem directly using the recipe above. There exists one problem of principle, which is that the definition of the initial data jump $\Delta\mathbf{w}$ makes no sense (as $\mathbf{w}_{\mathrm{L,R}}$ correspond to different models). Another problem is the difficulty of defining a sensible linearised state $\bar{\mathbf{w}}_{\mathrm{x}}$ at which to evaluate the matrix A (or its extension A_{x} in the multi-material case). It is usual to set $\bar{\mathbf{w}}_{\mathrm{x}}$ to some "average", $\bar{\mathbf{w}} \equiv \bar{\mathbf{w}}(\mathbf{w}_{\mathrm{L}}, \mathbf{w}_{\mathrm{R}})$, of the left and right states – for simplicity this is often the arithmetic average. In the multi-material case this clearly makes no sense.

An alternative approach is as follows. Assume that each model M_{x} satisfies the linearised equation

$$\partial_t \mathbf{w}_{\mathrm{x}} + \bar{A}_{\mathrm{x}} \partial_x \mathbf{w}_{\mathrm{x}} = \mathbf{0}, \tag{6.12}$$

for some choice of linearisation state $\bar{\mathbf{w}}_{\mathrm{x}}$, i.e. $\bar{A}_{\mathrm{x}} = A_{\mathrm{x}}(\bar{\mathbf{w}}_{\mathrm{x}})$. Also assume that we have chosen the variables $\mathbf{w}_{\mathrm{x}}$ so that the first $N_{\mathrm{L}} + N_{\mathrm{R}}$ variables are precisely those to which the algebraic compatibility conditions apply, i.e. for hydrodynamics the first two variables in $\mathbf{w}_{\mathrm{x}}$ will be the pressure and the normal velocity. Then we *assume* that the solution next to the interface can be written in the form

$$\mathbf{w}^{\star}_{\mathrm{L}} = \mathbf{w}_{\mathrm{L}} + \sum_{i=1}^{N_{\mathrm{L}}} C_i^{(\mathrm{L})} \mathbf{r}_{\mathrm{L}}^{(i)}, \tag{6.13a}$$

$$\mathbf{w}^{\star}_{\mathrm{R}} = \mathbf{w}_{\mathrm{R}} - \sum_{j=1}^{N_{\mathrm{R}}} C_j^{(\mathrm{R})} \mathbf{r}_{\mathrm{R}}^{(j)}. \tag{6.13b}$$

By our choice of variables, the first $N_{\mathrm{L}} + N_{\mathrm{R}}$ components of these equations must match across the interface (because the compatibility conditions are assumed to take the form $\Delta\mathbf{w}_j = 0$, where $j = 1, \ldots, N_{\mathrm{L}} + N_{\mathrm{R}}$). Therefore, we have $N_{\mathrm{L}} + N_{\mathrm{R}}$ equations of the form

$$0 = \mathbf{w}_{\mathrm{R}} - \mathbf{w}_{\mathrm{L}} = \sum_{j=1}^{N_{\mathrm{R}}} C_j^{(\mathrm{R})} \mathbf{r}_{\mathrm{R}}^{(j)} + \sum_{i=1}^{N_{\mathrm{L}}} C_i^{(\mathrm{L})} \mathbf{r}_{\mathrm{L}}^{(i)}, \tag{6.14}$$

which follow from the first $N_{\mathrm{L}} + N_{\mathrm{R}}$ components of equations (6.13) (carefully interpreted) containing $N_{\mathrm{L}} + N_{\mathrm{R}}$ unknowns $C_{i,j}^{(\mathrm{x})}$. This defines a linear system for these unknowns, which we assume has a unique solution. Given the solution, we can then use all components of equations (6.13) to construct the interface states required.

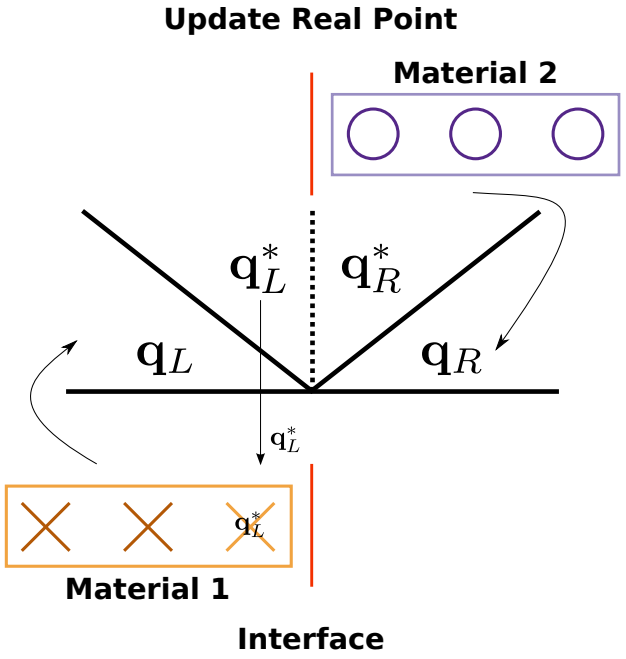

Figure 6.11 – When updating a *real* point, the left state is given by the same model as the *real* point. The point is then updated with the left star state $\mathbf{q}_{\mathrm{L}}^*$.

The only remaining question is the choice of $\bar{\mathbf{w}}_{\mathrm{x}}$ required to construct $\bar{A}_{\mathrm{x}}$ from which the eigenvectors follow. The simplest choice would be $\bar{\mathbf{w}}_{\mathrm{x}} = \mathbf{w}_{\mathrm{x}}$. However, it may be that this is not a good approximation. Another approach would be iterative. Set

$$\bar{\mathbf{w}}_{\mathrm{x}}^{(0)} = \mathbf{w}_{\mathrm{x}}, \tag{6.15a}$$

$$\bar{\mathbf{w}}_{\mathrm{x}}^{(n+1)} = \frac{1}{2}\left(\mathbf{w}_{\mathrm{x}} + \mathbf{w}_{\mathrm{x}}^{\star}\right), \tag{6.15b}$$

where $\mathbf{w}_{\mathrm{x}}^{\star}$ results from the above procedure with $\bar{\mathbf{w}}_{\mathrm{x}} = \bar{\mathbf{w}}_{\mathrm{x}}^{(n)}$. We would then iterate until $\|\bar{\mathbf{w}}_{\mathrm{x}}^{(n+1)} - \bar{\mathbf{w}}_{\mathrm{x}}^{(n)}\|$ is less than some tolerance. In practice, linearising about $\mathbf{w}_{\mathrm{x}}$ is adequate to approximate the multi-material Riemann problem for the cases we have considered.

Once the star states have been calculated, we follow the captured boundary algorithm 6.2.3 and update the appropriate cells. When updating a *real* point, the algorithm is represented by Figure 6.11. When updating a *ghost* point, the algorithm is represented by Figure 6.12. The no-iteration algorithm presented here can be seen as an alternative derivation of the method of Schoch et al. [155] and we will now describe their approach.

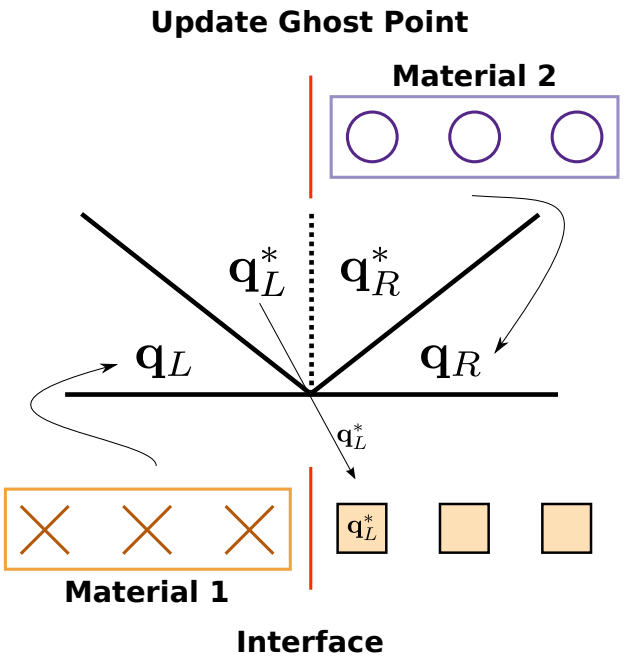

Figure 6.12 – When updating a *ghost* point, the left state is given by the same model as the *ghost* point. The states are flipped so that this is the case. The point is then updated with the left star state $\mathbf{q}_\mathrm{L}^*$.

6.3.4 Rarefaction-shock approach

Schoch et al. [155] have developed a new approximate solution to the multi-material Riemann problem based on a rarefaction-shock approach. This approach was developed to simulate interfaces between solid and liquid boundaries in explosives.

Their approach makes the assumption that the waves connecting the states in the Riemann problem are rarefaction-shocks. In comparison, we assume that the waves are a linear approximation to shock waves. Along a characteristic wave exists a set of invariant quantities, which travel at the characteristic velocity. These invariants can be obtained from the following relations

$$\mathbf{l}^{(i)} \cdot \mathrm{d}\mathbf{w} = 0, \tag{6.16}$$

where $\mathbf{l}^{(i)}$ are the left eigenvectors associated with the characteristic $\lambda^{(i)}$. These give a set of relations that connect the state in front of the wave to the state behind. In the mRGFM, these are equivalent to the coefficients C_i given in equation (6.11). The two methods differ when applies the updating procedure given in equation (6.15). Another advantage of the mRGFM is that the right eigenvectors are easier to calculate analytically than the left.

6.4 mRGFM Fluid Interfaces

6.4.1 Newtonian hydrodynamics

We now present the explicit equations for the mRGFM solution to the multi-material Riemann problem for two materials. First, we will consider the case where both materials are governed by the equations of Newtonian hydrodynamics. The conserved variables are $\mathbf{q} = (\rho, \rho v_j, \mathcal{E})^T$ with fluxes $\mathbf{f}^{(n)} = (\rho v^n, \rho v_j v^n + p\delta^n_j, (\mathcal{E}+p)v^n)^T$, where n is the direction normal to the interface. The compatibility conditions are

$$[[p]] = 0, \tag{6.17a}$$

$$[[v^n]] = 0. \tag{6.17b}$$

Rotate the coordinates so that x is the normal direction and that y, z are appropriate orthogonal directions. We choose to write the system using the variables $\mathbf{w} = (p, v^j, \rho)^T$. Applying the linearisation to give equation (6.12), the matrix $\bar{A}_{\mathrm{x}}$ has the explicit form

$$A_{\mathrm{x}}(\bar{\mathbf{w}}_{\mathrm{x}}) = \begin{pmatrix} v^x_{\mathrm{x}} & \rho_{\mathrm{x}} a^2_{\mathrm{x}} & 0 & 0 & 0 \\ \rho^{-1}_{\mathrm{x}} & v^x_{\mathrm{x}} & 0 & 0 & 0 \\ 0 & 0 & v^x_{\mathrm{x}} & 0 & 0 \\ 0 & 0 & 0 & v^x_{\mathrm{x}} & 0 \\ 0 & \rho_{\mathrm{x}} & 0 & 0 & v^x_{\mathrm{x}} \end{pmatrix}, \tag{6.18}$$

where the x indicates the left or right linearised state. There is one non-linear wave either side of the contact with eigenvalue $v^x_{\mathrm{x}} \pm a_{\mathrm{x}}$. The unnormalised right eigenvector is

$$\bar{\mathbf{r}}^{(\pm)}_{\mathrm{x}} = \begin{pmatrix} a^2_{\mathrm{x}} \\ \pm\dfrac{a_{\mathrm{x}}}{\rho_{\mathrm{x}}} \\ 0 \\ 0 \\ 1 \end{pmatrix}. \tag{6.19}$$

Thus, the linear system to solve will be given by the equations

$$p_{\mathrm{R}} - p_{\mathrm{L}} = C_1^{(\mathrm{R})} a^2_{\mathrm{R}} + C_1^{(\mathrm{L})} a^2_{\mathrm{L}}, \tag{6.20a}$$

$$v^x_{\mathrm{R}} - v^x_{\mathrm{L}} = C_1^{(\mathrm{R})} \frac{a_{\mathrm{R}}}{\rho_{\mathrm{R}}} - C_1^{(\mathrm{L})} \frac{a_L}{\rho_{\mathrm{L}}}. \tag{6.20b}$$

It follows that

$$C_1^{(\mathrm{R})} = \frac{\rho_\mathrm{R}}{a_\mathrm{R}} \frac{\Delta p + \rho_\mathrm{L} a_\mathrm{L} \Delta v}{\rho_\mathrm{R} a_\mathrm{R} + \rho_\mathrm{L} a_\mathrm{L}}, \tag{6.21a}$$

$$C_1^{(\mathrm{L})} = \frac{\rho_\mathrm{L}}{a_\mathrm{L}} \frac{\Delta p - \rho_\mathrm{R} a_\mathrm{R} \Delta v}{\rho_\mathrm{R} a_\mathrm{R} + \rho_\mathrm{L} a_\mathrm{L}}, \tag{6.21b}$$

where $\Delta w = w_\mathrm{R} - w_\mathrm{L}$. The star state for the left-hand side can then be calculated using Roe's linear approximation (6.13a) with the coefficient (6.21b) and the right eigenvector (6.19) for the left going wave,

$$p^* = p_\mathrm{L} + \frac{\rho_\mathrm{L}}{a_\mathrm{L}} \frac{\Delta p - \rho_\mathrm{R} a_\mathrm{R} \Delta v}{\rho_\mathrm{R} a_\mathrm{R} + \rho_\mathrm{L} a_\mathrm{L}} \cdot a_L^2, \tag{6.22a}$$

$$v^{x*} = v_\mathrm{L}^x - \frac{\rho_\mathrm{L}}{a_\mathrm{L}} \frac{\Delta p - \rho_\mathrm{R} a_\mathrm{R} \Delta v}{\rho_\mathrm{R} a_\mathrm{R} + \rho_\mathrm{L} a_\mathrm{L}} \cdot \frac{a_\mathrm{L}}{\rho_\mathrm{L}}, \tag{6.22b}$$

$$v_\mathrm{L}^{y*} = v_\mathrm{L}^y, \tag{6.22c}$$

$$v_\mathrm{L}^{z*} = v_\mathrm{L}^z, \tag{6.22d}$$

$$\rho_\mathrm{L}^* = \rho_\mathrm{L} + \frac{\rho_\mathrm{L}}{a_\mathrm{L}} \frac{\Delta p - \rho_\mathrm{R} a_\mathrm{R} \Delta v}{\rho_\mathrm{R} a_\mathrm{R} + \rho_\mathrm{L} a_\mathrm{L}} \cdot a_L^2. \tag{6.22e}$$

The right state can be calculated in the same way, but we focus on the left one because this is all that is needed in the captured boundary approach.

6.4.2 Newtonian, ideal magnetohydrodynamics

We shall now consider the case where the two materials are both governed by the equations of Newtonian, ideal magnetohydrodynamics. The conserved variables are

$$\mathbf{q} = (\rho, S_x, S_y, S_z, E, B_x, B_y, B_z)^T. \tag{6.23}$$

From the contact jump conditions (3.101a), (3.101b) and (3.101c) the set of variables at the contact should be

$$\mathbf{w} = (p, v_x, v_y, v_z, B_y, B_z, \rho)^T. \tag{6.24}$$

The number of variables has reduced by one, because the divergence of the magnetic field ensures that B_x cannot jump. However, due to numerical errors and the way that the initial data is chosen, the normal magnetic field may change across the contact.

Therefore, we fix the contact normal magnetic field to an arithmetic average of the left and right state. The matrix $\bar{A}_{\mathrm{x}}$ is

$$A_{\mathrm{x}}(\bar{\mathbf{w}}_{\mathrm{x}}) = \begin{pmatrix} v_{\mathrm{x}}^{x} & p_{\mathrm{x}}\gamma_{\mathrm{x}} & 0 & 0 & 0 & 0 & 0 \\ \rho_{\mathrm{x}}^{-1} & v_{\mathrm{x}}^{x} & 0 & 0 & \dfrac{B_{\mathrm{x}}^{y}}{\rho_{\mathrm{x}}} & \dfrac{B_{\mathrm{x}}^{z}}{\rho_{\mathrm{x}}} & 0 \\ 0 & 0 & v_{\mathrm{x}}^{x} & 0 & -\dfrac{B^{x}}{\rho_{\mathrm{x}}} & 0 & 0 \\ 0 & 0 & 0 & v_{\mathrm{x}}^{x} & 0 & -\dfrac{B^{x}}{\rho_{\mathrm{x}}} & 0 \\ 0 & B_{\mathrm{x}}^{y} & -B^{x} & 0 & v_{\mathrm{x}}^{x} & 0 & 0 \\ 0 & B_{\mathrm{x}}^{z} & 0 & -B^{x} & 0 & v_{\mathrm{x}}^{x} & 0 \\ 0 & \rho_{\mathrm{x}} & 0 & 0 & 0 & 0 & v_{\mathrm{x}}^{x} \end{pmatrix}. \tag{6.25}$$

The following eigenvectors are based on those given by Powell et al. [139] and Sriskantha and Ruffert [165],

$$\bar{\mathbf{r}}_{\mathrm{x}}^{(f\pm)} = \begin{pmatrix} \alpha_{f}^{\mathrm{x}}\gamma_{\mathrm{x}}p_{\mathrm{x}} \\ \pm\alpha_{f}^{\mathrm{x}}c_{f}^{\mathrm{x}} \\ \mp\alpha_{s}^{\mathrm{x}}c_{s}^{\mathrm{x}}\beta_{x}\beta_{y}^{\mathrm{x}} \\ \mp\alpha_{s}^{\mathrm{x}}c_{s}^{\mathrm{x}}\beta_{x}\beta_{z}^{\mathrm{x}} \\ \sqrt{\rho_{\mathrm{x}}}\alpha_{s}^{\mathrm{x}}a_{\mathrm{x}}\beta_{y}^{\mathrm{x}} \\ \sqrt{\rho_{\mathrm{x}}}\alpha_{s}^{\mathrm{x}}a_{\mathrm{x}}\beta_{z}^{\mathrm{x}} \\ \rho_{\mathrm{x}}\alpha_{f}^{\mathrm{x}} \end{pmatrix}, \quad \bar{\mathbf{r}}_{\mathrm{x}}^{(s\pm)} = \begin{pmatrix} \alpha_{s}^{\mathrm{x}}\gamma_{\mathrm{x}}p_{\mathrm{x}} \\ \pm\alpha_{s}^{\mathrm{x}}c_{s}^{\mathrm{x}} \\ \pm\alpha_{f}^{\mathrm{x}}c_{f}^{\mathrm{x}}\beta_{x}\beta_{y}^{\mathrm{x}} \\ \pm\alpha_{f}^{\mathrm{x}}c_{f}^{\mathrm{x}}\beta_{x}\beta_{z}^{\mathrm{x}} \\ -\sqrt{\rho_{\mathrm{x}}}\alpha_{f}^{\mathrm{x}}a_{\mathrm{x}}\beta_{y}^{\mathrm{x}} \\ -\sqrt{\rho_{\mathrm{x}}}\alpha_{f}^{\mathrm{x}}a_{\mathrm{x}}\beta_{z}^{\mathrm{x}} \\ \rho_{\mathrm{x}}\alpha_{s}^{\mathrm{x}} \end{pmatrix}, \quad \bar{\mathbf{r}}_{\mathrm{x}}^{(a\pm)} = \begin{pmatrix} 0 \\ 0 \\ \pm\beta_{z} \\ \mp\beta_{y} \\ -\beta_{z}^{\mathrm{x}}\beta_{x}\sqrt{\rho_{\mathrm{x}}} \\ \beta_{y}^{\mathrm{x}}\beta_{x}\sqrt{\rho_{\mathrm{x}}} \\ 0 \end{pmatrix}, \tag{6.26}$$

where

$$\beta_x = \mathrm{sgn}\left(B_x\right), \quad \beta_y^{\mathrm{x}} = \begin{cases} \dfrac{B_y^{\mathrm{x}}}{B_t^{\mathrm{x}}} & \text{if } B_t^{\mathrm{x}} > 0, \\ \dfrac{1}{\sqrt{2}} & \text{if } B_t^{\mathrm{x}} = 0, \end{cases} \quad \beta_z^{\mathrm{x}} = \begin{cases} \dfrac{B_z^{\mathrm{x}}}{B_t^{\mathrm{x}}} & \text{if } B_t^{\mathrm{x}} > 0, \\ \dfrac{1}{\sqrt{2}} & \text{if } B_t^{\mathrm{x}} = 0, \end{cases} \tag{6.27}$$

and

$$\alpha_f^{\mathrm{x}} = \begin{cases} \sin\phi & \text{if } c_f^{\mathrm{x}2} - c_s^{\mathrm{x}2} = 0, \\ 0 & \text{if } a_{\mathrm{x}}^2 - c_s^{\mathrm{x}2} = 0, \\ \sqrt{\dfrac{a_{\mathrm{x}}^2 - c_s^{\mathrm{x}2}}{c_f^{\mathrm{x}2} - c_s^{\mathrm{x}2}}} & \text{if } c_f^{\mathrm{x}2} - a_{\mathrm{x}}^2 = 0, \\ \sqrt{\dfrac{a_{\mathrm{x}}^2 - c_s^{\mathrm{x}2}}{c_f^{\mathrm{x}2} - c_s^{\mathrm{x}2}}} & \text{otherwise,} \end{cases} \quad \alpha_s^{\mathrm{x}} = \begin{cases} \cos\phi & \text{if } c_f^{\mathrm{x}2} - c_s^{\mathrm{x}2} = 0, \\ \sqrt{\dfrac{c_f^{\mathrm{x}2} - a_{\mathrm{x}}^2}{c_f^{\mathrm{x}2} - c_s^{\mathrm{x}2}}} & \text{if } a_{\mathrm{x}}^2 - c_s^{\mathrm{x}2} = 0, \\ 0 & \text{if } c_f^{\mathrm{x}2} - a_{\mathrm{x}}^2 = 0, \\ \sqrt{\dfrac{c_f^{\mathrm{x}2} - a_{\mathrm{x}}^2}{c_f^{\mathrm{x}2} - c_s^{\mathrm{x}2}}} & \text{otherwise.} \end{cases} \tag{6.28}$$

Finally

$$\phi = \arctan\left(\frac{\dfrac{|\mathbf{B}|_{\mathrm{x}}}{\sqrt{\rho_{\mathrm{x}}}} - c_a^{\mathrm{x}}}{|B_x| - a_{\mathrm{x}}}\right), \quad B_t^{\mathrm{x}} = \sqrt{B_y^{\mathrm{x}2} + B_z^{\mathrm{x}2}}. \tag{6.29}$$

Due to the complex nature of these eigenvectors, several alternative approaches can be used to calculate the coefficients $C^{\mathrm{L,R}}$. One alternative is to calculate the left eigenvectors and take the dot product between them and the difference vector

$$C_{(i)}^{\mathrm{x}} = \mathbf{l}_{\mathrm{x}}^{(i)} \cdot \Delta\mathbf{w}. \tag{6.30}$$

The left eigenvectors can be calculated numerically from the right eigenvectors or analytically. Another alternative is to calculate the coefficients by solving the linear system (6.14) numerically. This is our preferred method, because it works for all systems and doesn't require the calculation of the left eigenvectors, which usually involves a matrix inversion.

6.4.2.1 Degeneracies

The eigenvectors, given previously, have been specifically formulated to remain unique in the presence of degeneracies. However, in formulating the compatibility conditions, we made the assumption that the degeneracy that occurs when the normal magnetic field is zero is not present (3.102). This restores the full set of compatibility conditions (3.101). This assumption is made on the basis that any small perturbation away from this state will remove the degeneracy.

6.4.3 Special-relativistic hydrodynamics

The equations of special-relativistic hydrodynamics present a new difficulty in our formulation. The right eigenvectors of the matrix $\bar{A}_{\mathrm{x}}$ are difficult to compute, even using computer algebra. A solution exits, if one can calculate the right eigenvectors of the matrix $J = \partial \mathbf{f}(\mathbf{q})/\partial \mathbf{q}$. These eigenvectors were given in equations (3.74). We give them again for ease of reading,

$$\mathbf{r}_{\mathrm{x}}^{(-)} = \begin{pmatrix} 1 \\ h_{\mathrm{x}} W_{\mathrm{x}} \mathcal{A}_{-}^{\mathrm{x}} \lambda_{-}^{\mathrm{x}} \\ h_{\mathrm{x}} W_{\mathrm{x}} v_y^{\mathrm{x}} \\ h_{\mathrm{x}} W_{\mathrm{x}} v_z^{\mathrm{x}} \\ h_{\mathrm{x}} W_{\mathrm{x}} \mathcal{A}_{-}^{\mathrm{x}} - 1 \end{pmatrix}, \quad \mathbf{r}_{\mathrm{x}}^{(+)} = \begin{pmatrix} 1 \\ h_{\mathrm{x}} W_{\mathrm{x}} \mathcal{A}_{+}^{\mathrm{x}} \lambda_{+}^{\mathrm{x}} \\ h_{\mathrm{x}} W_{\mathrm{x}} v_y^{\mathrm{x}} \\ h_{\mathrm{x}} W_{\mathrm{x}} v_z^{\mathrm{x}} \\ h_{\mathrm{x}} W_{\mathrm{x}} \mathcal{A}_{+}^{\mathrm{x}} - 1 \end{pmatrix}, \tag{6.31}$$

where W_{x} is the Lorentz factor (2.34), h_{x} is the specific enthalpy (2.7) and $\mathcal{A}_{\pm}^{\mathrm{x}}$ is defined in equation (3.75). The right eigenvectors $\bar{\mathbf{r}}_{\mathrm{x}}$ for the variables $\bar{\mathbf{w}}_{\mathrm{x}}$ can be calculated by multiplying the eigenvectors given above by the matrix

$$\mathcal{J}_{\mathrm{x}} = \left(\frac{\partial \mathbf{q}_{\mathrm{x}}}{\partial \bar{\mathbf{w}}_{\mathrm{x}}} \right)^{-1}. \tag{6.32}$$

Therefore,

$$\bar{\mathbf{r}}_{\mathrm{x}}^{\pm} = \mathcal{J}_{\mathrm{x}} \mathbf{r}_{\mathrm{x}}^{\pm}. \tag{6.33}$$

6.4.4 Special-relativistic magnetohydrodynamics

Obtaining the right eigenvectors, derived from the interface variables $\bar{\mathbf{w}}_{\mathrm{x}}$, for the equations of special-relativistic, ideal magnetohydrodynamics proved quite difficult. The previous method of calculating the matrix $\mathcal{J}_{\mathrm{x}}$ (6.32) could not be computed using computational algebra. However, Balsara calculated a mapping from the covariant eigenvectors to the primitive right eigenvectors. This mapping can be used to transform from the eigenvectors $\tilde{\mathbf{r}}$ given by Antón et al. [14], defined in Appendix D.1, to interface eigenvectors $\bar{\mathbf{r}}$.

$$\bar{\mathbf{r}}^i_{\mathrm{x}} = \begin{pmatrix} \tilde{r}^i_{\mathrm{x}}(9) \\ -\dfrac{v^x_{\mathrm{x}}}{W_{\mathrm{x}}}\tilde{r}^i_{\mathrm{x}}(1) + \dfrac{1}{W_{\mathrm{x}}}\tilde{r}^i_{\mathrm{x}}(2) \\ -\dfrac{v^y_{\mathrm{x}}}{W_{\mathrm{x}}}\tilde{r}^i_{\mathrm{x}}(1) + \dfrac{1}{W_{\mathrm{x}}}\tilde{r}^i_{\mathrm{x}}(3) \\ -\dfrac{v^z_{\mathrm{x}}}{W_{\mathrm{x}}}\tilde{r}^i_{\mathrm{x}}(1) + \dfrac{1}{W_{\mathrm{x}}}\tilde{r}^i_{\mathrm{x}}(4) \\ b^y_{\mathrm{x}}\tilde{r}^i_{\mathrm{x}}(1) - b^0_{\mathrm{x}}\tilde{r}^i_{\mathrm{x}}(3) - W_{\mathrm{x}}v^y_{\mathrm{x}}\tilde{r}^i_{\mathrm{x}}(5) + W_{\mathrm{x}}\tilde{r}^i_{\mathrm{x}}(7) \\ b^z_{\mathrm{x}}\tilde{r}^i_{\mathrm{x}}(1) - b^0_{\mathrm{x}}\tilde{r}^i_{\mathrm{x}}(4) - W_{\mathrm{x}}v^y_{\mathrm{x}}\tilde{r}^i_{\mathrm{x}}(5) + W_{\mathrm{x}}\tilde{r}^i_{\mathrm{x}}(8) \\ \dfrac{\tilde{r}^i_{\mathrm{x}}(9)}{a^2_{\mathrm{x}}} - \dfrac{\rho^{1+\gamma_{\mathrm{x}}}_{\mathrm{x}}}{\gamma_{\mathrm{x}}p_{\mathrm{x}}}\tilde{r}^i_{\mathrm{x}}(10) \end{pmatrix}, \tag{6.34}$$

where (n) indicates the component of the covariant eigenvector and the index i indicates the eigenvector, i.e. fast, slow and Alfvén.

6.5 mRGFM Surfaces

So far, only interfaces between two fluids with the same underlying hyperbolic system have been discussed. At the surface of a neutron star, the interface will be between a fluid and vacuum or a charged fluid and a plasma. This section will give the first steps to constructing the mRGFM approach for a surface. It will consider the surface interface for a toy star between a Newtonian fluid and a vacuum in one dimension. To construct the surface, we must augment the Euler equations to include a gravitational source term. We follow the approach of Price [141] and add source terms that are proportional to the position in the domain. The source term takes the form

$$\mathbf{s} = \begin{pmatrix} 0 \\ -\rho x \\ -\rho v_x x \end{pmatrix}, \tag{6.35}$$

where x is the physical location. With this source term, the initial density and pressure profile of the star is defined as

$$\rho_0(x) = \left(1 - x^2\right), \tag{6.36a}$$

$$p_0(x) = \frac{\rho_0^(\gamma - 1)}{4(\gamma - 1)}, \tag{6.36b}$$

where $\gamma = 2$.

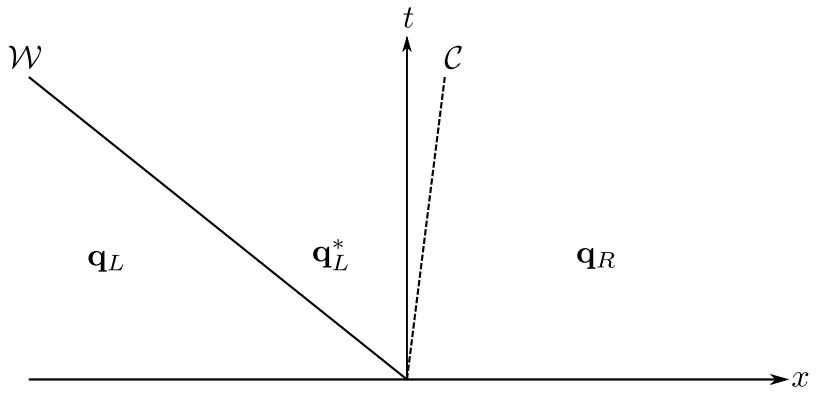

Figure 6.13 – This Riemann fan demonstrates the wave structure at a surface interface between Newtonian hydrodynamics and a vacuum state.

6.5.1 Surface jump conditions

The wave structure at the surface consists of one hydrodynamical wave and no waves on the vacuum side. Figure 6.13 demonstrates this structure. Following the mRGFM approach, there can only be one compatibility condition at the surface. Physically at the surface with vacuum, the pressure and density must go to zero. However, that implies two conditions. Therefore, the current interface variables $\bar{\mathbf{w}} = [p, v^x, \rho]^T$ are unsuitable. We can, however, use the property that the fluid is barotropic and replace the density with the specific entropy, which is finite at the surface. The specific entropy is defined as

$$K = \frac{p}{\rho^\gamma}. \tag{6.37}$$

Using the new set of interface variables $\bar{\mathbf{w}} = [p, v^x, K]^T$, the coefficient and right eigenvector are now

$$C_{\mathrm{L}} = \frac{p^{\frac{\gamma-1}{2\gamma}} K^{\frac{1}{2\gamma}}}{\sqrt{\gamma}}, \quad \bar{\mathbf{r}} = \left[-p^{\frac{1+\gamma}{2\gamma}} \sqrt{\gamma} K^{\frac{-1}{2\gamma}}, 1, 0 \right]^{\mathrm{T}}. \tag{6.38}$$

To prevent numerical problems arising with negative or extremely small values, we set a pressure floor of 1.0×10^{-30}. All the other variables can be determined from this floor and the velocity. This floor is significantly lower than the atmospheres currently used in numerical simulations [47, 141].

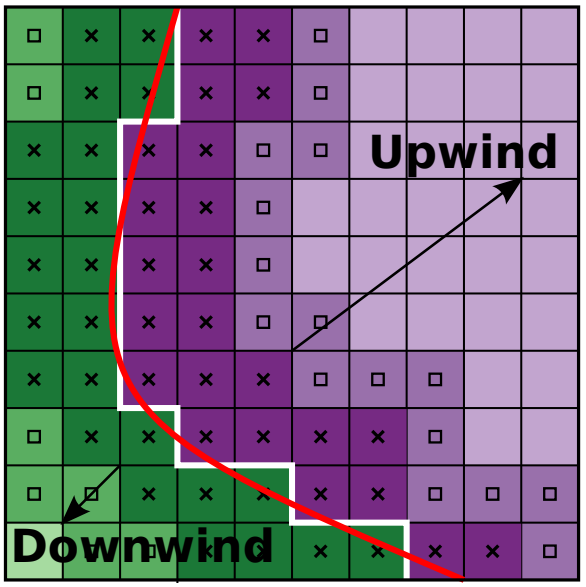

Figure 6.14 – The fast marching method works by marching away from the interface in an upwind or downwind direction. The points in the heap are those with squares. The accepted points have crosses. It is from these points the heap points are updated by extrapolation.

6.6 Fast Marching Method

Two different situations exist, where we wish to extrapolate data away from the interface, the extrapolation of *ghost* cells away from the interface and the reinitialisation of the level set. To perform both of these tasks we use the fast marching method [124, 156]. The main idea behind the fast marching method is to construct the data using only upwind or downwind values. From the band of points around the zero level set, one can construct all the *ghost* and positive level set points using only upwind points and all the negative level set points using downwind points. The algorithm works by firstly locating all the interface points. The data points are not updated. Next, all the points that neighbour an interface point are added to a heap. These points are ordered in the heap based on their distance from the zero contour. They are then updated by an extrapolation from their neighbours that have already been updated. Once a point is updated, the next point is added to the heap. Figure 6.14 shows the basic idea behind the fast marching method. The fast marching method works by marching away from the interface in an upwind or downwind direction. The points in the heap are those with squares. The accepted points have crosses. It is from these points the heap points are updated by extrapolation. The heap approach is an efficient method of updating points in order of distance away from the interface [124, 156].

6.7 Level Set Numerical Methods

The section discusses the numerical methods required to evolve the level set forward in time. The advection equation for the level set function (6.6) is a specific example of a more general class of equations, the Hamilton-Jacobi equations [124]. A Hamilton-Jacobi equation has the general form

$$\frac{\partial \phi}{\partial t} + H(\nabla \phi) = 0. \tag{6.39}$$

The level set Hamiltonian is

$$H(\nabla \phi) = v^i \frac{\partial \phi}{\partial x^i}. \tag{6.40}$$

Many techniques have been developed to solve Hamilton-Jacobi equations; we will use a Lax-Friedrich approach that is described in [124]. The evolution equation can be written as a set of ODEs so that we can use standard Runge-Kutta methods to integrate the equations. The Hamiltonian for the level set can be given by the approximation

$$H(\nabla \phi) = \hat{H}\left(\phi_x^-, \phi_x^+, \phi_y^-, \phi_y^+, \phi_z^-, \phi_z^+\right), \tag{6.41}$$

where $\phi_i^{\pm}$ is an approximation to the upwind and downwind derivatives in the i-direction. For the Lax-Friedrich scheme, we have implemented this Hamiltonian for each level-set

$$\begin{aligned} \hat{H} = H &\left[\frac{1}{2}\left(\phi_x^- + \phi_x^+\right), \frac{1}{2}\left(\phi_y^- + \phi_y^+\right), \frac{1}{2}\left(\phi_z^- + \phi_z^+\right)\right] \\ &- \hat{\alpha}^x \left[\frac{1}{2}\left(\phi_x^+ - \phi_x^-\right)\right] - \hat{\alpha}^y \left[\frac{1}{2}\left(\phi_y^+ - \phi_y^-\right)\right] - \hat{\alpha}^z \left[\frac{1}{2}\left(\phi_z^+ - \phi_z^-\right)\right], \end{aligned} \tag{6.42}$$

where $\hat{\alpha}^i$ are dissipation coefficients. For the advection equation, these have the simple form

$$\hat{\alpha}^i = |v^i|. \tag{6.43}$$

To determine the upwind and downwind derivatives, we use the WENO scheme for derivatives given by Shu [162].

6.8 Summary

In this chapter, we have presented the algorithm one should follow, when applying a ghost fluid method for neutron star interfaces. This method is based on the work of Sambasivan and Udaykumar [152] and Losasso et al. [106]. This is a general procedure that can use any approximate solver for the multi-material Riemann problem.

We have presented three different approximate solvers to the interface Riemann problem. One of those is the new mRGFM that has many advantages over the other two. It is a general method that can approximate the solution to the multi-material Riemann problem for any two systems of hyperbolic conservation laws that match its criteria. It is also consistent and robust in the presence of strong shocks.

We are now in the position to validate our numerical methods against standard tests. This will be done in the next chapter.

Chapter 7

Multi-model Results

We have now reached the point in this thesis where we can combine all of the different numerical methods. This will allow us to demonstrate our extension to the framework of Millmore and Hawke [114]. As before, we will use standard tests from the literature to validate our numerical methods. However, this chapter will be more focused on two-dimensional results.

Firstly in Subsection 7.1.1, we will consider a one-dimensional shock tube test that contains a helium slab and two interfaces. Secondly in Subsection 7.1.2, we present a test that demonstrates the failure of the original Ghost Fluid Method of Fedkiw et al. [55] to correctly capture the location of the shock wave. This test was developed by Hu and Khoo [84]. Thirdly in Subsection 7.1.3, we validate the mRGFM's ability to combine two different systems by simulating a star's surface. Using the toy star described by Price [141], we show that our method produces a stable surface by considering the maximum absolute velocity at each time step. These results also show that the crossing time of a wave in our toy star is close to the predicted result.

Finally, we will give a series of results depicting a "helium" bubble in a two-dimensional shock tube. We present results for Newtonian hydrodynamics, ideal magnetohydrodynamics and special-relativistic, ideal magnetohydrodynamics. The first special-relativistic bubble tests were performed by Millmore [113].

The Newtonian test in Subsection 7.2.1, once again, demonstrates the benefit of the mRGFM over the oGFM. We also examine the effectiveness of the captured boundary approach's ability to deal with a large topology change in Subsection 7.2.2.

For the magnetohydrodynamical tests in Subsection 7.2.3, we present the first demonstration of the Ghost Fluid approach with a magnetic field in two dimensions. Using different magnetic field strengths, we simulate a bubble test with a Mach 1.22 shock wave. The results show that the vorticity is no longer tied to the surface of the bubble as in the hydrodynamical case. The vorticity can be propagated away; this will have interesting effects on the dynamics in a neutron star. Last of all in Subsection 7.2.4, we give results for special-relativistic, ideal magnetohydrodynamics. A detailed analysis of the dynamics will be presented. Again, this is the first time such a result has been discussed.

7.1 One-dimensional Tests

Starting in one dimension, we will consider the slab test of Wang et al. [182], the strong shock test of Hu and Khoo [84] and the toy star of Price [141]

7.1.1 Helium slab test

The slab test is a one-dimensional shock tube with a helium slab located at $-0.1 \leq x \leq 0.1$ with air either side. The test domain is $-0.5 \leq x \leq 0.5$. At the left boundary, a shock wave is located at $x = -0.25$. The helium slab is an ideal fluid with $\gamma = 5/3$. The air is also an ideal fluid with $\gamma = 1.4$. The initial data is given in Table 7.1. This test was developed by Wang et al. [182].

Test name: Wang helium slab						
Domain	ρ	v^x	v^y	v^z	p	γ
$x \in [-0.5, -0.25]$	1.3765	0.3948	0	0	1.57	1.4
$x \in [-0.25, 0.1]$	1	0	0	0	1	1.4
$x \in [-0.1, 0.1]$	0.138	0	0	0	1	5/3
$x \in [0.1, 0.5]$	1	0	0	0	1	1.4
Total time: 0.3					level set: $\phi(x) = \lvert x \rvert - 0.1$	

Table 7.1 – The initial conditions for the Wang helium slab test [182].

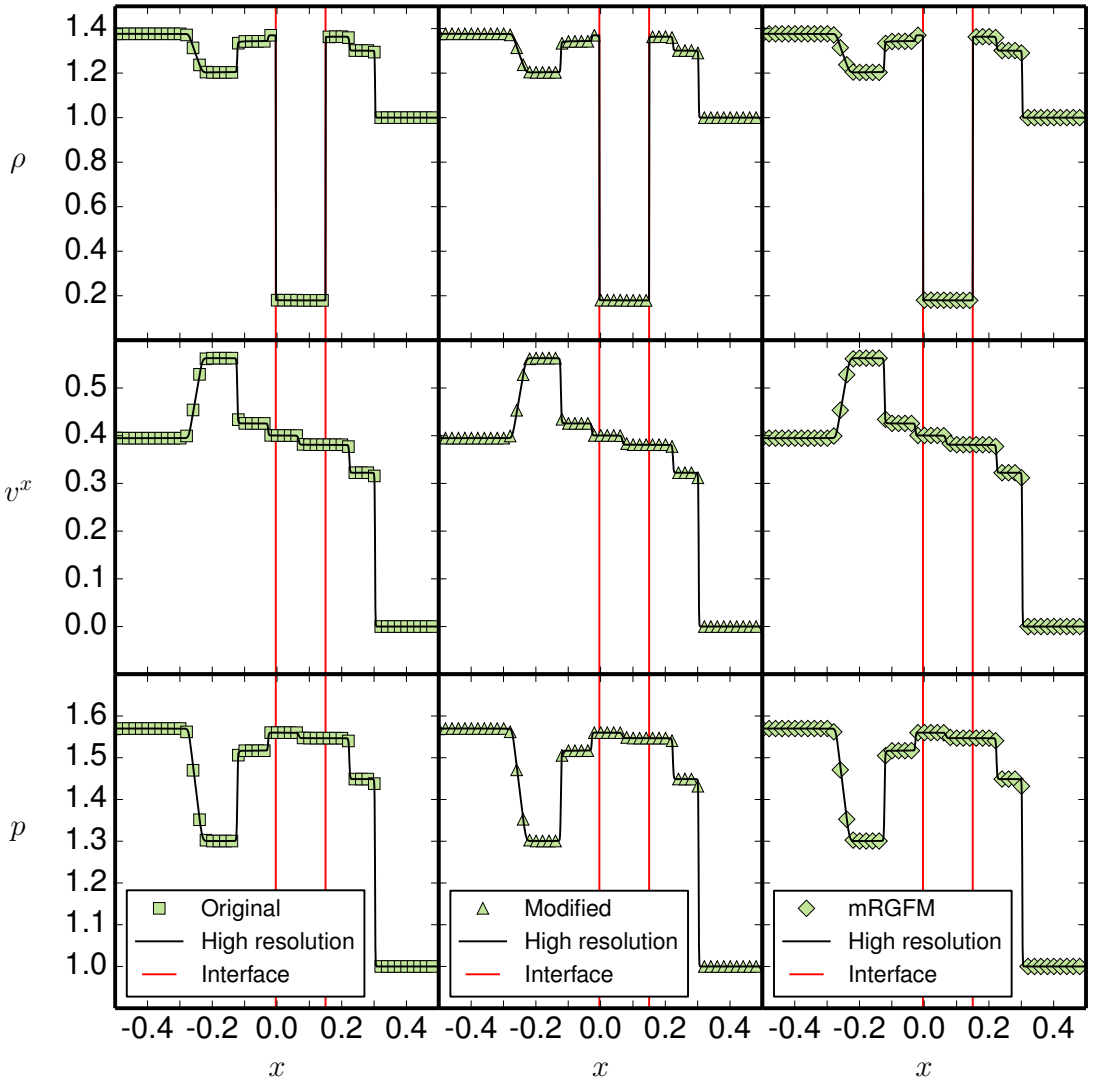

Figure 7.1 – The results for the Wang test plotted against a high-resolution solution for 800 points. The density, velocity and pressure are shown. All three Ghost Fluid Methods accurately capture the location of the interfaces and the other waves.

The results for this test are shown in the Figure 7.1. The density, normal velocity and pressure are plotted for 800 points. The approximate solutions are plotted against a high-resolution solution with only 50 points used for clarity. It is observed that all three approximate solutions obtained from the GFMs agree with the high-resolution solution.

These results show that our numerical methods can accurately approximate the solution to a multi-model shock tube problem in one dimension for weak shocks.

7.1.2 Strong shock test

Part of the motivation for deriving the Roe approximation in Chapter 6 was that the oGFM did not capture the location of a strong shock wave after it had interacted with an interface. This was shown to be true by Liu et al. [102]. We will now compare the performance of the oGFM, the mGFM and the mRGFM in the presence of a strong shock. The test we will use is test 2A of Hu and Khoo [84]. The initial data is given in Table 7.2 and is defined on the domain $-0.5 \leq x \leq 1.0$, with the Riemann problem located at $x = 0$. The material on the left is helium with $\gamma = 5/3$ and the material on the right is air with $\gamma = 1.4$.

Test name: Strong shock test						
Domain	ρ	v^x	v^y	v^z	p	γ
$x \in [0.0, 0.5]$	3.984	27.355	0	0	1000	5/3
$x \in [0.5, 1.0]$	0.01	0	0	0	1.0	1.4
Total time: 0.01			level set: $\phi(x) = x$			

Table 7.2 – The initial data for Hu and Khoo test 2A [84].

The results of this test are shown for 300 points in Figure 7.2 and 800 points in Figure 7.3. Figure 7.2 demonstrates that all three methods approximate the exact solution well. However, only the mRGFM correctly captures the location of all three waves. This is especially evident in the capturing of the shock wave in the velocity plot. Figure 7.3 focuses on the region of the contact and the shock wave. It clearly shows that the oGFM and mGFM do not capture the location of the shock illustrated by the yellow squares and blue triangles in the region $0.7 \leq x \leq 0.75$. They also struggle to correctly capture the contact wave. The mRGFM, on the other hand, shows improvement and manages to correctly capture the shock and contact locations.

7.1.3 Toy star vacuum surface

In Section 6.5, we discussed the coupling of Newtonian hydrodynamics to a pure vacuum state via the mRGFM. Here, we present our results for the toy star test based on the work of Price [141]. The initial conditions for this test are given in Table 7.3. The test is defined on a domain $0 \leq x \leq 1.2$ with the surface located at $x = 1$. The boundary at $x = 0$ has reflection boundary conditions. The fluid is an ideal fluid with $\gamma = 2$.

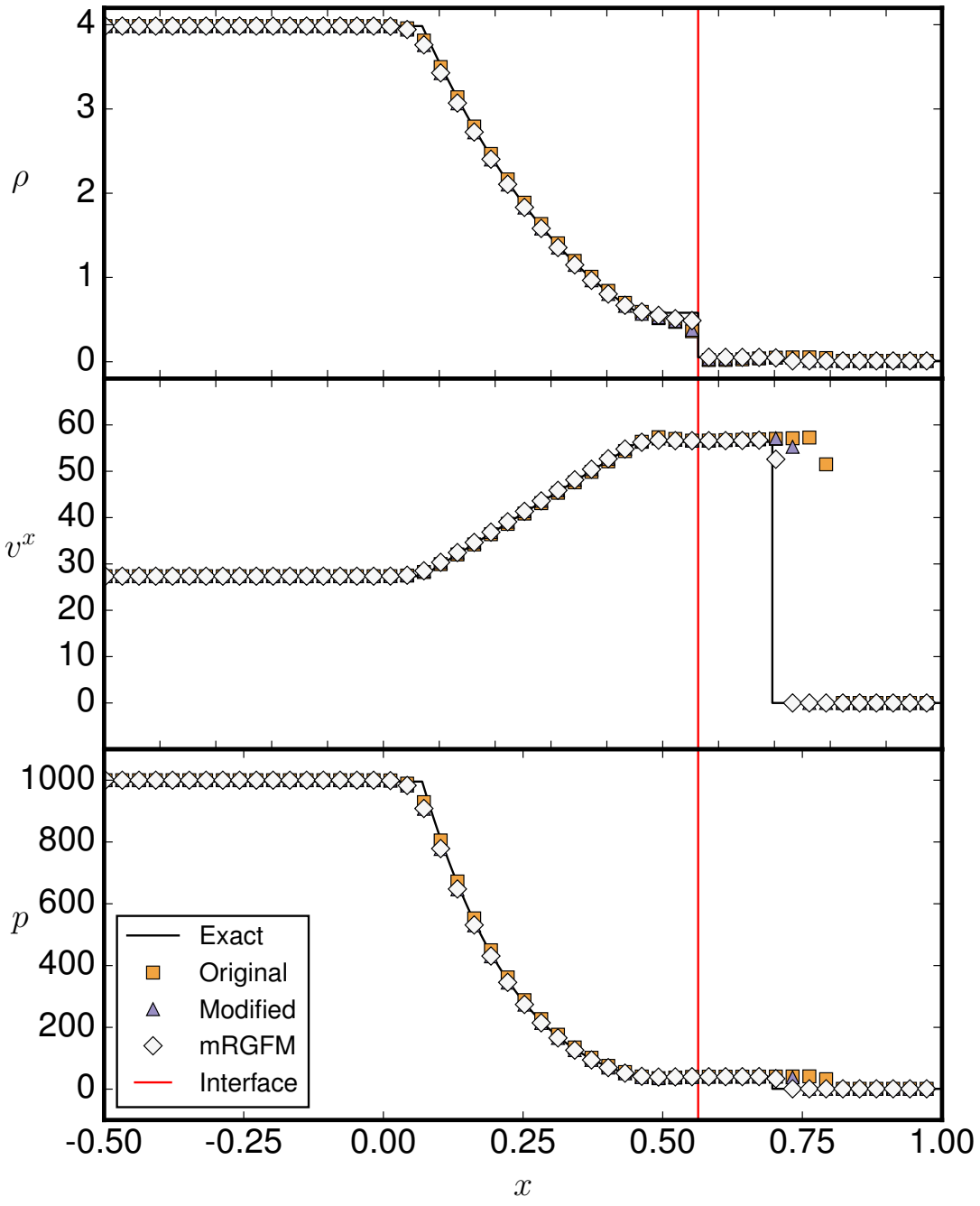

Figure 7.2 – Density, velocity and pressure plots for the 2A test of Hu and Khoo [84]. It contains the approximate solution for the oGFM, mGFM and mRGFM and the exact solution. The results show that the oGFM and mGFM fail to correctly capture the location of the shock and contact.

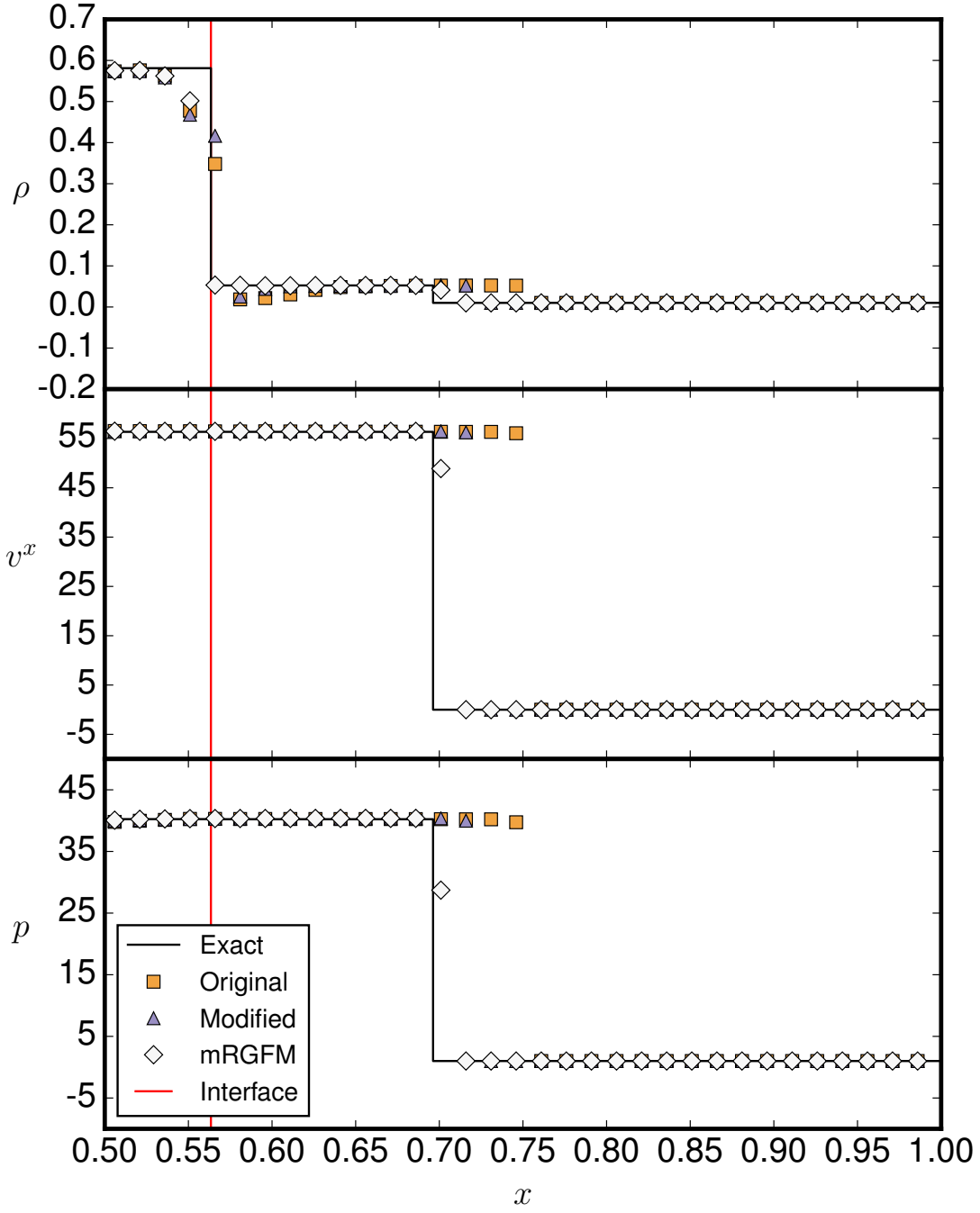

Figure 7.3 – The results for density, velocity and pressure are shown for the 2A test of Hu and Khoo [84]. This plot focuses in on the region containing the interface and the shock wave. Only the mRGFM has correctly captured the location of both waves. The mGFM shows some improvement over the oGFM.

Test name: Toy star						
	ρ	v^x	v^y	v^z	p	γ
interior	$\left(1-x^2\right)$	0	0	0	$\frac{\left(1-x^2\right)}{4}$	2
Total time: 100			level set: $\phi(x) = x - 1$			

Table 7.3 – The initial data for the toy star test. The surface of the star is located at $x = 1$ and the domain is $0 \leq x \leq 1.2$. The fluid is an ideal fluid with $\gamma = 2$.

When using the mRGFM, we employ the compatibility condition that the pressure must vanish. The coefficient and eigenvector in equation (6.38) can then be used to calculate K and v_x. However, the pressure is now zero. Therefore, we use a pressure floor of 1.0×10^{-30}. This allows us to recover a value for the density.

The initial data given above provides a static toy star. However, due to numerical errors from the evolution of the star and applying the captured boundary approach, the star begins to oscillate. The results in Figure 7.4 show that the maximum absolute value of the normal velocity decreases over time. It also demonstrates that this approach is stable and can be evolved for a long period of time. The results were sampled at intervals of $T = 0.1$.

The large spikes in the normal velocity in Figure 7.4 occur when the oscillation reaches the surface. The speed of sound is $a = \sqrt{(1-x^2)/8}$. The characteristic crossing time can be calculated by the following equation

$$\tau = \int_0^1 a^{-1} \, \mathrm{d}x. \tag{7.1}$$

The characteristic crossing time for an oscillation is $\tau = 4.44$. The spikes in the maximum velocity occur with a period of $T \approx 4.8$. The error is approximately 9%, which could be due to the rate of sampling and the discretisation of the domain.

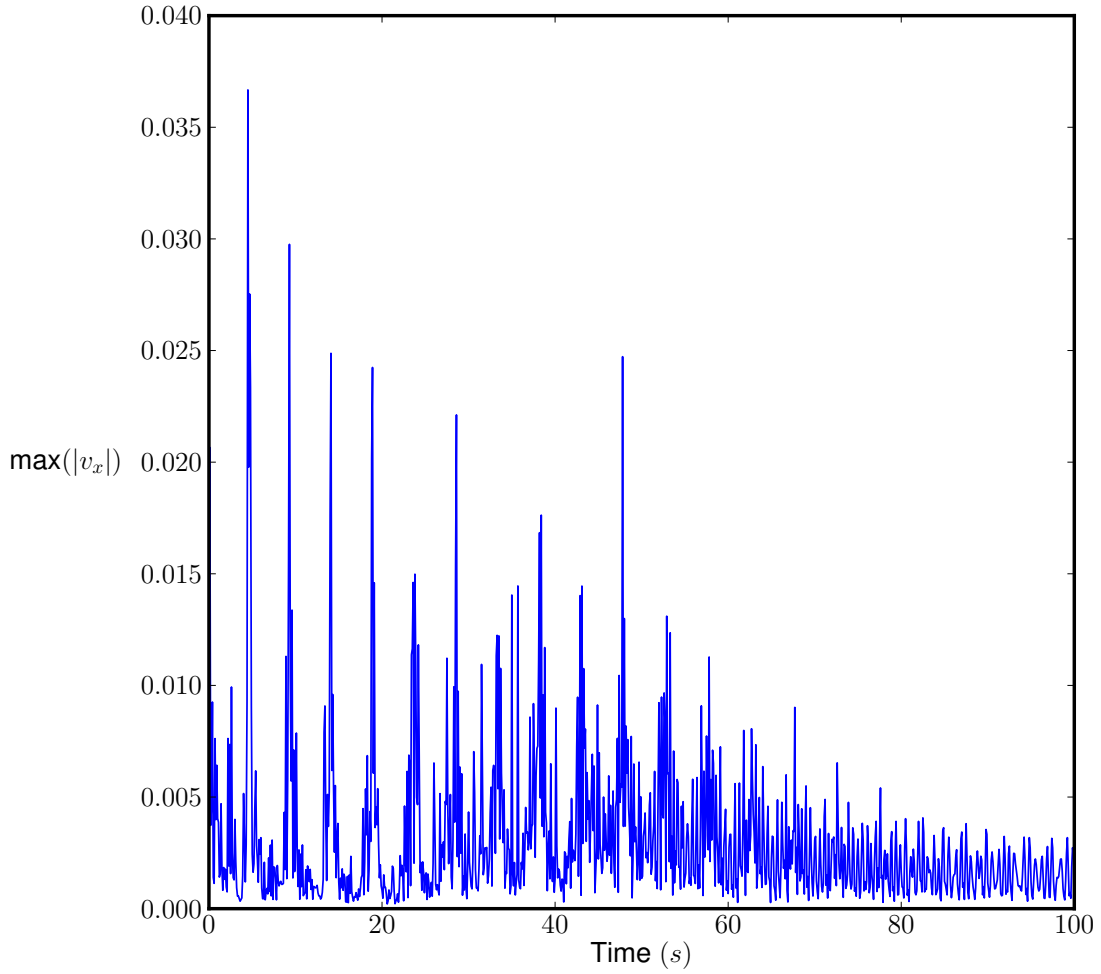

Figure 7.4 – The maximum absolute value of the normal velocity decreases over time. The results were sampled at intervals of $T = 0.1$.

7.2 Two-dimensional Bubble Tests

In two dimensions, we have focused on bubble tests for several reasons. Primarily, the topology of the bubble changes significantly with pinching and break up occurring. Therefore, these tests form a strong test for the robustness of our numerical methods. These tests have also been performed experimentally and our results can be compared both to published numerical simulations and experimental data. The first numerical tests where performed by Hu and Khoo [84]. Their test was based on the experiment of Bourne and Field [31]. Other experimental results have been obtained by Haas and Sturtevant [73]. Finally, there are lots of simulations being performed in this area forming a useful source of information. It should be noted that the bubble test is symmetric about the $y = 0$ line. Any deviation away from symmetry is due to numerical error.

Figure 7.5 – This figure is taken from the paper by Haas and Sturtevant [73]. It shows a helium bubble after a 1.22 Mach shock has passed through. The bubble is surrounded by air at normal atmospheric pressure.

7.2.1 Newtonian hydrodynamics Mach 1.22 bubble test

For the first bubble test, we will use the initial data of Hu and Khoo [84]. We have chosen this test as experimental results exist. The experiment was performed by Haas and Sturtevant [73] and their results are shown in Figure 7.5. The figure shows a helium bubble after a 1.22 Mach shock has passed through. The bubble is surrounded by air at normal atmospheric pressure. The initial data that we have used is given in Table 7.4. The test is defined on a domain $-75 \leq x \leq 325, -44.5 \leq y \leq 44.5$. The bubble's centre is located at $(175, 0)$ and it has a radius of 25. A Mach 1.22 shock wave is located at $x = 210$. The Mach number is the ratio of the velocity to the speed of sound,

$$M = \frac{v_s}{a}. \tag{7.2}$$

The test is evolved until $T = 300$. The boundary conditions at the top and bottom of the domain behave like solid walls. The left and right boundaries have outflowing boundary conditions.

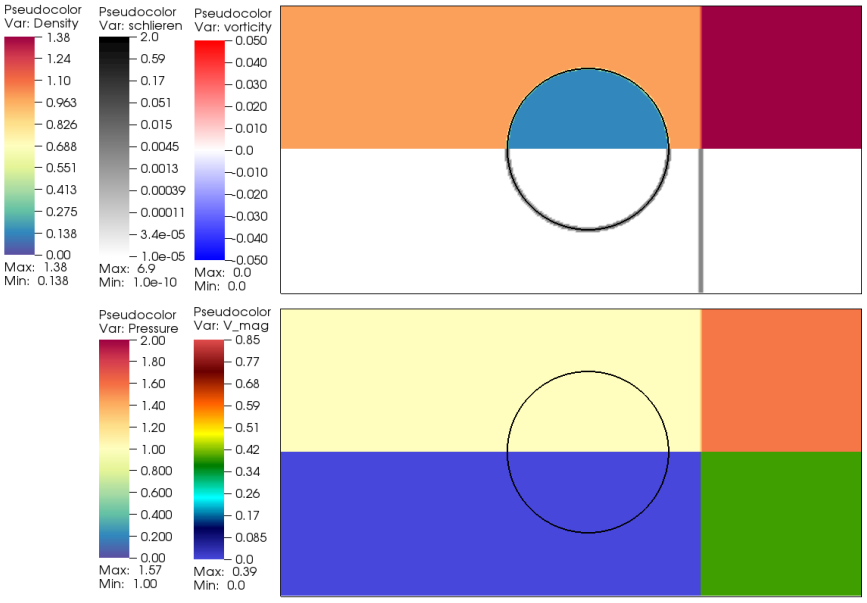

Figure 7.6 – The initial conditions for the Newtonian hydrodynamics bubble test of Hu and Khoo [84] with a Mach 1.22 shock wave. The shock wave is located to the right-hand side of the bubble. The top plot shows the pressure and the Schlieren split along the line of symmetry. The top portion is the density and the bottom portion is the Schlieren. The vorticity is plotted over the Schlieren. The bottom plot shows the pressure and the normal velocity split along the line of symmetry. The top portion shows the pressure and the bottom shows the velocity. The plots show the entire domain.

Test name: Newtonian hydrodynamics bubble Mach 1.22 shock wave						
Region	ρ	v^x	v^y	v^z	p	γ
pre-shocked air	1	0	0	0	1	1.4
post-shocked air	1.3764	-0.394	0	0	1.5698	1.4
helium bubble	0.138	0	0	0	1	5/3
Total time: 300		level set: $\phi(x,y) = 25 - \left((x-175)^2 + y^2\right)^{1/2}$				

Table 7.4 – The initial data for the Newtonian hydrodynamical bubble test. The bubble's centre is located at $(175, 0)$ and it has a radius of 25. A Mach 1.22 shock wave is located at $x = 210$ and the domain is $-100 \leq x \leq 325, -44.5 \leq y \leq 44.5$.

The initial state can be seen in Figure 7.6. The resolution for all these plots is 800×178. The top portion of the figure is split along the line of symmetry. The split separates the density and the Schlieren plots. The vorticity is plotted over the top of the Schlieren plot. However, there is zero vorticity in the initial data. The zero contour of the level set is shown as a black line.

The density is plotted with an inverted, spectral colour map with high density given by red colours. A Schlieren plot is a measure of the density gradients and is plotted with a X-ray colour map. The Schlieren are defined as

$$\mathcal{S} = |\nabla^2 \rho|, \tag{7.3}$$

where ∇^2 is the Laplace operator and the numerical factor is added so that the logarithm of the Schlieren can be taken. The vorticity is calculated from the curl of the velocity,

$$\omega_i = \epsilon_{ijk} \nabla^j v^k, \tag{7.4}$$

and we plot the z-component with a difference colour map. The bottom portion of the figure shows the pressure and the velocity magnitude, again split along the line of symmetry. The pressure is plotted with an inverted, spectral colour map and is the top portion of the bottom plot. The velocity is plotted with a hot-desaturtrated colour map and is the bottom portion of the bottom plot.

Figure 7.7 shows the density, $\mathcal{S}$, vorticity, pressure and velocity magnitude at $T = 10$. The shock wave has propagated to the left and has interacted with the bubble's surface. It has been transmitted through the surface and is travelling faster within the lower density helium bubble. It has also been reflected by the bubble's surface and a right propagating rarefaction wave has formed, seen as the lighter pressure region near the interface. Additionally, vorticity has formed at the surface of the bubble behind the shock wave.

In Figure 7.8 at $T = 28$, the shock wave has exited the bubble and continued to propagate to the left. It has also reflected off the front of the bubble and a wave has started propagating to the right. This wave is most clearly seen in the velocity magnitude. The part of the shock wave that remained outside and propagated in air has continued to about half way across the bubble. The high pressure region between the original shock and the first reflected wave has reached the solid boundaries. The vorticity has spread all along the surface, but it has reduced in magnitude.

The results in Figure 7.9 at $T = 70$ show that the waves reflected off the solid boundaries have interacted with the bubble. This has produced vorticity at the surface, which has resulted in the surface of the bubble curling up. A region of high-velocity magnitude has developed behind the bubble, while the top and bottom of the bubble are almost stationary.

In Figure 7.10 at $T = 100$, the waves that reflected off the solid boundaries have crossed each other and are now propagating to the opposite boundary. The surface of the bubble has continued to curl up; the vorticity has increased from the previous plot, Figure 7.9. Local regions of high vorticity magnitude are forming on the inside surface of the "lobe" structures. This is distorting the surface.

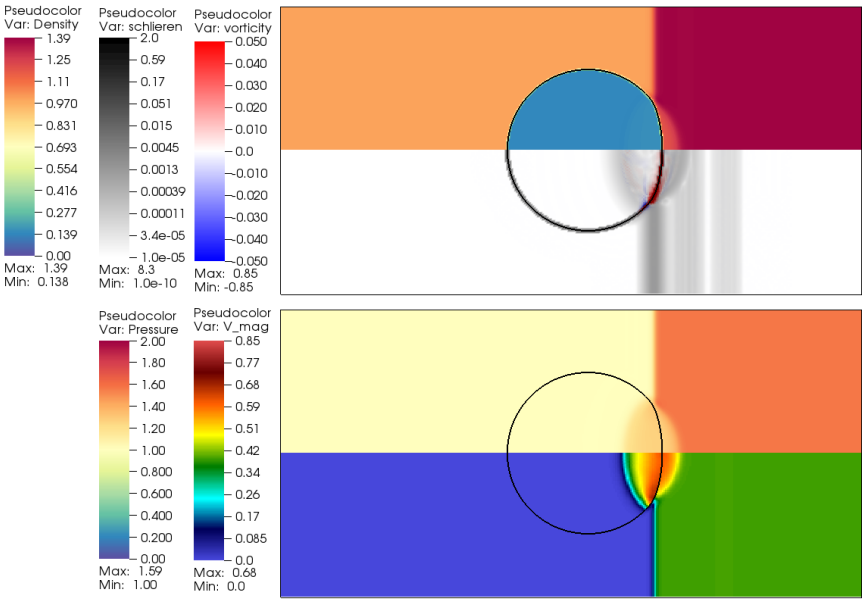

Figure 7.7 – mRGFM at $T = 10$. The shock wave has propagated to the left and has interacted with the bubble's surface. It has been transmitted through the surface and is travelling faster within the lower density helium bubble. It has also been reflected by the bubble's surface and a right propagating rarefaction wave has formed, seen as the lighter pressure region near the interface. Additionally, vorticity has formed at the surface of the bubble behind the shock wave.

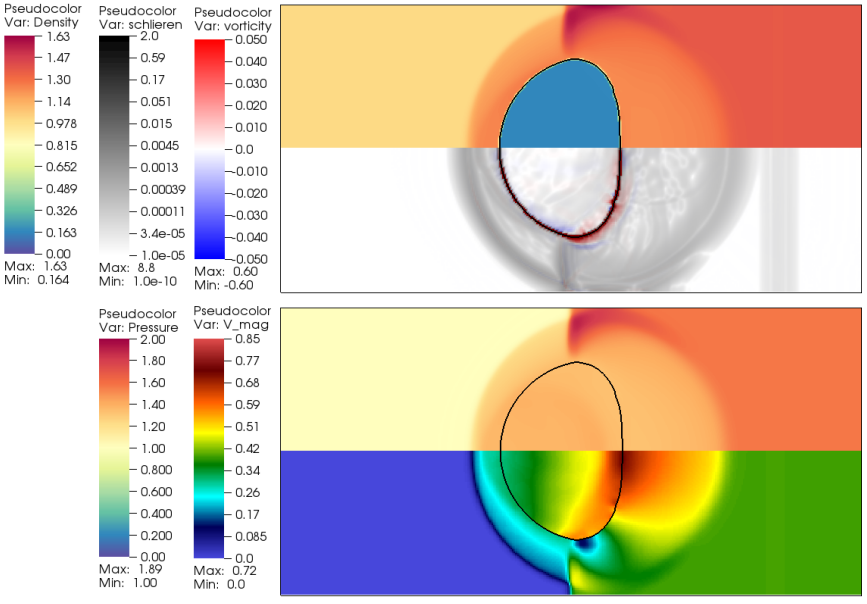

Figure 7.8 – mRGFM at $T = 28$. The shock wave has exited the bubble and continued to propagate to the left. It has also reflected off the front of the bubble and a wave has started propagating to the right. This wave is most clearly seen in the velocity magnitude. The part of the shock wave that remained outside and propagated in air has continued to about half way across the bubble. The high pressure region between the original shock and the first reflected wave has reached the solid boundaries. The vorticity has spread all along the surface, but it has reduced in magnitude.

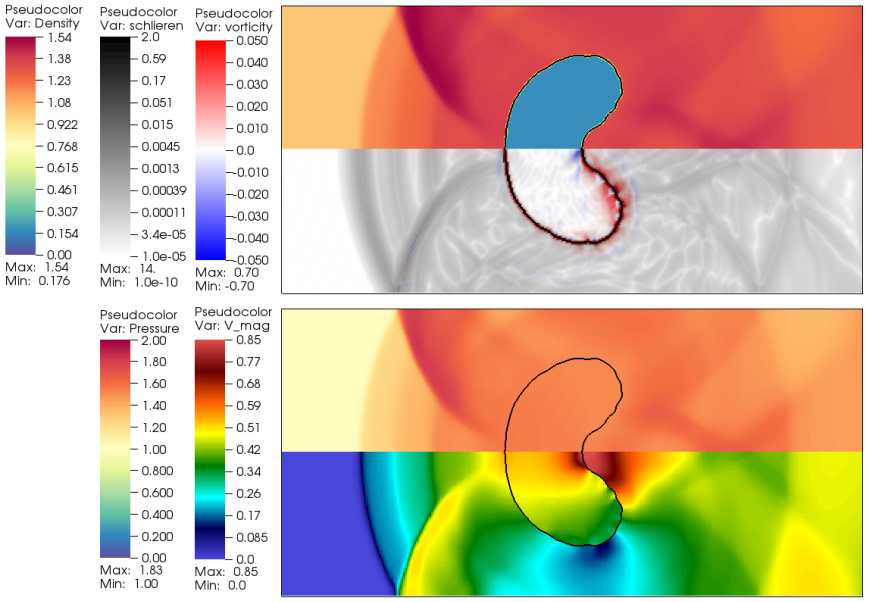

Figure 7.9 – mRGFM at $T = 70$. The waves have reflected off the solid boundaries and have interacted with the bubble. This has produced vorticity at the surface, which has resulted in the surface of the bubble curling up. A region of high velocity magnitude has developed behind the bubble while the top and bottom of the bubble are almost stationary.

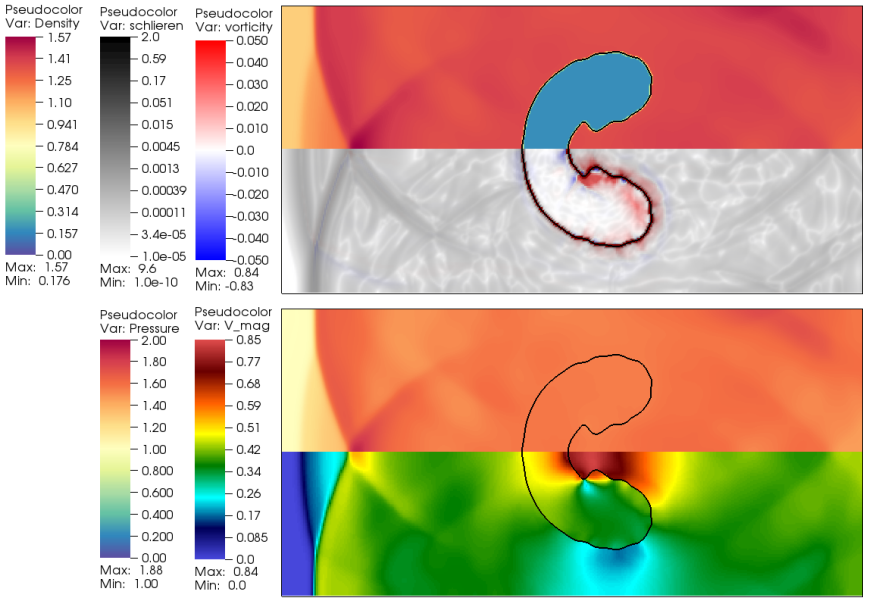

Figure 7.10 – mRGFM at $T = 100$. The waves that reflected off the solid boundaries have crossed each other and are now propagating to the opposite boundary. The surface of the bubble has continued to curl up; the vorticity has increased from the previous plot. Local regions of high vorticity magnitude are forming on the inside surface of the "lobe" structures. This is distorting the surface.

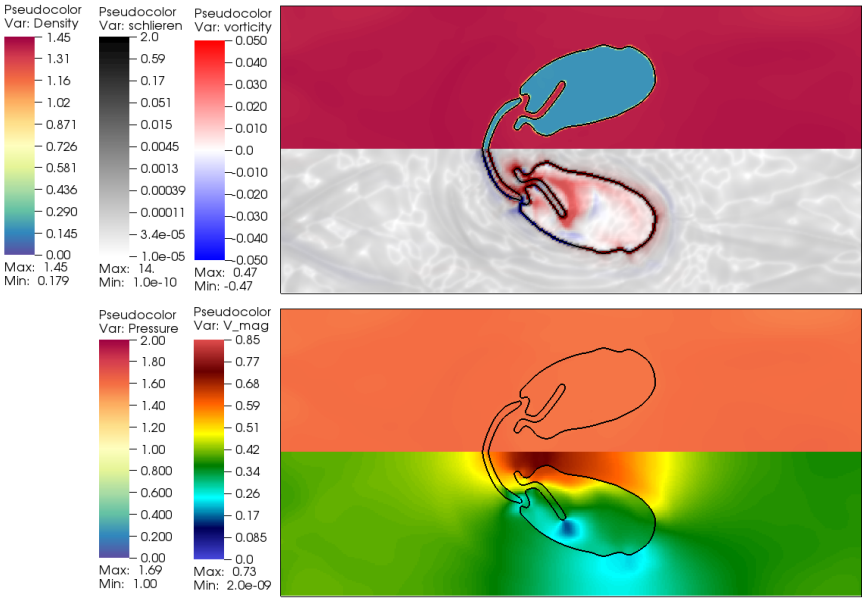

Figure 7.11 – mRGFM at $T = 180$. The bubble has broken up into three distinct pieces. Two regions of high vorticity magnitude have formed a finger-like regions. All the strong waves have propagated away from the bubble or cancelled each other out.

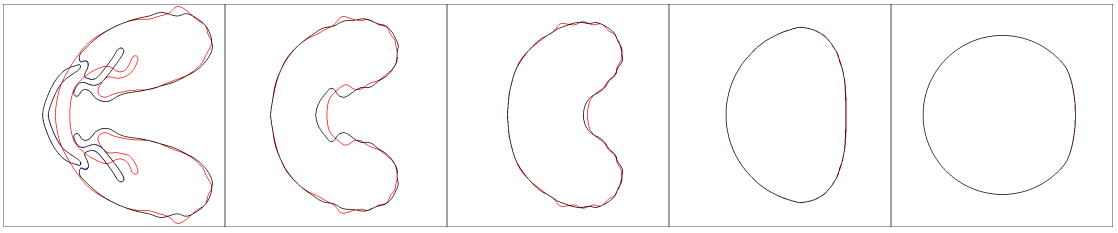

Figure 7.12 – This figure compares the mRGFM results with those obtained using the oGFM and mGFM by comparing their respective interface locations at each time. The mRGFM level set contour is black, the mGFM's is blue and the oGFM's is red. The mRGFM and mGFM produced such similar results that any difference cannot be distinguished by eye. However, the oGFM's results vary quite significantly from the results of the other two. The left most image shows that the oGFM interface has not split, while the other interfaces have.

In Figure 7.11 at $T = 180$, the bubble has broken up into three distinct pieces. Two regions of high vorticity magnitude have formed finger-like regions. All the strong waves have propagated away from the bubble or cancelled each other out.

The results presented above were all obtained using the mRGFM. Figure 7.12 compares these results with those obtained using the oGFM and mGFM by comparing their respective interface locations at each time step. The mRGFM level set contour is black, the mGFM's is blue and the oGFM's is red. The mRGFM and mGFM produced such similar results that any difference cannot be distinguished by eye. However, the oGFM's results vary quite significantly from the results of the other two. The left most image shows that the oGFM interface has not split, while the other interfaces have.

The results presented in this subsection agree with those presented by Hu and Khoo [84]. However, they are not exactly the same due to use of different numerical methods. We have used the higher-order WENO reconstruction. Our results also agree with those produced by Haas and Sturtevant [73].

7.2.2 Newtonian hydrodynamics Mach 40 bubble test

To demonstrate the capability of our numerical methods to deal with strong shocks, we will consider Mach 40 shock wave impacting on a helium bubble. This test has been chosen because this strong shock disrupts the interface significantly. Therefore, our methods must be robust enough to enable stable evolution. The initial data that we have used for the mRGFM is given in Table 7.5.

The test is defined on a domain $0 \leq x \leq 300, -45 \leq y \leq 45$. The bubble's centre is located at $(250, 0)$ and it has a radius of 25. A Mach 40 shock wave is located at $x = 280$. The Mach number is the ratio of the shock velocity to the speed of sound. The boundary conditions at the top and bottom of the domain behave like solid walls. The left and right boundaries have outflow boundary conditions and the test is run for $T = 5$. The resolution is 1200 x 360.

Test name: Newtonian hydrodynamics bubble Mach 40 shock wave						
Region	ρ	v^x	v^y	v^z	p	γ
pre-shocked air	1	0	0	0	1	1.4
post-shocked air	5.98130841	-39.4158816	0	0	1866.5	1.4
helium bubble	0.138	0	0	0	1	5/3
Total time: 5	level set: $\phi(x, y) = 25 - \left((x - 250)^2 + y^2\right)^{1/2}$					

Table 7.5 – The initial data for the Newtonian hydro bubble test. The bubble's centre is located at $(250, 0)$ and it has a radius of 25 . A Mach 40 shock wave is located at $x = 280$ and the domain is $-0 \leq x \leq 300, -45 \leq y \leq 45$

The initial state is similar to Figure 7.6. However, the maximum values have changed.

Figure 7.13 shows that the shock wave has already exited the bubble after $T = 1$. The strength of the shock wave has resulted in a large build up of density ahead of the bubble. The bubble has also been severely flattened. Features seen in the lower resolution run, given in Figure E.1, are more distinct, such as, the indent in the tails.

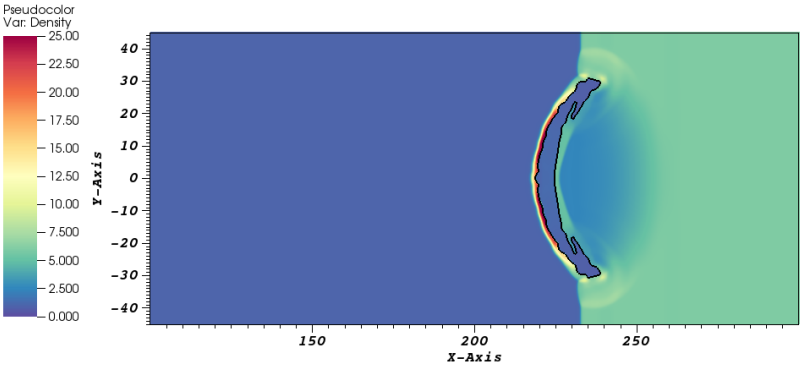

Figure 7.13 – The shock wave has already exited the bubble at $T = 1$. The strength of the shock wave has resulted in a large build up of density ahead of the bubble.

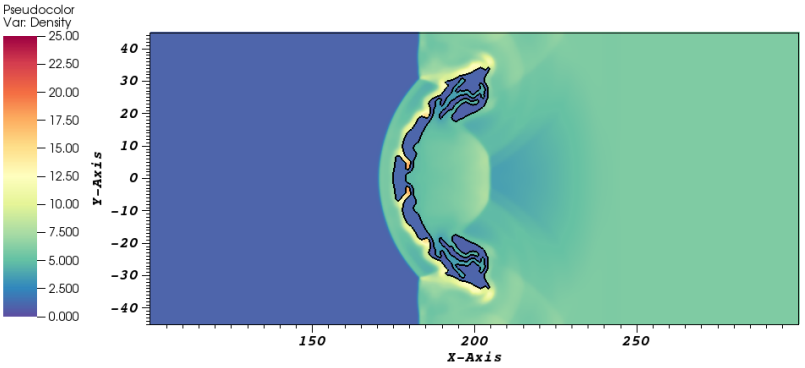

Figure 7.14 – mRGFM at $t = 2$. The bubble's surface has become distorted. The results are symmetric, which demonstrates that our numerical methods are symmetric.

In Figure 7.14 the bubble's surface has become distorted. It should be noted that the results are symmetric about the $y = 0$ line. This demonstrates that our numerical methods are symmetric. In comparison to Figure E.2, the distortion of the bubble's interface is much more intricate but still similar.

Figure 7.15 shows that the bubble's surface has continued to curl up and become distorted. Finger-like regions have developed and regions have separated off. As explained in Subsection 6.2.1, our numerical method will begin to rely on a fallback mechanism, due to a lack of resolution. These fallbacks ensure that two different models are always used in the multi-material Riemann problem. Numerical errors introduced by these fallback mechanisms could be prevented by using adaptive mesh refinement. In comparison to Figure E.3, the distortion of the bubble's interface is much larger. The lower resolution figure shows no separation.

In the final plot, shown in Figure 7.16, the bubble has continued to break up. The bubble is still symmetric which has been lost in Figure E.4.

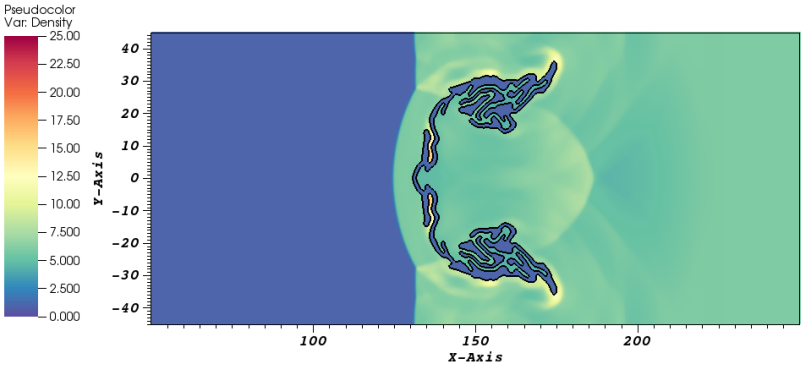

Figure 7.15 – mRGFM at $T = 3$. The bubble's surface has continued to curl up and become distorted. Finger-like regions have developed. As explained in Subsection 6.2.1, our numerical method will begin to rely on fallback mechanisms, due to a lack of resolution.

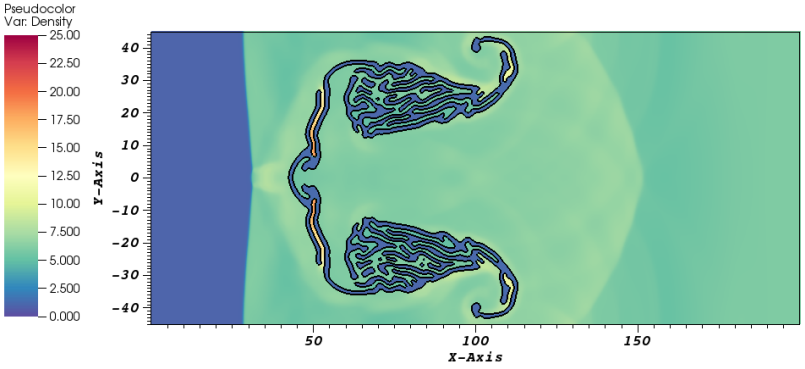

Figure 7.16 – mRGFM at $T = 5$. The bubble has continued to break up. However, the results are still symmetric

7.2.3 Vorticity propagation

We now turn our attention to bubble tests with charged fluids and different magnetic field strengths in the presence of a 1.22 Mach shock. The magnetic field is aligned along the x-axis going left to right. The initial conditions for these tests are given in Table 7.6. The domain is defined as $0 \leq x \leq 220, -50 \leq y \leq 50$ with the shock located at $x = 210$. The resolution in these tests are 220×100. Final time is $T = 180$.

Test name: Ideal magnetohydrodynamics bubble test								
Region	ρ	v^x	v^y	v^z	p	B^y	B^z	γ
pre-shocked air	1	0	0	0	1	0	0	1.4
post-shocked air	1.3764	-0.394	0	0	1.5698	0	0	1.4
helium bubble	0.138	0	0	0	1	0	0	5/3
Total time: 180	level set: $\phi(x,y) = 25 - \left((x-175)^2 + y^2\right)^{1/2}$					$B^x = -\sqrt{2/\beta_{\rm m}}$		

Table 7.6 – The initial data for the Newtonian magnetohydrodynamics bubble test with $\beta_{\rm m} = [1000, 100, 10, 1, 0.1]$. The bubble's centre is located at $(150, 0)$ and it has a radius of 25. A Mach 1.22 shock wave is located at $x = 210$ and the domain is $0 \leq x \leq 220, -50 \leq y \leq 50$.

We have performed five different tests with a varying plasma beta parameter, $\beta_{\rm m}$, defined in equation (2.40). The values of the parameter are $\beta_{\rm m} = [1000, 100, 10, 1, 0.1]$. We have taken samples every $T = 15$ and plotted them in Figure 7.17. The left column is hydrodynamically dominated with $\beta_{\rm m} = 1000$. The columns then vary by powers of ten down to $\beta_{\rm m} = 0.1$. The samples show the density in the top and the vorticity below. The key result from these tests is that as the plasma beta parameter approaches unity, the vorticity is propagated away with a greater velocity from the bubble. The vorticity is propagated via the Alfvén waves. This means that during the merger phase of a neutron star binary system, vorticity that develops at interfaces will be propagated away. This provides a mechanism to redistribute angular momentum throughout the star; a process that is absent with a single, perfect, non-charged fluid. This will have an effect on the dynamics of the system and therefore the gravitational wave template.

7.2.4 Special-relativistic magnetohydrodynamics

This test incorporates the mRGFM with the captured boundary approach, special relativity and a magnetic field. The initial conditions for the test are given in Table 7.7. This test has a plasma beta parameter of $\beta_{\rm m} = 1000$. This means that the test is dominated by hydrodynamical interactions. The bubble's centre is located at $(150, 0)$ with a radius of 25. The Mach 1.5 shock wave is located at $x = 178$ and the domain is $0 \leq x \leq 180, -50 \leq y \leq 50$. The final time is $T = 300$. The Mach number in relativity is [89],

$$M = \frac{\dfrac{v_s}{\sqrt{1 - v_s^2}}}{\dfrac{a}{\sqrt{1 - a^2}}}. \tag{7.5}$$

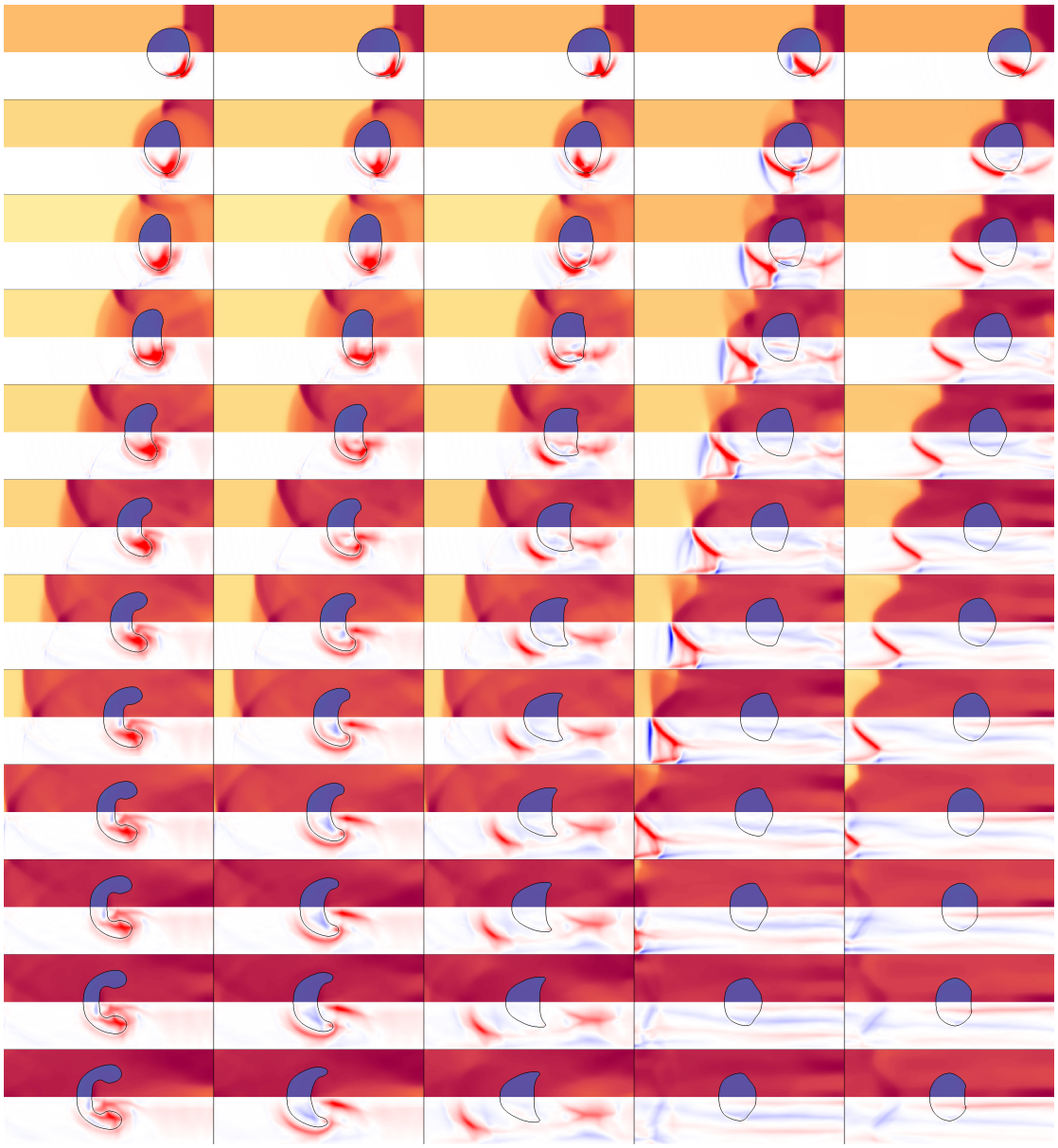

Figure 7.17 – The left column is hydrodynamically dominated with $\beta_{\mathrm{m}} = 1000$. The columns then vary by powers of ten down to $\beta_{\mathrm{m}} = 0.1$. The rows indicate different times starting at $T = 15$ and increasing in jumps of $T = 15$. The samples show the density in the top and the vorticity below. Each test uses a 1.22 Mach shock and a resolution of 220×100. The key result from these tests is that as the plasma beta parameter approaches unity, the vorticity is propagated away with a greater velocity from the bubble. The vorticity is propagated via the Alfvén waves.

Test name: Special-relativistic magnetohydrodynamics bubble $\beta_{\mathrm{m}} = 1000$								
Region	ρ	v^x	v^y	v^z	p	B^y	B^z	γ
pre-shocked air	1	0	0	0	1	0	0	1.4
post-shocked air	1.9697	-0.3759	0	0	2.6383	0	0	1.4
helium bubble	0.138	0	0	0	1	0	0	5/3
Total time: 300, level set: $\phi(x,y) = 25 - \left((x-150)^2 + y^2\right)^{1/2}$, $B^x = -0.0044$								

Table 7.7 – The initial data for the special-relativistic magnetohydrodynamics bubble test with $\beta_{\mathrm{m}} = 1000$. The bubble's centre is located at $(150, 0)$ and it has a radius of 25. A Mach 1.5 shock wave is located at $x = 178$ and the domain is $0 \leq x \leq 180, -50 \leq y \leq 50$.

The following Figures 7.18, 7.19, 7.20 and 7.21 contain ten snapshots taken at intervals of $T = 30$. The first five plots are given in the left column and the latter five in the right column.

Figure 7.18 shows the density plotted in the top half of each section with a spectral colour map. The density scale is located at the left of the picture and runs between 0.138 and 2.5. Vorticity and Schlieren are plotted in the bottom half of each section.

Figure 7.19 shows the pressure plotted in the top half of each section with a spectral colour map. The pressure scale is located to the left of the plots and runs between 1 and 4. The velocity magnitude is plotted in the bottom half of each snapshot with a hot-desaturated colour map. The velocity scale is located to the left of the pots and runs between 0 and 1.

Figure 7.20 shows the x-component of the velocity plotted in the top half of each section with a hot-desaturated colour map. The v_x-scale is located to the left of the plots and runs between -1 and 0. The bottom of each plot shows the y-component of the velocity using a difference colour map. The scale is to the left of the plots and runs between -0.2 and 0.2.

Figure 7.21 shows the x-component of the magnetic field plotted in the top half of each section with a hot-desaturated colour map. The B_x scale is located to the left of the plots and runs between -1 and 1. The bottom of each plot shows the y-component of the magnetic field using a difference colour map. The scale is to the left of the plots and runs between -0.4 and 0.4.

At time $T = 30$, the shock wave has hit the bubble and has propagated half way through. Vorticity has been produced at the bubble's surface due to the interaction with the shock.

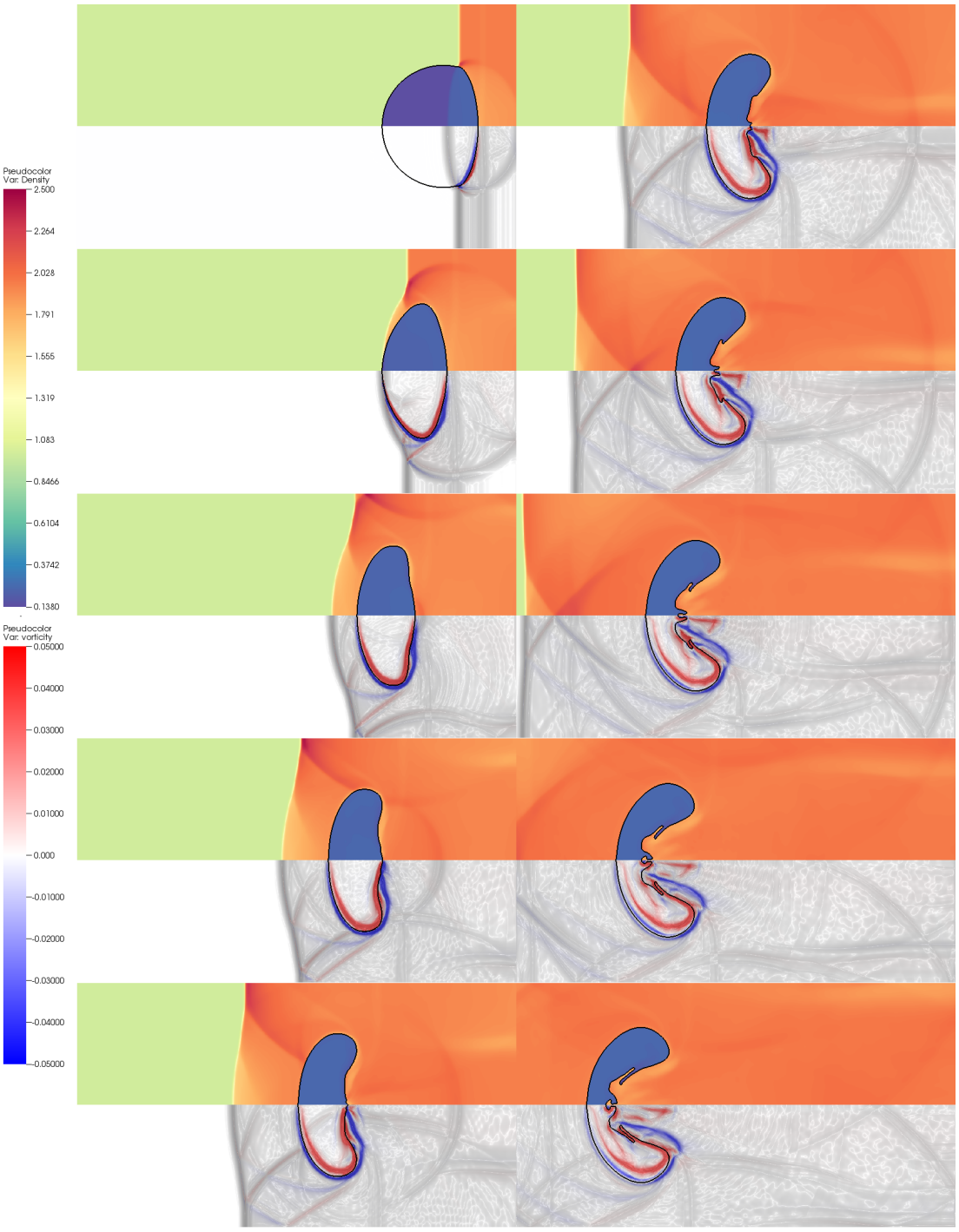

Figure 7.18 – This figure contains ten snapshots taken at intervals of $T = 30$ for the special-relativistic, ideal, magnetohydrodynamical bubble test with a 1.5 Mach shock wave. The first five are in the left column and the second five in the right column. The density is plotted in the top half of each section with a spectral colour map. The density scale is located to the left of the plots and runs between 0.138 and 2.5. Vorticity and Schlieren are plotted in the bottom half of each section.

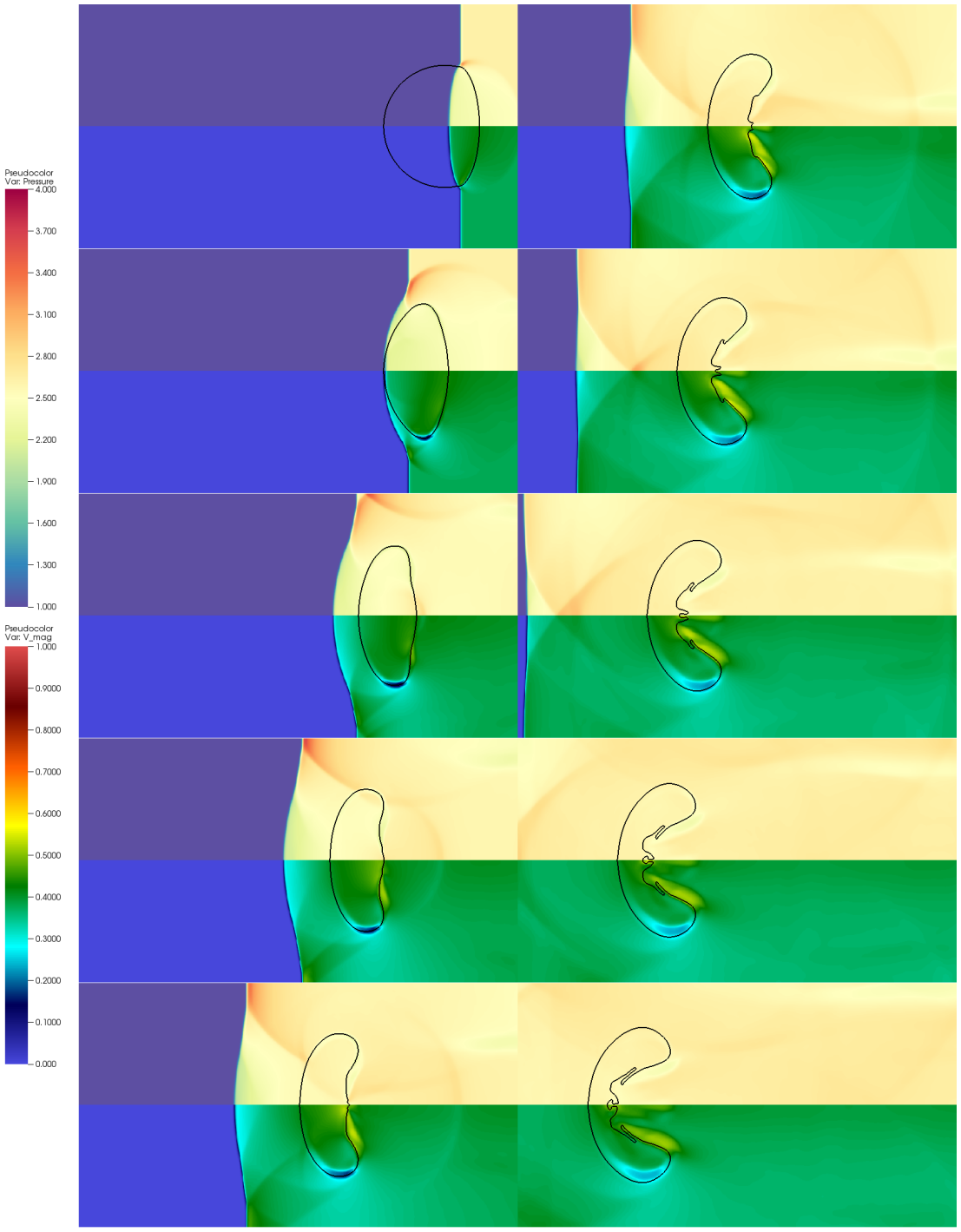

Figure 7.19 – This figure contains ten snapshots taken at intervals of $T = 30$ for the special-relativistic, ideal, magnetohydrodynamical bubble test. The first five are in the left column and the second five in the right column. The pressure is plotted in the top half of each section with a spectral colour map. The pressure scale is located to the left of the plots and runs between 1 and 4. The velocity magnitude is plotted in the bottom half of each snapshot with a hot-desaturated colour map. The velocity scale is located to the left of the plots and runs between 0 and 1.

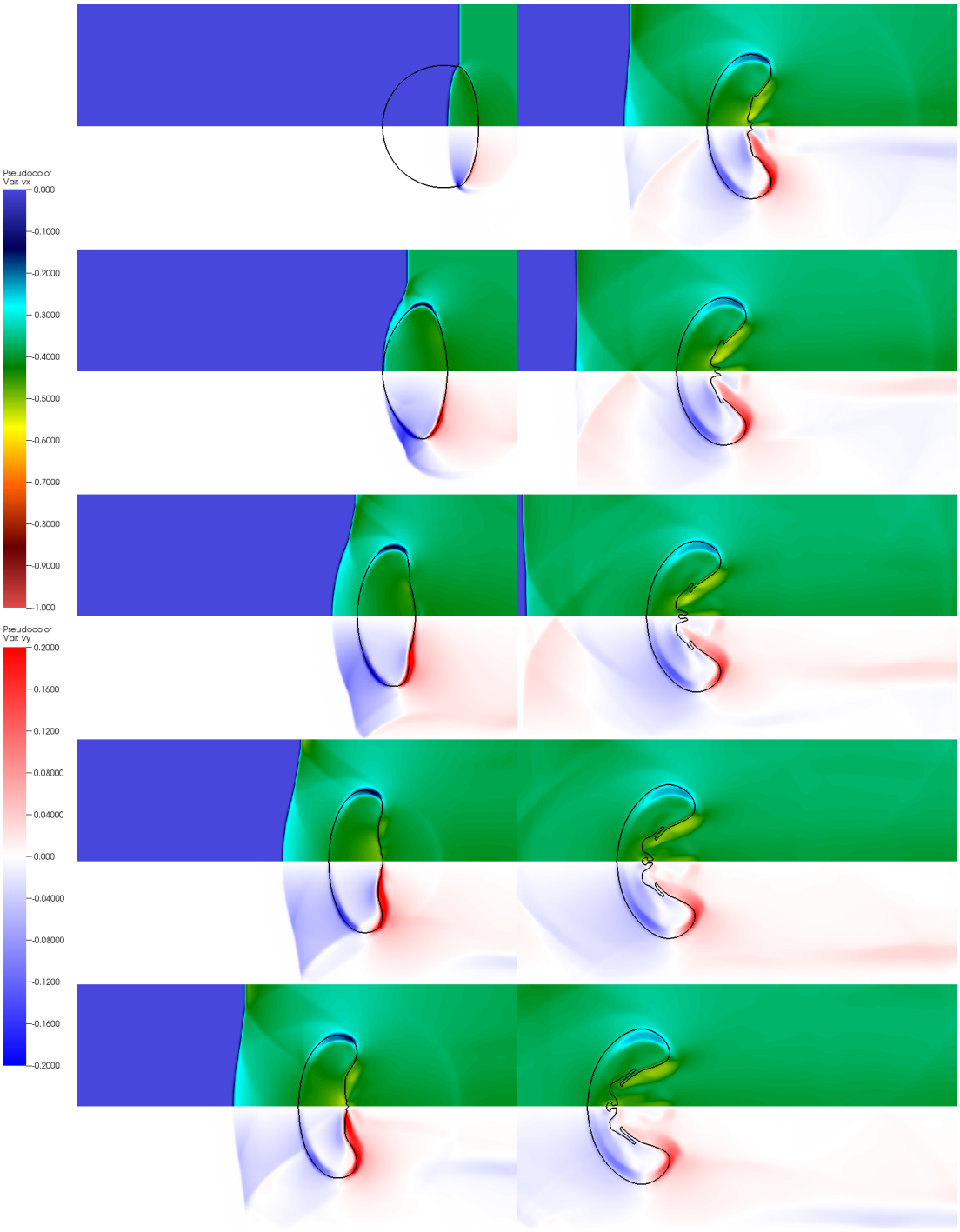

Figure 7.20 – This figure contains ten snapshots taken at intervals of $T = 30$ for the special-relativistic, ideal, magnetohydrodynamical bubble test. The first five are in the left column and the second five in the right column. This figure shows the x-component of the velocity plotted in the top half of each section with a hot-desaturated colour map. The v_x-scale is located to the left of the plots and runs between -1 and 0. The bottom of each plot shows the y-component of the velocity using a difference colour map. The scale is to the left of the plots and runs between -0.2 and 0.2.

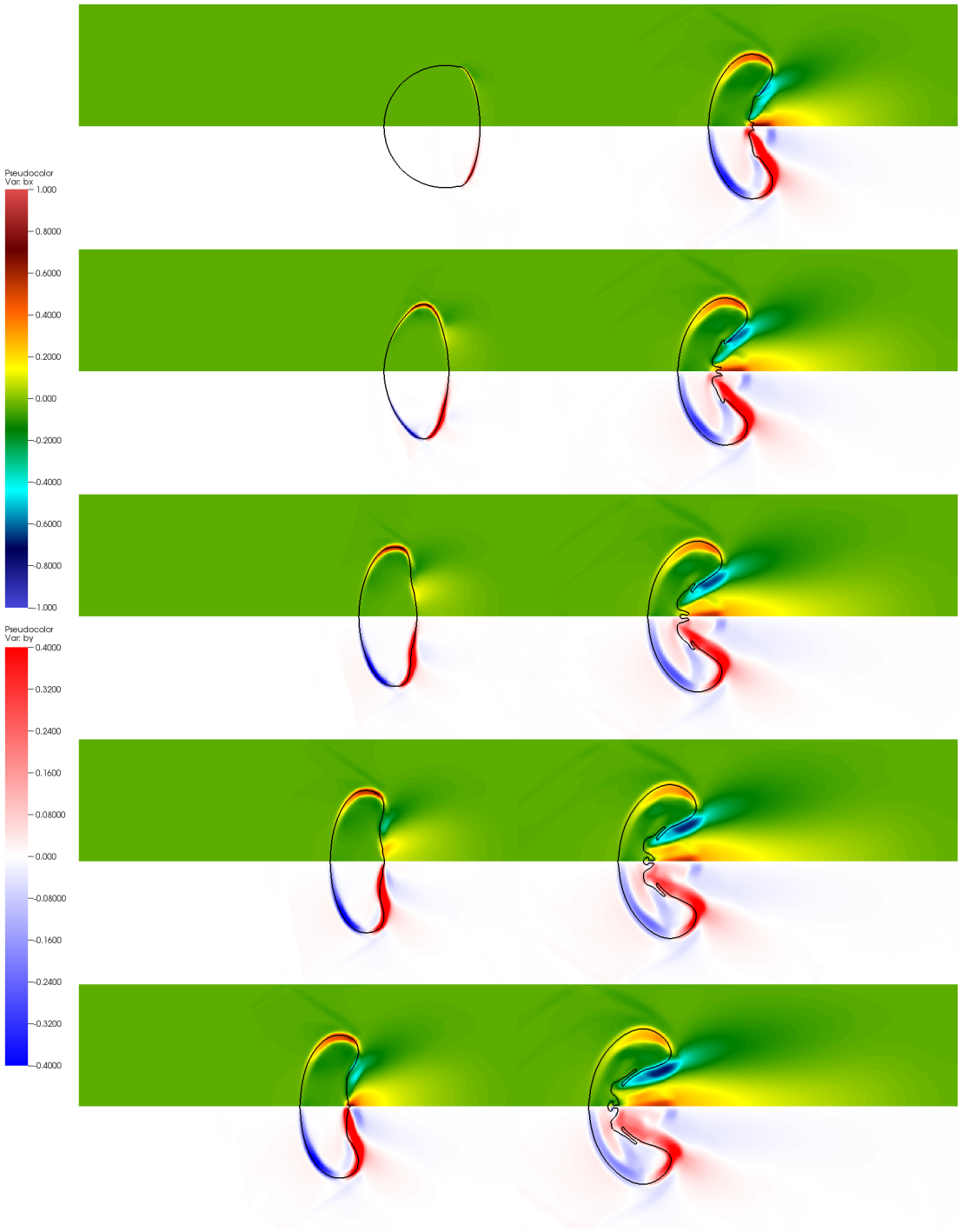

Figure 7.21 – This figure contains ten snapshots taking at intervals of $T = 30$ for the special-relativistic, ideal, magnetohydrodynamical bubble test. The first five are in the left column and the second five in the right column. This figure shows the x-component of the magnetic field plotted in the top half of each section with a hot-desaturated colour map. The B_x-scale is located to the left of the plots and runs between -1 and 1. The bottom of each plot shows the y-component of the magnetic field using a difference colour map. The scale is to the left of the plots and runs between -0.4 and 0.4.

The compression of the back-side of the bubble and the shock interaction has created a region of tangential velocity behind the shock. Inside of the bubble, the fluid is flowing away from the centre. Behind the bubble, the tangential velocity is flowing towards the $y = 0$ line. The motion of the bubble's surface goes across magnetic field lines. This causes magnetic stresses to build, which produce the magnetic field changes.

In the second snapshot at $T = 60$, the shock wave has begun to exit the bubble. Regions of large vorticity are located either side of the surface. A region of low velocity magnitude has developed at the top and bottom of the bubble. This is where the bubble surface aligns with the magnetic field. The fluid flow can be seen in the v_y plot. The interface is dragging the fluid around and thus the magnetic field, which leads to an area of positive B_x forming at the top and bottom. This picture continues in the snapshots $T = 90$ and $T = 120$.

Between $T = 120$ and $T = 180$ the back of the bubble overtakes the lobes that have developed; the kidney shape forms. This occurs because the surface at the back of the bubble is perpendicular to the magnetic field. This means that the magnetic field does not oppose the motion of the bubble. A new region of negative B_x develops as the fluid flows from the lobes towards the back. Between these times, the reflected shock waves from the boundaries cross the centre of the bubble. This produces a feature at the back of the bubble as the density and pressure increase. These processes described in this section continue to distort the bubble until the end of simulation.

Some key differences can be seen between the results presented by Millmore [113]. The vorticity is not tied to the surface. However, the effect is reduced in relativity compared to the results presented in Figure 7.17. This is related to the relativistic length compression seen between Newtonian and special-relativity by Millmore [113]. The lobes are more extended in the magnetohydrodynamical case compared to the hydrodynamical one due to the magnetic field resisting the motion at the top and bottom.

7.3 Summary

In this chapter, we have presented a selection of results that have demonstrated that the mRGFM is a suitable method for implementing in a neutron star simulation. First, we demonstrated that the mRGFM reproduces the results of Hu and Khoo [84] and it matches the other approximate solvers in the weak shock regime. Second, a strong shock test was performed, which demonstrated the failing of the oGFM of Fedkiw et al. [55] compared to the numerically expensive mGFM and our analytic mRGFM. Thirdly, we considered the mRGFM in two dimensions. Once again, it matched the results obtained by using the mGFM.

We have also demonstrated that the captured boundary approach based on the work of Sambasivan and Udaykumar [152] combined with the mRGFM is capable of dealing with large topology change. This is essential as the merger of a binary system is a highly chaotic process.

We have shown that the mRGFM allows on to combine Newtonian hydrodynamics to a pure vacuum state. This is the first time that such a result has been achieved. Using the approach described in Section 6.5, we have produced results for the toy star developed by Price [141]. The results in Figure 7.4 demonstrate that our method is stable.

Finally, we have extended the framework of Millmore and Hawke [114] to incorporate a magnetic field. We present results in two dimension for the first time in both Newtonian and special-relativistic, ideal, magnetohydrodynamics. These results show that the vorticity can be propagated away from the surface. The rate that this happens at is dependant on the strength of the magnetic field. This result has implications for the calculation of gravitational wave templates for neutron star binary inspiral. This mechanism facilitates the redistribution of angular momentum throughout the star. This redistribution could change the length of time between the merger of the stars and their collapse to a black hole because current simulations use the ideal perfect fluid approximation for the entire star. In this approximation, there is no mechanism to redistribute angular momentum.

Chapter 8

Discussion

The direct detection of gravitational waves from a binary neutron star system requires accurate gravitational wave templates. To determine these gravitational wave templates, one must perform numerical simulations of binary neutron star inspirals and mergers. Current simulations do not include a neutron star's internal, stratified structure and the transitions between these layers. However, these transitions and layers will become important during the merger phase. Building upon the work of Millmore and Hawke [114], this thesis has continued to address this omission. In this thesis, we have focused on the inclusion of the magnetic field in these transitions by developing a method of combining different systems of equations that approximate different regions of a star. This has led to the development of a framework for including a proper vacuum surface of a neutron star. Our results indicate that this framework produces stable evolutions. We have also demonstrated that the magnetic field facilitates the propagation of vorticity away from interfaces. This provides a mechanism for redistributing angular momentum throughout a star during merger. Such a process will qualitatively change the gravitational wave template, by e.g. changing the time for black hole formation from remnant collapse.

The majority of the original work in this thesis can be found in Chapter 6 and Chapter 7. Chapter 6 starts by describing the captured boundary approach. This approach combines many different ideas present in the literature [55, 124, 152, 156]. We follow the method given by Sambasivan and Udaykumar and describe our algorithm in detail [152]. The captured boundary approach sets up the multi-material Riemann problem that can be used to determine the data either side of an interface [114]. It starts by determining the location of the initial data for the multi-material Riemann problem. This is done by following the algorithm outlined in Subsection 6.2.3.

Once the initial data has been given, the multi-material Riemann problem can be solved. This thesis introduces a new approach to solve the multi-material Riemann problem called the multi-material Riemann Ghost Fluid Method (mRGFM). This approach has several key advantages over current methods:

- It allows two different hyperbolic systems of equations to be combined across an interface.
- It is capable of handling strong shock waves.
- It also imposes the physical compatibility conditions.
- It can be used in a relativistic framework.

Chapter 7 begins with a set of validation results that demonstrate that the validity of the captured boundary approach and the mRGFM. The first test results show that this framework converges to a high-resolution solution for the helium slab test of Wang et al. [182]. This test contains two interfaces that contain a helium slab surrounded by air and the results are presented in Figure 7.1. The second test highlights the ability of the mRGFM to correctly capture the location of strong shocks while also revealing the failure of other standard methods. This test was developed by Hu and Khoo [84] to demonstrate the failure of the oGFM to correctly capture the location of strong shock waves. The results are shown in Figures 7.2 and 7.3. The third test combines Newtonian hydrodynamics and a pure vacuum state. This is the first time that such a result has been achieved. Using the approach described in Section 6.5, we have produced results for the toy star developed by Price [141]. The results in Figure 7.4 demonstrate that our method is stable. The problem was evolved for a large number of time steps and the maximum absolute value of the velocity normal to the surface decreased. Oscillations develop in the star due to numerical error. The crossing time for an oscillation in our model is close the expected value based on the initial conditions.

We then consider a set of two-dimensional, multi-material tests called "bubble" tests. These are shock tubes that contain a helium bubble and are based on the test of Hu and Khoo [84]. Experimental results have been obtained in the laboratory by Haas and Sturtevant [73].

The first test compares three different approximate Riemann solvers: oGFM, mGFM and mRGFM. The results for this test are shown in Figures 7.7, 7.8, 7.9, 7.10 and 7.11. The results in Figure 7.12 show that the mRGFM method matches the mGFM, but the oGFM produces different results. These results resemble those found by Haas and Sturtevant [73] in their laboratory experiments. The mGFM is based on an all-shock approximation and is more accurate than the oGFM method. However, the mGFM requires one to perform a root find on the pressure, which is numerical expensive.

The second test was designed to highlight the ability of the captured boundary approach to deal with large topological changes. A Mach 40 shock wave is used to disrupt the surface of the bubble. The test continues to evolve after the bubble has separated in several smaller pieces. The results for this test are shown in Figures E.1, E.2, E.3 and E.4.

The third test examines a bubble in the presence of a magnetic field aligned with the x-axis using the mRGFM. This is the first time that such a result has been presented. We run several different tests with a varying magnetic field strength. This magnetic field strength is determined by the plasma beta parameter (2.40). The plasma beta parameter β_{m} takes the values $[1000, 100, 10, 1, 0.1]$. The results are plotted in Figure 7.17 and show an interesting physical effect. In the hydrodynamical bubble tests, vorticity develops at the surface of the bubble. This causes the surface to deform. However, in the presence of a magnetic field, the vorticity can be propagated away from the surface. The rate that this happens at is dependant on the strength of the magnetic field. A stronger field leads to a quicker propagation velocity, because the vorticity is propagated with the Alfvén velocity. This result has implications for the calculation of gravitational wave templates for neutron star binary inspiral. The mechanism facilitates the redistribution of angular momentum throughout the star. This redistribution could change the length of time between the merger of the stars and their collapse to a black hole because current simulations use the ideal perfect fluid approximation for the entire star. In this approximation, there is no mechanism to redistribute angular momentum. We also find that the divergence cleaning method is best suited to simulations with interfaces in the presence of a magnetic field.

The fourth test presents the first bubble test performed in special-relativistic, ideal magnetohydrodynamics. The results in Figures 7.18, 7.19, 7.20 and 7.21 show the same compression as demonstrated by Millmore for special-relativistic hydrodynamics [113]. However, the vorticity has still detached from the surface of the bubble. The mRGFM was used in this test. In the relativistic case, the divergence of the magnetic field, due to the presence of the interface, requires careful consideration of the parameters used. We have been unable to reproduce results for $\beta_{\mathrm{m}} < 1$ shown in Figure 7.17, due to the strength of the magnetic field. However, in the context of neutron stars, this regime is not very important due to the extreme densities.

8.1 Conclusions

This thesis has demonstrated for the first time the multi-material Riemann Ghost Fluid Method. The major advantage of the mRGFM, compared to other approximate Riemann solvers, is that it can combine different systems of hyperbolic partial differential equations where a set of appropriate compatibility conditions exists. These compatibility conditions equate the physical continuity conditions at a contact wave. The mRGFM explicitly imposes these conditions at the interface between two materials. It also is capable of handling strong shock waves where other methods fail.

We have also demonstrated the application of the general Ghost Fluid Method to a two-dimensional system with a magnetic field for the first time. This has been achieved in both the Newtonian and special-relativistic regimes. We have observed that the vorticity, normally associated with the surface in hydrodynamical simulations, is propagated away from the surface along the magnetic field lines.

Finally, this thesis has proposed a proper treatment of the stellar surface that utilises the mRGFM. By applying this approach to the toy star problem of Price [141], we have demonstrated that our approach is stable and for the first time couples a hydrodynamical interior to a vacuum exterior.

Incorporating the first two developments into the framework of Millmore and Hawke [114] and utilising the captured boundary approach of Sambasivan and Udaykumar [152], one will be able to include interfaces into a neutron star model with a magnetic field. This is the obvious extension of this work. Using this model in a binary merger simulation will produce new and interesting results. This is because the vorticity propagation provides a mechanism for the redistribution of angular momentum within the system. This redistribution will lead to a change in the time of collapse into a black hole. This is the most notable extension of this work.

Another extension is to include a proper surface treatment into neutron star simulation with a magnetic field. This requires the coupling of an ideal magnetohydrodynamical interior to a force-free, electro-vacuum or pure vacuum exterior. The current approach would first need to be extended to higher dimensions and special-relativity before adding a magnetic field. The extension to three dimensions is simple and Millmore has shown that the extension to general-relativity can be done [114]. As well as the physical quantities jumping at the surface, the derivates of these quantities also change discontinuously. Incorporating this into the solution via the derivative Riemann problem may be necessary.

The overriding aim would be to combine these two extensions together to give an accurate neutron star model. This model can then be used to calculate gravitational wave templates with higher accuracy.

Appendices

Appendix A

Ohm's Law from a Multi-Fluid Approach

A.1 Newtonian Resistive Multi-Fluid

The following calculation is based on the relativistic one presented by Andersson [7]. The multi-fluid approach treats each individual particle species as a fluid.

Starting from the particle fluxes n^{μ}_{x}, the individual species' current can be defined as

$$j^{\mu}_{\mathrm{x}} = q_{\mathrm{x}} n^{\mu}_{\mathrm{x}}, \tag{A.1}$$

where j^{μ} is the current and q_{x} is the charge. The four-vector flux associated with the species x is

$$n^{\mu}_{\mathrm{x}} = n_{\mathrm{x}} u^{\mu}_{\mathrm{x}}, \tag{A.2}$$

where u^{μ}_{x} is the four-velocity and n_{x} the number density of the species x. It should be noted that x is a label and not an index. The total current is the source of the electromagnetic field and the sum of the individual species' currents,

$$j^{\mu} = \sum_{\mathrm{x}} j^{\mu}_{\mathrm{x}}. \tag{A.3}$$

The chemical potential – the amount of energy required to add a particle to the system – is modified by the addition of the electromagnetic field,

$$\bar{\mu}^{\mu}_{\mathrm{x}} = \mu^{\mu}_{\mathrm{x}} + q_{\mathrm{x}} A^{\mu}, \tag{A.4}$$

where A^{μ} is the four-vector potential. We wish to work in the low velocity limit, therefore we can define the charge density as

$$\sigma = \frac{1}{c} \sum_{\mathrm{x}} n_{\mathrm{x}} q^{\mathrm{x}} W_{\mathrm{x}} \approx \frac{1}{c} \sum_{\mathrm{x}} n_{\mathrm{x}} q^{\mathrm{x}}, \tag{A.5}$$

where W_{x} is the individual particle Lorentz factor and approximately equal to one in the low velocity limit. We can calculate the spatial components of the total charge current in the low velocity limit,

$$j^{i} = \sum_{\mathrm{x}} j^{i}_{\mathrm{x}} = \frac{1}{c} \sum_{x} n_{\mathrm{x}} q^{\mathrm{x}} W_{\mathrm{x}} v^{i}_{\mathrm{x}} \approx \frac{1}{c} \sum_{x} n_{\mathrm{x}} q^{\mathrm{x}} v^{i}_{\mathrm{x}} = \frac{1}{c} J^{i}. \tag{A.6}$$

Equations (A.1) to (A.6) contain all the ingredients required to see how the momentum equation for charged fluids differs from the Euler equations. Taking the multi-fluid momentum equation from Andersson and Comer [8], we balance the equation with the Lorentz force in the multi-fluid approach,

$$\rho_{\mathrm{x}} (\partial_t + v^{j}_{\mathrm{x}} \nabla_j) v^{\mathrm{x}}_{i} + \rho_{\mathrm{x}} \nabla_i \tilde{\mu}^{\mathrm{x}} = f^{\mathrm{x}}_{i}. \tag{A.7}$$

The Lorentz force in the multi-fluid picture is given by

$$f^{\mathrm{x}}_{i} = n_{\mathrm{x}} q^{\mathrm{x}} (E_i + \epsilon_{ijk} v^{j}_{\mathrm{x}} B^{k}). \tag{A.8}$$

This is very similar to the single-fluid Lorentz force given previously (2.20).

A.1.1 Proton-electron plasma

This derivation will focus on the particular case, where the charged fluid is a proton-electron fluid. The label (x) will be replaced with (e) for the electron and (p) for the proton. In this specific case, the charge density σ (A.5) becomes

$$\sigma = \frac{e}{c} (n_{\mathrm{p}} - n_{\mathrm{e}}). \tag{A.9}$$

The total current can be defined in terms of the proton and electron fluids using the current equation (A.6),

$$J^{i} = e(n_{\mathrm{p}} v^{i}_{\mathrm{p}} - n_{\mathrm{e}} v^{i}_{\mathrm{e}}). \tag{A.10}$$

The work in this thesis concerns a single-fluid model, which must be recovered from the multi-fluid approach. This can be done by defining two velocities, the transport velocity v_i and the velocity difference $w_i = v^i_{\rm p} - v^i_{\rm e}$. The transport velocity gives the bulk motion of the fluid and is defined by

$$\rho v_i = \rho_{\rm p} v^{\rm p}_i + \rho_{\rm e} v^{\rm e}_i, \tag{A.11}$$

where $\rho = \rho^{\rm p} + \rho^{\rm e}$ is total density. These relations can be combined to replace the individual fluid velocities,

$$v^i_{\rm p} = v^i + \frac{\rho_{\rm e}}{\rho} w^i, \tag{A.12}$$

$$v^i_{\rm e} = v^i - \frac{\rho_{\rm p}}{\rho} w^i. \tag{A.13}$$

Two different momentum equations can be obtained by substituting the proton velocity (A.12) and the electron velocity (A.13) into the momentum equation (A.7). By adding the proton momentum equation to the electron momentum equation, an average momentum equation can be calculated. A difference momentum equation can also be derived by subtracting the electron momentum equation from the proton one. The average equation is given by

$$\begin{aligned}\rho(\partial_t + v^j\nabla_j)v_i + w_i\nabla_j\left(\frac{\rho_{\rm p}\rho_{\rm e}}{\rho}w^j\right) + \rho_{\rm p}w^j\nabla_j w_i + \frac{\rho_{\rm p}\rho_{\rm e}}{\rho}w^j\nabla_j w_i + \nabla_i p \\ = e(n_{\rm p} - n_{\rm e})(E_i + \epsilon_{ijk}v^j B^k) + e\frac{n_{\rm e}\rho_{\rm e}}{\rho}\left(1 + \frac{m_{\rm e}}{m_{\rm p}}\right)\epsilon_{ijk}w^j B^k.\end{aligned} \tag{A.14}$$

The gradient of the pressure $\nabla_i p$ has been substituted in above and is given by

$$\nabla_i p = \rho_{\rm p}\nabla_i\tilde{\mu}_{\rm p} + \rho_{\rm e}\nabla_i\tilde{\mu}_{\rm e}. \tag{A.15}$$

The difference equation is given by

$$\begin{aligned}(\partial_t + v^j\nabla_j)w_i + w^j\nabla_j v_i + \left(\frac{\rho_{\rm e} - \rho_{\rm p}}{\rho}\right)w^j\nabla_j w_i - w_i w^j\nabla_j\left(\frac{\rho_{\rm p}}{\rho}\right) + \nabla_i(\tilde{\mu}_{\rm p} - \tilde{\mu}_{\rm e}) \\ = \frac{e}{m_{\rm p}m_{\rm e}}(m_{\rm e} + m_{\rm p})(E_i + \epsilon_{ijk}v^j B^k) + \frac{e}{\rho}\frac{1}{m_{\rm p}m_{\rm e}}(m_{\rm e}\rho_{\rm e} - m_{\rm p}\rho_{\rm p})\epsilon_{ijk}w^j B^k.\end{aligned} \tag{A.16}$$

Rewriting the current J^i in terms of the difference and average velocities gives

$$J^i = e(n_p - n_e)v^i + \frac{e}{\rho}n_p n_e(m_p + m_e)w^i. \tag{A.17}$$

In an old, cold neutron star, the bulk fluid is expected to be charge neutral. This is a sensible approximation to make, because any charged regions have had enough time to attract particles of the opposite charge neutralising the charged region.

This approximation can be mathematically expressed by setting $n_\mathrm{p} = n_\mathrm{e}$. In this approximation, the charge density (A.9) is zero. Therefore, from Gauss's law (2.15) the divergence of the electric field is also zero

$$\nabla_i E^i = 0. \tag{A.18}$$

Taking the divergence of Ampere's law (2.18) reveals that the divergence of the current vanishes as well, because the divergence of the curl is identically zero,

$$\nabla_i J^i = 0. \tag{A.19}$$

Several other approximations will be made. The first is that the electron mass can be ignored: when compared to the proton mass, the electron mass is much smaller; $m_\mathrm{p} \gg m_\mathrm{e}$. Secondly, it will be assumed that the velocity difference, w^i, is small. This means that quadratic and higher-order terms in the velocity difference can be ignored. These approximations greatly simplify the average and difference momentum equations,

$$\rho(\partial_t + v^j\nabla_j)v_i + \nabla_i p = \epsilon_{ijk}J^j B^k, \tag{A.20}$$

$$E_i + \epsilon_{ijk}v^j B^k = -\frac{m_\mathrm{e}}{e}\left[(\partial_t + v^j\nabla_j)w_i + w^j\nabla_j v_i + \nabla_i(\tilde{\mu}_\mathrm{p} - \tilde{\mu}_\mathrm{e}) - \frac{1}{\rho_\mathrm{e}}\epsilon_{ijk}J^j B^k\right]. \tag{A.21}$$

The current equation can also been simplified to

$$J_i = \frac{e n_\mathrm{e}\rho_\mathrm{p}}{\rho} w_i. \tag{A.22}$$

So far, the multi-fluid approach has not included any form of friction between different particle species. A phenomenological force can be used to represent the interaction

$$f_i^\mathrm{e} = \eta(v_i^\mathrm{p} - v_i^\mathrm{e}) = -f_i^\mathrm{p}, \tag{A.23}$$

where η is the coefficient of resistivity. The addition of this resistive force does not change the average equation, but adds a new term to the difference equation. The difference equation now takes the form

$$E_i + \epsilon_{ijk}v^j B^k - \eta\left(\frac{\rho}{n_e e\rho_p}\right)^2 J_i = -\frac{m_e}{e}[\ldots], \tag{A.24}$$

Ignoring the right-hand side, one recovers the generalised Ohm's law (2.21).

Appendix B

Exact Solvers

The following sections contain information required to construct the exact solution to the Riemann problem for Newtonian hydrodynamics, special-relativistic hydrodynamics and ideal magnetohydrodynamics.

B.1 Newtonian Hydrodynamics Wave Solutions

To construct the exact solution to the one-dimensional Riemann problem in Newtonian hydrodynamics, one must be able to calculate the states behind the non-linear waves and combine them at the contact wave. The resulting system requires a root find on the pressure. This is given in equation (3.53). This section will first consider a shock wave and then a rarefaction wave. These relations come from the book by Toro [173].

B.1.1 Solution across a shock wave

In the case where the state in front of the wave, $\mathbf{q}_{\{\mathrm{a}\}}$, is known, the state behind the wave, $\mathbf{q}_{\{\mathrm{b}\}}$, can be calculated from the Rankine-Hugoniot conditions (3.23). This is most easily done in the frame of the shock. The following calculation assumes that the pressure, $p_{\{\mathrm{b}\}}$, is known a priori. From the state $\mathbf{q}_{\{\mathrm{a}\}}$, one can calculate the primitive variables $\mathbf{u}_{\{\mathrm{a}\}}$ and the pressure $p_{\{\mathrm{a}\}}$. For the specific case of the Euler equations, this is a simple analytic operation. The next step is to perform a Galilean transformation into the shock frame. This gives a set of transformed velocities

$$\hat{v}_{\{\mathrm{a,b}\}} = v_{\{\mathrm{a,b}\}} - v_s. \tag{B.1}$$

In the shock speed frame, the Rankine-Hugoniot conditions are

$$\rho_{\{a\}}\hat{v}_{\{a\}} = \rho_{\{b\}}\hat{v}_{\{b\}}, \tag{B.2a}$$

$$\rho_{\{a\}}\hat{v}_{\{a\}}^2 + p_{\{a\}} = \rho_{\{b\}}\hat{v}_{\{b\}}^2 + p_{\{b\}}, \tag{B.2b}$$

$$\hat{v}_{\{a\}}\left(\hat{\mathcal{E}}_{\{a\}} + p_{\{a\}}\right) = \hat{v}_{\{b\}}\left(\hat{\mathcal{E}}_{\{b\}} + p_{\{b\}}\right). \tag{B.2c}$$

We then define the mass flux Q as

$$Q \equiv \mp\rho_{\{a\}}\hat{v}_{\{a\}} = \mp\rho_{\{b\}}\hat{v}_{\{b\}}, \tag{B.3}$$

where the sign changes for the wave direction. Here, the minus sign indicates a right going wave and the positive sign a left going wave. Rearranging the momentum flux (B.2b) in terms of the mass flux (B.3) gives

$$Q = \pm\frac{p_{\{b\}} - p_{\{a\}}}{\hat{v}_{\{b\}} - \hat{v}_{\{a\}}}, \tag{B.4}$$

This can be rewritten in terms of the state velocities using the transformed velocity relation (B.1) to give

$$Q = \pm\frac{p_{\{b\}} - p_{\{a\}}}{v_{\{b\}} - v_{\{a\}}}. \tag{B.5}$$

Rearranging in terms of the unknown $v_{\{b\}}$ gives

$$v_{\{b\}} = v_{\{a\}} \pm \frac{p_{\{b\}} - p_{\{a\}}}{Q}. \tag{B.6}$$

Using the definition of the mass flux (B.3), the momentum flux (B.5) can be rewritten in terms of the unknown density $\rho_{\{b\}}$ to give

$$Q^2 = \pm\frac{p_{\{b\}} - p_{\{a\}}}{\dfrac{1}{\rho_{\{a\}}} - \dfrac{1}{\rho_{\{b\}}}}. \tag{B.7}$$

The energy flux (B.2c) can be rewritten in terms of the unknown density by using the EOS to give

$$\rho_{\{b\}} = \rho_{\{a\}} \left[\frac{\left(\frac{\gamma_x - 1}{\gamma_x + 1}\right) + \left(\frac{p_{\{b\}}}{p_{\{a\}}}\right)}{\left(\frac{\gamma_x - 1}{\gamma_x + 1}\right)\left(\frac{p_{\{b\}}}{p_{\{a\}}}\right) + 1} \right], \tag{B.8}$$

where the label x can be used to construct an exact solver for the multi-model problem by using the EOS associated with the left or the right state of the contact wave. Substituting the energy flux (B.8) into the momentum flux (B.7) removes the explicit dependence on the post-shock density by giving a relation for the mass flux

$$Q = \left(\frac{p_{\{b\}} + B_{\{a\}}}{A_{\{a\}}} \right)^{1/2}, \tag{B.9}$$

where

$$A_{\{a\}} = \frac{2}{(\gamma_x + 1)\rho_{\{a\}}}, \tag{B.10}$$

and

$$B_{\{a\}} = \frac{\gamma_x - 1}{\gamma_x + 1} p_{\{a\}}. \tag{B.11}$$

Finally, the unknown velocity $v_{\{b\}}$ (B.6) can be expressed entirely in terms of known quantities,

$$v_{\{b\}} = v_{\{a\}} \pm \left(p_{\{b\}} - p_{\{a\}}\right) \left[\frac{A_{\{a\}}}{p_{\{b\}} + B_{\{a\}}} \right]^{1/2}. \tag{B.12}$$

Hence, all other unknown quantities for the state $\mathbf{q}_{\{b\}}$ can be calculated.

B.1.2 Rarefaction wave

Next, consider the rarefaction wave in the one-dimensional Euler equations. Again, consider two states $\mathbf{q}_{\{a\}}$ and $\mathbf{q}_{\{b\}}$, separated by a rarefaction wave, where the state $\mathbf{q}_{\{a\}}$ and the pressure $p_{\{b\}}$ are known. The rarefaction wave is bounded by the characteristics

$$\xi_{\{a\}} = v_{\{a\}} \pm a_{x\{a\}}, \quad \xi_{\{b\}} = v_{\{b\}} \pm a_{x\{b\}}. \tag{B.13}$$

An example of a rarefaction wave is given in the Figure 3.3. The figure shows a rarefaction wave bounded by the blue characteristics. Between the waves the characteristics diverge to fill the gap created by the diverging waves.

A rarefaction wave for the Euler equations is adiabatic, which means that the entropy does not change across it. As well as the entropy, other quantities known as Riemann invariants are constant across a rarefaction wave. For the Euler equations the second Riemann invariant is

$$r_2 = v_n \mp \frac{2a_{\mathrm{x}}}{\gamma_{\mathrm{x}} - 1}, \tag{B.14}$$

where as before v_n is the normal velocity, a_{x} is the speed of sound and γ_{x} is the ratio of specific heat capacities for the EOS x. Equating the Riemann invariant (B.14) either side of the wave results in the relation

$$v_{\{\mathrm{b}\}} = v_{\{\mathrm{a}\}} \pm \frac{2}{\gamma_{\mathrm{x}} - 1}(a_{\mathrm{x}\{\mathrm{b}\}} - a_{\mathrm{x}\{\mathrm{a}\}}). \tag{B.15}$$

We can use the fact that a rarefaction wave is adiabatic to rewrite the unknown speed of sound $a^{\mathrm{x}}_{\{\mathrm{b}\}}$ in terms of known quantities. For an ideal fluid with constant entropy, the following relation holds

$$p \propto \rho^{\gamma_{\mathrm{x}}}. \tag{B.16}$$

The speed of sound obeys a similar relation,

$$a_{\mathrm{x}} \propto \rho^{(\gamma_{\mathrm{x}}-1)/2}. \tag{B.17}$$

Hence, a relation between the pressures and the speed of sound is given by

$$p_{\{\mathrm{b}\}} = p_{\{\mathrm{a}\}} \left(\frac{a_{\mathrm{x}\{\mathrm{b}\}}}{a_{\mathrm{x}\{\mathrm{a}\}}} \right)^{2\gamma_{\mathrm{x}}/(\gamma_{\mathrm{x}}-1)}. \tag{B.18}$$

This can be used in the velocity relation (B.15) to determine the unknown velocity $v_{\{\mathrm{b}\}}$ from known quantities

$$v_{\{\mathrm{b}\}} = v_{\{\mathrm{a}\}} \pm \frac{2a_{\mathrm{x}\{\mathrm{a}\}}}{\gamma_{\mathrm{x}} - 1} \left[\left(\frac{p_{\{\mathrm{b}\}}}{p_{\{\mathrm{a}\}}} \right)^{(\gamma_{\mathrm{x}}-1)/(2\gamma_{\mathrm{x}})} - 1 \right]. \tag{B.19}$$

B.2 Special-relativistic Hydrodynamics

We now turn our attention to finding the exact solution to the Riemann problem from special-relativistic hydrodynamics. The x-direction is normal to the Riemann problem. These relations come from Pons et al. [135].

B.2.1 Shock wave

When considering a shock wave, one uses the Rankine-Hugoniot conditions to determine the shock speed from the jump in the variables. Taub derived the relativistic Rankine-Hugoniot conditions [170] and they are

$$[[\rho u^{\mu}]]\, n_{\mu} = 0, \quad [[T^{\mu\nu}]]\, n_{\nu} = 0, \tag{B.20}$$

where n_{μ} is the unit normal to a space-time slice. The unit normal in the lab frame with a shock speed v_s is

$$n_{\mu} = W_s(-v_s, 1, 0, 0), \tag{B.21}$$

where W_s is the Lorentz factor associated with the shock speed v_s.

As in the Newtonian case, it is assumed that the state in front of the shock $\mathbf{q}_{\{\mathrm{a}\}}$ and the pressure in both states is known. In this section, we will follow the description given by Font [58]. As before, we use the Rankine-Hugoniot condition of the continuity equation to determine the mass flux across the shock

$$Q \equiv W_s \rho_{0,\{\mathrm{a}\}} v^x_{\{\mathrm{a}\}} (v_s - v^x_{\{\mathrm{a}\}}) = W_s \rho_{0,\{\mathrm{b}\}} v^x_{\{\mathrm{b}\}} (v_s - v^x_{\{\mathrm{b}\}}). \tag{B.22}$$

The Rankine-Hugoniot conditions (B.20) can be rewritten in terms of the conserved variables (3.69) to give

$$[[v^x]] = -\frac{Q}{W_s}\left[\left[\frac{1}{D}\right]\right], \tag{B.23a}$$

$$[[p]] = \frac{Q}{W_s}\left[\left[\frac{S^x}{D}\right]\right], \tag{B.23b}$$

$$\left[\left[\frac{S^y}{D}\right]\right] = 0, \tag{B.23c}$$

$$\left[\left[\frac{S^z}{D}\right]\right] = 0, \tag{B.23d}$$

$$[[v^x p]] = \frac{Q}{W_s}\left[\left[\frac{\tau}{D}\right]\right], \tag{B.23e}$$

where D is the rest-mass density in an Eulerian frame (3.60), S^i is the momentum (3.63) and τ is the kinetically dominated energy (3.66).

The jump conditions on the tangential momenta (B.23c), (B.23d) imply that the tangential velocities do not change across a shock.

Using the relation between the momentum and the total energy density (3.64), one can give the velocity behind the shock as

$$v^x_{\{\mathrm{b}\}} = \frac{\left[h_{\{\mathrm{a}\}} W_{\{\mathrm{a}\}} v^x_{\{\mathrm{a}\}} + \dfrac{W_s \left(p_{\{\mathrm{b}\}} - p_{\{\mathrm{a}\}}\right)}{Q}\right]}{h_{\{\mathrm{a}\}} W_{\{\mathrm{a}\}} + \left(p_{\{\mathrm{b}\}} - p_{\{\mathrm{a}\}}\right)\left(\dfrac{W_s v^x_{\{\mathrm{a}\}}}{Q} + \dfrac{1}{\rho_{0,\{\mathrm{a}\}} W_{\{\mathrm{a}\}}}\right)}, \tag{B.24}$$

where h is the specific enthalpy defined in equation (2.7). The tangential velocities behind the shock can be derived from the momentum jump conditions (B.23c), (B.23d) to give

$$v^{y,z}_{\{\mathrm{b}\}} = h_{\{\mathrm{a}\}} W_{\{\mathrm{a}\}} v^{y,z}_{\{\mathrm{a}\}} \left[\frac{1 - \left(v^x_{\{\mathrm{b}\}}\right)^2}{h^2_{\{\mathrm{b}\}} + \left(h_{\{\mathrm{a}\}} W_{\{\mathrm{a}\}} v^{y,z}_{\{\mathrm{a}\}}\right)^2}\right]^{1/2}. \tag{B.25}$$

This requires the enthalpy behind the shock, $h_{\{\mathrm{b}\}}$, which can be found by solving a quadratic equation derived from the Taub adiabat for an ideal EOS [109],

$$\begin{aligned}\left[1 + \frac{\left(\gamma_{\mathrm{x}} - 1\right)\left(p_{\{\mathrm{a}\}} - p_{\{\mathrm{b}\}}\right)}{\gamma_{\mathrm{x}} p_{\{\mathrm{b}\}}}\right] h^2_{\{\mathrm{b}\}} - \left[\frac{\left(\gamma_{\mathrm{x}} - 1\right)\left(p_{\{\mathrm{a}\}} - p_{\{\mathrm{b}\}}\right)}{\gamma_{\mathrm{x}} p_{\{\mathrm{b}\}}}\right] h_{\{\mathrm{b}\}} \\ + \left[\frac{h_{\{\mathrm{a}\}}\left(p_{\{\mathrm{a}\}} - p_{\{\mathrm{b}\}}\right)}{\rho_{\{\mathrm{a}\}}} - h^2_{\{\mathrm{a}\}}\right] = 0.\end{aligned} \tag{B.26}$$

This quadratic equation produces two enthalpies, one positive and physical, the other negative and unphysical. Finally, the shock speed is also required and it can be derived from the Rankine-Hugoniot conditions,

$$v_s = \frac{\rho^2_{\{\mathrm{a}\}} W^2_{\{\mathrm{a}\}} v^x_{\{\mathrm{a}\}} \pm |Q| \sqrt{Q^2 + \rho^2_{\{\mathrm{a}\}} W^2_{\{\mathrm{a}\}} \left(1 - v^{x2}_{\{\mathrm{a}\}}\right)}}{\rho^2_{\{\mathrm{a}\}} W^2_{\{\mathrm{a}\}} + Q^2}. \tag{B.27}$$

B.2.2 Rarefaction wave

As in the Newtonian case, a rarefaction wave is bounded by the characteristics $\lambda_\pm$ (3.73). As before, it will be assumed that the state in front of the wave $\mathbf{q}_{\{\mathrm{a}\}}$ and the pressure $p_{\{\mathrm{b}\}}$ behind the wave are known. The velocity in the rarefaction wave is given by the solution to the following ODE

$$\frac{\mathrm{d}v^x}{\mathrm{d}p} = \pm \frac{1}{\rho_{\{\mathrm{a}\}} h_{\{\mathrm{a}\}} W^2_{\{\mathrm{a}\}} a_{\{a\}}} \left[1 + g\left(\lambda_\pm, v^x_{\{\mathrm{a}\}}, v^t_{\{\mathrm{a}\}}\right)\right]^{-1/2}, \tag{B.28}$$

where $v^t_{\{\mathrm{a}\}} = \left[\left(v^y_{\{\mathrm{a}\}}\right)^2 + \left(v^z_{\{\mathrm{a}\}}\right)^2\right]^{1/2}$ and

$$g(\lambda_\pm, v^x_{\{\mathrm{a}\}}, v^t_{\{\mathrm{a}\}}) = \frac{\left(v^t_{\{\mathrm{a}\}}\right)^2 \left(\lambda_\pm^2 - 1\right)}{\left(1 - \lambda_\pm v^x_{\{\mathrm{a}\}}\right)^2}. \tag{B.29}$$

The tangential velocity magnitude is given by

$$v^t_{\{\mathrm{b}\}} = h_{\{\mathrm{a}\}} W_{\{\mathrm{a}\}} v^t_{\{\mathrm{a}\}} \left[\frac{1 - \left(v^x_{\{\mathrm{b}\}}\right)^2}{h^2_{\{\mathrm{b}\}} + \left(h_{\{\mathrm{a}\}} W_{\{\mathrm{a}\}} v^t_{\{\mathrm{a}\}}\right)^2}\right]. \tag{B.30}$$

To find the exact solution at the contact, a root find can be performed on the pressure.

B.3 Ideal MHD

These relations as well as those given for the Alfvén wave in Subsection 3.5.4 allow one to construct an exact solver in Newtonian, ideal magnetohydrodynamics. The following relations are given by Torrilhon [175].

B.3.1 Shock waves

When the density jumps, i.e. $[[\rho]] \neq 0$, a shock wave occurs. The momentum Rankine-Hugoniot condition (3.100b) shows that the tangential magnetic field divided by the density is parallel to the tangential velocity. The magnetic Rankine-Hugoniot condition (3.100c) illustrates that the tangential magnetic field is parallel to the tangential velocity. The jump in density means that tangential magnetic field is collinear. Therefore, the Rankine-Hugoniot conditions for a shock are as follows,

$$Q^2 \left[[V]\right] + \left[\left[p + \frac{1}{2}B_t^2\right]\right] = 0, \tag{B.31a}$$

$$Q^2 \left[[V\mathbf{B}_t]\right] - B_x^2[[\mathbf{B}_t]] = 0, \tag{B.31b}$$

$$\frac{1}{\gamma_{\mathrm{x}} - 1}\left[\left[\frac{p}{\rho}\right]\right] + \frac{1}{2}(p_{\{\mathrm{a}\}} + p_{\{\mathrm{b}\}})\left[[V]\right] + \frac{1}{4}[[V]]\left([[B_t]]\right)^2 = 0. \tag{B.31c}$$

Following the approach of Torrilhon [175], the Rankine-Hugoniot conditions can be rewritten in terms of dimensionless quantities

$$\hat{V} = \frac{V_{\{\mathrm{b}\}}}{V_{\{\mathrm{a}\}}}, \quad \hat{p} = \frac{p_{\{\mathrm{b}\}}}{p_{\{\mathrm{a}\}}}, \quad \hat{B}_t = \frac{B_t^{\{b\}}}{\sqrt{p_{\{\mathrm{a}\}}}}, \quad \hat{\mathbf{v}}_t = \frac{\mathbf{v}_t^{\{b\}}}{a_{\mathrm{x}\{\mathrm{a}\}}}. \tag{B.32}$$

These dimensionless quantities are chosen, because they behave well as the normal magnetic field goes to zero, $B_n \to 0$. The Rankine-Hugoniot conditions for a shock wave now read

$$\hat{p} - 1 + \gamma_{\mathrm{x}} M_{\mathrm{x}\{\mathrm{a}\}}^2 \left(\hat{V} - 1\right) + \frac{1}{2}\left(\hat{B}_t^2 - A^2\right) = 0, \tag{B.33a}$$

$$\gamma_{\mathrm{x}} M_{\mathrm{x}\{\mathrm{a}\}}^2 \left(\hat{V}\hat{B}_t - A\right) - B^2\left(\hat{B}_t - A\right) = 0, \tag{B.33b}$$

$$\frac{1}{\gamma_{\mathrm{x}} - 1}\left(\hat{p}\hat{V} - 1\right) + \frac{1}{2}\left(\hat{V} - 1\right)(\hat{p} + 1) + \frac{1}{4}\left(\hat{V} - 1\right)\left(\hat{B}_t - A\right)^2 = 0, \tag{B.33c}$$

where the three parameters are

$$A = \frac{B_t^{\{a\}}}{\sqrt{p_{\{\mathrm{a}\}}}}, \quad B = \frac{B_n}{\sqrt{p_{\{\mathrm{a}\}}}}, \quad M_{\mathrm{x}\{\mathrm{a}\}} = \frac{v_n}{a_{\mathrm{x}}}. \tag{B.34}$$

B.3.1.1 Fast shock wave

The fast shock in ideal MHD is very similar to the shock waves in hydrodynamics. In the limit as the magnetic field approaches zero, $B \to 0$, the fast wave speed c_f approaches the speed of sound a.

The solution to the Riemann problem is given by the intersection of the Hugoniot curve and the Rayleigh line [175]. The Hugoniot curve is the curve in the pressure-volume phase space given by the energy Rankine-Hugoniot condition (B.33a). The Rayleigh line is the line in the pressure-volume phase space given by the momentum Rankine-Hugoniot condition (B.33c). The tangential magnetic field can be rewritten in terms of the parameters $A, B, M_{\mathrm{x}\{\mathrm{a}\}}$ and the specific volume $\hat{V}$,

$$\hat{B}_t(\hat{V}, M_{\{\mathrm{a}\}}, A, B) = A\frac{\gamma_{\mathrm{x}} M_{\mathrm{x}\{\mathrm{a}\}}^2 - B^2}{\gamma_{\mathrm{x}} M_{\{\mathrm{a}\}}^2 \hat{V} - B^2}. \tag{B.35}$$

This implies that the Hugoniot curve and the Rayleigh line can be written in terms of the parameters $A, B, M_{\{\mathrm{a}\}}$ and $\hat{V}$. Solving for the pressure gives

$$\hat{p}_{\mathrm{Ray}} = 1 - \gamma_{\mathrm{x}} M_{\mathrm{x}\{\mathrm{a}\}}^2 \left(\hat{V} - 1\right) - \frac{1}{2}\left(\left[A\frac{\gamma_{\mathrm{x}} M_{\mathrm{x}\{\mathrm{a}\}}^2 - B^2}{\gamma_{\mathrm{x}} M_{\mathrm{x}\{\mathrm{a}\}}^2 \hat{V} - B^2}\right]^2 - A^2\right), \tag{B.36}$$

$$\hat{p}_{\mathrm{Hug}} = \frac{\hat{V} - \dfrac{\gamma_{\mathrm{x}}+1}{\gamma_{\mathrm{x}}-1} + \dfrac{1}{2}\left(\hat{V}-1\right)\left(A - \left[A\dfrac{\gamma_{\mathrm{x}} M_{\mathrm{x}\{\mathrm{a}\}}^2 - B^2}{\gamma_{\mathrm{x}} M_{\mathrm{x}\{\mathrm{a}\}}^2 \hat{V} - B^2}\right]\right)^2}{1 - \dfrac{\gamma_{\mathrm{x}}+1}{\gamma_{\mathrm{x}}-1}\hat{V}}. \tag{B.37}$$

These equations are combined to form a cubic equation for the specific volume $\hat{V}$, which must be solved numerically. The valid solution lies in the interval $\left(\hat{V}_{\min}, 1\right)$, where $\hat{V}_{\min}$ is defined as

$$\hat{V}_{\min} = \begin{cases} \dfrac{\gamma_{\mathrm{x}}-1}{\gamma_{\mathrm{x}}+1}, & \dfrac{B^2}{\gamma_{\mathrm{x}} M_{\mathrm{x}\{\mathrm{a}\}}^2} < \dfrac{\gamma_{\mathrm{x}}-1}{\gamma_{\mathrm{x}}+1}, \\ \dfrac{B^2}{\gamma_{\mathrm{x}} M_{\{\mathrm{a}\}}^2}, & \dfrac{B^2}{\gamma_{\mathrm{x}} M_{\mathrm{x}\{\mathrm{a}\}}^2} > \dfrac{\gamma_{\mathrm{x}}-1}{\gamma_{\mathrm{x}}+1}. \end{cases} \tag{B.38}$$

The pressure and the tangential magnetic field magnitude can then be calculated from the specific volume.

B.3.1.2 Slow shock wave

The slow shock wave exhibits a different behaviour to that of the fast shock wave. Quantities such as the pressure do not vary monotonically with the speed of the fluid as they do with a fast wave. This means that the approach taken for the fast wave is not valid. Instead, the tangential magnetic field will be used as a parameter in the Hugoniot curve and Rayleigh line. The Mach number will be replaced by

$$M_{\mathrm{x}\{\mathrm{a}\}}\left(\hat{V}, \hat{B}_t, A, B\right) = \sqrt{\frac{B^2}{\gamma_{\mathrm{x}}}\frac{\hat{B}_t - A}{\hat{B}_t \hat{V} - A}}. \tag{B.39}$$

The Hugoniot curve and Rayleigh line can be equated to form a quadratic equation for the specific volume $\hat{V}$,

$$a\hat{V}^2 + b\hat{V} + c = 0, \tag{B.40}$$

where the coefficients (a, b, c) are given by

$$a = \frac{\hat{B}_t}{2}\left(4\frac{\gamma_\mathrm{x}}{\gamma_\mathrm{x}-1} + \left(\hat{B}_t - A\right)^2 + \frac{\gamma_\mathrm{x}+1}{\gamma_\mathrm{x}-1}\left(A^2 - \hat{B}_t^2\right)\right) - \frac{\gamma_\mathrm{x}+1}{\gamma_\mathrm{x}-1}B^2\left(\hat{B}_t - A\right), \tag{B.41}$$

$$b = \frac{\gamma_\mathrm{x}}{\gamma_\mathrm{x}-1}\left(A\left(\hat{B}_t^2 - A^2\right) + 2B^2\left(\hat{B}_t - A\right) - 2\left(\hat{B}_t + A\right)\right), \tag{B.42}$$

$$c = \frac{2\gamma_\mathrm{x}}{\gamma_\mathrm{x}-1}A - \left(A^2 + B^2\right)\left(\hat{B}_t - A\right). \tag{B.43}$$

The two solutions $\hat{V}^+, \hat{V}^-$ are found using the quadratic formula. Only $\hat{V}^+$ is valid at all times and lies in the range $\left[(\gamma_\mathrm{x}+1)(\gamma_\mathrm{x}-1)^{-1}, 1\right]$. This approach requires the tangential magnetic magnitude of state $\{b\}$ to be known.

B.3.2 Rarefaction wave

If a rarefaction wave occurs, then both the fast and the slow waves can be determined from the solution of a system of ordinary differential equations for the primitive variables $\mathbf{u}$ replacing the specific energy with the pressure. The ordinary differential equations are parametrised by the variable s. The integration parameter has the range $s = (0, s_\mathrm{end})$ where s_end is defined as

$$s_\mathrm{end} = \begin{cases} s_\mathrm{max}\tanh(-\psi_f) & \text{fast rarefaction,} \\ -\psi_s & \text{slow rarefaction.} \end{cases} \tag{B.44}$$

s_max is defined as the point, where the magnitude of the tangential magnetic field is zero and $\psi_{f,s}$ are path variables that are used as part of the root finding process. Positive values of ψ indicate a shock and negative values indicate a rarefaction. The equations for the density and pressure can be integrated to give

$$\rho(s) = \rho_{\{\mathrm{a}\}}e^{-s}, \tag{B.45}$$

$$p(s) = p_{\{\mathrm{a}\}}e^{-\gamma s}. \tag{B.46}$$

The remaining primitive variables are acquired by solving the following ordinary differential equations

$$\frac{\mathrm{d}v_x(s)}{\mathrm{d}s} = \mp c_{s,f}(s), \tag{B.47}$$

$$\frac{\mathrm{d}\mathbf{v}_t(s)}{\mathrm{d}s} = \frac{c_{s,f}(s)}{\left(\frac{c_a(s)}{c_{s,f}(s)}\right)^2 - 1}\frac{\mathbf{B}_t(s)}{B_n}, \tag{B.48}$$

$$\frac{\mathrm{d}B_t(s)}{\mathrm{d}s} = \frac{B_t(s)}{\left(\frac{c_a(s)}{c_{sf}(s)}\right)^2 - 1}. \tag{B.49}$$

These equations are solved numerically.

A root find then needs to be performed on the path variables, the angle of rotation at both Alfvén waves and the pressure and normal velocity. For the shock waves the path variables have the following effect

$$\begin{cases} \psi_f, & v_s = c_f + \psi_f, \\ \psi_s, & B_t^{\{b\}} = A - \psi_s. \end{cases} \tag{B.50}$$

Appendix C

Convergence Results

This chapter presents convergence results for the single model, one-dimensional tests in Chapter 5. All tests have used ten resolutions between $N = 100$ and $N = 1000$ and calculated the order of convergence using the infinity norm (5.2). The third order Runge-Kutta time integrator and the third order WENO method are used.

The first test considered is the Euler Sod test, with initial data given in Table 5.1. The order of convergence was calculated to be 0.98. The convergence results are plotted in Figure C.1.

The next we considered the special-relativistic shock tube, with initial data given in Table 5.2. The order of convergence was calculated to be 1.00. The convergence results are plotted in Figure C.2.

The special-relativistic, blast wave test was considered next, with initial data given in Table 5.3. The order of convergence was calculated to be 1.16. The convergence results are plotted in Figure C.3.

The ideal MHD, shock tube test was considered, with initial data given in Table 5.4. The order of convergence was calculated to be 0.99. The convergence results are plotted in Figure C.4.

Finally, the special-relativistic, ideal MHD, shock tube test was considered. The initial data was given in Table 5.5. The order of convergence was calculated to be 1.06. The convergence results are plotted in Figure C.5.

All of test achieved the expected level of convergence for solutions that contain discontinuities.

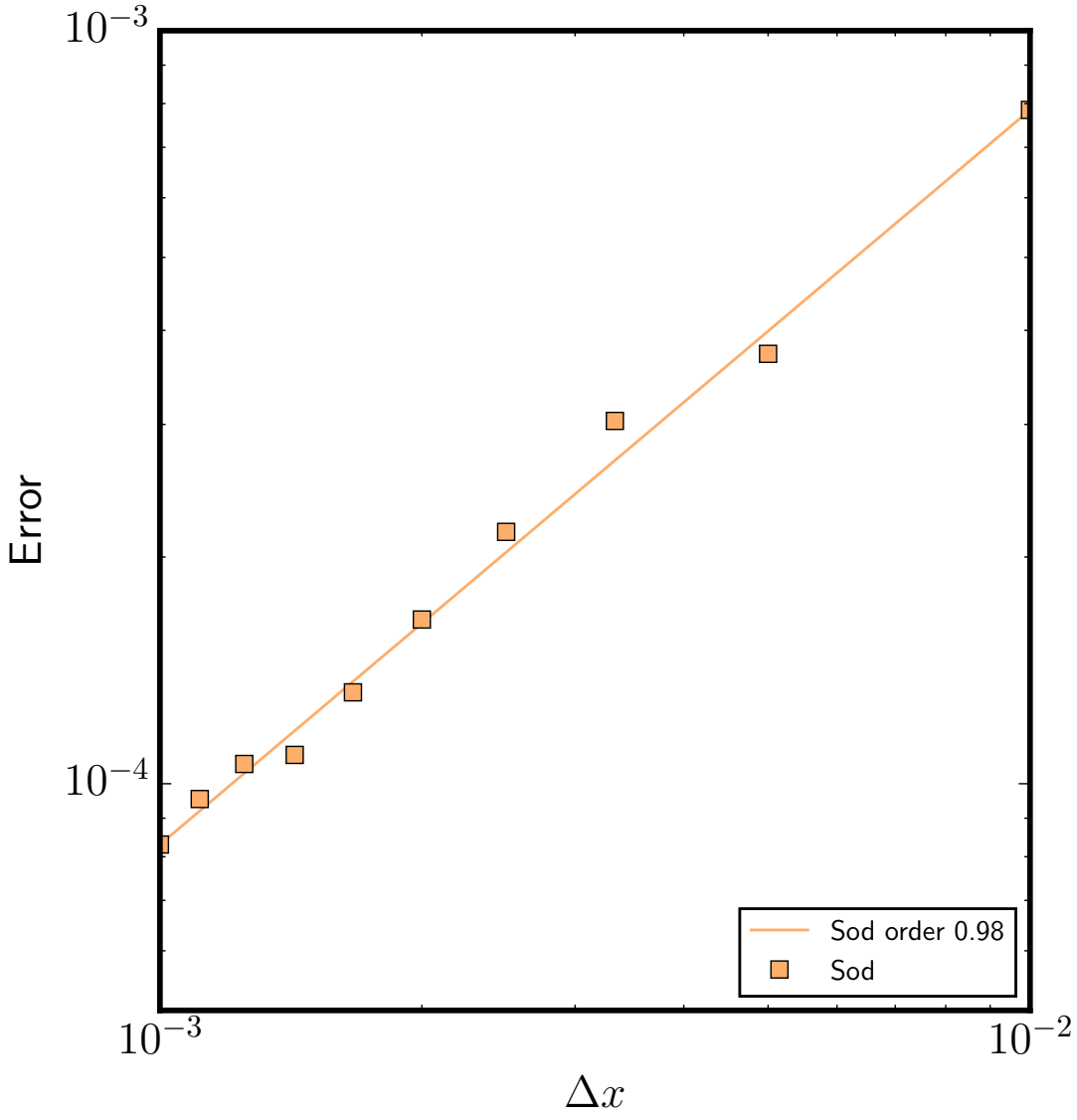

Figure C.1 – Newtonian Sod convergence results. Ten resolutions are used between: 100 and 1000 cells. The rate of convergence obtained is 0.98. This sub-linear convergence is due to the presence of two discontinuities in the density.

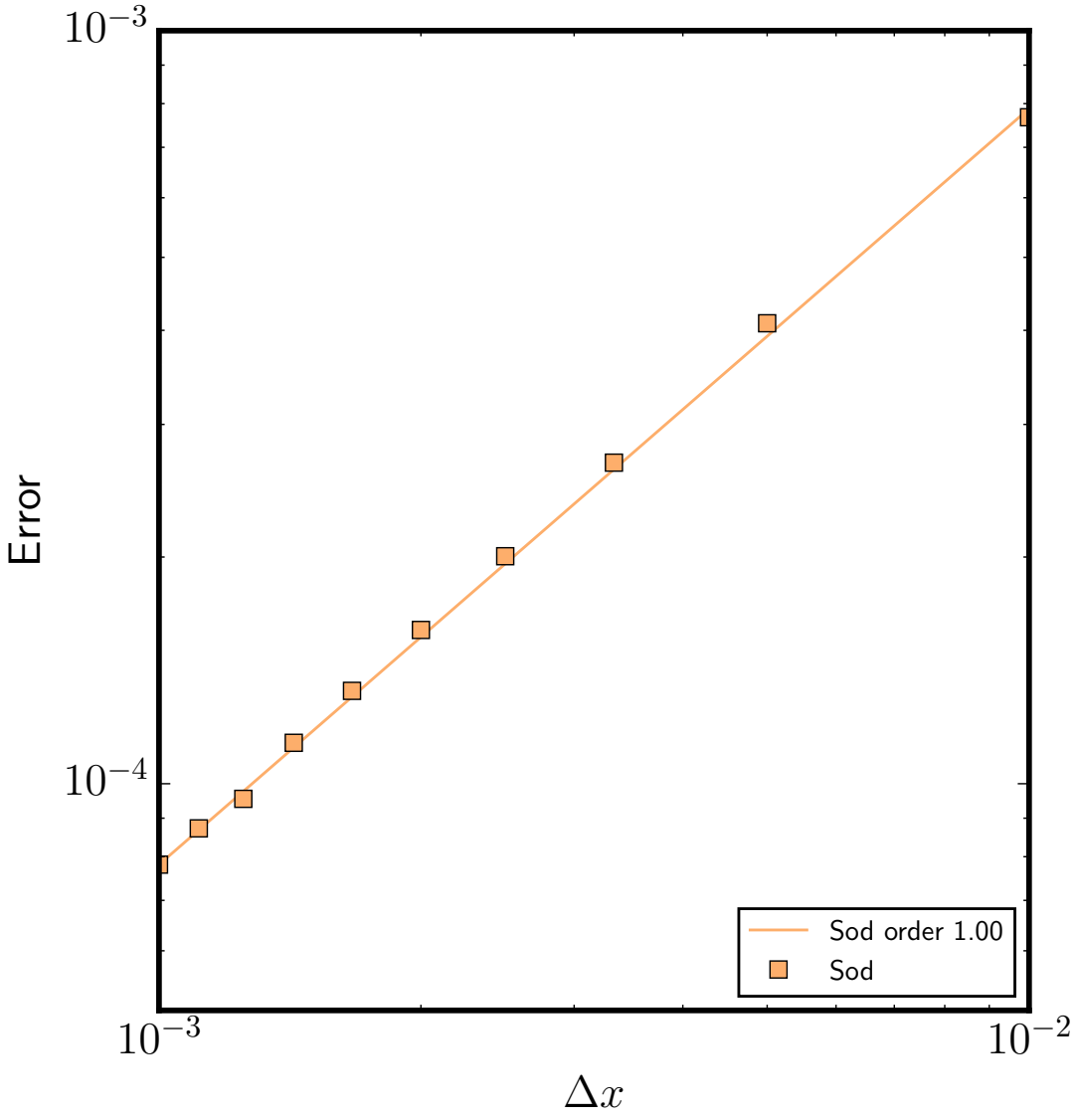

Figure C.2 – SR Sod convergence results. Ten resolutions are used between: 100 and 1000 cells. The rate of convergence obtained is 1.0. This linear convergence is due to the presence of two discontinuities in the density.

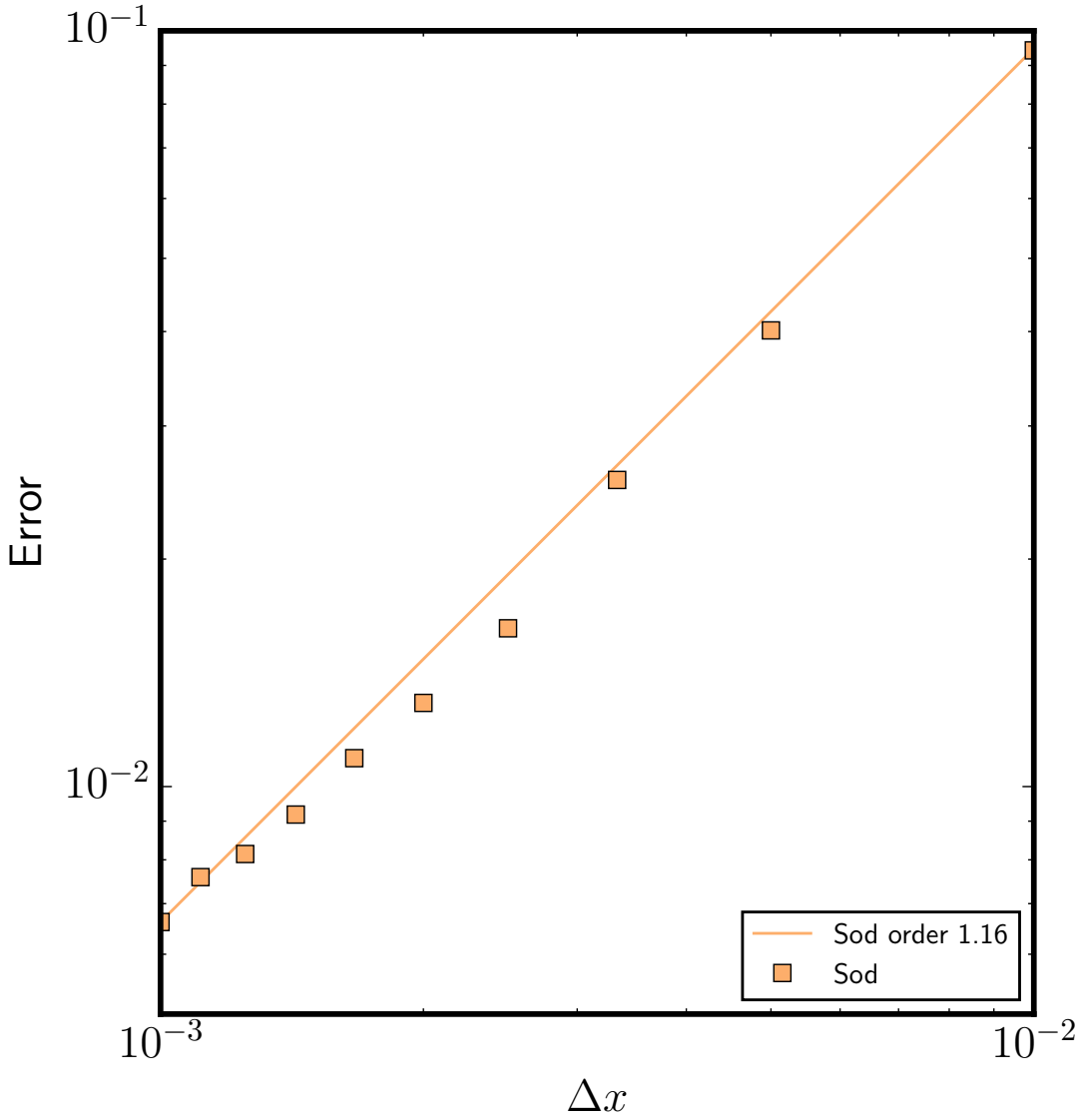

Figure C.3 – SR blast convergence results. Ten resolutions are used between: 100 and 1000 cells. The rate of convergence obtained is 1.16. This above-linear convergence is due to the presence of two discontinuities in the density close together. This feature is hard to resolve at low resolution and this results in a higher error.

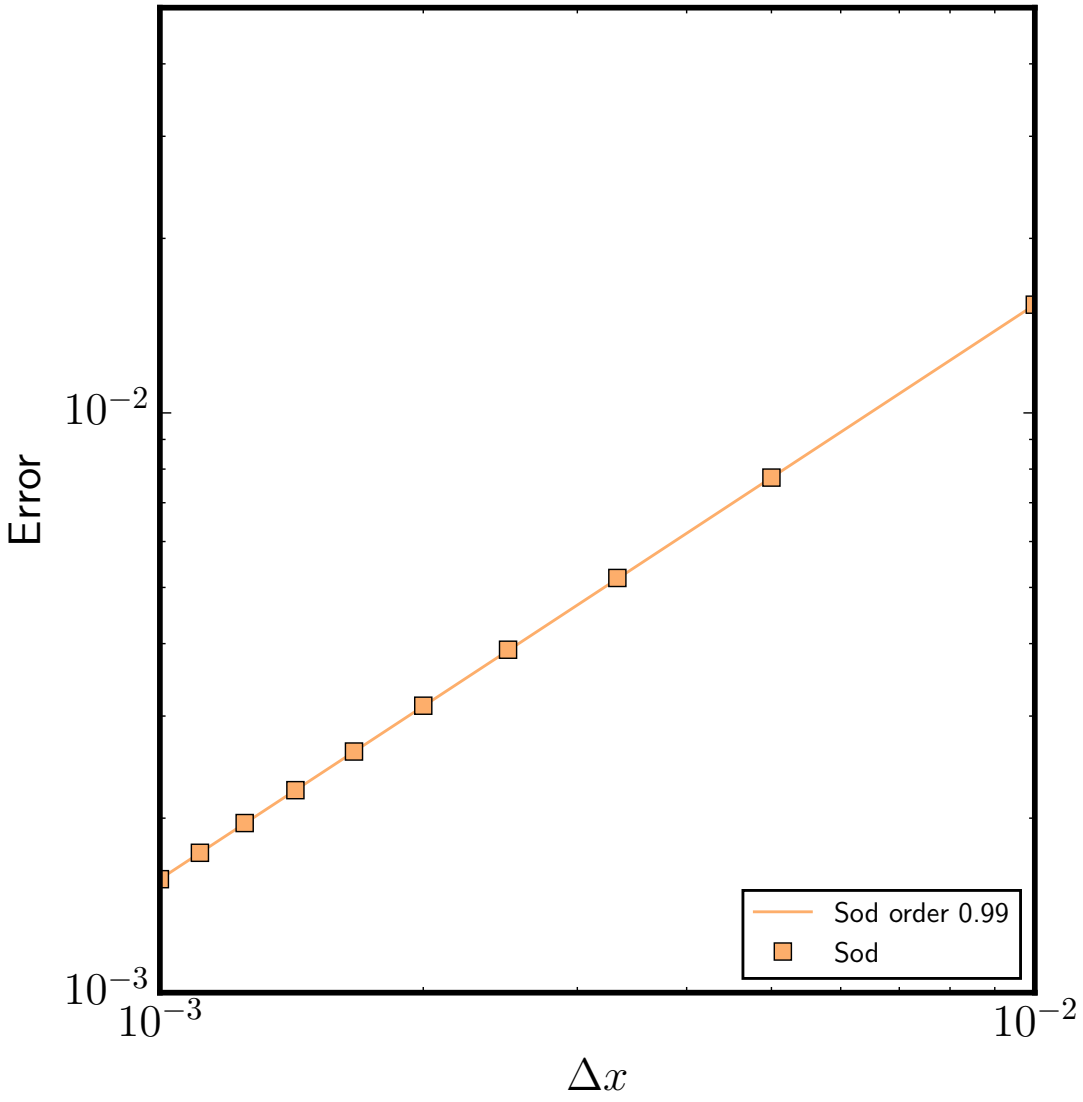

Figure C.4 – MHD convergence results. Ten resolutions are used between: 100 and 1000 cells. The rate of convergence obtained is 0.99.

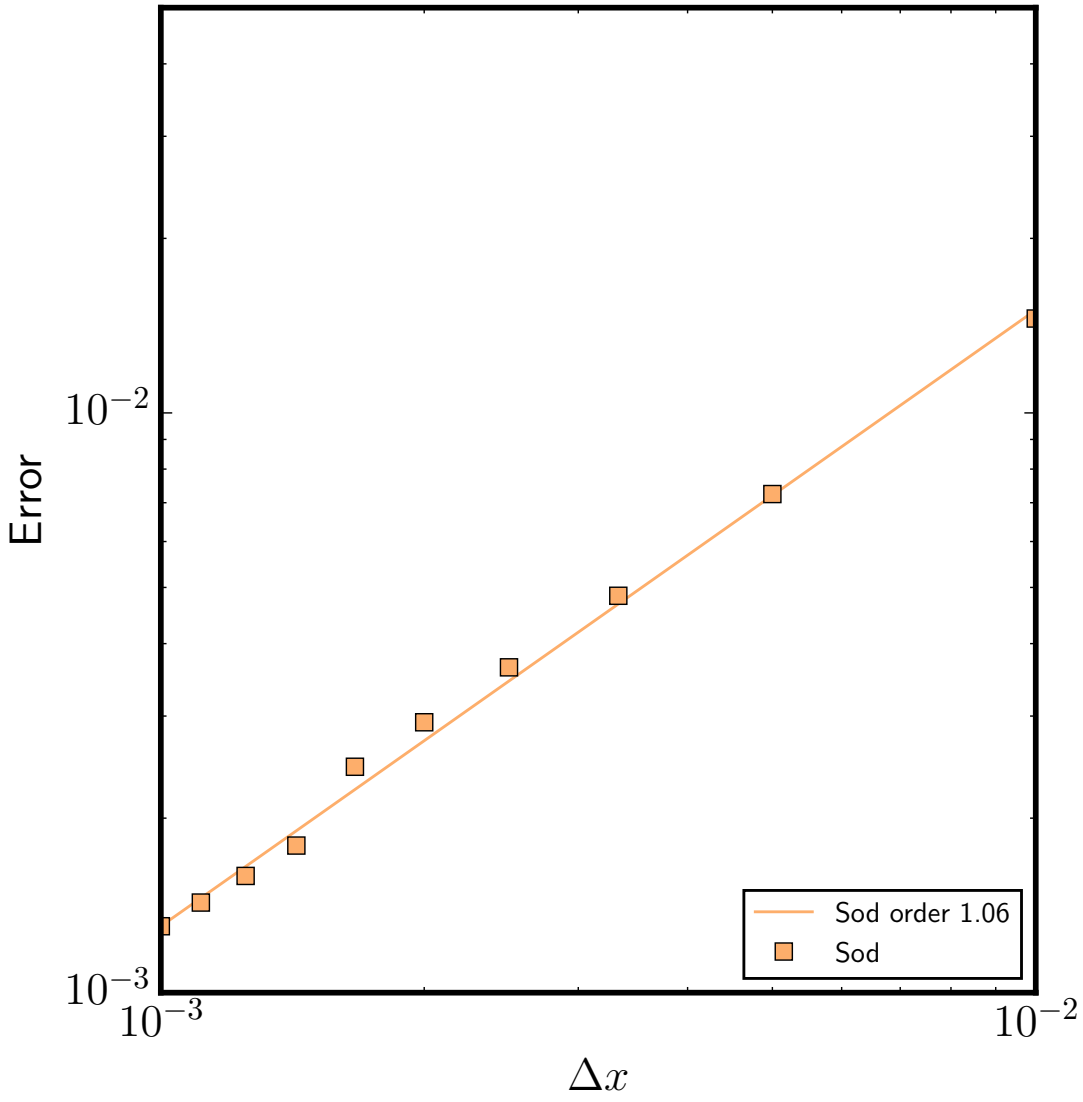

Figure C.5 – SRMHD blast convergence results. Ten resolutions are used between: 100 and 1000 cells. The rate of convergence obtained is 1.06.

Appendix D

Special-relativistic Magnetohydrodynamics

The eigenvectors provided in this section can be used to construct the conserved eigenvectors and the interface eigenvectors.

D.1 Covariant Eigenvectors

Anton et al. [14] provide a set of covariant eigenvectors that remain independent. The covariant variables are based on those calculated by Anile [13].

$$\tilde{u} = \left(u^{\mu}, b^{\mu}, p, \mathfrak{s}\right)^{T}. \tag{D.1}$$

The entropy eigenvector is

$$r^{e} = \left(0^{\mu}, 0^{\mu}, 0, 1\right)^{T}, \tag{D.2}$$

and the Alfvén eigenvector is

$$\tilde{r}_{a}^{\pm} = \left(f_1\alpha_1^{\mu} + f_2\alpha_2^{\mu}, \mp\sqrt{\mathcal{C}}\left(f_1\alpha_1^{\mu} + f_2\alpha_2^{\mu}\right), 0, 0\right)^{T}, \tag{D.3}$$

where

$$f_{1,2} = \begin{cases} \dfrac{g_{1,2}}{\sqrt{g_1^2 + g_2^2}} & \text{if normal or Type I degeneracy,} \\ \dfrac{1}{\sqrt{2}} & \text{if Type II or Type II',} \end{cases} \tag{D.4}$$

$$\alpha_1^{\mu} = W\left(v^z, \lambda v^z, 0, 1 - \lambda v^x\right), \tag{D.5}$$

$$\alpha_2^{\mu} = -W\left(v^y, \lambda v^y, 1 - \lambda v^x, 0\right), \tag{D.6}$$

$$\mathcal{C} = \rho h + b^2, \tag{D.7}$$

and

$$g_1 = \frac{1}{W}\left(B^y + \frac{\lambda v^y}{1-\lambda v^x}B^x\right), \tag{D.8}$$

$$g_2 = \frac{1}{W}\left(B^z + \frac{\lambda v^z}{1-\lambda v^x}B^x\right). \tag{D.9}$$

The magnetosonic eigenvector is

$$\tilde{r}_m^{\pm} = \left(d^\mu, L^\mu, C, 0\right)^T. \tag{D.10}$$

Its components depend on wether the wave's velocity is closer or further away to the Alfvén velocity. The components are

$$d^\mu = \begin{cases} -\dfrac{AC}{\rho h a^2\left(G+A^2\right)}\left(\phi^\mu + Au^\mu\right) - \left(\dfrac{\mathcal{B}}{A}\right)_m^{\pm}\dfrac{1}{\rho}\dfrac{b_t^\mu}{b_t} & \text{if closer,} \\ \dfrac{A}{\rho h a^2\left(G+A^2\right)}\left(\phi^\mu + Au^\mu\right) - \left(\dfrac{\mathcal{B}}{A}\right)_m^{\pm}\dfrac{Gbt^\mu}{\rho h\left(\rho h A^2 - b^2 G\right)} & \text{if further away,} \end{cases} \tag{D.11}$$

$$L^\mu = \begin{cases} -\left(\dfrac{\mathcal{B}}{A}\right)_m^{\pm}\dfrac{C}{\rho h}u^\mu - \left(1+\dfrac{A^2}{G}\right)\dfrac{b_t^\mu}{b_t} & \text{if closer,} \\ \left(\dfrac{\mathcal{B}}{A}\right)_m^{\pm}\dfrac{1}{\rho h}u^\mu - \left(1+\dfrac{A^2}{G}\right)\dfrac{Gb_t^\mu}{\rho h\left(\rho h A^2 - b^2 G\right)} & \text{if further away,} \end{cases} \tag{D.12}$$

$$C = \begin{cases} -\dfrac{\left(G+A^2\right)a^2}{A^2-\left(G+A^2\right)a^2}b_t & \text{if closer,} \\ -1 & \text{if further away,} \end{cases} \tag{D.13}$$

where

$$A = u^\mu \phi_\mu, \tag{D.14}$$

$$G = \phi^\mu \phi_\mu, \tag{D.15}$$

$$\phi_\mu = (-\lambda, 1, 0, 0), \tag{D.16}$$

$$\frac{b_t^\mu}{b_t} = \frac{\left(f_1\alpha_{12} + f_2\alpha_{22}\right)\alpha_1^\mu - \left(f_1\alpha_{11} + f_2\alpha_{12}\right)\alpha_2^\mu}{\sqrt{\left(\alpha_{11}\alpha_{22} - \alpha_{12}^2\right)\left(f_1^2\alpha_{11} + 2f_1f_2\alpha_{12} + f_2^2\alpha_{22}\right)}}, \tag{D.17}$$

$$\alpha_{11} = \alpha_1^\mu \alpha_{1\mu}, \tag{D.18a}$$

$$\alpha_{22} = \alpha_2^\mu \alpha_{2\mu}, \tag{D.18b}$$

$$\alpha_{12} = \alpha_1^\mu \alpha_{2\mu}, \tag{D.18c}$$

and

$$b_t^\mu = C_1 \alpha_1^\mu + C_2 \alpha_2^\mu, \tag{D.19}$$

$$C_1 = \frac{g_1 \alpha_{12} + g_2 \alpha_{22}}{\alpha_{11}\alpha_{22} - \alpha_{12}^2} W \left(1 - \lambda v^x\right), \tag{D.20}$$

$$C_2 = -\frac{g_1 \alpha_{11} + g_2 \alpha_{12}}{\alpha_{11}\alpha_{22} - \alpha_{12}^2} W \left(1 - \lambda v^x\right), \tag{D.21}$$

$$b_t = \sqrt{b_t^\mu b_{t\mu}}, \tag{D.22}$$

$$\frac{b_t^\mu}{\rho h A^2 - b^2 G} = \begin{cases} \dfrac{b_t^\mu}{\rho h A^2 - b^2 G} & \text{if not Type II'}, \\ 0 & \text{if Type II'}, \end{cases} \tag{D.23}$$

finally,

$$\left(\frac{\mathcal{B}}{A}\right)_\pm^m = \mp \sqrt{\left(\rho h + \frac{b^2}{a^2}\right) - \rho h \left(\frac{1}{a^2} - 1\right) \frac{A^2}{G}}. \tag{D.24}$$

Appendix E

Mach 40 Newtonian Bubble: Lower Resolution

The results presented in this chapter can be used to compare against those presented in Subsection 7.2.2. This resolution in this section is 600 x 180 and the initial conditions are given in Table 7.5.

Figure E.1 shows that the shock wave has already exited the bubble after 1s. The strength of the shock wave has resulted in a large build up of density ahead of the bubble. The bubble has also been severely flattened. The vorticity compared to Figure 7.8 is an order of magnitude higher.

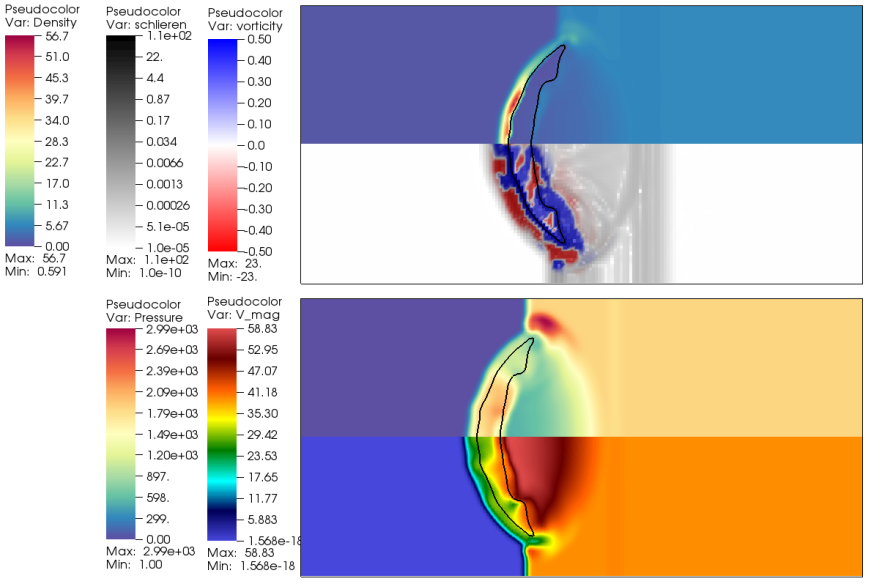

Figure E.1 – The shock wave has already exited the bubble at $T = 1$. The strength of the shock wave has resulted in a large build up of density ahead of the bubble. The bubble has also been severely flattened. The vorticity compared to Figure 7.8 is an order of magnitude higher.

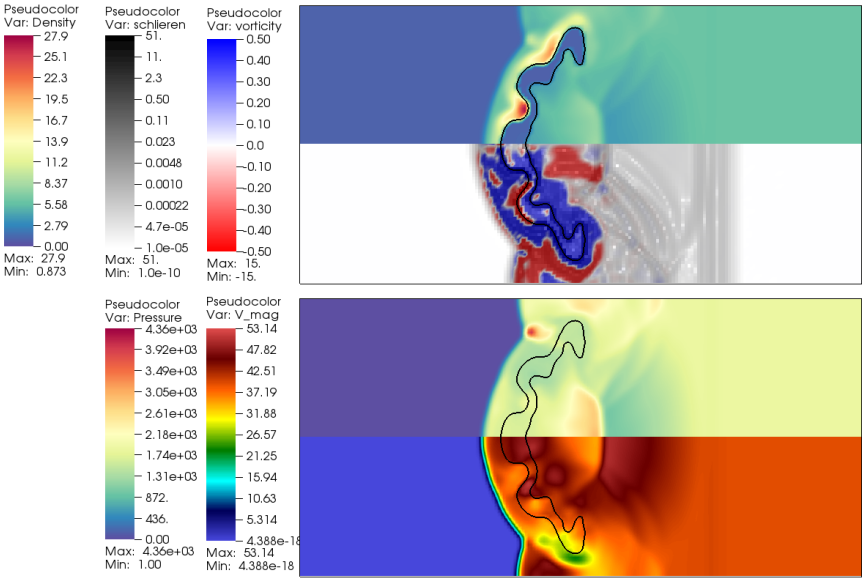

Figure E.2 – mRGFM at $T = 2$. The bubble's surface has become distorted due to the vorticity. The results are symmetric, which demonstrates that our numerical methods are symmetric.

In Figure E.2 the bubble's surface has become distorted due to the vorticity. It should be noted that the results are symmetric about the $y = 0$ line. This demonstrates that our numerical methods are symmetric.

Figure E.3 shows that the bubble's surface has continued to curl up and become distorted. Finger-like regions have developed. As explained in Subsection 6.2.1, our numerical method will begin to rely on fallback mechanism, due to a lack of resolution. These fallbacks ensure that two different models are always used in the multi-material Riemann problem. Numerical errors introduced by these fallback mechanisms could be prevented by using adaptive mesh refinement.

In the final plot, shown in Figure E.4, the bubble has started to break up. The numerical errors mentioned in Figure E.3 are now clearly noticeable. The bubble is no longer symmetric as shown by the zero contour of the level set.

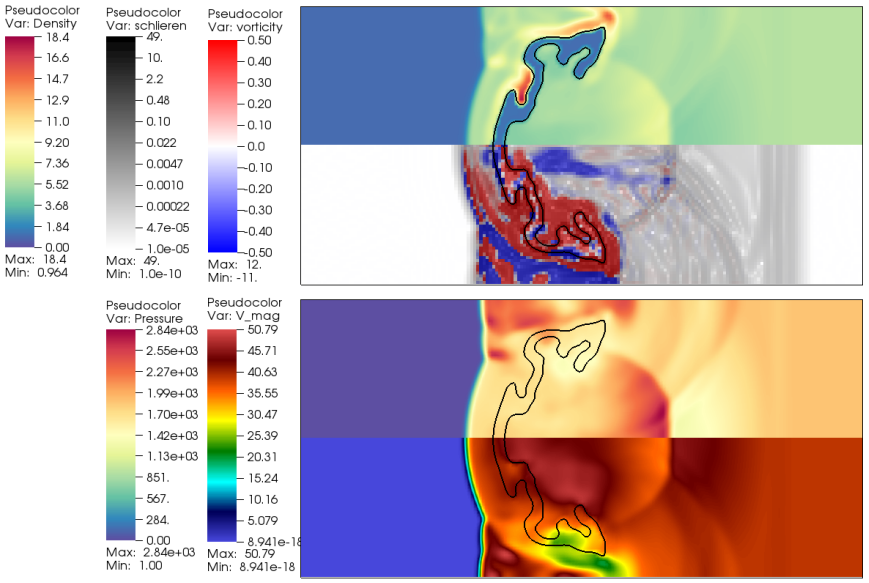

Figure E.3 – mRGFM at $T = 3$. The bubble's surface has continued to curl up and become distorted. Finger-like regions have developed. As explained in Subsection 6.2.1, our numerical method will begin to rely on fallback mechanisms, due to a lack of resolution.

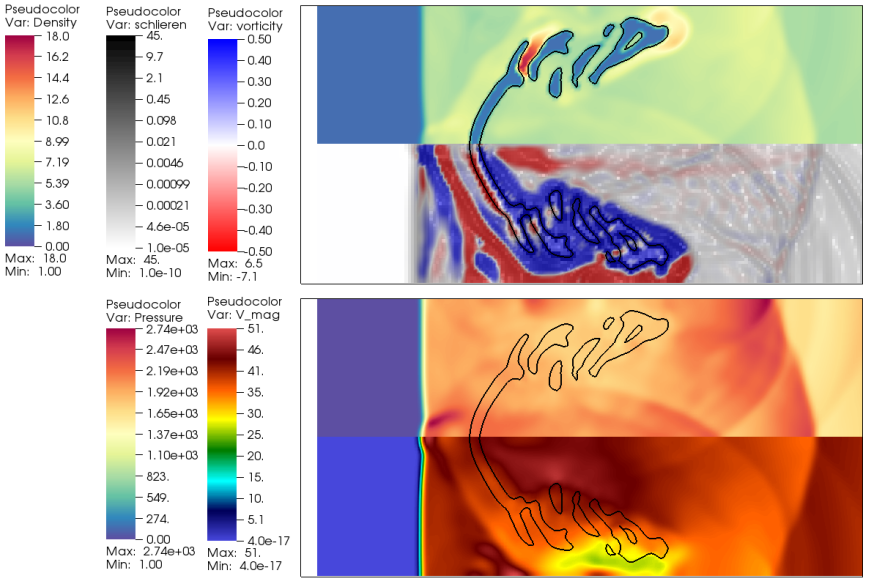

Figure E.4 – mRGFM at $T = 5$. The bubble has started to break up. The numerical errors mentioned in Figure E.3 are now clearly noticeable. The bubble is no longer symmetric.

References

[1] Abgrall, R. and Karni, S. (2001). Computations of Compressible Multifluids. *Journal of Computational Physics*, 169:594–623.

[2] Alcubierre, M. (2008). *Introduction to 3 + 1 numerical relativity*. Oxford Univ. Press.

[3] Alfvén, H. (1942). Existence of Electromagnetic-Hydrodynamic Waves. Nature, 150:405–406.

[4] Aloy, M. A. and Rezzolla, L. (2006). A Powerful Hydrodynamic Booster for Relativistic Jets. ApJ, 640:L115–L118.

[5] Anderson, M., Hirschmann, E. W., Lehner, L., Liebling, S. L., Motl, P. M., Neilsen, D., Palenzuela, C., and Tohline, J. E. (2008). Magnetized Neutron-Star Mergers and Gravitational-Wave Signals. *Physical Review Letters*, 100(19):191101.

[6] Andersson, N. (2003). Gravitational waves from instabilities in relativistic stars. *Classical and Quantum Gravity*, 20:105.

[7] Andersson, N. (2012). Resistive relativistic magnetohydrodynamics from a charged multifluids perspective. Phys. Rev. D, 86(4):043002.

[8] Andersson, N. and Comer, G. L. (2007). Relativistic Fluid Dynamics: Physics for Many Different Scales. *Living Reviews in Relativity*.

[9] Andersson, N., Comer, G. L., and Glampedakis, K. (2005). How viscous is a superfluid neutron star core? *Nuclear Physics A*, 763:212–229.

[10] Andersson, N., Ferrari, V., Jones, D. I., Kokkotas, K. D., Krishnan, B., Read, J. S., Rezzolla, L., and Zink, B. (2011). Gravitational waves from neutron stars: promises and challenges. *General Relativity and Gravitation*, 43:409–436.

[11] Andersson, N., Sidery, T., and Comer, G. L. (2006). Mutual friction in superfluid neutron stars. MNRAS, 368:162–170.

[12] Anile, A. and Pennisi, S. (1987). On the mathematical structure of test relativistic magnetofluiddynamics. In *Annales de l'IHP Physique théorique*, volume 46, pages 27–44. Elsevier.

[13] Anile, A. M. (1989). *Relativistic fluids and magneto-fluids : with applications in astrophysics and plasma physics*. Cambridge Univ. Press.

[14] Antón, L., Miralles, J. A., Martí, J. M., Ibáñez, J. M., Aloy, M. A., and Mimica, P. (2010). Relativistic Magnetohydrodynamics: Renormalized Eigenvectors and Full Wave Decomposition Riemann Solver. ApJS, 188:1–31.

[15] Baade, W. and Zwicky, F. (1934). Remarks on Super-Novae and Cosmic Rays. *Physical Review*, 46:76–77.

[16] Baiko, D. A., Haensel, P., and Yakovlev, D. G. (2001). Thermal conductivity of neutrons in neutron star cores. A&A, 374:151–163.

[17] Baiotti, L., Damour, T., Giacomazzo, B., Nagar, A., and Rezzolla, L. (2010). Analytic Modeling of Tidal Effects in the Relativistic Inspiral of Binary Neutron Stars. *Physical Review Letters*, 105(26):261101.

[18] Baiotti, L., Damour, T., Giacomazzo, B., Nagar, A., and Rezzolla, L. (2011). Accurate numerical simulations of inspiralling binary neutron stars and their comparison with effective-one-body analytical models. Phys. Rev. D, 84(2):024017.

[19] Baiotti, L., Giacomazzo, B., and Rezzolla, L. (2008). Accurate evolutions of inspiralling neutron-star binaries: Prompt and delayed collapse to a black hole. Phys. Rev. D, 78(8):084033.

[20] Balsara, D. (2001). Total Variation Diminishing Scheme for Relativistic Magnetohydrodynamics. ApJS, 132:83–101.

[21] Balsara, D. S. and Spicer, D. S. (1999). A staggered mesh algorithm using high order godunov fluxes to ensure solenoidal magnetic fields in magnetohydrodynamic simulations. *Journal of Computational Physics*, 149(2):270 – 292.

[22] Barack, L. (2009). Gravitational self-force in extreme mass-ratio inspirals. *Classical and Quantum Gravity*, 26(21):213001.

[23] Barton, P. T., Obadia, B., and Drikakis, D. (2011). A conservative level-set based method for compressible solid/fluid problems on fixed grids. *Journal of Computational Physics*, 230:7867–7890.

[24] Baumgarte, T. W. and Shapiro, S. L. (1999). Numerical integration of Einstein's field equations. Phys. Rev. D, 59(2):024007.

[25] Baym, G. and Pethick, C. (1979). Physics of neutron stars. ARA&A, 17:415–443.

[26] Beckwith, K. and Stone, J. M. (2011). A Second-order Godunov Method for Multi-dimensional Relativistic Magnetohydrodynamics. ApJS, 193:6.

[27] Berger, M. J. and Colella, P. (1989). Local adaptive mesh refinement for shock hydrodynamics. *Journal of Computational Physics*, 82:64–84.

[28] Beskin, V. S. (2009). *MHD Flows in Compact Astrophysical Objects: Accretion, Winds and Jets*. Springer.

[29] Bethe, H. A., Börner, G., and Sato, K. (1970). Nuclei in Neutron Matter. A&A, 7:279.

[30] Blanchet, L. (2006). Gravitational Radiation from Post-Newtonian Sources and Inspiralling Compact Binaries. *Living Reviews in Relativity*, 9.

[31] Bourne, N. K. and Field, J. E. (1992). Shock-induced collapse of single cavities in liquids. *Journal of Fluid Mechanics*, 244:225–240.

[32] Boyko, B., Bykov, A., Dolotenko, M., Kolokolchikov, N., Markevtsev, I., Tatsenko, O., and Shuvalov, K. (1999). With record magnetic fields to the 21st Century. In *Pulsed Power Conference, 1999. Digest of Technical Papers. 12th IEEE International*, volume 2, pages 746–749. IEEE.

[33] Brackbill, J. U. and Barnes, D. C. (1980). The effect of nonzero $\nabla \cdot B$ on the numerical solution of the magnetohydrodynamic equations. *Journal of Computational Physics*, 35:426–430.

[34] Brio, M. and Wu, C. (1988). An upwind differencing scheme for the equations of ideal magnetohydrodynamics. *Journal of Computational Physics*, 75(2):400 – 422.

[35] Chadwick, J. (1932). The existence of a neutron. *Proceedings of the Royal Society of London. Series A, Containing Papers of a Mathematical and Physical Character*, 136(830):pp. 692–708.

[36] Chamel, N. and Haensel, P. (2008). Physics of Neutron Star Crusts. *Living Reviews in Relativity*, 11.

[37] Chandrasekhar, S. (1935). The highly collapsed configurations of a stellar mass (Second paper). MNRAS, 95:207–225.

[38] Chen, F. (1984). *Introduction to Plasma Physics and Controlled Fusion, Volume 1*. Springer.

[39] Courant, R., Friedrichs, K., and Lewy, H. (1967). On the Partial Difference Equations of Mathematical Physics. *IBM Journal of Research and Development*, 11:215–234.

[40] Davis, S. F. (1992). An interface tracking method for hyperbolic systems of conservation laws. *Applied Numerical Mathematics*, 10(6):447 – 472.

[41] Dedner, A., Kemm, F., Kröner, D., Munz, C.-D., Schnitzer, T., and Wesenberg, M. (2002). Hyperbolic Divergence Cleaning for the MHD Equations. *Journal of Computational Physics*, 175:645–673.

[42] Del Zanna, L., Bucciantini, N., and Londrillo, P. (2003). An efficient shock-capturing central-type scheme for multidimensional relativistic flows. II. Magnetohydrodynamics. A&A, 400:397–413.

[43] Del Zanna, L., Zanotti, O., Bucciantini, N., and Londrillo, P. (2007). ECHO: a Eulerian conservative high-order scheme for general relativistic magnetohydrodynamics and magnetodynamics. A&A, 473:11–30.

[44] Diener, P. (2003). A new general purpose event horizon finder for 3D numerical spacetimes. *Classical and Quantum Gravity*, 20:4901–4917.

[45] D'Inverno, R. A. (1992). *Introducing Einstein's relativity*. Clarendon Press.

[46] D'Inverno, R. A. and Smallwood, J. (1980). Covariant 2+2 formulation of the initial-value problem in general relativity. Phys. Rev. D, 22:1233–1247.

[47] Dionysopoulou, K., Alic, D., Palenzuela, C., Rezzolla, L., and Giacomazzo, B. (2013). General-relativistic resistive magnetohydrodynamics in three dimensions: Formulation and tests. Phys. Rev. D, 88(4):044020.

[48] Dumbser, M., Balsara, D. S., Toro, E. F., and Munz, C.-D. (2008). A unified framework for the construction of one-step finite volume and discontinuous galerkin schemes on unstructured meshes. *Journal of Computational Physics*, 227(18):8209 – 8253.

[49] Duncan, R. C. and Thompson, C. (1992). Formation of very strongly magnetized neutron stars - Implications for gamma-ray bursts. ApJ, 392:L9–L13.

[50] Einstein, A. (1915). Die Feldgleichungen der Gravitation. *Sitzungsberichte der Königlich Preußischen Akademie der Wissenschaften (Berlin), Seite 844-847.*, pages 844–847.

[51] Enright, D., Fedkiw, R., Ferziger, J., and Mitchell, I. (2002). A Hybrid Particle Level Set Method for Improved Interface Capturing. *Journal of Computational Physics*, 183:83–116.

[52] Espinoza, C. M., Lyne, A. G., Kramer, M., Manchester, R. N., and Kaspi, V. M. (2011a). The Braking Index of PSR J1734-3333 and the Magnetar Population. ApJ, 741:L13.

[53] Espinoza, C. M., Lyne, A. G., Stappers, B. W., and Kramer, M. (2011b). A study of 315 glitches in the rotation of 102 pulsars. MNRAS, 414:1679–1704.

[54] Evans, C. R. and Hawley, J. F. (1988). Simulation of magnetohydrodynamic flows - A constrained transport method. ApJ, 332:659–677.

[55] Fedkiw, R. P., Aslam, T., Merriman, B., and Osher, S. (1999a). A Non-oscillatory Eulerian Approach to Interfaces in Multimaterial Flows (the Ghost Fluid Method). *Journal of Computational Physics*, 152:457–492.

[56] Fedkiw, R. P., Marquina, A., and Merriman, B. (1999b). An Isobaric Fix for the Overheating Problem in Multimaterial Compressible Flows. *Journal of Computational Physics*, 148:545–578.

[57] Flowers, E. and Itoh, N. (1979). Transport properties of dense matter. II. ApJ, 230:847–858.

[58] Font, J. A. (2008). Numerical Hydrodynamics and Magnetohydrodynamics in General Relativity. *Living Reviews in Relativity*, 11.

[59] Fryer, C. L. and New, K. C. B. (2011). Gravitational Waves from Gravitational Collapse. *Living Reviews in Relativity*, 14.

[60] Gerolymos, G. A., Sénéchal, D., and Vallet, I. (2009). Very-high-order WENO schemes. *Journal of Computational Physics*, 228:8481–8524.

[61] Giacomazzo, B. and Perna, R. (2013). Formation of Stable Magnetars from Binary Neutron Star Mergers. ApJ, 771:L26.

[62] Giacomazzo, B. and Rezzolla, L. (2006). The exact solution of the Riemann problem in relativistic magnetohydrodynamics. *Journal of Fluid Mechanics*, 562:223–259.

[63] Giacomazzo, B., Rezzolla, L., and Baiotti, L. (2011). Accurate evolutions of inspiralling and magnetized neutron stars: Equal-mass binaries. Phys. Rev. D, 83(4):044014.

[64] Gingold, R. A. and Monaghan, J. J. (1977). Smoothed particle hydrodynamics - Theory and application to non-spherical stars. MNRAS, 181:375–389.

[65] Godunov, S. K. (1959). A difference method for numerical calculation of discontinuous solutions of the equations of hydrodynamics. *Mat. Sb. (N.S.)*, 47 (89):271–306.

[66] Goedbloed, J. and Poedts, S. (2004). *Principles of magnetohydrodynamics: with applications to laboratory and astrophysical plasmas*, volume 6. Cambridge Univ. Press.

[67] Gold, T. (1968). Rotating Neutron Stars as the Origin of the Pulsating Radio Sources. Nature, 218:731–732.

[68] Goldreich, P. and Julian, W. H. (1969). Pulsar Electrodynamics. ApJ, 157:869.

[69] Gottlieb, D. and Orszag, S. A. (1983). *Numerical analysis of spectral methods: theory and applications*. SIAM.

[70] Gottlieb, S. (2005). On high order strong stability preserving runge?kutta and multi step time discretizations. *Journal of Scientific Computing*, 25(1):105–128.

[71] Gottlieb, S., Ketcheson, D., and Shu, C.-W. (2009). High order strong stability preserving time discretizations. *Journal of Scientific Computing*, 38(3):251–289.

[72] Gundlach, C., Hawke, I., and Erickson, S. J. (2012). A conservation law formulation of nonlinear elasticity in general relativity. *Classical and Quantum Gravity*, 29(1):015005.

[73] Haas, J.-F. and Sturtevant, B. (1987). Interaction of weak shock waves with cylindrical and spherical gas inhomogeneities. *Journal of Fluid Mechanics*, 181:41–76.

[74] Hannam, M. (2009). Status of black-hole-binary simulations for gravitational-wave detection. *Classical and Quantum Gravity*, 26(11):114001.

[75] Harding, A. K. and Lai, D. (2006). Physics of strongly magnetized neutron stars. *Reports on Progress in Physics*, 69:2631–2708.

[76] Harten, A., Lax, P. D., and van Leer, B. (1983). On Upstream Differencing and Godunov-Type Schemes for Hyperbolic Conservation Laws. *SIAM Review*, 25(1):35–61.

[77] Harten, A. and Osher, S. (1987). Uniformly High-Order Accurate Nonoscillatory Schemes. I. *SIAM Journal on Numerical Analysis*, 24:279–309.

[78] Hewish, A., Bell, S. J., Pilkington, J. D. H., Scott, P. F., and Collins, R. A. (1968). Observation of a Rapidly Pulsating Radio Source. Nature, 217:709–713.

[79] Hinder, I., Buonanno, A., Boyle, M., Etienne, Z. B., Healy, J., Johnson-McDaniel, N. K., Nagar, A., Nakano, H., Pan, Y., Pfeiffer, H. P., Pürrer, M., Reisswig, C., Scheel, M. A., Schnetter, E., Sperhake, U., Szilágyi, B., Tichy, W., Wardell, B., Zenginoğlu, A., Alic, D., Bernuzzi, S., Bode, T., Brügmann, B., Buchman, L. T., Campanelli, M., Chu, T., Damour, T., Grigsby, J. D., Hannam, M., Haas, R., Hemberger, D. A., Husa, S., Kidder, L. E., Laguna, P., London, L., Lovelace, G., Lousto, C. O., Marronetti, P., Matzner, R. A., Mösta, P., Mroué, A., Müller, D., Mundim, B. C., Nerozzi, A., Paschalidis, V., Pollney, D., Reifenberger, G., Rezzolla, L., Shapiro, S. L., Shoemaker, D., Taracchini, A., Taylor, N. W., Teukolsky, S. A., Thierfelder, M., Witek, H., and Zlochower, Y. (2013). Error-analysis and comparison to analytical models of numerical waveforms produced by the NRAR Collaboration. *Classical and Quantum Gravity*, 31(2):025012.

[80] Hirt, C. W. and Nichols, B. D. (1981). Volume of fluid /VOF/ method for the dynamics of free boundaries. *Journal of Computational Physics*, 39:201–225.

[81] Ho, W. C. G. and Andersson, N. (2012). Rotational evolution of young pulsars due to superfluid decoupling. *Nature Physics*, 8:787–789.

[82] Hobbs, G., Coles, W., Manchester, R. N., Keith, M. J., Shannon, R. M., Chen, D., Bailes, M., Bhat, N. D. R., Burke-Spolaor, S., Champion, D., Chaudhary, A., Hotan, A., Khoo, J., Kocz, J., Levin, Y., Oslowski, S., Preisig, B., Ravi, V., Reynolds, J. E., Sarkissian, J., van Straten, W., Verbiest, J. P. W., Yardley, D., and You, X. P. (2012). Development of a pulsar-based time-scale. MNRAS, 427:2780–2787.

[83] Howison, S. (2005). *Practical applied mathematics: modelling, analysis, approximation*. Cambridge Univ. Press.

[84] Hu, X. and Khoo, B. (2004). An interface interaction method for compressible multifluids. *Journal of Computational Physics*, 198(1):35 – 64.

[85] Hulse, R. A. and Taylor, J. H. (1975). Discovery of a pulsar in a binary system. ApJ, 195:L51–L53.

[86] Hussaini, M. Y. and Zang, T. A. (1987). Spectral methods in fluid dynamics. *Annual Review of Fluid Mechanics*, 19:339–367.

[87] Ianniello, S. and Di Mascio, A. (2010). A self-adaptive oriented particles Level-Set method for tracking interfaces. *Journal of Computational Physics*, 229:1353–1380.

[88] Jiang, G.-S. and Shu, C.-W. (1996). Efficient Implementation of Weighted ENO Schemes. *Journal of Computational Physics*, 126:202–228.

[89] Keppens, R., Meliani, Z., van der Holst, B., and Casse, F. (2008). Extragalactic jets with helical magnetic fields: relativistic MHD simulations. A&A, 486:663–678.

[90] Keppens, R., Meliani, Z., van Marle, A. J., Delmont, P., Vlasis, A., and van der Holst, B. (2012). Parallel, grid-adaptive approaches for relativistic hydro and magnetohydrodynamics. *Journal of Computational Physics*, 231:718–744.

[91] Kokkotas, K. D. (2008). *Gravitational Wave Astronomy*. Wiley-VCH Verlag GmbH & Co. KGaA.

[92] Komissarov, S. S. (1999). A Godunov-type scheme for relativistic magnetohydrodynamics. MNRAS, 303:343–366.

[93] Komissarov, S. S. (2011). 3+1 magnetodynamics. MNRAS, 418:L94–L98.

[94] Lander, S. K. and Jones, D. I. (2011). Oscillations and instabilities in neutron stars with poloidal magnetic fields. MNRAS, 412:1730–1740.

[95] Lander, S. K., Jones, D. I., and Passamonti, A. (2010). Oscillations of rotating magnetized neutron stars with purely toroidal magnetic fields. MNRAS, 405:318–328.

[96] Laney, C. B. (1998). *Computational gasdynamics*. Cambridge Univ. Press.

[97] Large, M. I., Vaughan, A. E., and Mills, B. Y. (1968). A Pulsar Supernova Association? Nature, 220:340–341.

[98] Lattimer, J. M. and Prakash, M. (2004). The Physics of Neutron Stars. *Science*, 304:536–542.

[99] Lax, P. and Wendroff, B. (1960). Systems of conservation laws. *Communications on Pure and Applied Mathematics*, 13(2):217–237.

[100] LeVeque, R. J. (1992). *Numerical methods for conservation laws*. Birkhäuser.

[101] Lichnerowicz, A. (1967). *Relativistic Hydrodynamics and Magnetohydrodynamics*. W. A. Benjamin.

[102] Liu, T. G., Khoo, B. C., and Yeo, K. S. (2003). Ghost fluid method for strong shock impacting on material interface. *Journal of Computational Physics*, 190:651–681.

[103] Liu, X.-D., Osher, S., and Chan, T. (1994). Weighted Essentially Non-oscillatory Schemes. *Journal of Computational Physics*, 115:200–212.

[104] Löffler, F., Faber, J., Bentivegna, E., Bode, T., Diener, P., Haas, R., Hinder, I., Mundim, B. C., Ott, C. D., Schnetter, E., Allen, G., Campanelli, M., and Laguna, P. (2012). The Einstein Toolkit: a community computational infrastructure for relativistic astrophysics. *Classical and Quantum Gravity*, 29(11):115001.

[105] Lorimer, D. R. (2008). Binary and Millisecond Pulsars. *Living Reviews in Relativity*, 11.

[106] Losasso, F., Shinar, T., Selle, A., and Fedkiw, R. (2006). Multiple interacting liquids. *ACM Trans. Graph.*, 25(3):812–819.

[107] Lundquist, S. (1949). Experimental Investigations of Magneto-Hydrodynamic Waves. *Physical Review*, 76:1805–1809.

[108] Manchester, R. N., Hobbs, G. B., Teoh, A., and Hobbs, M. (2005). The Australia Telescope National Facility Pulsar Catalogue. AJ, 129:1993–2006.

[109] Martí, J. M. and Müller, E. (1994a). Analytical solution of the Riemann problem in relativistic hydrodynamics. *Journal of Fluid Mechanics*, 258:317–333.

[110] Martí, J. M. and Müller, E. (1994b). The analytical solution of the Riemann problem in relativistic hydrodynamics. *Journal of Fluid Mechanics*, 258:317.

[111] Martí, J. M. and Müller, E. (2003). Numerical Hydrodynamics in Special Relativity. *Living Reviews in Relativity*, 6.

[112] Marx, J., Danzmann, K., Hough, J., Kuroda, K., McClelland, D., Mours, B., Phinney, S., Rowan, S., Sathyaprakash, B., Vetrano, F., Vitale, S., Whitcomb, S., and Will, C. (2011). The Gravitational Wave International Committee Roadmap: The future of gravitational wave astronomy. *ArXiv e-prints*.

[113] Millmore, S. T. (2010). *Interfaces in Numerical Relativistic Hydrodynamics*. PhD thesis, The University of Southampton.

[114] Millmore, S. T. and Hawke, I. (2010). Numerical simulations of interfaces in relativistic hydrodynamics. *Classical and Quantum Gravity*, 27(1):015007.

[115] Misner, C., Thorne, K., and Wheeler, J. (1973). *Gravitation*. W. H. Freeman.

[116] Miyoshi, T. and Kusano, K. (2005). A multi-state HLL approximate Riemann solver for ideal magnetohydrodynamics. *Journal of Computational Physics*, 208:315–344.

[117] Monaghan, J. J. (1992). Smoothed particle hydrodynamics. ARA&A, 30:543–574.

[118] Nichols, B. D., Hirt, C. W., and Hotchkiss, R. S. (1980). SOLA-VOF: A solution algorithm for transient fluid flow with multiple free boundaries. *NASA STI/Recon Technical Report N*, 81:14281.

[119] Noble, S. C., Gammie, C. F., McKinney, J. C., and Del Zanna, L. (2006). Primitive Variable Solvers for Conservative General Relativistic Magnetohydrodynamics. ApJ, 641:626–637.

[120] Ockendon, J. (2003). *Applied partial differential equations*. Oxford Univ. Press.

[121] Olausen, S. A. and Kaspi, V. M. (2014). The McGill Magnetar Catalog. ApJS, 212:6.

[122] Oppenheimer, J. R. and Volkoff, G. M. (1939). On Massive Neutron Cores. *Physical Review*, 55:374–381.

[123] Orszag, S. A. and Tang, C.-M. (1979). Small-scale structure of two-dimensional magnetohydrodynamic turbulence. *Journal of Fluid Mechanics*, 90:129–143.

[124] Osher, S. and Fedkiw, R. P. (2003). *Level set methods and dynamic implicit surfaces*. Springer.

[125] Ott, C. D., Abdikamalov, E., Mösta, P., Haas, R., Drasco, S., O'Connor, E. P., Reisswig, C., Meakin, C. A., and Schnetter, E. (2013). General-relativistic Simulations of Three-dimensional Core-collapse Supernovae. ApJ, 768:115.

[126] Page, D. and Reddy, S. (2006). Dense Matter in Compact Stars: Theoretical Developments and Observational Constraints. *Annual Review of Nuclear and Particle Science*, 56:327–374.

[127] Palenzuela, C. (2013). Modelling magnetized neutron stars using resistive magnetohydrodynamics. MNRAS, 431:1853–1865.

[128] Palenzuela, C., Lehner, L., Liebling, S. L., Ponce, M., Anderson, M., Neilsen, D., and Motl, P. (2013a). Linking electromagnetic and gravitational radiation in coalescing binary neutron stars. Phys. Rev. D, 88(4):043011.

[129] Palenzuela, C., Lehner, L., Ponce, M., Liebling, S. L., Anderson, M., Neilsen, D., and Motl, P. (2013b). Electromagnetic and Gravitational Outputs from Binary-Neutron-Star Coalescence. *Physical Review Letters*, 111(6):061105.

[130] Pareschi, L. and Russo, G. (2005). Implicit?explicit runge?kutta schemes and applications to hyperbolic systems with relaxation. *Journal of Scientific Computing*, 25(1):129–155.

[131] Paschalidis, V., Etienne, Z. B., and Shapiro, S. L. (2013). General-relativistic simulations of binary black hole-neutron stars: Precursor electromagnetic signals. Phys. Rev. D, 88(2):021504.

[132] Passamonti, A., Haskell, B., and Andersson, N. (2009). Oscillations of rapidly rotating superfluid stars. MNRAS, 396:951–963.

[133] Peralta, C., Melatos, A., Giacobello, M., and Ooi, A. (2006). Transitions between Turbulent and Laminar Superfluid Vorticity States in the Outer Core of a Neutron Star. ApJ, 651:1079–1091.

[134] Pitkin, M., Reid, S., Rowan, S., and Hough, J. (2011). Gravitational Wave Detection by Interferometry (Ground and Space). *Living Reviews in Relativity*, 14.

[135] Pons, J. A., Ma Martí, J., and Müller, E. (2000). The exact solution of the Riemann problem with non-zero tangential velocities in relativistic hydrodynamics. *Journal of Fluid Mechanics*, 422:125–139.

[136] Pons, J. A., Martí, J. M., and Müller, E. (2001). An exact riemann solver for multidimensional special relativistic hydrodynamics. In Toro, E., editor, *Godunov Methods*, pages 699–705. Springer US.

[137] Pons, J. A., Viganò, D., and Rea, N. (2013). A highly resistive layer within the crust of X-ray pulsars limits their spin periods. *Nature Physics*, 9:431–434.

[138] Potekhin, A. (2010). The physics of neutron stars. *Uspekhi Fizicheskih Nauk*, 180(12):1279.

[139] Powell, K. G., Roe, P. L., Linde, T. J., Gombosi, T. I., and De Zeeuw, D. L. (1999). A Solution-Adaptive Upwind Scheme for Ideal Magnetohydrodynamics. *Journal of Computational Physics*, 154:284–309.

[140] Pretorius, F. (2005). Evolution of Binary Black-Hole Spacetimes. *Physical Review Letters*, 95(12):121101.

[141] Price, D. J. (2004). *Magnetic fields in Astrophysics*. PhD thesis, Cambridge.

[142] Reifenstein, E. C., Brundage, W. D., and Staelin, D. H. (1969). Crab Nebula Pulsar NPO527. *Physical Review Letters*, 22:311–311.

[143] Reinecke, M., Hillebrandt, W., Niemeyer, J. C., Klein, R., and Gröbl, A. (1999). A new model for deflagration fronts in reactive fluids. A&A, 347:724–733.

[144] Reisenegger, A. (2003). Origin and evolution of neutron star magnetic fields. In *Proceedings of the International Workshop on Strong Magnetic Fields and Neutron Stars*, page 16.

[145] Rezzolla, L. (2003). Gravitational Waves from Perturbed Black Holes and Relativistic Stars. In *ICTP Lecture Series*, page 47.

[146] Rezzolla, L., Baiotti, L., Giacomazzo, B., Link, D., and Font, J. A. (2010). Accurate evolutions of unequal-mass neutron-star binaries: properties of the torus and short GRB engines. *Classical and Quantum Gravity*, 27(11):114105.

[147] Rezzolla, L., Giacomazzo, B., Baiotti, L., Granot, J., Kouveliotou, C., and Aloy, M. A. (2011). The Missing Link: Merging Neutron Stars Naturally Produce Jet-like Structures and Can Power Short Gamma-ray Bursts. ApJ, 732:L6.

[148] Rezzolla, L. and Zanotti, O. (2002). New Relativistic Effects in the Dynamics of Nonlinear Hydrodynamical Waves. *Physical Review Letters*, 89(11):114501.

[149] Roe, P. L. (1981). Approximate Riemann Solvers, Parameter Vectors, and Difference Schemes. *Journal of Computational Physics*, 43:357–372.

[150] Roe, P. L. and Balsara, D. S. (1996). Notes on the eigensystem of magnetohydrodynamics. *SIAM Journal on Applied Mathematics*, 56(1):pp. 57–67.

[151] Ryu, D. and Jones, T. W. (1995). Numerical magetohydrodynamics in astrophysics: Algorithm and tests for one-dimensional flow‘. ApJ, 442:228–258.

[152] Sambasivan, S. K. and Udaykumar, H. S. (2009). Ghost Fluid Method for Strong Shock Interactions Part 1: Fluid-Fluid Interfaces. *AIAA Journal*, 47:2907–2922.

[153] Sathyaprakash, B. S. and Schutz, B. F. (2009). Physics, Astrophysics and Cosmology with Gravitational Waves. *Living Reviews in Relativity*, 12.

[154] Schiesser, W. E. (1991). *The Numerical Method of Lines: Integration of Partial Differential Equations*. Academic Press.

[155] Schoch, S., Nordin-Bates, K., and Nikiforakis, N. (2013). An eulerian algorithm for coupled simulations of elastoplastic-solids and condensed-phase explosives. *Journal of Computational Physics*, 252(0):163 – 194.

[156] Sethian, J. A. (1999). *Level set methods and fast marching methods: evolving interfaces in computational geometry, fluid mechanics, computer vision, and materials science*. Cambridge Univ. Press.

[157] Shapiro, S. L. and Teukolsky, S. A. (1983). *Black holes, white dwarfs, and neutron stars: the physics of compact objects*. John Wiley and Sons.

[158] Shibata, M. and Nakamura, T. (1995). Evolution of three-dimensional gravitational waves: Harmonic slicing case. Phys. Rev. D, 52:5428–5444.

[159] Shibata, M. and Taniguchi, K. (2006). Merger of binary neutron stars to a black hole: Disk mass, short gamma-ray bursts, and quasinormal mode ringing. Phys. Rev. D, 73(6):064027.

[160] Shibata, M., Taniguchi, K., and Uryū, K. ō. (2008). Merger of black hole and neutron star in general relativity. In *Astrophysics of Compact Objects*, volume 968 of *American Institute of Physics Conference Series*, pages 297–306.

[161] Shibata, M. and Uryū, K. ō. (2000). Simulation of merging binary neutron stars in full general relativity: Γ=2 case. Phys. Rev. D, 61(6):064001.

[162] Shu, C.-W. (1998). Essentially non-oscillatory and weighted essentially non-oscillatory schemes for hyperbolic conservation laws. Technical report, NASA, Langley.

[163] Sidery, T., Passamonti, A., and Andersson, N. (2010). The dynamics of pulsar glitches: contrasting phenomenology with numerical evolutions. MNRAS, 405:1061–1074.

[164] Sod, G. A. (1978). A survey of several finite difference methods for systems of nonlinear hyperbolic conservation laws. *Journal of Computational Physics*, 27:1–31.

[165] Sriskantha, H. and Ruffert, M. (2013). A partially dimensionally-split approach to numerical MHD. MNRAS, 432:2579–2590.

[166] Staelin, D. H. and Reifenstein, III, E. C. (1968). Pulsating Radio Sources near the Crab Nebula. *Science*, 162:1481–1483.

[167] Steinbach, I. (2009). Phase-field models in materials science. *Modelling Simul. Mater. Sci. Eng.*, 17(7):073001.

[168] Strang, G. (1968). On the Construction and Comparison of Difference Schemes. *SIAM Journal on Numerical Analysis*, 5:506–517.

[169] Tan, S. and Shu, C.-W. (2011). A high order moving boundary treatment for compressible inviscid flows. *Journal of Computational Physics*, 230:6023–6036.

[170] Taub, A. H. (1948). Relativistic Rankine-Hugoniot Equations. *Physical Review*, 74:328–334.

[171] Taylor, Jr., J. H. (1994). Binary pulsars and relativistic gravity. *Reviews of Modern Physics*, 66:711–719.

[172] Thornburg, J. (2007). Event and Apparent Horizon Finders for 3+1 Numerical Relativity. *Living Reviews in Relativity*, 10.

[173] Toro, E. F. (2009). *Riemann Solvers and Numerical Methods for Fluid Dynamics: A Practical Introduction*. Springer.

[174] Toro, E. F., Spruce, M., and Speares, W. (1994). Restoration of the contact surface in the HLL-Riemann solver. *Shock Waves*, 4:25–34.

[175] Torrilhon, M. (2002). Exact solver and uniqueness conditions for Riemann problems of ideal magnetohydrodynamics. Technical report, Eidgenössische Technische Hochschule.

[176] Torrilhon, M. (2003). Non-uniform convergence of finite volume schemes for Riemann problems of ideal magnetohydrodynamics. *Journal of Computational Physics*, 192:73–94.

[177] Torrilhon, M. and Balsara, D. S. (2004). High order WENO schemes: investigations on non-uniform convergence for MHD Riemann problems. *Journal of Computational Physics*, 201:586–600.

[178] Tóth, G. (2000). The $\nabla \cdot B = 0$ Constraint in Shock-Capturing Magnetohydrodynamics Codes. *Journal of Computational Physics*, 161:605–652.

[179] van Kerkwijk, M. H., Breton, R. P., and Kulkarni, S. R. (2011). Evidence for a Massive Neutron Star from a Radial-velocity Study of the Companion to the Black-widow Pulsar PSR B1957+20. ApJ, 728:95.

[180] Vigelius, M. and Melatos, A. (2010). Gravitational-wave Spin-down and Stalling Lower Limits on the Electrical Resistivity of the Accreted Mountain in a Millisecond Pulsar. ApJ, 717:404–410.

[181] Wang, C. W., Liu, T. G., and Khoo, B. C. (2006). A real ghost fluid method for the simulation of multimedium compressible flow. *SIAM J. Sci. Comput.*, 28(1):278–302.

[182] Wang, S.-P., Anderson, M. H., Oakley, J. G., Corradini, M. L., and Bonazza, R. (2004). A thermodynamically consistent and fully conservative treatment of contact discontinuities for compressible multicomponent flows. *J. Comput. Phys.*, 195(2):528–559.

[183] Weber, J. (1968). Gravitational-Wave-Detector Events. *Physical Review Letters*, 20:1307–1308.

[184] Weisberg, J. M., Nice, D. J., and Taylor, J. H. (2010). Timing Measurements of the Relativistic Binary Pulsar PSR B1913+16. ApJ, 722:1030–1034.

[185] Weymouth, G. D. and Yue, D. K.-P. (2010). Conservative Volume-of-Fluid method for free-surface simulations on Cartesian-grids. *Journal of Computational Physics*, 229:2853–2865.

[186] Winkler, K. and Norman, M. (1986). *Astrophysical radiation hydrodynamics*. Springer Netherlands, Dordrecht.

[187] Xu, L. and Liu, T. G. (2011). Accuracies and conservation errors of various ghost fluid methods for multi-medium Riemann problem. *Journal of Computational Physics*, 230:4975–4990.

[188] Yakovlev, D. G., Kaminker, A. D., and Levenfish, K. P. (1999). Neutrino emission due to Cooper pairing of nucleons in cooling neutron stars. A&A, 343:650–660.